UCLouvain
Louvain Drug Research Institute
Biomedical Magnetic Resonance
Advanced Drug Delivery and Biomaterials

Assessment of strategies for a blood-brain barrier opening in glioblastoma

Jérôme Conq

Thèse présentée en vue de l'obtention du grade de docteur en sciences biomédicales et pharmaceutiques

Director: Pr Bernard Gallez
Co-director: Pr Véronique Préat

2024

FOREWORD

Glioblastoma (GB) is the most common and malignant type of primary brain cancer in adults, with poor prognosis. Its aggressiveness, heterogeneity and resistance to current standard treatment with high recurrence rates makes it a formidable challenge in the realm of neuro-oncology. The blood-brain barrier (BBB) complicates treatment by hindering drug delivery to the tumor site, especially to the infiltrative cells in the margin of the tumor, which are mainly responsible for tumor recurrence. Therefore, innovative strategies are needed to enhance drug delivery in the core and in the margins of the tumor. Nowadays, strategies to open the BBB have been described as promising to achieve this objective.

The aim of this Ph.D. thesis is thus to assess different strategies of BBB opening in GB, using various investigative methods based on imaging and histology analyses. The strategies used in this work include osmotic shock using hypertonic mannitol solution, irradiation at increasing doses and normalization of tumor vessels via anti-angiogenic agents.

Chapter I – Introduction explains the concepts necessary for understanding this thesis, where the GB, methods for diagnosis, current treatment options and mouse models are first described. Then, BBB features with its associated challenges in GB treatment and the various strategies to open the BBB are explained. After that, currently available methods to assess BBB opening based on imaging techniques and markers/biomarkers of vascular integrity are depicted.

In **Chapter II – Aim of the thesis**, the rationale of the thesis project with the objectives and methodology are described.

In **Chapter III – Assessment of hyperosmolar BBB opening in Glioblastoma via histology with Evans blue and DCE-MRI**, **Chapter IV – Exploring the impact of irradiation on glioblastoma BBB permeability: insights from DCE-MRI and histological analysis** and **Chapter V – Changes in perfusion and permeability in glioblastoma model induced by the anti-angiogenic agents cediranib and thalidomide**, we evaluate the impact of three different BBB opening strategies on the tumor perfusion and vascular permeability in glioblastoma.

Finally, **Chapter VI – Discussion and perspectives** gathers the major findings of this Ph.D. thesis. The advantages and limitations of the strategies used in our studies and the methods for evaluating them are discussed. In addition, we provide perspectives regarding strategies to open

the BBB, the assessment of techniques to tackle BBB opening and the effectiveness of the combination of BBB opening together with anticancer drugs.

ACKNOWLEDGEMENTS

Je tiens à exprimer ma profonde gratitude à toutes les personnes qui ont contribué de près ou de loin à la réalisation de cette thèse. Je suis conscient que cette thèse n'aurait pas été possible sans l'aide précieuse de chacun d'entre vous. Vos contributions ont été cruciales et je suis profondément reconnaissant de vous avoir eu à mes côtés tout au long de ce voyage académique.

Tout d'abord, je voudrais remercier chaleureusement mon promoteur de thèse, Pr **Bernard Gallez**, pour son soutien indéfectible et son expertise précieuse tout au long de ce parcours de recherche. Votre patience, votre engagement et vos conseils avisés ont été des éléments essentiels qui m'ont permis de réaliser cette thèse.

Je souhaite également adresser mes sincères remerciements à ma co-promotrice, Pr **Véronique Préat**, pour sa contribution précieuse à ce travail et pour son assistance continue qui a grandement enrichi cette thèse.

Je remercie les membres de mon comité, Pr **Pierre Sonveaux**, Pr **Thierry Duprez**, Pr **Jean-François Baurain** et Pr **Anne des Rieux** pour leur temps, leurs commentaires constructifs et leurs suggestions avisées qui ont contribué à améliorer la qualité de ce travail. De plus je remercie **Anne** pour l'opportunité qu'elle m'a donnée de faire mon stage de fin d'études de pharmacie au sein de l'équipe ADDB. Sans elle je n'aurais sûrement pas entamé cette thèse en Belgique et je ne serais pas là où je suis aujourd'hui, alors encore merci pour ton accueil chaleureux. Je remercie également Dr **Laurent Lemaire** et Dr **Samuel Valable** qui ont accepté de faire partie de mon jury de thèse, ainsi que pour les discussions et remarques intéressantes lors de ma défense de thèse privée qui ont permis de perfectionner la qualité de ce manuscrit.

Je souhaite ensuite remercier toute **l'équipe REMA**. Merci à **Chloé**, **Natacha**, **Barbara**, **Natalie**, **Mélina**, **Caner**, **Chantale**, **Mohammad**, **Lionel** et **Nicolas** pour tous ces moments passés ensembles et pour avoir rendu la vie de rat de laboratoire plus agréable (surtout quand on n'a pas de fenêtre). Merci pour les sorties escape game, quizz, restaurants, les congrès que l'on a passés ensemble, et surtout pour toutes les discussions postprandiales où l'on cherchait souvent un prétexte pour ne pas retourner travailler, la plupart du temps c'était le chiffre des minutes qui n'était pas (ou plus) le bon pour y retourner. Je tiens à tout particulièrement remercier **Nicolas**, qui m'a soutenu tout au long de cette thèse, surtout au début où ce n'était pas le moment le plus facile, en m'aidant à chaque fois que j'en avais besoin, que ce soit pour

l'IRM (elle ne va pas me manquer celle-là) ou pour le logiciel Matlab (lui non plus ne va pas me manquer), ou encore pour ton aide précieuse pour me faire répéter avant mes comités.

Je tiens également à remercier **l'équipe ADDB**, dans laquelle j'ai fait mes débuts au LDRI. Merci à **Bernard** évidemment, qui, en plus d'être un collègue merveilleux toujours là pour aider tout le monde, est devenu un formidable ami. Merci pour toutes les bières du vendredi soir ensemble, à discuter de tout et de rien et à bien rigoler. J'espère que tu viendras me voir à Amsterdam. Merci à **Mathilde**, toujours le sourire aux lèvres et toujours présente pour discuter, rigoler ensemble ou sortir prendre un verre. Tu es devenue une très bonne amie au fil de ces années et j'espère que l'on arrivera à garder contact malgré la distance de nos nouveaux pays respectifs. Merci à **Kevin**, pour m'avoir toujours apporté ton aide précieuse lorsque j'en avais besoin, ainsi que pour ta gentillesse et pour nos discussions lors des afterworks. Merci à **Yasmine**, **Mingchao**, **Elia**, **Giulia**, **Ariane**, **Floriane**, **Viridiane**, **Alessio** et **Marie** pour tous les bons moments que nous avons pu passer ensemble, au labo et en dehors du labo. Merci également à **Murielle** pour l'aide précieuse que tu m'as apportée pour l'impression de ce manuscrit.

À mes amis/colocataires que j'ai eu le plaisir de rencontrer et côtoyer lors de ces 5 années en Belgique. **Thomas**, **Simon**, **Elise**, **Martin**, **Fanny**, **Hélène**, **Antoine**, **Clémence**, **Lamine**, **Maxime**, **Ariane** et **Quentin**, vous avez été des colocataires magnifiques et êtes devenus des amis tout aussi merveilleux. Nos soirées ensemble vont me manquer, que ce soit les soirées bar, les soirées bouffes à la coloc, les soirées posées devant la télé, les soirées jeu de société ou encore la fameuse Kermesse de Purnode. Un merci tout particulier à **Thomas** (dit Tomtom, Thomiche, Thomou, Toto, ou encore « la poutre » d'après ses dires) qui aura partagé ces 5 années de colocation tout du long avec moi. Merci de m'avoir écouté me plaindre tous les soirs (visiblement c'est mon côté français), d'avoir su supporter mes accès de débilité, de m'avoir transporté en voiture tout autour de la Belgique pour découvrir ce beau pays, de m'avoir fait partager ta passion pour le fromage, et merci pour toutes ces bonnes soirées de beuverie ensemble.

À mes coéquipiers de badminton du jeudi soir, **Nicolas**, **Hrag**, **Pierre-Jean**, **Julien** et **Bernard**, merci pour toutes ces parties de badminton me permettant de me défouler après une dure journée au labo, et surtout merci pour tous ces restaus après l'entraînement qui étaient toujours une bonne occasion de discuter et rire ensemble autour d'un bon repas et d'une (plusieurs) bonne(s) bière(s).

À mes amis de Paris que j'ai laissés derrière moi en venant habiter à Bruxelles, **Romain** (que j'ai hâte de retrouver prochainement à Amsterdam), **Claire**, **Ben**, **Inès**, **Doudou**, **Marie**, **Paul** et **Juliette**, même si l'on n'a pas eu l'occasion de beaucoup se voir ces dernières années, c'était toujours une joie de tous vous revoir lorsque je rentrais à Paris.

À **Julie** également, une bonne amie que j'ai pu rencontrer à Amsterdam par l'intermédiaire d'Anaïs, toujours de bonne humeur et toujours présente pour partager de bons moments de convivialité.

Je tiens ensuite à tout particulièrement remercier une des personnes les plus importantes dans ma vie et qui m'a le plus apporté, **Anaïs**. Tu as toujours été là pour moi depuis que l'on s'est rencontrés sur les bancs de l'université, que ce soit dans les bons comme dans les mauvais moments. Malgré la distance qui nous séparait durant ces 5 années, tu as toujours su me transmettre ton amour, ta joie et ta bonne humeur. Tu as également su me supporter durant toutes ces années, et ça ce n'est pas une mince affaire. Tes encouragements, ton soutien et ta présence réconfortante ont joué un rôle déterminant dans la réalisation de cette thèse, je ne pense pas que j'aurais réussi à aller au bout si tu n'avais pas été là. Un immense merci de faire partie de ma vie, et j'attends avec impatience de venir te retrouver à Amsterdam pour pouvoir enfin commencer notre vie ensemble.

Enfin, un immense merci à **ma famille** pour leur soutien inconditionnel, leur amour et leur compréhension pendant cette période exigeante. Merci à mes parents, **Alain** et **Catherine**, pour avoir toujours cru en moi et pour m'avoir toujours aidé dans les moments difficiles. Vos encouragements et votre soutien ont été un moteur essentiel dans la réalisation de ce projet. Si j'en suis arrivé là où j'en suis aujourd'hui c'est grâce à vous. Merci à ma sœur, **Elodie**, toujours à prendre de mes nouvelles, à me demander comment se passait mon travail et si ma nouvelle vie à Bruxelles se passait bien. Tu as toujours été là pour moi quand j'en avais besoin et je t'en remercie, j'ai énormément de chance d'avoir une sœur aussi aimante que toi. Merci à ma grand-mère, **Christiane**, toujours pleine d'amour, à se soucier de mon bien-être à Bruxelles et à s'intéresser à mon travail de thèse. Enfin, bien qu'ils ne soient plus parmi nous aujourd'hui, je tiens également à remercier mes autres grands-parents, **Jacques**, **Lucienne** et **Henri**.

ABBREVIATIONS

2HG	2 hydroxyl-glutarate
11C-MET	Carbon-11 methionine
18F-FET	Fluorine-18 fluoroethyltyrosine
A2AR	Adenosine 2A receptor
ADC	Apparent diffusion coefficient
Ang-2	Angiopoietin 2
AIC	5-amino-imidazole-4-carboxamide
AMT	Adsorption mediated transcytosis
ASL	Arterial spin labelling
ATRX	α-thalassemia/mental-retardation-syndrome-X-linked
AUC	Area under the curve
B2R	Bradykinin type 2 receptor
BBB	Blood-brain barrier
BTB	Blood-tumor barrier
BOLD	Blood-oxygen-level dependent
CBF	Cerebral blood flow
CDKN2A/B	Cyclin-dependent kinase inhibitor 2A/B
CED	Convection-enhanced delivery
cIMPACT	Consortium to inform molecular and practical approaches to CNS tumor taxonomy
CLX	Cell-line xenograft
CMT	Carrier-mediated transport
CNS	Central nervous system
CSF	Cerebrospinal fluid
CT	Computed tomography
CTLA-4	Cytotoxic T-lymphocyte associated protein 4
Cy5	Cyanine 5
DAPI	Diamidino-2-phenylindole
DCE	Dynamic contrast enhanced
DNA	Deoxyribonucleic acid
DSC	Dynamic susceptibility contrast

DTI	Diffusion tensor imaging
EANO	European association of neuro-oncology
EB	Evans blue
EES	Extravascular extracellular space
EGFR	Epidermal growth factor receptor
ELISA	Enzyme-linked immunosorbent assay
EMEM	Eagle's minimum essential medium
EPI	Echoplanar imaging
FDA	Food and Drug Administration
FITC	Fluorescein isothiocyanate
FLAIR	Fluid attenuated inversion recovery
FLASH	Fast low-angle shot
fMRI	Functional magnetic resonance imaging
FUS	Focused ultrasound
GB	Glioblastoma
GBCA	Gadolinium-based contrast agent
Gd-BOPTA	Gadobenate dimeglumine
Gd-DOTA	Gadolinium-gadoteric acid
Gd-DTPA	Gadolinium-diethylenetriamine penta-acetic acid
GEM	Genetically engineered mouse
GLUT-1	Glucose transporter 1
HRP	Horseradish peroxidase
HSP70	Heat shock protein 70
IDH1/2	Isocitrate dehydrogenase 1 and 2
IgG	Immunoglobulin G
IV	Intravenous
IVIS	In vivo imaging system
IVM	Intravital microscopy
K_{ATP}	ATP-sensitive potassium
KPS	Karnofsky Performance Status
LAT	Large neutral amino acid transporter
LC-MS	Liquid chromatography-mass spectrometry

LC-MS/MS	Liquid chromatography coupled to tandem mass spectrometry
LDLR	Low density lipoprotein receptor
LDR	Low dose rate
LRP1-2	Low density lipoprotein receptor-related protein 1 and 2
MAPK	Mitogen-activated protein kinase
MB	Microbubble
MGMT	O6-methylguanine-DNA methyl-transferase
MPa	Megapascal
MRI	Magnetic resonance imaging
MRS	Magnetic resonance spectroscopy
MTIC	3-methyl-(triazen-1-yl)imidazole-4-carboxamide
nAChRS	Nicotinic acetylcholine receptors
NaF	Sodium fluorescein
NIR	Near-infrared
NOD	Non-obese/diabetic
NOS	Not Otherwise Specified
NSG	NOD/SCID/gamma
OCT	Optimal cutting temperature compound
PCT	Perfusion computed tomography
PD-1	Programmed cell death-1
PD-L1	Programmed death ligand-1
PDX	Patient-derived xenograft
PECAM-1	Platelet endothelial cell adhesion molecule-1
PET	Positron emission tomography
PKA	Protein kinase A
PFA	Paraformaldehyde
PLS	Post-labeling delay
pO_2	Partial pressure of oxygen
QAlb	CSF/serum quotient of albumin
QIgG	CSF/serum quotient of IgG
RARE	Rapid acquisition with refocused echoes
RMT	Receptor-mediated transcytosis

ROI	Region of interest
RT	Radiotherapy
SCID	Severe combined immunodeficient
SD	Sprague-Dawley
SD	Standard deviation
SOC	Standard of care
SPECT	Single photon emission computed tomography
SR-B1	Scavenger receptors class B type 1
TERT	Telomerase reverse transcriptase
TfR	Transferrin receptor
TMZ	Temozolomide
TTF	Tumor-treating fields
VEGF	Vascular endothelial growth factor
VEGFR	Vascular endothelial growth factor receptor
USPIO	Ultrasmall superparamagnetic iron oxid
WHO	World Health Organization
ZO-1	Zonula occludens-1

CHAPTER I
INTRODUCTION

TABLE OF CONTENTS

I. GLIOBLASTOMA

I.1. EPIDEMIOLOGY

Glioblastoma (GB) is the most aggressive and common malignant primary brain tumor in adults, accounting for more than 50% of all gliomas [1-3]. It has an incidence of less than 10 per 100,000 persons and occurs slightly more frequently in males than in females (1.6:1) and in Caucasians compared with other ethnic groups [4-6]. The median age of diagnosis is 64 [1,7] but it can occur at any age. The prognosis for patients with GB remains poor, with a high recurrence rate, a median overall survival of 10 to 16 months and a five-year survival rate of 5%, making it a public health issue [8-11].

I.2. PHYSIOPATHOLOGY AND CLASSIFICATION

In recent years, there have been many changes in the way to classify glioblastoma. The latest classifications by the World Health Organization (WHO) were made in 2007, 2016 and 2021.

I.2.1. 3rd edition of WHO classification

During the 3rd edition of WHO classification in 2007, the WHO established a classification of brain tumors based essentially on the histological characteristics of the tumor [12].

This classification proposes a typing of gliomas according to the predominant cytological type (astrocytic, oligodendrocytic or mixed) and grade (from I benign to IV malignant), the grade being based on the absence or presence of malignant histological criteria.

Glioblastoma is classified as a grade IV diffuse glioma arising from astrocytes [12,13]. Its histopathological features are as follows: rapid endothelial cells proliferation, infiltration of healthy tissues, vascular proliferation with increased blood vessel diameter, thickened basement membranes, necrosis areas with pseudopalisading features and peri-tumoral oedema [14,15] (Figure 1)

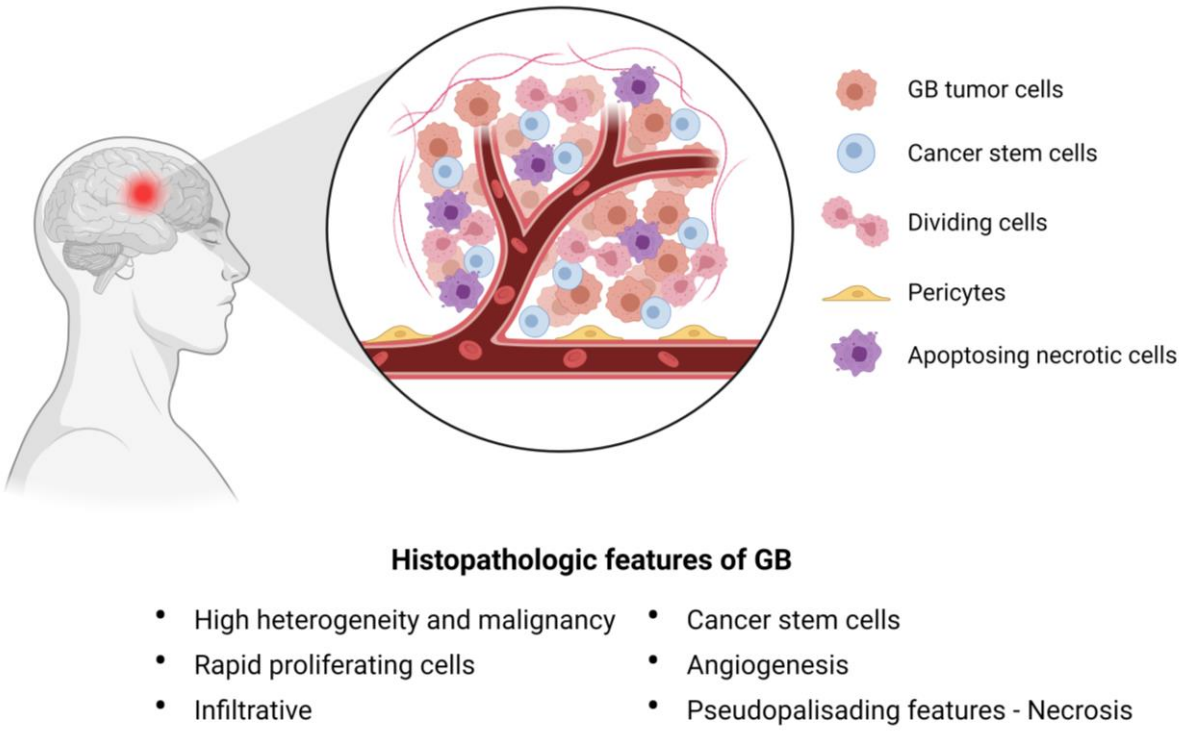

Figure 1. Histopathologic features of GB. Glioblastoma is characterized by intra- and inter-tumoral heterogeneity, rapid proliferation of endothelial cells, heavy infiltration of healthy tissue, extensive vascular proliferation, necrotic areas with pseudopalisading features and peritumoral oedema.

In this classification, a distinction is made between primary (or *de novo*) and secondary GB. Primary GB is the most common (90% of GB). It occurs in patients aged over 60 and is characterized by a short clinical history (< 3 months) with no previous history of glioma (hence the term *de novo*). Secondary GB results from the anaplastic transformation of a grade II or III infiltrating glioma. It occurs in younger patients (45 years), has a longer clinical history, less necrosis and a better prognosis [16].

Although this classification is essential for optimizing treatment, it is still too general and does not reflect the genetic and epigenetic characteristics of the tumor, which can complete the histological analyses and guide the choice of treatment.

I.2.2. Clinically relevant genetic and epigenetic abnormalities in GB

I.2.2.1. IDH1/2 gene mutation

One of the most important discoveries resulting from high-throughput genomic studies, which has led to a remodeling of the understanding of gliomas, including GB, has been the identification of mutations in the genes of metabolic enzymes isocitrate dehydrogenase 1 and 2 (IDH1/2) [17]. The

majority of grade 2, 3 gliomas and secondary GB have this mutation, suggesting that the IDH1/2 mutation could be used as a genetic marker for this type of GB.

IDH is an enzyme involved in the Krebs cycle, allowing the decarboxylation of isocitrate to α-ketoglutarate. The mutated IDH1/2 enzymes have acquired the ability to transform isocitrate not into α-ketoglutarate but into 2-hydroxyl-glutarate (2HG). IDH1/2 mutant cells will have a greatly increased level of 2HG, allowing rapid identification of an IDH mutation in cancer cells. This reduction in α-ketoglutarate production will inhibit the enzymes involved in histone demethylation and therefore in epigenetic regulation. Indeed, histone demethylases are α-ketoglutarate-dependent and cannot function correctly without their cofactors.

These epigenetic changes target notably an important gene in GB genetics: the gene coding for O^6-methylguanine-DNA methyl-transferase (MGMT).

I.2.2.2. MGMT promotor methylation

The promoters of several genes are hypermethylated in GB, leading to an alteration in the expression of tumor suppressor genes.

One of the most clinically important DNA methylation markers in GB is the MGMT promoter, encoding the O^6-methylguanine-DNA methyl-transferase (MGMT) [17]. MGMT is a DNA repair enzyme that has the ability to restore guanine from O^6-methylguanine, which is the type of genomic damage induced by alkylating agents such as temozolomide (chemotherapy used in the treatment of GB) (Figure 3). Promoter methylation of this enzyme results in its inactivation and, consequently, improved efficacy of chemotherapy due to the absence of reparation. It is therefore a good predictive marker of response to the alkylating agents used in GB [18-22]. It is found in around 40% of patients with primary GB. In secondary GB, methylation of the MGMT promoter is generally correlated with the presence of the hypermethylation phenotype induced by IDH mutation, so the majority of secondary GB have the MGMT promoter methylated. Therefore, the IDH mutation also represents a prognostic marker of response to treatment [23].

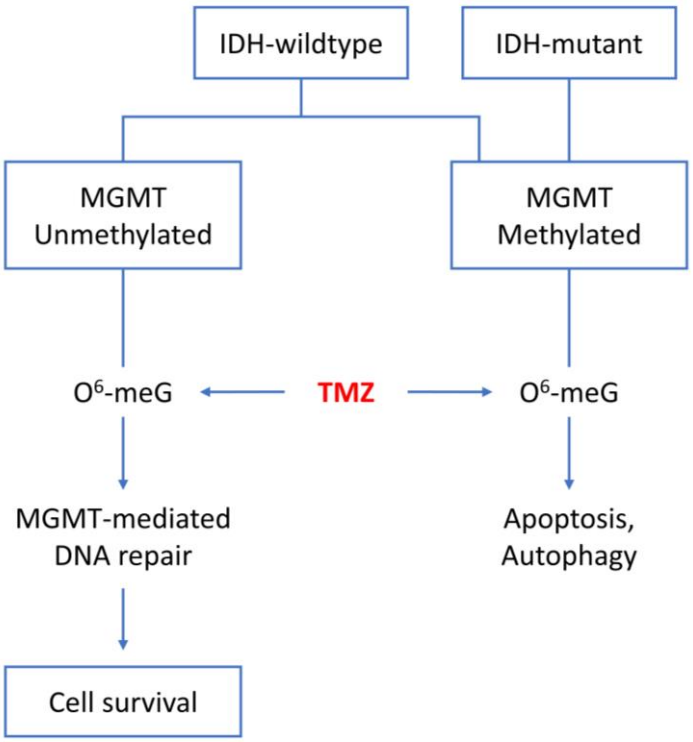

Figure 2. MGMT promoter methylation as a predictive marker for Temozolomide (TMZ) treatment. MGMT is a DNA repair enzyme can restore guanine from O6-methylguanine, which is the type of genomic damage induced by alkylating agents such as temozolomide. Promoter methylation of this enzyme results in its inactivation and, consequently, improved efficacy of chemotherapy due to the absence of reparation. It is therefore a good predictive marker of response to the alkylating agents used in GB. IDH-mutant glioblastomas mainly present a methylated MGMT promoter and therefore have a good response to TMZ treatment, contrarily to IDH-wildtype glioblastomas that can present either a methylated or an unmethylated MGMT promoter. Thus, the IDH mutation also represents a prognostic marker of response to treatment.
Abbreviations: IDH = Isocitrate dehydrogenase; MGMT = O^6-methylguanine-DNA methyl-transferase; O^6-meG = O^6-methylguanine; TMZ = Temozolomide.

Thus, advances in genomic technology have enabled the identification of different molecular subtypes, emphasizing the intra- and inter-tumoral heterogeneity of GB and leading to a revision of the WHO classification in 2016 and 2021.

I.2.3. 4th and 5th editions of WHO classification

The 2016 4th edition of WHO classification incorporates the mutation status of IDH1/2 to characterize the tumor. Thus, diffuse gliomas including oligodendrogliomas and astrocytomas, either low-grade (grade 2 or 3) or glioblastomas (grade 4), were divided into 3 categories: IDH-wildtype, IDH-mutant and NOS (Not Otherwise Specified, for tumors with inconclusive or unavailable genetic testing). IDH-wildtype GB closely corresponds to previously defined primary GB while IDH-mutant most often corresponds to secondary GB [3,16,24].

In 2021, the 5th edition of the WHO classification adopted some recommendations of the "Consortium to Inform Molecular and Practical Approaches to CNS Tumor Taxonomy (cIMPACT)", moving further to advance the role of molecular diagnosis but remaining rooted in the other established approaches to tumor characterization, including histology and immunohistochemistry [25,26]. Indeed, molecular markers, such as *TERT* promoter mutation, *EGFR* gene amplification, +7/-10 chromosome copy-number alterations or the presence of *CDKN2A/B* homozygous deletion, are now involved in the diagnosis of grade 4 diffuse gliomas. In this new classification, a subdivision of diffuse gliomas between adult-type and pediatric-type was added and the classification of adult-type diffuse gliomas was simplified (Table 1). While each grade previously had a specific type of name, the grade within tumor types is now used.

Table 1. Diffuse gliomas in WHO CNS 5 (Adapted from [26]).

Diffuse glioma types	**CNS WHO grade**
Adult-type diffuse gliomas	
Oligodendroglioma, IDH-mutant, and 1p/19q-codeleted	2/3
Astrocytoma, IDH-mutant	2/3/4
Glioblastoma, IDH-wildtype	4
Pediatric-type diffuse low-grade gliomas	
Diffuse astrocytoma, *MYB*-or *MYBL1*-altered	1
Angiocentric glioma	1
Polymorphous low-grade neuroepithelial tumor of the young	1
Diffuse low-grade glioma, MAPK pathway-altered	NA
Pediatric-type diffuse high-grade gliomas	
Diffuse midline glioma, H3 K27-altered	4
Diffuse hemispheric glioma, H3 G34-mutant	4
Diffuse pediatric-type high-grade glioma, H3-wildtype and IDH-wildtype	4
Infant-type hemispheric glioma	NA

Abbreviations: CNS = Central nervous system; IDH = Isocitrate dehydrogenase; NA = Not assigned; WHO = World health organization.

Thus, since 2021, GB is defined as an IDH-wildtype, grade 4, diffuse astrocytic glioma. IDH-mutant diffuse astrocytic glioma, grade 4, is now part of the astrocytoma, IDH-mutant type [25]. Table 2 gathers the definition, genetic alterations and management of these two high-grade adult-type diffuse astrocytic gliomas.

Table 2. Definition of the adult-type grade 4 diffuse gliomas (Adapted from [25-27]).

	Astrocytoma, IDH-mutant, grade 4	**Glioblastoma, IDH-wildtype, grade 4**
Definition	IDH-mutant diffuse infiltrative astrocytic glioma with one or more of the following features: • Microvascular proliferation • Necrosis • *CDKN2A/B* homozygous deletion	IDH-wildtype, H3-wildtype, diffuse infiltrative astrocytic glioma with one or more of the following features: • Microvascular proliferation • Necrosis • *TERT* promoter mutation • *EGFR* gene amplification • +7/-10 chromosome copy-number alterations
Recurrent genetic alterations	*IDH1* or *IDH2* mutation, ATRX loss, *TP53* mutation, *CDKN2A/B* homozygous deletion.	*TERT* promoter mutation, *EGFR* gene amplification, +7/-10 chromosome copy-number alterations, and frequently *MGMT* promoter methylation.
Management and prognosis	Resection and radiation ± alkylating therapy. More indolent than GB, IDH-wildtype, but *CDKN2A/B* deletion is associated with poor prognosis.	Resection and radiation ± alkylating therapy. *MGMT* promoter methylation is associated with better treatment response.

Abbreviations: ATRX = α-thalassemia/mental-retardation-syndrome-X-linked; CDKN2A/B = Cyclin-dependent kinase inhibitor 2A/B; EGFR = Epidermal growth factor; GB = Glioblastoma; IDH = Isocitrate dehydrogenase; MGMT = O^6-methylguanine-DNA methyl-transferase; TERT = Telomerase reverse transcriptase; TP53 = Tumor protein 53.

This clarification in the new WHO classification implies that genetic understanding of GB is essential for diagnosis and will help guide therapeutic management.

I.3. DIAGNOSTIC

I.3.1. Clinical signs and symptoms

There is a wide variety of neurological symptoms depending on the areas of the brain affected by the tumor and its size. However, it is possible to distinguish 3 main syndromic frameworks:

- Motor, sensory, visual neurological deficits and/or disorders of higher, cognitive, language functions.

- Intracranial hypertension syndrome: this is linked to the tumor growth, a significant oedematous peritumoral reaction and/or a blockage of the cerebrospinal fluid outflow tract leading to obstructive hydrocephalus.

- An epileptic syndrome: this may be partial, secondarily generalized, or generalized from the outset. This affects 20-25% of GB patients.

These clinical signs, that are often progressive and insidious, can significantly compromise patients' quality of life and require in-depth medical assessment to establish a precise diagnosis and implement an appropriate treatment plan.

I.3.2. Medical imaging

I.3.2.1. Magnetic resonance imaging (MRI)

Magnetic resonance imaging (MRI) is a non-invasive technique that can provide detailed and multi-parametric information on the anatomy, function and metabolism of the brain. Today, MRI is the reference technique for the management of GB. If GB is suspected, a "multimodal" brain MRI with T1-weighted, T1-weighted with the injection of contrast agent, T2-weighted, FLAIR, diffusion and perfusion sequences should be performed (Figure 3).

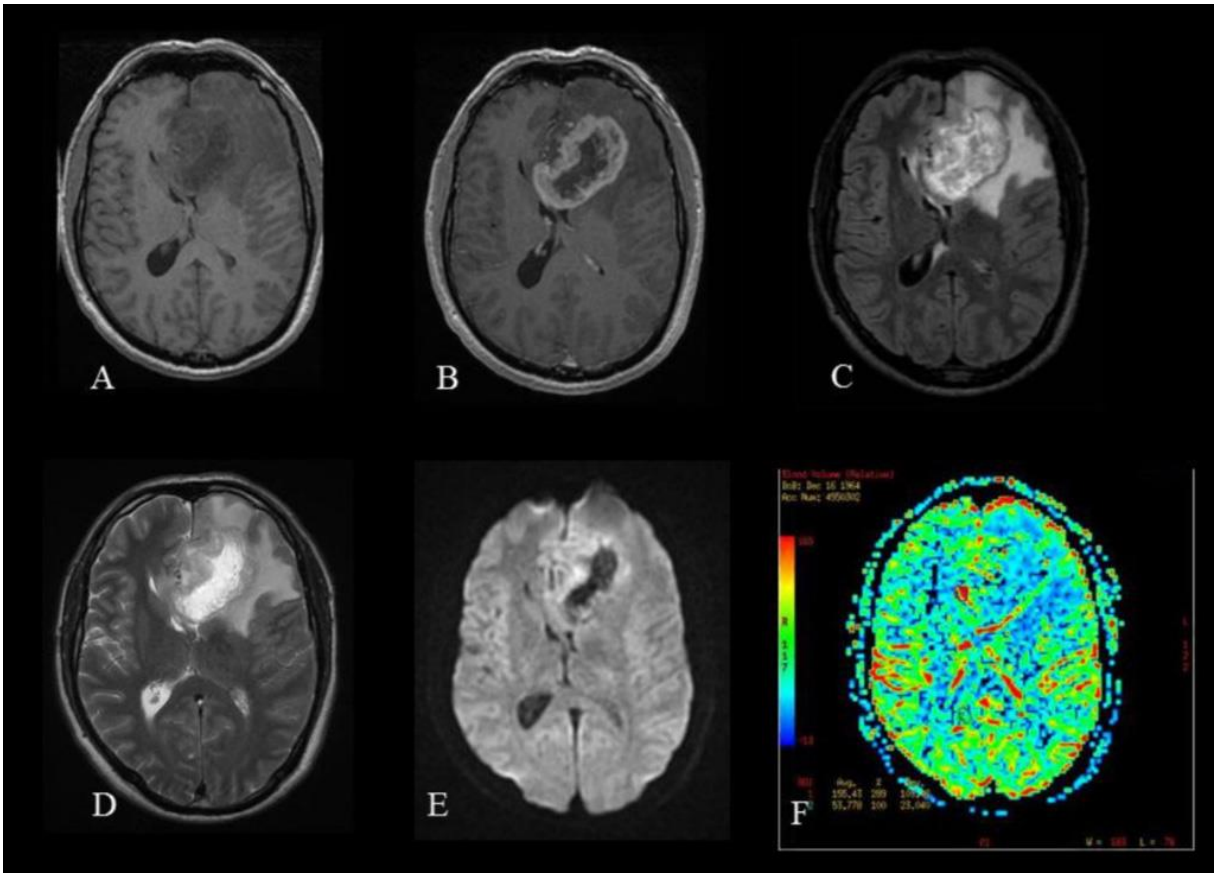

Figure 3. Multimodal brain MRI using T1-weighted (A), T1-weighted with injection of contrast agent (B), FLAIR (C), T2-weighted (D), diffusion (E) and perfusion (F) sequences (adapted from [28]).

I.3.2.1.1 Conventional structural MRI

Several acquisition modes are used in conventional structural MRI [29]:

- T1-weighted imaging: The contrast and brightness of a T1-weighted image are predominately determined by the T1 (spin-lattice relaxation time) properties of tissue. Regions with short T1 (such as fat) appear hyperintense while areas with long T1 (such as CSF) will appear dark. Tumors here will correspond to a hypointense signal. T1-weighted images are considered better for gross structural information.

- T1-weighted imaging with enhancement by a contrast agent (usually gadolinium) [30]: These images will show a hypersignal correlated with the disruption of the blood-brain barrier (BBB). Under normal circumstances, gadolinium does not cross the intact BBB. However, when the BBB is compromised, as in glioblastoma, the gadolinium extravasates from the blood into the brain tissue due to its small size, causing signal enhancement.

- T2-weighted imaging: The contrast and brightness of a T2-weighted image are predominately determined by the T2 (spin-spin relaxation time) properties of tissue. Regions with short T2 appear dark while areas with long T2 will appear bright (such as CSF or regions with high water content). A hyperintense signal is suggestive of a tumor and provides biological information about the tumor (e.g., the presence of oedema).

I.3.2.1.1 FLAIR MRI

FLAIR (Fluid Attenuated Inversion Recovery) is a sequence that suppresses the signal from cerebrospinal fluid (CSF). This sequence is well suited to cerebral imaging and improves the detection of brain parenchyma lesions, particularly those located at the brain parenchyma-CSF interface. Lesions of the brain parenchyma (tumor, inflammation, demyelination processes) appear hyperintense and are particularly well highlighted [31].

I.3.2.1.2 Diffusion MRI

Diffusion MRI enables the study of water molecule movements within biological tissues without the use of an exogenous contrast agent, providing nuanced insights into cellular microstructure. One key parameter derived from diffusion MRI is the Apparent Diffusion Coefficient (ADC). The ADC quantifies the ease with which water molecules move through tissues, offering valuable information about cellular density. Generally, a low ADC can be interpreted as a low water mobility, meaning a high cell density. Thus, ADC is a good factor for assessing tumor grade; the higher the grade, the higher the cell density and therefore the lower the ADC. The lowest ADC is obtained for GB as it is a tumor with a high cellular component [32].

As well as helping to establish the diagnosis, diffusion MRI can also be used to assess the efficacy of cytotoxic treatments used to treat GB (e.g. chemotherapy, radiotherapy). Indeed, the evolution of the ADC and therefore of the cell density allows the monitoring of a potential cytotoxic effect of the treatment on the tumor cells [33-35].

I.3.2.1.3 Perfusion MRI

Perfusion MRI allows to explore the microcirculation and tissue perfusion of the tumor, as well as the permeability of the blood-brain barrier (BBB). This will therefore enable the assessment of tumor angiogenesis and provide information about its malignancy. Two methods are commonly used to measure perfusion using MRI: dynamic susceptibility contrast (DSC) and dynamic contrast enhanced (DCE).

- DSC-MRI: DSC perfusion imaging begins with a bolus of contrast agent (usually gadolinium) injected intravenously, followed by a series of rapidly acquired gradient-echo images of the organ of interest. This technique, also known as bolus tracking MRI, depends only on the first pass of the contrast agent. The image acquisition time here is therefore very short (around 2 min). During its first pass through the systemic circulation, gadolinium remains largely confined to the intravascular space. Because of its paramagnetic properties, gadolinium distorts the local magnetic field around the vessels, causing a T2 (T2*) phase shift and a loss of signal as the bolus passes through. By measuring signal intensity as a function of time and fitting it to a mathematical model, various perfusion parameters such as blood volume, blood flow and mean transit time can be extracted. The variations in these different perfusion parameters can be used to determine which regions of the lesion show hyper-microvascularization.

- DCE-MRI: As with DSC-MRI, DCE-MRI also requires an exogenous administration of a gadolinium-based contrast agent. However, DCE-MRI exploits the T1-shortening effects of gadolinium, acquiring repeated T1-weighted images over an interval of approximately 5 to 10 minutes. During this time, gadolinium contrast accumulates in the extracellular tissue space at a rate determined by perfusion, capillary permeability and surface area. Image data can be analyzed visually or semi-quantitatively. Full quantification can be obtained by applying a mathematical model to obtain several physiological parameters such as the transfer constant (Ktrans), plasma fractional volume (Vp) or tissue extracellular space fractional volume (Ve).

Ktrans can be used to distinguish high- and low-grade gliomas with a sensitivity and specificity of over 90%, but DCE remains an experimental technique and is not yet widely used in clinical practice [36-39].

I.3.2.1.4 Functional MRI

Cerebral functional magnetic resonance imaging (or fMRI) is based on real-time observation of variations in blood oxygenation, without the injection of contrast agents [40]. This is a cerebral imaging technique that measures the activity of brain areas in vivo by detecting local changes in blood flow. Indeed, any neuronal activation is associated with a local increase in blood flow in order to cover the metabolic needs related to this activation (neurovascular coupling). This will modify the local ratio between oxyhaemoglobin (diamagnetic) and deoxyhaemoglobin (paramagnetic), resulting in the appearance of a measurable magnetic signal, the BOLD signal (Blood-Oxygen-Level Dependent). Statistical analyses are used to extract the signal, and brain activity is then visualized graphically by superposing the BOLD signal and an anatomical MRI scan. fMRI is not used here to make the diagnosis as such, but is performed as part of the pre-operative work-up to identify functional regions in the proximity of the tumor.

I.3.2.2. CT-scanner

CT-scanner is a medical imaging technique that combines a series of X-ray images taken from different angles around the body and uses computer processing to create cross-sectional images. It is used as a first-line imaging procedure for primary care in emergency departments, due to its ease and speed of access. It is therefore an essential part of the diagnostic management of glioblastoma, although MRI remains the gold standard for chronic fine-tuning. Historically, CT scan was also mainly used for patients with medical devices contraindicated for MRI, such as pacemakers, hearing implants and automated injection equipment (insulin pumps), but nowadays these medical devices are more and more compatible with MRI.

I.3.2.3. Positron emission tomography

Even though its resolution is lower than MRI, Positron emission tomography (PET) is still widely used nowadays in neurooncology to facilitate the diagnosis of gliomas. Indeed, PET with amino-acid radiotracers, including carbon-11 methionine (11C-MET) and fluorine-18 fluoroethyltyrosine (18F-FET), is a well-established tool in the evaluation of glioma patients in different phases of disease. In particular, it is accepted that PET can provide added value in the diagnosis of progression versus pseudoprogression in glioblastoma and can also provide additional arguments, such as more metabolic information of the tumor, in the event of an ambiguous situation on MRI [41-45].

I.3.3. Biopsy

Tumor tissue is required for histological and molecular determination of the grade and type of glioma. Sufficient material must be collected to allow analysis of molecular factors in order to clarify the diagnosis and prognosis and/or provide potential therapeutic targets, such as determining the methylation status of the MGMT promoter [46].

I.4. THERAPEUTIC PROCEDURE

I.4.1. Standard of care for GB

The current standard of care (SOC) for GB is based on a protocol described by Stupp et al. in 2005 [47]. The treatment consists of removing as much tumor tissue as possible by surgical resection, followed by adjuvant radiotherapy and chemotherapy to eradicate residual tumor cells and prevent recurrence.

I.4.1.1. Surgery

Surgery is an individual approach, which involves striking the right balance to minimize morbidity while maximizing quality of life and prolonging survival. Surgery aims to relieve intracranial pressure by reducing the tumor mass. Depending on the location of the tumor and its accessibility, a standard craniotomy, awake craniotomy or biopsy is performed [48].

Standard craniotomy is performed in the majority of GB surgeries. The tumor is targeted beforehand using various imaging techniques, and the resection must be as wide and as precise as possible to remove as much tumor tissue as possible while sparing healthy tissue and functional areas of the brain. When the GB is close to eloquent areas of the cortex, awake craniotomy can be considered, even though it is rarely performed in clinics as it is complex to set up (few hospitals have the necessary equipment) and can be traumatic for the patient. For patients with unresectable tumors or multiple co-morbidities unable to tolerate extensive cranial surgery, they will only undergo a stereotactic needle biopsy. This is the least invasive way to obtain tissue for diagnosis. In newly diagnosed GB, complete surgical resection provides better survival than biopsy or subtotal resection [49,50]. However, the highly invasive nature of the tumor with infiltrating tumor cells extending well beyond the visible tumor mass as well as the location of the tumor render total resection difficult or even impossible and lead to inevitable recurrences [51].

I.4.1.2. Radiotherapy

Post-operative radiotherapy is one of the mainstays of GB treatment. It has been shown to improve survival and quality of life compared with supportive care alone [52]. The standard dose of irradiation is 60 Gy divided into 30 sessions over 6 weeks [53,54]. However, the dose of irradiation administered varies according to the patient's age and the Karnofsky Performance Status (KPS) due to tolerance problems. The KPS is a scale that allows the estimation of the ability of patients to perform daily living activities and ranges from 0 (dead) to 100 (no evidence of disease) [55]. A KPS score higher than 70, ensuring independence in daily activities, is considered a good prognostic factor [56]. Therefore, for patients aged over 70, a dose of 50 Gy fractionated over 28 sessions is better tolerated [57]. Patients with unfavorable prognostic factors (defined by age and/or KPS) can also be treated with hypofractionated radiotherapy such as 40 Gy in 15 fractions. Radiotherapy also remains the treatment of choice for unresectable tumors.

I.4.1.3. Chemotherapy

Temozolomide (TMZ) is the standard drug used in the treatment of glioblastoma. It is a DNA alkylating agent of the imidazotetrazine class whose mechanism of action is described in Figure 4.

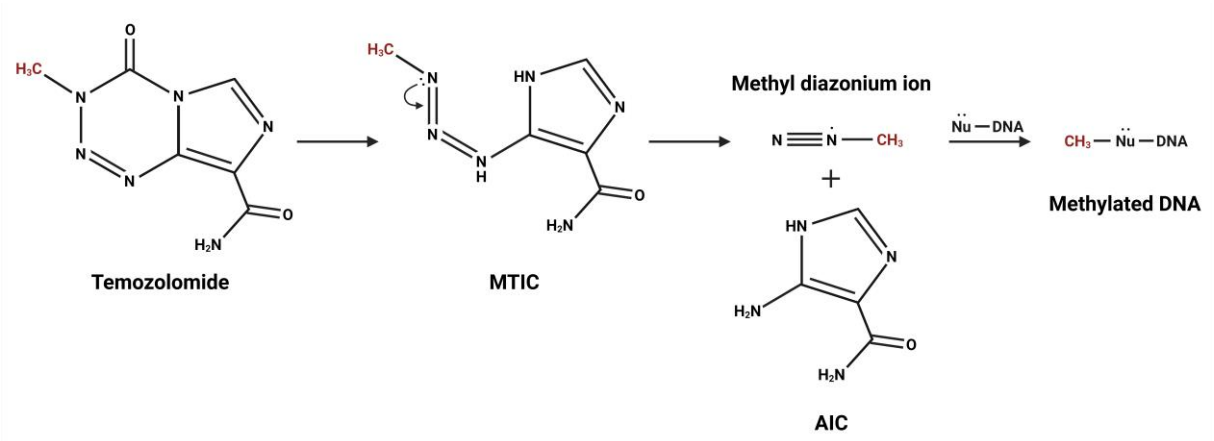

Figure 4. Temozolomide mechanism of action [58]. At physiological pH, TMZ is spontaneously hydrolyzed into 3-methyl-(triazen-1-yl)imidazole-4-carboxamide (MTIC). MTIC is then hydrolyzed into 5-amino-imidazole-4-carboxamide (AIC) and methyldiazonium ions. Methyldiazonium ions react with the DNA and transfer their methyl groups to it. This DNA methylation causes single and double DNA strand breaks and leads to cell apoptosis.

TMZ is a small (194 Da) hydrophilic molecule (logP = -1.153). It is a stable prodrug at acidic pH, allowing oral administration, but is unstable above pH 7, with a plasmatic half-life of 1.8 h. At physiological pH, TMZ is hydrolyzed into 3-methyl-(triazen-1-yl)imidazole-4-carboxamide (MTIC). MTIC is then hydrolyzed into 5-amino-imidazole-4-carboxamide (AIC) and methyldiazonium ions. Methyldiazonium ions react with the DNA and transfer their methyl groups

to it. This DNA methylation causes single and double DNA strand breaks and leads to cell apoptosis [59].

TMZ (Temodal®) is administered orally at a daily dose of 75 mg/m^2 throughout radiotherapy. Four weeks later, maintenance treatment begins with a dose of TMZ of 150 to 200 mg/m^2 per day for 5 consecutive days and six cycles (28 days between each cycle). The dose administered during this maintenance treatment will depend on the patient's tolerance [54,60]. This is the standard of care for adults with newly diagnosed glioblastoma who are in good general and neurological condition and are aged <70 years.

Nevertheless, around 55% of GB patients will be resistant to temozolomide due to their DNA repair system via the MGMT enzyme. Indeed, as described previously, when the MGMT promoter is not methylated, the MGMT enzyme is functional and will repair the genomic damages caused by TMZ. However, MGMT promoter methylation, occurring in 35-45% of GB, results in the inactivation of the enzyme and, consequently, improved efficacy of TMZ due to the absence of reparation [19,23]. Thus, the benefit from temozolomide is largely limited to patients with MGMT promoter-methylated glioblastoma.

To summarize, in order to be more effective, treatment is adapted according to various factors such as:

- The age of the patients: age above 70 years is an unfavorable prognostic factor [56];

- The general conditions of the patients, based on the KPS score: KPS higher than 70 is considered as a good prognostic factor [55];

- The methylation status of the O^6-methylguanine-DNA methyl-transferase (MGMT) promoter: MGMT promoter methylation gives a better response to TMZ and is considered as a good prognostic factor [18-22].

A summary of the recommended adaptation of GB treatment depending on these prognostic factors is presented in Figure 5, taken from the European Association of Neuro-Oncology (EANO) clinical guidelines [56].

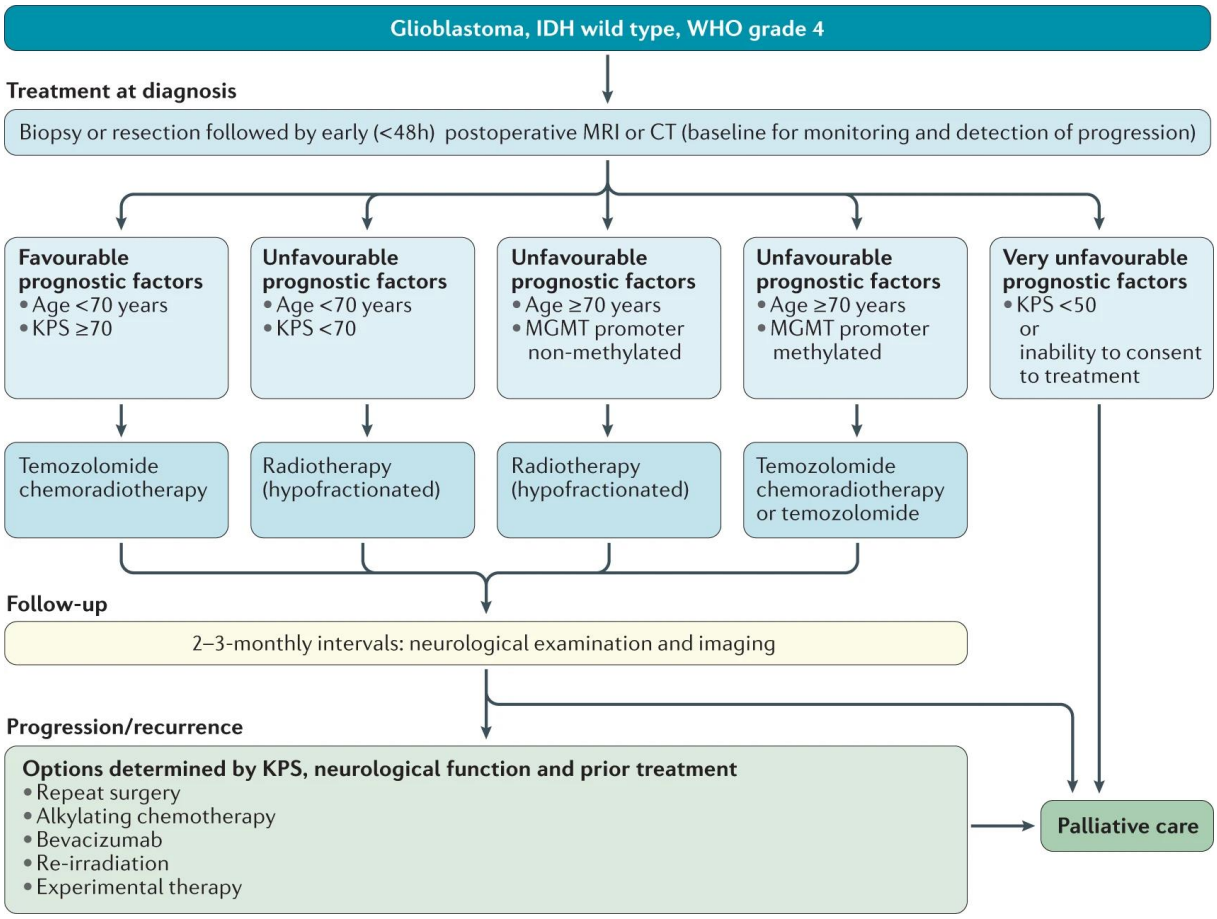

Figure 5. Clinical pathway for glioblastoma treatment, from the EANO guidelines on the diagnosis and treatment of diffuse gliomas of adulthood [56]. Abbreviations: CT = Computed tomography; IDH = Isocitrate dehydrogenase; KPS = Karnofsky Performance Status; MGMT = O^6-methylguanine-DNA methyl-transferase; MRI = Magnetic resonance imaging; WHO = World Health Organization.

However, it is important to note that a recent phase III trial showed that TMZ did not add benefit in the treatment of IDH wildtype glioblastoma compared with radiotherapy alone, regardless of MGMT promoter status [61]. Nonetheless, these findings require a new well-powered prospective clinical study to confirm or refute the real efficacy of TMZ treatment in this patient population. If this is confirmed, it will have a major impact on the therapeutic management of glioblastoma and will require a redesign of the therapeutic protocol presented previously.

I.4.2. Treatment for recurrent GB

Despite maximal initial resection and multimodal treatment, approximately 70% of patients with GB will experience disease recurrence within one year after diagnosis [54]. There is no clear standard of care for the treatment of recurrent GB. The treatment is selected on the basis of prior therapy, age, KPS, MGMT promoter methylation status and patterns of disease progression. It would consist of resection, second-line chemotherapy and/or re-irradiation (Figure 5) [56,62].

Regarding resection, this is considered for certain patients if it is possible. Indeed, surgical reduction can reduce the mass effect and symptoms, such as convulsions and motor deficits, frequently observed in recurrence [60].

For chemotherapy, repeated administration of temozolomide may be considered, although it is often less effective as a second-line agent due to the development of resistance by tumor cells. Bevacizumab (Avastin®), an anti-angiogenic monoclonal antibody that target and inhibit the vascular endothelial growth factor (VEGF), is the most widely used second-line treatment since FDA approval in 2009 (not approved by the European Medicines Agency (EMA)) following phase II trial data [63-66]. However, it is not used as a first-line treatment because, in patients with newly diagnosed GB, the addition of bevacizumab to the SOC protocol did not improve survival time and increased the rate of adverse events [67-69]. Other agents such as carboplatin (Paraplatin®), etoposide (Toposar®), irinotecan (Camptosar®) and nitrosourea-based chemotherapy (lomustine) can be tried as monotherapy or as part of therapeutic regimens [70-73].

Concerning re-irradiation, additional radiation may be possible for some patients, but the tolerance of healthy brain tissue to radiation is limited due to the increased risk of radionecrosis. A wide variety of radiotherapy techniques, including brachytherapy, gamma knife and stereotactic radiosurgery, can be used for the treatment of recurrent GB [74].

Despite this aggressive treatment, the prognosis remains poor. Indeed, the median overall survival of patients diagnosed with GB is approximately 10–16 months, with a 2-year life expectancy lower than 30% [8,9,67]. For patients with unresectable GB (up to 35–40% of patients), which can only be treated with chemoradiotherapy, the prognosis is even worse with a median overall survival of less than 9 months [49-51,75].

I.4.3. Symptomatic treatments

I.4.3.1. Intracranial hypertension treatment

Corticosteroids enable rapid reduction of peri-tumor oedema, thereby reducing intracranial pressure, and also treat inflammation, two factors that are known to influence the prognosis of GB and the patients' quality of life [76,77]. It should be stressed that this is only really effective on benign oedema. Steroids are not necessary in patients without increased intracranial pressure or in the absence of neurological deficits associated with oedema. There is also no benefit in prolonging corticosteroid therapy after tumor resection or as prophylaxis during radiotherapy in asymptomatic patients. However, particular caution is required when administering these drugs to elderly patients

due to the potential risk of delirium, which could lead to a reduction in quality of life [57]. In addition, the use of steroids is now being questioned because of the associated side effects, including severe immunosuppression and risk of infection, which may dampen GB patients' survival. Indeed, recent studies demonstrated that postoperative dexamethasone administration was associated with lower survival as well as steroid dependency and higher infection rate in GB patients [78,79].

I.4.3.2. Epilepsy treatment

Anti-epileptic therapy is indicated only in patients with epileptic seizures. The use of anti-epileptic drugs should be minimized, both to limit the dose to the minimum necessary to control seizures and to use only one drug if possible. This limits side effects and interactions with other drugs such as chemotherapy agents [57].

I.4.4. New therapies

I.4.4.1. Tumor treating fields

Tumor treating fields (TTF) are a treatment modality that can be added to the SOC. This treatment consists of placing electrodes on the patient's scalp to deliver a low-intensity transcutaneous electric field. This electric field delivered to the tumor has an antimitotic effect, interfering with tumor cell division [80]. Approved in 2011 for recurrent GB and in 2015 as adjuvant therapy for newly diagnosed GB, TTF improves patients' survival [9,81]. However, the proportion of patients benefiting from TTF remains low due to its high cost and difficulty of implementation (this treatment must be delivered more than 18 hours/day to be effective).

I.4.4.2. Targeted therapy

Several targeted therapies have been tested in recent years in phase II and III clinical trials for the treatment of glioblastoma.

Bevacizumab in particular, as already mentioned in I.4.2. Treatment for recurrent GB section, which is an anti-angiogenic agent that targets and inhibits VEGF. It has demonstrated efficacy in phase II clinical trials for recurrent glioblastoma and has been approved by the FDA as a second-line treatment in 2009 [64,82,83]. However, it is not indicated as a first-line treatment for GB, as phase III clinical studies showed that the addition of bevacizumab to the SOC protocol for the treatment of newly diagnosed GB did not increase patient survival and increased the rate of adverse effects [67,68].

Cilengitide (a selective inhibitor of αvβ3 and αvβ5 integrins, acting as an anti-angiogenic) [84,85], erlotinib (an anti-EGFR tyrosine kinase inhibitor) [86], gefitinib (an anti-EGFR tyrosine kinase inhibitor) [87], nimotuzumab (an anti-EGFR monoclonal antibody) [88] or cetuximab (an anti-EGFR monoclonal antibody) [89] have also been the subject of clinical trials in both newly diagnosed and recurrent glioblastoma, but have not shown significant clinical improvement.

Recent studies have also focused on the inhibition of IDH 1 and 2 in the treatment of gliomas. Although IDH inhibitors for the treatment of gliomas are still under investigation, two phase I studies evaluating ivosidenib (mIDH1 inhibitor) and vorasidenib (mIDH1/2 inhibitor) showed stable disease prolongation and reduced growth of non-enhancing tumors for patients treated with ivosidenib, and an overall response rate of 18% in non-enhancing gliomas for patients treated with vorasidenib [90,91].

I.4.4.3. Immunotherapy

The success of immunotherapy in oncology in recent years has led to its use in developing therapeutic strategies for GB. Several approaches are currently being tested in glioblastoma, either as first-line treatment or at recurrence. These include vaccination, "adoptive" immunotherapy and immunological checkpoint inhibitors [92].

Vaccination consists of inducing and/or restoring a non-productive immune response against tumor antigens. For this strategy, sitoiganap (Gliovac™), a vaccine based on freshly extracted tumor cells and lysates that stimulates the patient's immune system to recognize and reject cancer cells, is currently undergoing a phase II clinical trial for recurrent GB (NCT01903330) and recently received FDA Fast Track designation in 2022 for recurrent GB [93]. We can also mention rindopepimut, a conjugate vaccine directed against an amino acid of EGFRvIII, which showed promising results in a phase II clinical trial with an increase in median overall survival [94].

Regarding "adoptive" immunotherapy, it involves using autologous T cells, activating them ex-vivo against specific tumor antigens and then injecting them into the same patient. In glioblastoma, an adoptive immunotherapy approach using chimeric receptors targeting HER-2 or EGFRvIII has shown encouraging preclinical results [95,96].

Finally, a last strategy to improve the immune response against cancer is by modulating immune checkpoints to potentiate T cells. The main immune checkpoints that have been successfully targeted in cancer treatments are PD-1 (programmed cell death- 1), its ligand PD-L1, and CTLA-4 (cytotoxic T-lymphocyte-associated protein 4). Inhibition of these T cell negative regulators with monoclonal antibodies increases the immune response in many cancers (e.g., melanoma and non-

small-cell lung cancer) [97,98]. Several clinical trials are currently ongoing for this strategy in glioblastoma, such as phase II clinical trial evaluating blockade of the PD-1/PD-L1 pathway with durvalumab (NCT02336165), or phase I and III clinical trials evaluating combined blockade of the CTLA-4 and PD-1/PD-L1 pathways with the dual therapy nivolumab (anti-PD-1) and ipilimumab (anti-CTLA-4) (NCT02311920, NCT02017717).

I.4.4.4. Local delivery

Local administration strategies offer many significant advantages, such as bypassing the BBB and exposing the tumor to high concentrations of chemotherapy while minimizing systemic toxicity [99]. The drug is protected from degradation and the clearance system until it is released. In the 1990s, convention enhanced delivery (CED) for intratumoral administration, wafers and rigid implants for localized treatment in the resection cavity were developed, leading to the approval by the FDA of Gliadel® implants in 1996 (it is the only biodegradable interstitial chemotherapy approved to date by the FDA for GB) [100]. In the 2000s, hydrogels and nanofibers were studied to increase the efficacy and the biocompatibility of the treatment [101]. And finally, innovative drug delivery systems such as spray devices are currently under investigation [102].

I.5. MOUSE MODELS OF GLIOBLASTOMA

Preclinical mouse models are essential for analyzing the biology of glioblastoma, identifying new therapeutic targets, and evaluating the potential of new therapeutic strategies. Current preclinical glioblastoma models are classified into three categories: xenografts, syngeneic and genetically engineered mouse models (Figure 6).

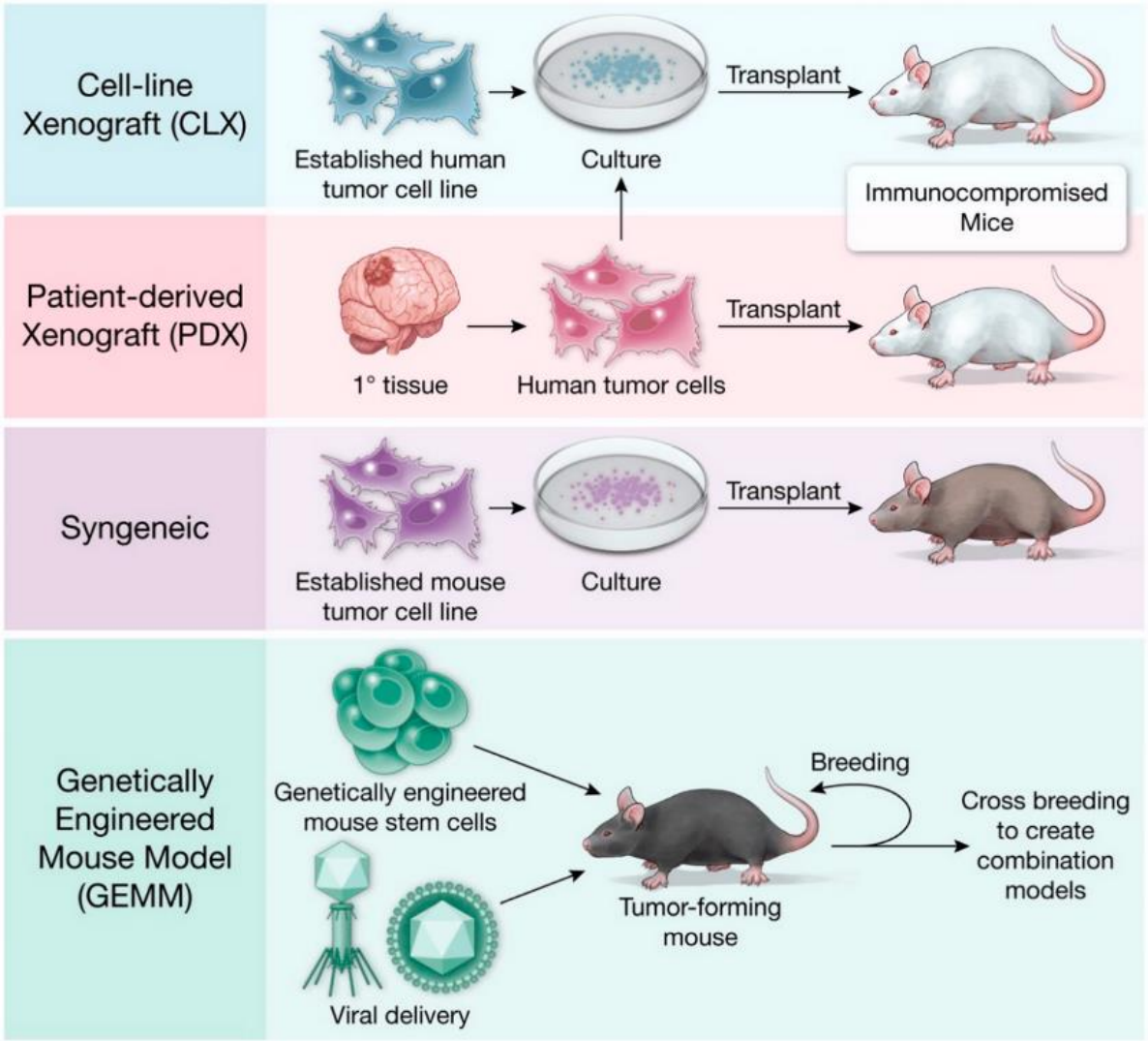

Figure 6. Murine preclinical cancer models (adapted from [103]). Current preclinical glioblastoma models are classified into three categories: xenografts, syngeneic and genetically engineered mouse models. Xenografts mouse models are subclassified into two categories: human glioblastoma cell-line xenografts (CLX) and patient-derived xenografts (PDX). CLX are experimental models in which human glioblastoma tumor cells are transplanted into mice. PDX involve the harvesting of tumor tissue directly from glioblastoma patients, which is then transplanted into mice. Syngeneic mouse models transplant murine glioblastoma cells into mice. Finally, genetically engineered mouse (GEM) models involve the manipulation of the mouse genome to induce tumor formation.

I.5.1. Xenograft mouse models

Xenografts mouse models are subclassified into two categories: human glioblastoma cell-line xenografts (CLX) and patient-derived xenografts (PDX).

I.5.1.1. Human glioblastoma cell-line xenografts

Human glioblastoma cell-line xenografts (CLX) are experimental models in which human glioblastoma tumor cells are transplanted into non-human host organisms, usually mice. Human glioblastoma cell-lines commonly used for xenografts include, among others, U87, U251, T98G and A172. CLXs are a quick and reproducible strategy for studying glioblastoma. Indeed, these models generally offer the advantages of high engraftment and growth rates, good reproducibility as well as reliable disease growth and progression. Moreover, immortalized cell lines can be easily expanded for an unlimited number of *in vitro* passages, producing large numbers of tumor cells for experimental use [104].

However, studies have reported that glioblastoma CLXs do not reflect the clinical characteristics of the patient's original tumors [105]; they often result in well-circumscribed tumors that lack the typical infiltrative and proliferative pattern that is observed in human glioblastomas [106-108]. In addition, due to the selective pressures of cell culture, CLXs show phenotypic and genomic differences from the patient's original tumors, such as a loss of tumor heterogeneity [104,109-112]. Thus, CLXs do not truly reflect the biological nature of glioblastoma, which is a limitation for preclinical trials.

Nevertheless, it has been shown that the U87MG model presents an enhancement of the post-contrast T1 signal (gadolinium-DOTA as contrast agent) in the bulk of the tumor but not in its periphery (Figure 7), thus illustrating that this model has a disrupted BTB in the core of the tumor and an intact BTB in the periphery which is the tumor characteristic that mainly interests us here for the studies we have carried out.

Another drawback of CLX models is that they can only be established in immunodeficient mice such as nude mice, non-obese/diabetic mice (NOD), severe combined immunodeficient mice (SCID), and the combination NOD/SCID and NOD/SCID/gamma (NSG) mice [103]. CLX models will therefore have no immune response, resulting in a tumor microenvironment that is not representative of glioblastoma and, more importantly, does not allow to study immunology and immunotherapy in glioblastoma.

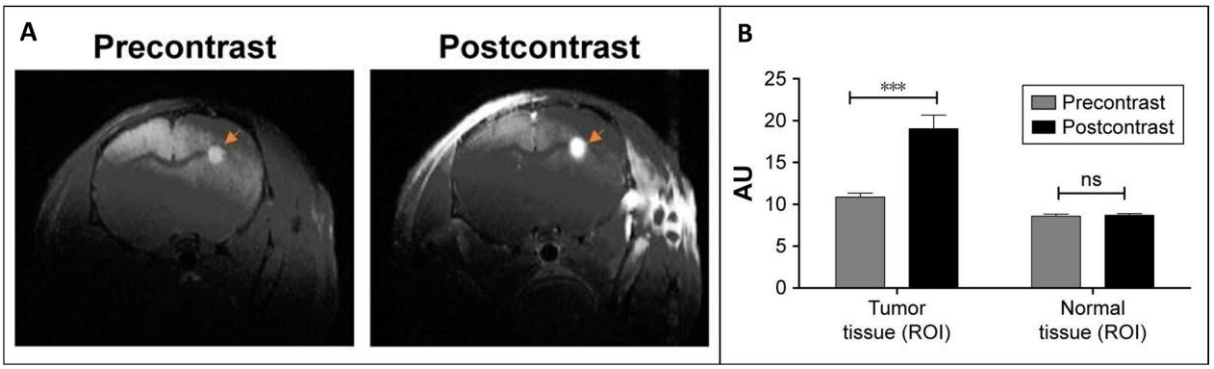

Figure 7. Illustration of BBB disruption in U87MG glioblastoma model (Adapted from [113]). (**A**) Representation of pre- and postcontrast MRI images of brain tissue highlighting the tumor region (right). Accumulation of T1 contrast agent (Gd-DOTA) enhanced the signal intensity and can be visualized from pre- and postcontrast images. (**B**) Quantification of signal intensity in ROI of tumor tissue versus normal tissue shows a significant difference in signal intensity values between pre- and postcontrast tumor tissue, whereas there is no difference in the normal regions. This illustrates that the U87MG model has a disrupted BTB in the core of the tumor and an intact BTB in the periphery of the tumor.

I.5.1.2. Patient-derived xenografts

Patient-derived xenografts (PDX) involve the harvesting of tumor tissue directly from glioblastoma patients, which is then transplanted into host animals, usually mice. In contrast to CLX models, PDX models have the advantage of preserving the histological and genetic characteristics of the original tumor [114,115]. Indeed, as PDX models have minimal or no exposure to *in vitro* culture, PDX cells are therefore not subject to the stress that can occur in cell culture, thus preserving the features of the original tumor. It should also be highlighted that PDX models are highly variable, reflecting the inter-patient heterogeneity of glioblastoma, but it is advantageous due to their clinical relevance. Thus, PDX models are better suited to summarize the characteristics of parental tumors than CLX models [116].

However, PDX models also have disadvantages. They cannot be established from all patient tumors and take a long time to produce. Indeed, even if the graft is successful, it generally takes between 2 and 11 months to obtain tumors [117]. In addition, due to the high variability of these models, standardization and experimental planning can be difficult [104].

Moreover, as with CLX models, they cannot fully reflect the antitumoral immunity of human glioblastoma given that these models are only established in immunodeficient mice (using the same mice as those described for CLX models) [114]. Nevertheless, recent studies have shown that PDX models can be established in humanized mice. Humanized mice are generated with a competent human immune system. This would provide PDX models with a competent human immune system that could be used to study immunology and immunotherapy in glioblastoma [118,119].

I.5.2. Syngeneic mouse models

Syngeneic mouse models have long been used as indispensable tools in glioblastoma research. As for CLX models, these models transplant glioblastoma tumor cells into mice. But for syngeneic mouse models, the cell lines used are established from spontaneous (e.g., P560) or chemically induced (e.g., GL261, GL26 and CT-2A) murine gliomas [120]. The creation of such models takes a short period of time, since transplanted cells grow in the animal within a few weeks.

GL261 models are probably the most widely used glioblastoma syngeneic mouse models. These models are thought to well recapitulate the histological and biological characteristics of glioblastoma. Furthermore, the greatest advantage of syngeneic models is that they use immunocompetent mice and are therefore suitable for analyzing the immunology of glioblastoma tumors and for immunotherapeutic research.

However, like other models based on cell-lines propagation, syngeneic mouse models are subject to genetic drift [108]. In addition, since syngeneic models involve exclusively mouse tissues, they present challenges for translating results into human cancer. Thus, these models do not fully recapitulate the morphological characteristics of human glioma [121].

I.5.3. Genetically engineered mouse models

Genetically engineered mouse (GEM) models involve the manipulation of the mouse genome to induce tumor formation. These models are particularly useful to identify the molecular events responsible for tumor initiation and progression, as well as to analyze tumor susceptibility to treatment [122]. Furthermore, GEM models enable the activation of relevant oncogenes at specific time points in tissue development, allowing to test potential therapeutic agents at various stages of tumorigenesis. As with syngeneic models, a key advantage of this model compared to xenograft models is that it can be used on immunocompetent mice. These GEM models are therefore also useful to analyze the role of microenvironment in tumor biology [103].

However, it is uncertain whether the genetic modifications involved in these models actually reflect tumor-associated events in human glioblastomas. Furthermore, GEM tumors are generally composed of cells with specific and homogeneous genetic modifications and therefore cannot fully reflect the intratumoral genomic and phenotypic heterogeneity of glioblastoma. Thus, these different properties offer distinct advantages over the other models described previously.

I.5.4. Heterotopic versus orthotopic models

Whether syngeneic or xenogeneic, heterotopic and orthotopic grafting models each have their advantages and disadvantages.

Heterotopic models are generally easier to optimize. Indeed, the grafting technique requires little equipment, is quick and easy, and therefore suffers little variability between technicians. Tumor growth or regression can be directly observed and the volume measured using a caliper. Moreover, surgical removal of the tumor can be easily performed, as the tumor is very accessible. However, the anatomical graft site of the heterotopic model is usually very different from the organ in which the tumor normally develops. The tumor's interactions with the microenvironment will therefore not be superimposable with the pathological process to be evaluated. In addition, a tumor's response to treatment depends partly on its localization, making this model a poor predictor of therapeutic response.

It was therefore crucial to develop orthotopic models. Indeed, although less easy to implement, a tumor implanted on an orthotopic site will be more likely to reflect the cellular composition of the original tumor than one implanted on a heterotopic site. Interactions with the tumor microenvironment will also be more representative of the tumor to be modeled. Furthermore, as mentioned above, the diffusion of a molecule varies from one tissue to another, so testing the action of a new treatment on an orthotopic model is more relevant from a pharmacological point of view. Nevertheless, depending on the type of cancer and therefore the site of implantation, the tumor will probably be more difficult to observe and measure than in the heterotopic model.

I.6. CHALLENGES ASSOCIATED WITH THE DELIVERY OF DRUGS TO GLIOBLASTOMA

While there have been advances in clinical practice and technology, the combinations of therapeutic methods available today to treat GB have not yet overcome the high mortality and recurrence rates.

A key obstacle in the treatment of GB is the blood-brain barrier (BBB). Indeed, it significantly inhibits the passage of drugs from the bloodstream to the brain, greatly reducing the efficacy of systemic administration of chemotherapeutic agents [123,124]. In GB, although the integrity of the BBB is compromised in the core of the tumor, making it relatively permeable, an intact BBB is still found peritumorally (Figure 8) [125,126]. This heterogeneity in the tumoral BBB permeability limits the delivery of drugs to the tumor site, especially for the most infiltrative tumor cells still protected by an intact BBB in the tumor margins, which are responsible of the tumor recurrence [127-129]. These anatomical limitations will therefore restrict the choice of chemotherapy to be used.

Although TMZ can cross the BBB in glioblastoma due to its small size, its efficacy in the treatment of GB remains relative. Indeed, a recent phase III trial showed that TMZ did not add benefit in the treatment of IDH-wildtype GB compared with radiotherapy alone, regardless of MGMT promoter status [61]. Clearly, the restriction imposed by the structure of the BBB for the choice of chemotherapies is an obstacle that needs to be overcome in order to be able to use therapeutic agents that are more effective than TMZ.

Over the last years, new therapeutic strategies have emerged to overcome these limitations, and this is what we are going to see in this second part.

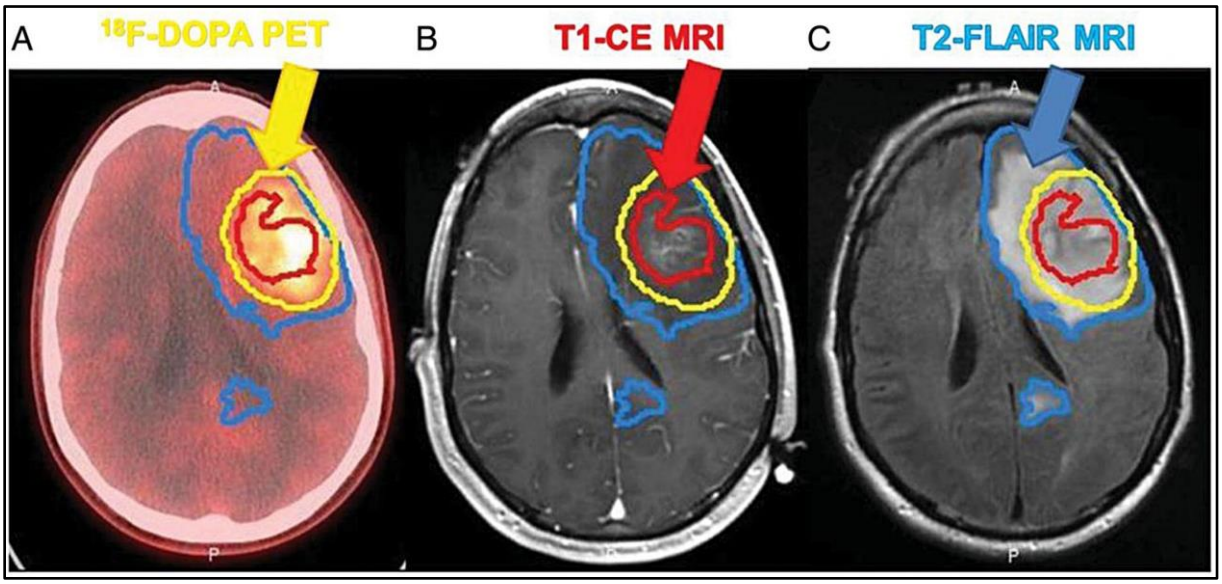

Figure 8. Illustration of the BBB heterogeneity in Glioblastoma. (Adapted from [126]). Here are represented images from the same patient of (**A**) 18F-DOPA uptake imaged by PET-CT delineated in yellow, (**B**) regions of contrast accumulation in the same location defined by a T1 postcontrast enhanced MRI delineated in red, (**C**) regions of tumor-associated edema as defined by a T2-FLAIR MRI delineated in blue. These images illustrate that significant tumor burden exists beyond the disrupted BBB defined by the contrast enhancement and confirm the heterogenous characteristic of the BBB in glioblastoma with a fenestrated BBB in the tumor core and an intact BBB in the tumoral periphery.

II. OVERCOMING THE BBB: INNOVATIVE THERAPEUTIC STRATEGIES

II.1. BBB

II.1.1. BBB structure

The BBB is a complex multicellular structure separating the central nervous system (CNS) from the systemic circulation. It acts as a selective filter that regulates the passage of essential biological substances (ions, oxygen, nutrients, …) between blood and brain compartments, while limiting the invasion of toxins and pathogens in order to protect nervous tissue. This brain protection function complicates drug treatments since many active molecules cannot cross the BBB [130,131].

To fulfil its function, the BBB has a unique anatomy (Figure 9): it is composed of adjacent endothelial cells, a basal lamina, pericytes and astrocytes [132].

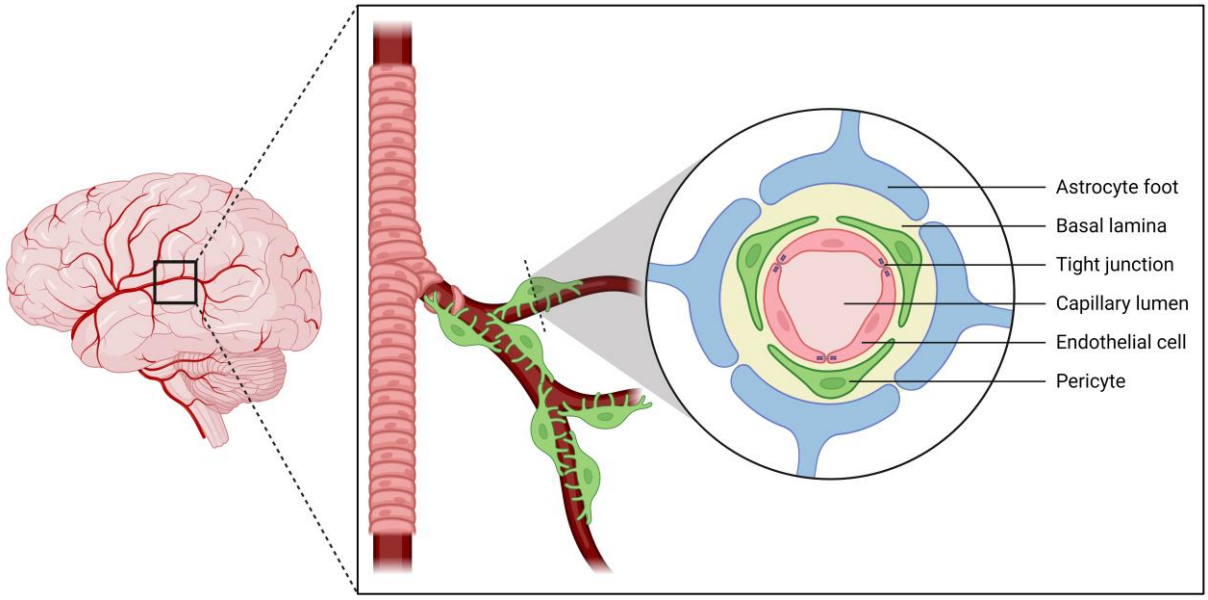

Figure 9. The anatomical structure of the BBB [133]. The blood-brain barrier (BBB) is a complex anatomical structure that protects the brain from harmful substances and regulates the passage of molecules between the bloodstream and the brain. It is mainly composed of endothelial cells tightly interconnected by tight junctions, a basal lamina, pericytes and astrocytes.

II.1.1.1. Endothelium

Endothelial cells are the main unit of the BBB. They cover the lumen of cerebral capillaries in a continuous monolayer, creating a wall of around 200 nm thickness. These cells are tightly interconnected by tight junctions and do not present fenestration [134].

Cerebral endothelium differs from peripheral endothelium and epithelium in its high expression of tight junction proteins, such as occludin and claudin-5, creating an even tighter network of tight junctions [135].

These tight junctions are a key feature of the BBB impermeability. They seal inter-endothelial spaces, making paracellular diffusion almost impossible and only allowing the highly selective transcellular pathway to pass through. They also anchor to the cytoskeleton, providing structural support.

II.1.1.2. Pericytes

Pericytes constitute a discontinuous layer of cells on the abluminal side of the capillary wall and share a common basal membrane with endothelial cells.

Their close association with the endothelium allows the exchange of ions, metabolites and second messengers between the two cell types [136]. Pericytes have an important role to play in regulating cerebral blood flow. Indeed, these cells have contractile characteristics similar to smooth muscle cells and can regulate (to a certain extent) capillary diameter and therefore cerebral blood flow [137,138].

Pericytes also regulate BBB permeability. They control the expression and alignment of endothelial cell tight junction proteins and the transcytosis of vesicles across the BBB [139]. However, the molecular pathways between endothelial cells and pericytes that could be manipulated to open the BBB "on demand" for drug delivery remain largely unknown [140]. In addition, pericytes show phagocytic functions that help to eliminate toxic metabolites [141].

II.1.1.3. Astrocytes

Astrocytes are the most abundant cells in the CNS and are involved in a variety of physiological and biochemical functions. These include compartmentalization of neural parenchyma, maintenance of ion homeostasis in the extracellular space, regulation of pH, uptake and processing of neurotransmitters by providing energy-rich substrates to neurons, and mediation of signals from neurons to the vasculature [142].

Astrocytes also play an essential role in the functioning of the BBB [143]. They interact with the endothelial cells by projecting their terminal feet onto the cerebral capillaries, thus covering the majority of the abluminal surface of the BBB. Such interactions are important for the synchronization of metabolite levels and the regulation of brain water content [144].

Astrocytes are also a key cellular support for BBB integrity. Recent studies have shown that several effector molecules released by astrocytic terminal feet aim to improve and maintain the tightness of the BBB. These include members of the Hedgehog pathway [145], the renin-angiotensin hormone system [146] and apolipoprotein E [147]. The release of apolipoprotein E, for example, regulates the tight junctions of endothelial cells.

II.1.2. BBB transport mechanisms

Given the properties of the BBB, substances can only cross the endothelial layer by paracellular/transmembrane diffusion or by using transcellular transport mechanisms [148].

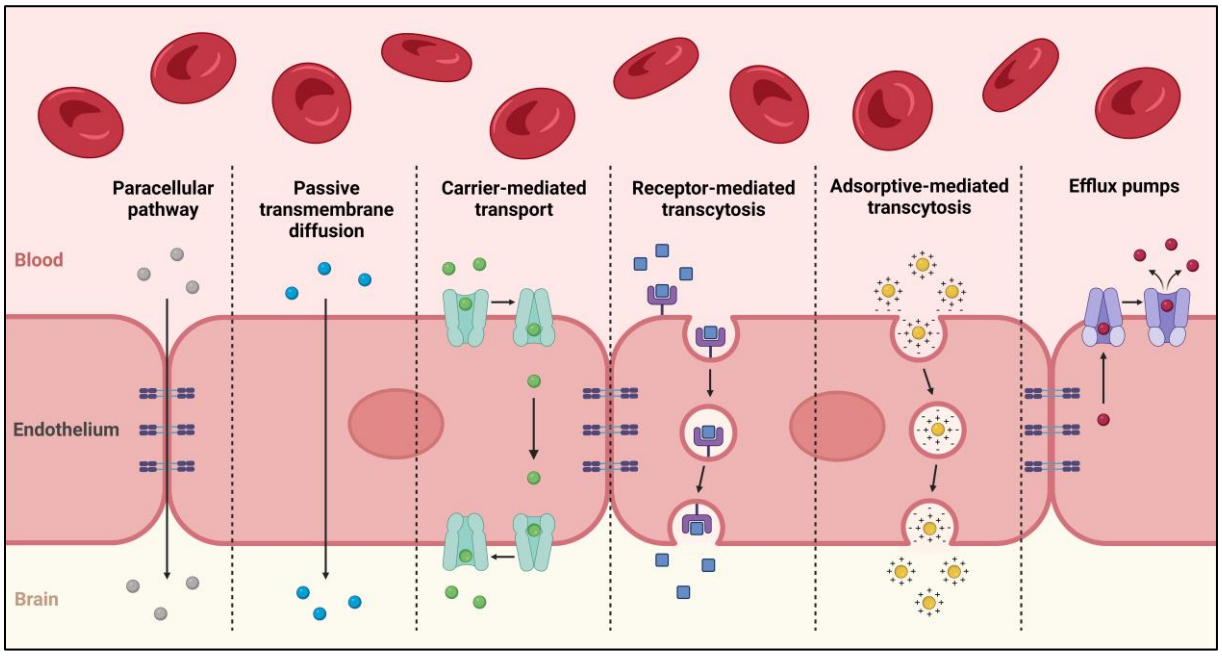

Figure 10. BBB transport mechanisms (adapted from [133]). Substances can cross the BBB endothelial layer by paracellular/transmembrane diffusion or by using transcellular transport mechanisms such as carrier-mediated transport, receptor-mediated transcytosis, adsorptive-mediated transcytosis or efflux pumps.

II.1.2.1. Paracellular and transmembrane diffusion

Tight junctions between endothelial cells severely restrict the passage of molecules via the paracellular pathway, allowing only very small hydrophilic substances to pass through. Regarding transmembrane diffusion, only small lipophilic, non-ionized molecules with a low molecular weight (less than 400 Da) or small gas molecules such as CO_2 or O_2 can diffuse freely. Substances that do not present these physicochemical characteristics have to use transcellular transport mechanisms to potentially cross the BBB [149,150].

II.1.2.2. Transcellular transport mechanisms

II.1.2.2.1 Carrier-mediated transport

To transport specific molecules such as nutrients or amino acids to the brain, transport proteins are present on the luminal and basolateral sides of endothelial cells. These include the glucose transporter (GLUT-1), the large neutral amino acid transporters (LAT), nucleoside transporters as well as organic cation and anion transporters. They all have an important role to play in the maintenance of the brain's high metabolic needs [151,152]. Their substrates can therefore cross the BBB by transport mediated by these carriers.

II.1.2.2.2 Receptor-mediated transcytosis

Endogenous molecules that have no specific transporter, such as insulin, leptin or transferrin, can also reach the brain via receptor-mediated transcytosis (RMT).

Transcytosis involves three phases: endocytosis, intracellular vesicular traffic and exocytosis [153]. Indeed, molecules bind to their receptors on the luminal side of the endothelial cells and endocytosis is initiated. The receptor-ligand complex is invaginated, leading to the formation of intracellular transport vesicles. The vesicles are then sorted and those selected for exocytosis cross the cell to release the ligand on its basolateral side. The receptor is then recycled [154].

Some of the receptors found on the luminal side of the BBB are transferrin receptor (TfR), insulin and insulin-like growth factor receptor, low-density lipoprotein receptor (LDLR), low-density lipoprotein receptor-related protein 1 and 2 (LRP1 and LRP2), scavenger receptors class B type I (SR-B1), leptin receptors and lactoferrin receptors [155]. More recently, nicotinic acetylcholine receptors (nAChRs) and the diphtheria toxin receptor have also been described [156].

II.1.2.2.3 Adsorption-mediated transcytosis

Another potential physiological pathway to cross the BBB is adsorption-mediated transcytosis (AMT), also known as pinocytosis. Whereas RMT requires an interaction between a ligand and a receptor, AMT is a non-specific pathway. As a result, the binding affinity of AMT is low, but its binding capacity is high, leading to a transcytosis efficiency similar to RMT [156,157]. AMT is produced by electrostatic interaction between a positively charged molecule, protein or peptide and the negatively charged luminal membrane of brain endothelial cells.

II.1.2.2.4 Efflux Pumps

In addition to all these transport mechanisms, there are also efflux pumps that are responsible for expelling both endogenous and exogenous compounds, such as drugs, from the brain into the

blood. Of particular importance, active drug efflux transporters of the ATP-binding cassette (ABC) family are important determinants in the elimination of drugs from the CNS. This mechanism is considered to be a significant obstacle as it may limit the distribution of beneficial drugs for the treatment of CNS diseases [158,159].

II.1.3. The BBB in glioblastoma: the BTB

In GB, abnormal angiogenesis, due to an overproduction of pro-angiogenic factors such as vascular endothelial growth factor (VEGF), produces blood vessels with an abnormal physiological structure, leading to an altered BBB known as the blood-tumor barrier (BTB) [160].

The BTB is characterized by an aberrant distribution of pericytes, a loss of astrocytic endings and an alteration of tight junction proteins between endothelial cells. In addition to the abnormal structure of tumor vessels due to pro-angiogenic factors, invading tumor cells can physically displace BTB cells and disrupt BTB integrity [161,162]. All these characteristics result in a compromised BTB with an increased permeability. Unlike the healthy BBB, this leaky BTB allows the passage of rather large molecules, such as drugs, between the endothelial cells in the damaged paracellular pathway [163,164].

However, the BTB permeability is highly heterogeneous and varies not only between GB but also within the same tumor, leading to a highly heterogeneous drug delivery [160] (Figure 11). Indeed, although the BTB is often compromised in the tumor core allowing the passage of drugs, an intact BTB is still found in the tumor rim [127,129], limiting significantly the passage of drugs, especially to reach the infiltrative tumor cells lying behind this intact BTB which are at the origins of the tumor recurrence [165-168]. Thus, reliance on either passive or targeted delivery to only the pathologically disrupted tumor BBB regions in the glioblastoma core will not eliminate all tumor cells, and a subsequent GB recurrence will be likely. It therefore remains important to establish strategies that can deliver drugs evenly throughout the whole tumor volume.

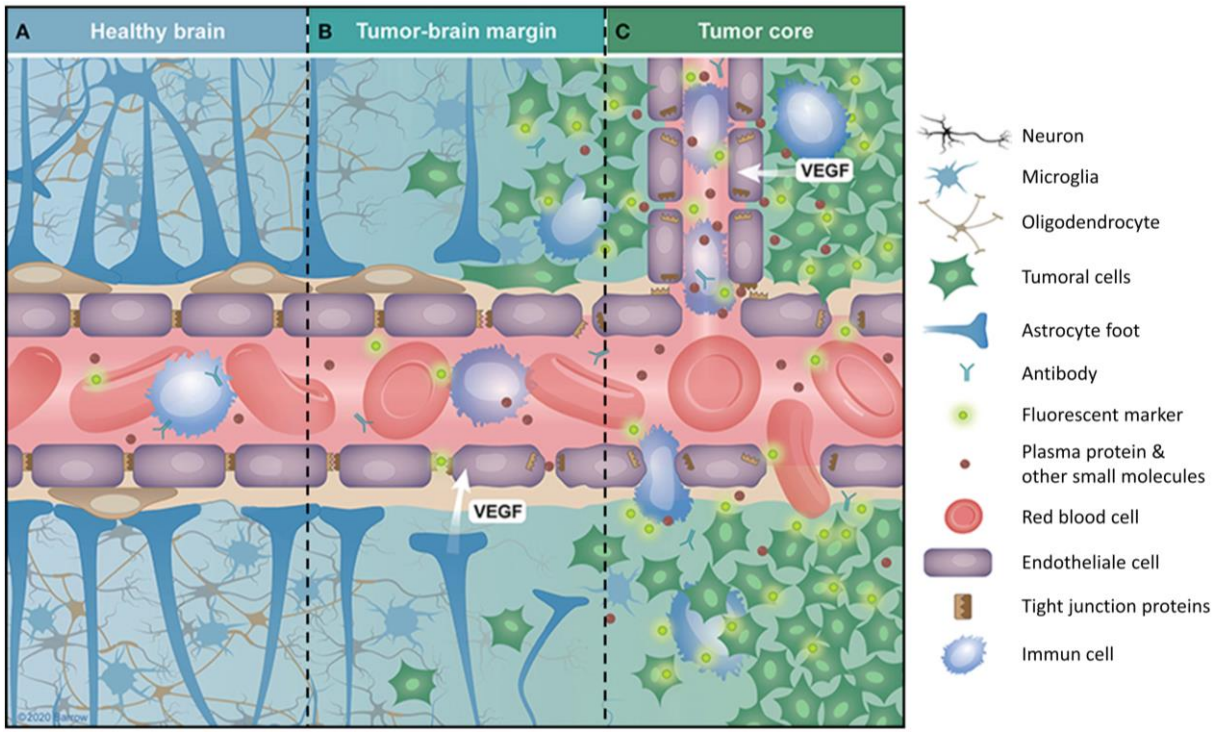

Figure 11. Representation of BTB heterogeneity [149]. While the BTB is disrupted in the core of the GB tumor, an intact BTB is still found peritumorally. This heterogeneous disruption leads to the protection of most infiltrative GB cells and limits the delivery of the therapeutics to the tumor site.
Abbreviations: BTB = Blood-Tumor Barrier; VEGF = Vascular endothelial growth factor.

II.2. STRATEGIES TO OVERCOME THE BBB

For many years, the blood-brain barrier has been a major obstacle to the treatment of cerebral pathologies. Several strategies have been described to overcome the BBB and improve drug delivery to the tumor site, such as:

- Open the BBB to increase its permeability: mainly by weakening endothelial tight junctions through osmotic shock [169], irradiation [170], FUS with microbubbles [171], or biochemical modulation (e.g., bradykinin) [127];
- Increase tumor perfusion, allowing more drugs to reach the BBB: tumor vessels normalization [172];
- Bypass the BBB: local delivery using intrathecal/intraventricular administration [131], convection-enhanced delivery (CED) [173-179], implants (e.g., polymer systems, gels, microchips, etc.) [100,180,181], or intranasal administration [182-185];
- Take advantage of BBB's physiological transport systems: change the physicochemical characteristics of drugs to target transport mechanisms, facilitate paracellular/transmembrane diffusion or decrease affinity to efflux transporters [186], or modulate the expression and/or activity of efflux transporters to prevent elimination of

the molecule of interest [158], or even modulate the expression and/or activity of vesicular transport to improve drugs transport [127].

In this section, we mainly focus on strategies to open the BBB and increase tumor perfusion that have emerged in recent years.

II.2.1. Osmotic shock

The first studies on BBB disruption by osmotic shock were carried out in the early 1970s by Rapoport [169,187]. This method is based on the intra-arterial administration of a hypertonic solution (e.g., mannitol, arabinose).

During this perfusion, the endothelial cells will shrink due to dehydration, which will contract the cytoskeleton of the cells, creating tension on the tight junctions, widening them and leading to a transient opening of the BBB (Figure 12) [188]. This opening would allow better delivery of therapeutic agents via the paracellular route. However, obstacles to this procedure have been identified that compromise patient safety. Non-selective opening of the BBB will induce a massive and uncontrolled influx of compounds throughout the brain from the bloodstream, which may cause neurotoxicity, limiting the use of this procedure in clinical practice [126,167]. Nevertheless, as GB is a disease with a very poor prognosis and a standard of care that is still not very effective, the benefit-risk balance for the application of this strategy is not the same as for other diseases and can therefore be considered for GB.

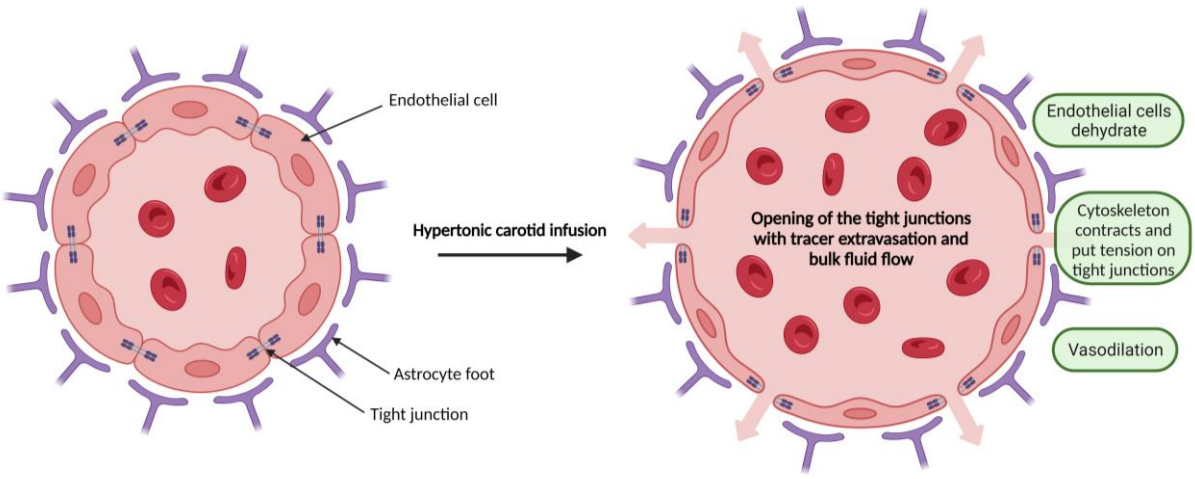

Figure 12. Model for the opening of the inter-endothelial tight junctions by carotid infusion of a hypertonic solution. During infusion, endothelial cells dehydrate, water leaves the brain leading to a vasodilation and the endothelial cell cytoskeleton contracts. Tension is exerted on tight junctional areas due to each of these factors, leading to a reversible opening of the tight junctions [189].

II.2.2. Radiotherapy

It has been shown in preclinical animal models and clinical trials that irradiation can permeabilize the healthy BBB or tumor vascular bed in other cancers than glioblastoma [190-195]. Indeed, radiotherapy is thought to affect the endothelium of the BBB by weakening it, particularly at the level of tight junctions, thus causing more or less BBB permeabilization depending on the dose of irradiation received [194,196] (Figure 13). For instance, a recent study investigated the effect of irradiation on claudin 5, one of the most enriched tight-junction proteins, demonstrating that a 20 Gy single-dose irradiation in a Sprague-Dawley (SD) rat model (healthy BBB in this model) caused downregulation of claudin 5 with an increase in the delivery of an antiangiogenic agent (anlotinib) injected IV concomitantly [170].

Other studies have also revealed an increase in drug delivery after irradiation in glioblastoma and other gliomas [170,197,198], reflecting an opening of the BBB/BTB in cerebral tumors. One of these clinical studies has reported that irradiation with 20 to 40 Gy facilitated the entry of chemotherapeutics such as methotrexate in glioblastoma patients, increasing survival time [197].

Thus, as radiotherapy is included in the standard therapeutic protocol, improvement of delivery by opening the BBB through irradiation would maximize the synergistic effect between radiotherapy and chemotherapy by adapting the timing of the therapeutic protocol.

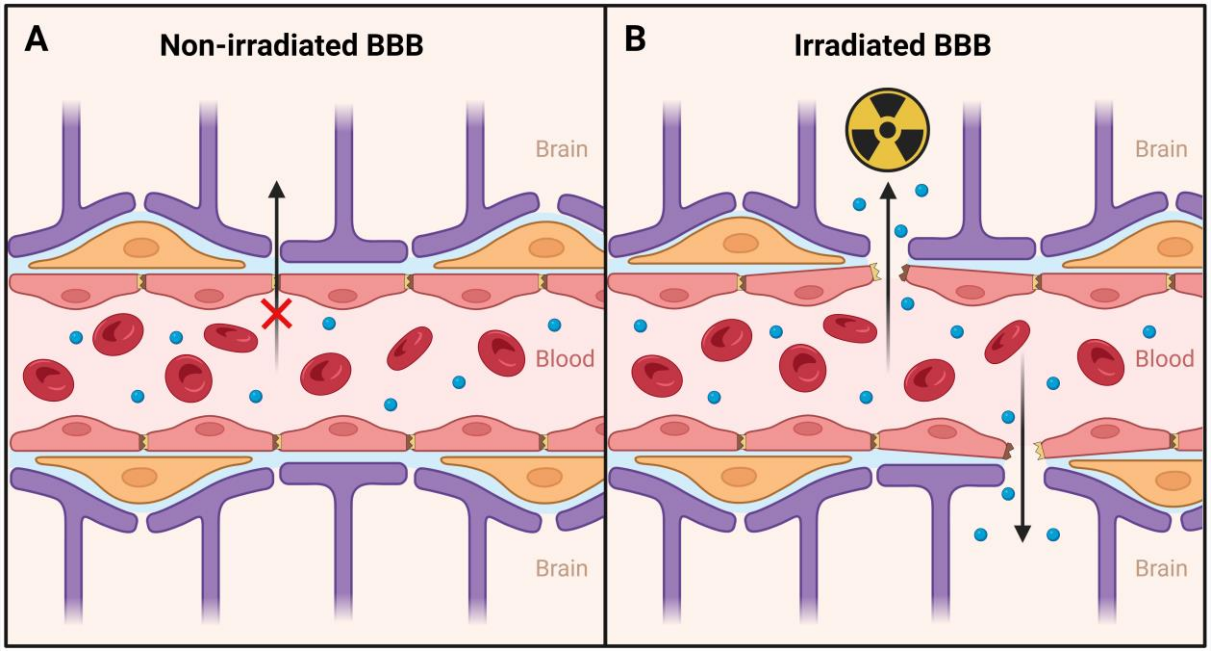

Figure 13. Illustration of the effect of irradiation on the BBB. Radiotherapy affects the endothelium of the BBB by weakening it, particularly at the level of tight junctions, thus causing more or less BBB permeabilization depending on the dose of irradiation received.

II.2.3. Tumor vessel normalization

It has been shown that during the early phase of an anti-angiogenic treatment, originally developed to starve tumors, a transient effect of tumor vessels normalization can be observed with an improvement in the outcome of anticancer drugs administered during this normalization window [172,199-202]. Indeed, this normalization effect results in a remodeling of the tumoral vasculature, making it more structured and functional, leading to an improvement in blood perfusion as well as a reduction in tumor hypoxia and intratumoral pressure, thus facilitating the delivery and penetration of anticancer drugs into the tumor (Figure 14) [203-206].

However, there are several important features to be considered for this normalization effect. Firstly, the dose of anti-angiogenic agent used is important. If the anti-angiogenic agent is too potent or if the dose is too high, this may lead to a rapid and excessive pruning of the vessels and may not improve the results of concomitant therapies. Alternatively, doses that are too low may induce resistance to treatment by the activation of other proangiogenic pathways, and the tumor would start producing abnormal vessels again [201,204].

It's also important to emphasize that tumor vessels normalization is transient, and only occurs at the very beginning of the anti-angiogenic treatment [206,207]. Following the normalization time window, one of the two scenarios described previously should occur, depending on the dose of anti-angiogenic agent administered: either excessive pruning of tumor vessels preventing any concomitant therapy, or resistance to anti-angiogenic treatment [204,205]. In this way, normalization would be dose- and time-dependent.

In addition, the size of anticancer agents injected concurrently is important. Indeed, the restructuration of blood vessels during normalization reduces the pore size of the fenestrated tumor vascular wall, and thus enhanced delivery to the tumor site will only be seen for small-sized drugs [207-209]. A study carried out in a breast cancer model exposed that blocking VEGFR2 improved the delivery of small nanoparticles (12-nm nab-paclitaxel) while hindering the delivery of larger nanoparticles (125-nm liposomal doxorubicin) [210]. No study has yet been carried out in GB concerning the impact of anticancer agents' size on their delivery during the normalization effect.

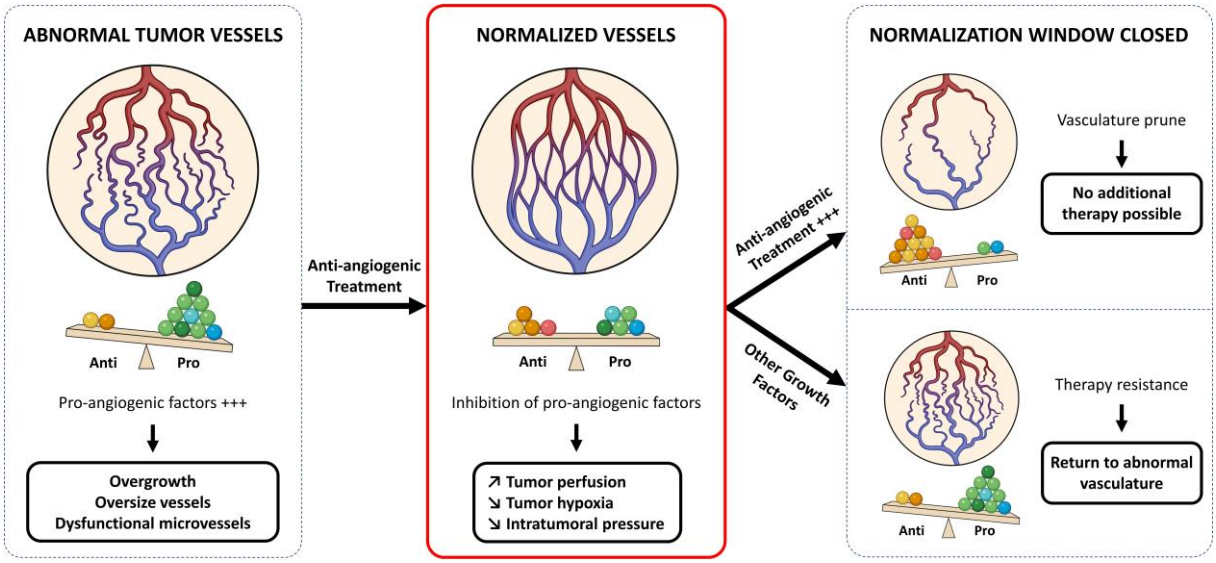

Figure 14. Representation of the normalization effect on tumor vasculature (adapted from [204]).
Due to excessive amounts of pro-angiogenic factors such as VEGF, tumor angiogenesis is chaotic with oversized vessels and numerous dysfunctional microvessels (left panel). At the beginning of an anti-angiogenic treatment, the anti- and pro-angiogenic balance is partially restored and a phenomenon of vessel normalization can be observed (middle panel). The vasculature is remodeled, making it more structured and functional. This will improve tumor perfusion as well as a reduction in tumor hypoxia and intratumoral pressure, leading to a better outcome of concurrently injected anticancer agents. Afterwards, the normalization window closes, either because the dose of anti-angiogenic agents is too high, leading to an excessive tumor vasculature prune and thus preventing improvement in the delivery of a concurrent therapy (right top panel), or because the dose of anti-angiogenic agents is too low, causing therapy resistance and a return to abnormal tumor vasculature (right bottom panel).

II.2.4. Focused Ultrasound in association with microbubbles

Focused ultrasound (FUS) combined with systemic administration of microbubbles (MBs) is a slightly invasive, localized and transient method for a targeted opening of the BBB [171]. This technique is based on a transcranial application of low-frequency ultrasound to a specific region of the brain, combined with intravenous (IV) administration of preformed lipid-coated microbubbles. MBs oscillation in the presence of FUS leads to a precise and transient mechanical disruption of tight junctions between endothelial cells in the BBB. Although ultrasound alone can disrupt the BBB, the addition of MBs allows lower frequencies to be used to achieve the same opening effect. In addition, by harnessing the effects of ultrasound with MBs, it is possible to apply FUS transcranially without significant heating of the skull.

Pre-clinical studies for this strategy have shown promising results in GB. Chemotherapies were administered in combination with FUS and MB, leading to an increase in the concentration of chemotherapies in brain tumors, a reduction in tumor growth and an improvement of median survival in rodents [211-213].

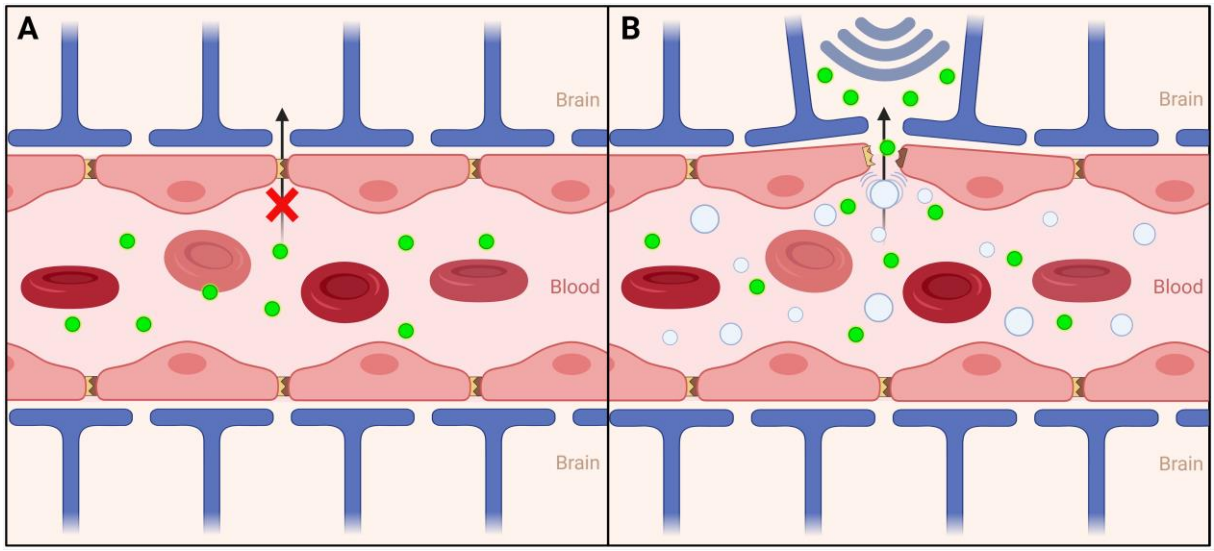

Figure 15. Illustration of drug delivery at the BBB before (**A**) and after (**B**) application of FUS with MB. MBs oscillation in the presence of FUS leads to a precise and transient mechanical disruption of tight junctions between endothelial cells in the BBB. Although ultrasound alone can disrupt the BBB, the addition of MBs allows lower frequencies to be used to achieve the same opening effect.

These promising pre-clinical studies have led to clinical trials for GB or recurrent GB treatment, that are currently ongoing and summarized in Table 3 below.

Carpentier et al. [214] report the interim results of clinical trial NCT02253212. The use of FUS (sonocloud implantable device) with systemically injected microbubbles (SonoVue) in recurrent GB using T1-weighted gadolinium contrast enhancement imaging to assess the BBB opening showed a transient BBB disruption with a threshold pressure dose of 0.8 megapascal (MPa). Additionally, an increased quality of BBB disruption up to a dose of 1.1 MPa was observed, without detectable adverse effects on radiologic (MRI) or clinical examination.

Table 3. Clinical trials for GB or recurrent GB treated using ultrasound [215].

Trial identifier	Treatment	Clinical phase / status
NCT02253212	Transient opening of BBB by low intensity pulsed ultrasound (sonocloud implantable device) in combination with carboplatin in recurrent GB	Phase 1-2 / ongoing
NCT03744026	Transient opening of BBB by low intensity pulsed ultrasound (sonocloud-9 implantable device) in recurrent GB eligible for surgery and carboplatin chemotherapy	Phase 1-2 / ongoing
NCT04614493	Transient opening of BBB by low intensity pulsed ultrasound (sonocloud implantable device) in combination with concurrent temoradiation and adjuvant temozolomide in newly diagnosed GB	Phase 2 / ongoing

NCT05864534	Immune modulation (balstilimab, botensilimab) with chemotherapy (liposomal doxorubicin) in combination with ultrasound-mediated BBB opening (sonocloud-9 implantable device) in newly diagnosed GB	Phase 2a / ongoing
NCT04446416	Bevacizumab in combination with FUS (NaviFUS system) and MB (SonoVue®) in recurrent GB	No FDA defined phase / ongoing
NCT04440358	Transient opening of BBB by FUS (Exablate Neuro Model 4000 Type 2 system) with MB in combination with carboplatin in recurrent GB	Phase 1-2 / ongoing
NCT04417088	Transient opening of BBB by FUS (Exablate Neuro Model 4000 Type 2 system) with MB in combination with carboplatin in recurrent GB	Phase 1-2 / ongoing
NCT04528680	Transient opening of BBB by low intensity pulsed ultrasound (sonocloud implantable device) in combination with Albumin-bound Paclitaxel and carboplatin in recurrent GB	Phase 1-2 / ongoing
NCT05879120	Transient opening of BBB by FUS (Exablate Neuro Model 4000 Type 2 system) with MB in combination with Neo-adjuvant and Adjuvant Pembrolizumab in recurrent GB	Phase 2 / ongoing
NCT05902169	Transient opening of BBB by low intensity pulsed ultrasound (sonocloud implantable device) in combination with carboplatin in first recurrent GB	Phase 3 / ongoing

Abbreviations: BBB = Blood-Brain Barrier; FDA = Food and Drug Administration; FUS = Focused Ultrasound; GB = Glioblastoma; MB = Microbubble.

II.2.5. Biochemical modulation

Biochemical opening relies on the use of pharmacological agents (Table 4) that modulate the expression of tight junction proteins such as occludin, claudin 5 or zonula occludens-1 (ZO-1), causing their downregulation and allowing the BBB to open [127].

Bradykinin and its analogs (activators of bradykinin B2 receptors) are the most widely described and used pharmacological agents for this strategy. Indeed, it has been shown that the activation of bradykinin B2 receptors can occur the opening of tight junctions [216,217]. These findings were so promising that one of the bradykinin analogs, RMP-7 (Cereport® from Alkermes Inc.), reached clinical trials with the aim of enhancing brain delivery of antitumor medications. However, the clinical trial was stopped due to lack of efficacy in phase II and III studies when administered in combination with carboplatin [186].

Table 4 below summarizes different biochemical compounds and their mechanism of action that can be used to modulate the BBB opening.

Table 4. Biochemical modulation for circumventing the tumoral BBB (adapted from [127]).

Drugs	Biochemical modulation	Tight junction effects	References
Bradykinin and analogs	Activate bradykinin type 2 receptor (B2R)	ZO-1↓, Occludin↓, Claudin-5↓	[218-228]
Minoxidil sulfate	Activate ATP-sensitive potassium channel (K_{ATP} channel)	Occludin↓, Claudin-5↓	[229-231]
Lexiscan	Activate Adenosine 2A receptor (A2AR)	Occludin↓, Claudin-5↓	[232-234]
Papaverine	Involvement of protein kinase A (PKA) and heat shock protein 70 (HSP70)	Occludin↓, Claudin-5↓	[235-238]

Abbreviations: A2AR = Adenosine 2A Receptor; ATP = Adenosine Triphosphate; B2R = Bradykinin type 2 Receptor; HSP70 = Heat Shock Protein 70; K_{ATP} channel = ATP-sensitive potassium channel; PKA = Protein Kinase A; ZO-1 = Zonula Occludens-1.
Note: Down-regulated ↓.

III. ASSESSMENT OF BBB OPENING

III.1. IMAGING TECHNIQUES

The basic functioning principles of MRI and CT have already been explained in the I.3.2. Medical imaging section, and will not be described here again.

III.1.1. Magnetic Resonance Imaging

DCE-MRI is one of the most widely used MRI techniques to assess BBB permeability by examining leakage of contrast agents, usually gadolinium-based contrast agent (GBCA), into the brain parenchyma [239-242]. Indeed, GBCAs such as Gadolinium-gadoteric acid (Gd-DOTA) or Gadolinium-diethylenetriamine penta-acetic acid (Gd-DTPA) do not cross the intact BBB due to their hydrophilic property [243]. However, in the case of a disrupted BBB, vessels become permeable and GBCAs can cross the BBB. Extravasation leads to a regional signal change in brain parenchyma, due to the magnetic properties of GBCAs, which cause shortening of T1 relaxation times. In DCE-MRI, several T1-weighted images are acquired over time after GBCA injection, allowing tracking of the movement of Gd between blood and extravascular space and thus measuring BBB permeability [244-246]. The image data can be analyzed qualitatively or semi-quantitatively. Full quantification can be obtained by applying a suitable pharmacokinetic model, allowing several physiological parameters to be derived, including the transfer constant between blood and extravascular space (Ktrans), transfer constant between extravascular space and blood (Kep), fractional plasma volume (Vp), and fractional volume of the tissue extracellular space (Ve) [245,247,248].

A simple T1-weighted structural MRI after GBCA injection can also be used to determine BBB permeability. Although this is not a dynamic monitoring of the contrast agent, it allows us to qualitatively determine whether or not the BBB is open, as well as the brain region where permeabilization occurs. An advantage of using this MRI technique is that acquisition time is much shorter than for DCE-MRI.

An important point to emphasize regarding the use of these MRI methods is that safety concerns have been raised following lastly reports of Gd deposition in the brain that might be toxic for the patient [249,250]. The probability of Gd deposits in the brain is higher for linear chelates (Gd-DTPA and analogs) than for macrocyclic agents (Gd-Dota and analogues) [251].

III.1.2. Computed tomography

In computed tomography (CT) imaging, iodinated contrast agents can be used to assess BBB integrity. As for MRI, a distinction is made here between standard CT-scan and perfusion CT (PCT).

Standard CT-scan with contrast agent injection allows visualization of brain's blood vessels and identifies any vascular abnormalities, providing a rather qualitative overview of BBB opening.

PCT with iodinated contrast injection is on the other hand a dynamic method allowing hemodynamic parameters of the tumor to be determined, thus providing a quantitative overview of the BBB opening [252]. PCT involves the acquisition of serial CT scans acquired over time after contrast injection. This enables to track the distribution of contrast in the brain over time. The application of tracer kinetics models that describe the distribution of contrast in blood vessels and extravascular space of the tissue allows several physiological parameters to be derived that reflect quantitatively the permeability state of the BBB [253,254]. Those parameters measured are the permeability surface area product (PS) and the transendothelial transfer constant (K).

III.1.3. PET and SPECT

Positron emission tomography (PET) and single photon emission computed tomography (SPECT) are functional imaging techniques that use radiolabeled tracers to visualize specific biological processes. As suggested by their names, PET uses positron-emitting radioisotopes, while SPECT uses single photon-emitting radioisotopes. Thus, the use of PET and SPECT imaging with suitable radiolabelled tracers can provide information on BBB permeability [160,255].

Regarding PET, it allows the absolute quantification of radiotracer concentrations in tissues, providing precise quantitative measurements [256]. Gallium tracers such as [^{68}Ga]Diethylenetriamine pentaacetate or [^{68}Ga]Ethylenediaminetetraacetic acid are commonly used to evaluate paracellular BBB permeability as they do not cross the BBB under normal, physiological conditions. [^{18}F]2-Fluoro-2-deoxy-sorbitol has been recently described as a reliable, effective and quantitative maker of BBB permeability [257].

For the evaluation of paracellular BBB permeability with SPECT, [^{99m}Tc]lTPA, [^{99m}Tc]sestamibi, ^{201}Tl and [^{67}Ga]citrate are examples of tracers that can be used as they are unable to cross the healthy intact BBB. Their brain accumulation, therefore, is an indication of altered BBB permeability [258]. When compared with PET, SPECT has the disadvantages of a lower sensitivity and spatial

resolution [255]. However, SPECT has not been completely replaced by PET because of the benefit of a tracer with longer stability, lower cost and greater accessibility.

It is important to add that since these two techniques use radioactive tracers, they expose patients to radiation doses, although these doses are generally considered safe and justifiable in a clinical context.

III.1.4. Optical Imaging

III.1.4.1. In vivo imaging system

In vivo optical imaging systems (including IVIS®) are imaging instruments for detecting and quantifying light signals (bioluminescence, infrared or and fluorescence photons) from small animals and culture dishes and plates.

In order to assess the BBB opening, what will be of interest here is its ability to track the distribution of a optically-active tracer in the organism [259]. A better detection is achieved using the near-infrared (NIR) domain of the electromagnetic spectrum. Indeed, NIR wavelengths are the ones that best penetrate biological tissues, enabling better detection of the fluorophore deep in the tissue. Moreover, the natural fluorescence of biological tissues is minimal in the NIR region, reducing background and improving detection sensitivity [260]. However, even with an NIR tracer, the sensitivity of detection remains low, and this imaging method can only assess BBB opening qualitatively on a macroscopic observation scale with very low resolution. An example of a fluorescent tracer that can be used with IVIS to assess BBB opening is Evans blue [261]. It will be described in more detail in the III.2.2. Exogenous markers section.

III.1.4.2. Intravital microscopy

While MRI and nuclear imaging techniques are powerful in providing macroscopic information with full brain coverage and can do so in a highly specific manner to probe individual mechanisms of BBB dysfunction, they lack the spatial resolution necessary to elucidate the cellular/molecular foundations of these observations. This resolution can be achieved using intravital microscopy (IVM). High-resolution fluorescent in vivo microscopy can quantify and localize cellular components, including junctional proteins and leakage of tracers across the BBB at the level of the vessel [262]. As with IVIS, since this is also in vivo fluorescence imaging, the use of tracers that fluoresce in the near infrared is preferred. Commonly tracers used are fluorescent dextrans. Large dextrans are retained within vessels and are useful for imaging vascular density and morphology.

Smaller dextrans (< 3 kDa) can pass through the impaired BBB; this can be imaged to quantify BBB leakage [263,264].

However, IVM is highly invasive, requiring a craniotomy or thinning of the skull for optical imaging of the brain. Cranial thinning is less invasive and more suitable for mice, whose meninges are more translucent and cranium less dense than those of rats [265]. However, this technique diminishes resolution as a result of optical scattering by the remaining skull. Craniotomy, on the other hand, is associated with inflammation and edema, which need to be minimized by careful aseptic technique and surgery [265,266].

III.1.4.3. Fluorescence microscopy

Fluorescence microscopy is a highly invasive imaging method, as it can only be performed by histological study of brain tissue sections. However, as it is no longer in vivo, this method allows the use of tracers that fluoresce in a much wider range of wavelengths, and not just restricted to near-infrared fluorescent tracers. Fluorescence microscopy has also the advantage of high spatial resolution, enabling precise visualization of the fluorescent agent distribution in the different parts of brain parenchyma [267]. The various fluorescent markers that can be used to assess BBB opening, such as Evans blue, sodium fluorescein, horseradish peroxidase, or even fluorescent labeled albumin (e.g., FITC-albumin) will be described in more detail in III.2.2. Exogenous markers section.

In addition, this approach allows visualization of BBB structures and tumor vasculature, by immunohistological staining for the endothelial cell marker CD31. Indeed, CD31, also known as PECAM-1 (Platelet Endothelial Cell Adhesion Molecule-1), is a transmembrane glycoprotein expressed by endothelial cells, and its labeling enables specific visualization of blood vessels in tissue sections by fluorescence microscopy, allowing direct assessment of BBB integrity.

III.1.5. Electron microscopy

Electron microscopy offers sub-cellular resolution, enabling visualization of interactions at the level of cell membranes, tight junctions and other intracellular structures. This approach can help to understand the mechanisms by which molecules pass through the BBB, and to study ultrastructural changes associated with barrier permeability [268]. It is particularly useful for in-depth investigations requiring detailed analysis of cellular structures.

III.2. BIOMARKERS AND EXOGENOUS MARKERS TO ASSESS BBB INTEGRITY

For all the biomarkers and exogenous markers described below (except BBB components), the principle for assessing BBB permeability is that they are unable to cross the BBB when it is not fenestrated. This is mainly due to their size, which prevents them from using the paracellular pathway, but also to their inability to use the active transcellular pathway, or, for the smallest of them, to their hydrophilic nature, which prevents them from diffusing via the transmembrane pathway. Thus, their detection in brain parenchyma (or in blood for biomarkers with cerebral origin) would indicate BBB permeabilization (more or less extensive, depending on the marker size). Characteristics of biomarkers and exogenous markers that can be used to assess BBB opening are summarized in Table 5.

Table 5. Summary of different markers that can be used for BBB permeability studies.

Categories	Markers	Size (Da)	Advantages	Disadvantage	Clinical application	References
Biomarkers	Albumin	69,000	Can be examined without tracer Radiolabeled version allows accurate quantification Fluorescent-labeled version can be visualized by optical microscope	QAlb requires collect of CSF and blood serum contemporaneously Not suitable for small BBB permeability Radiolabeled version requires radioactive license	Yes	[269-273]
	IgG	155,000	Can be examined without tracer	QIgG requires collect of CSF and blood serum contemporaneously Not suitable for small BBB permeability	Yes	[270,274-279]
	S100B	11,000	Can be examined without tracer Only need blood sample	No detection of BBB breakdown in a specific brain region	Yes	[280-283]
	Tight junctions (claudin-5, occludin, ZO-1)	NA	Direct reflection of BBB breakdown	Dosage in the blood and CSF is unreliable	No	[170,274,277]
Exogenous markers	Evans blue	961	Visual investigation and qualitative assessment are feasible using different microscope techniques Allow assessment of BBB permeability to macromolecules due to its extensive binding to albumin	Quantification is unreliable Not suitable for small BBB permeability prediction Binds to tissues Potential in vivo toxicity	No	[284-287]
	Sodium fluorescein	376	Detectable at very low concentrations Suitable for small BBB permeability prediction Nontoxic even at high dosage Can be visually assessed	Binds to plasmatic proteins	No	[277,288]
	Radiolabeled sucrose	342	Accurate quantification Uncharged Metabolically stable No interaction with proteins No interactions with BBB transporters Suitable for small BBB permeability prediction	Requires radioactive license Over-time degradation Cannot be visualized	No	[289-292]

Table 5. (Continued)

Categories	Markers	Size (Da)	Advantages	Disadvantages	Clinical application	References
Exogenous markers	[^{13}C]sucrose	354	Non-radioactive Sensitive and specific method of detection with accurate quantification Uncharged Metabolically stable No interaction with protein No interaction with BBB transporters Suitable for small BBB permeability prediction	Requires LC–MS/MS device for detection Cannot be visualized	No	[290,293]
	Horseradish peroxidase	44,000	Easily visualized under optical and electron microscope	Not suitable for small BBB permeability prediction Quantification is unreliable Degranulation of mast cells with histamine and serotonin release	No	[276,294,295]
	Dextrans	1,500 to 2,000,000	It can be used for a broad range of molecular weights Can be visualized with both optical and electron microscope due to conjugation with biotin or fluorophore	Stability issue May be toxic at high concentrations	No	[295-299]

Abbreviations: BBB = Blood-brain barrier; CSF = Cerebrospinal fluid; Da = Dalton; IgG = Immunoglobulin G; LC-MS/MS = Liquid chromatography coupled to tandem mass spectrometry; NA = Not applicable; QAlb = CSF/serum quotient of albumin; QIgG = CSF/serum quotient of IgG; ZO-1 = Zonula occludens-1.

III.2.1. Biomarkers

III.2.1.1. Plasmatic proteins: Albumin and Immunoglobulin G

Albumin is the most abundant plasmatic protein mainly confined to the vascular space, excluded from the brain parenchyma by the BBB due to its high molecular weight (69kDa). In the event of BBB alterations, abnormal amounts of albumin can leach into the brain, providing a useful indicator of BBB disruption. The parameter mainly used in the literature for this analysis is the CSF/serum quotient of albumin (QAlb), representing the ratio between the amount of albumin measured in the CSF and the one measured in the blood. This quantification is usually carried out by Western blot. Thus, an increase in QAlb can be indicative of BBB leakage. This investigation of plasma albumin extravasation into the brain parenchyma has the advantage of being able to be done without using any tracer, but gives a low-precise quantification. This is why albumin can also be used as an exogenous marker by injecting it conjugated to a radiolabel or fluorescent marker, with the main advantage of giving a much more accurate quantification [269,300].

Another plasmatic protein used to assess BBB opening is Immunoglobulin G (IgG). As with albumin, IgG cannot cross intact BBB. However, although IgG is mainly found in the blood, a small amount of IgG can be found in the CSF due to an intrathecal synthesis, produced by a limited number of lymphocyte clones which are active in the CNS. Thus, BBB permeability is determined by calculating QIgG (CSF/serum quotient of IgG), which is the ratio between IgG measured in the CSF and IgG measured in the blood. This quantification is usually carried out by Western blot. An elevated QIgG may indicate increased BBB permeability [270,274-277]. However, as with unlabeled albumin, quantification with this method remains less accurate than methods using radiolabeled markers.

III.2.1.2. Tight Junction Proteins

Tight junction proteins, such as occludin, claudin-5 or zonula occludens-1 (ZO-1), are crucial components for maintaining the integrity of BBB. Measuring their expression in the BBB enables to assess BBB integrity. Thus, downregulation of these proteins is associated with increased in BBB permeability [170,274,277].

Furthermore, when the BBB is disrupted, tight junction proteins can detach from the BBB and end up in the blood or CSF. Thus, increased levels of tight junction proteins in blood or CSF would also indicate BBB leakage.

III.2.1.3. S100B

S100B is a small homodimeric calcium-binding protein (molecular weight 21 kDa) of the S100 protein family. It is mainly expressed by astrocytic cells and is involved in various biological processes such as neuronal differentiation, cell motility and proliferation [280]. Under physiological conditions, S100B does not cross the BBB and its concentration in the cerebrospinal fluid is reported to be about 100-fold higher than in serum [301]. Indeed, S100B protein is not brain-specific and is also expressed in melanocytes, chondrocytes, adipocytes and skeletal muscle [302,303]. After the BBB lesion, S100B released from damaged glial cells can diffuse into the bloodstream. Detection of S100B levels in blood serum can be achieved by immunological techniques such as enzyme-linked immunosorbent assay (ELISA) or liquid chromatography-mass spectrometry (LC-MS). Thus, a significant increase in S100B blood levels may suggest impaired BBB integrity.

III.2.2. Exogenous markers

The ideal characteristics for an exogenous marker to explore BBB opening are as follows: metabolically inert, non-toxic at the doses applied, non-bondable to other molecules such as proteins in plasma or tissues, available in a range of sizes to assess both small and large BBB openings, visualizable in the range from the naked eye to the electron microscopical level, and reliably quantifiable.

To date, there is no single available marker that fulfills all those criteria. Thus, a combination of different markers (including biomarkers) is currently the most reliable approach to sufficiently assess BBB integrity. Characteristics of the most commonly used exogenous markers are detailed below. MRI, CT, PET and SPECT contrast agents, which can also be considered as exogenous markers of BBB integrity, already described in the III.1 Imaging techniques section will not be detailed here.

III.2.2.1. Evans blue

Evans blue dye (EB) is the most extensively used dye in animal and human studies. It has the particularity to extensively binds to serum albumin as soon as it gets to the vascular system and was used for a long time for plasma volume measurements [285]. Nowadays, Evans blue is widely used as a high-molecular-weight permeability marker to study BBB permeability. Indeed, EB- albumin complex cannot cross the healthy intact BBB due to its size, but in the event of BBB disruption, the dye can leak through and stains the brain parenchyma where the BBB is impaired. Thus, an increase in the amount of Evans Blue in brain tissue indicates an increase in BBB permeability [286,287].

EB diffusion can be assess qualitatively by a simple visualization of blue coloration within sectioned brain tissue or by fluorescence, and quantitatively, though not very precise, by spectrophotometry or spectrophotofluorometry in a homogenized brain tissue sample [304,305]. A major disadvantage of these assessment methods is that they are highly invasive, requiring the animal sacrifice in order to collect the brain tissue.

However, EB distribution can also be assessed qualitatively on live animals using in vivo fluorescent imaging techniques such as IVIS. However, this can only be used to assess major BBB fenestrations, with large quantities of EB penetrating the brain parenchyma, as insufficient quantities of EB in the brain will not be detected through the skin and skull by this method.

Other major drawbacks for the use of EB are that it does not only bind to albumin, but also to tissues, and it shows a potential lethal toxicity in vivo [306,307].

III.2.2.2. Sodium fluorescein

Sodium fluorescein (NaF), a 376 Da molecule, was the first visualizable small molecular-sized marker to be introduced into the BBB permeability assessment field [308,309].

It has the advantage to be nontoxic even at high dosage (LD50 around 4738 mg/kg body weight), detectable at very low concentrations, and an effective marker for slight BBB breakdown due to its low molecular weight [310]. As it is a fluorescent compound (excitation at 440 nm and emission at 525 nm), its measurement can be done by spectrophotofluorimetry [286].

III.2.2.3. Sucrose

Radiolabeled [^{14}C]sucrose (342 Da) et [^{13}C]sucrose (354 Da) are two small markers that enable precise measurement of paracellular BBB permeability. Sucrose is substantially better than other markers as being uncharged, not subjected to protein binding, metabolically stable after parenteral administration, able to assess small BBB disruptions due to its low molecular weight, and not a substrate for active or facilitative BBB transporters [290].

Radiolabeled [^{14}C]sucrose has been extensively used for accurate quantitative determination of BBB permeability [291,292]. However, radiotracer use is associated with special handling and licensing requirements. To overcome the drawbacks of radiolabeled tracer, [^{13}C]sucrose has been introduced as a superior non-radioactive marker, which can be precisely quantified by a sensitive and highly specific LC–MS/MS (Liquid chromatography coupled to tandem mass spectrometry) technique [293].

III.2.2.4. Horseradish peroxidase

Horseradish peroxidase (HRP) has been used for years as an indicator of BBB permeability in morphological studies [276,294,311]. Indeed, in addition to being able to cross the BBB only when this one is permeabilized, the reaction product of this peroxidase can be made electron-dense, so it is possible to visualize it under electron microscopy [312,313]. It is important to mention that the introduction of HRP into blood-brain barrier studies has led to significant advances in understanding blood-brain barrier biology. Notably, its use allowed to establish the ultrastructural basis for the barrier at the cerebrovascular interface between blood and brain, showing that the primary barrier was the intercellular tight junction between adjacent endothelial cells [314].

However, there is a limitation that needs to be addressed when using this tracer. HRP can cause degranulation of mast cells leading to the release of histamine and serotonin, which subsequently affect vascular permeability [315]. This problem can be avoided by concurrently treating the animal with antihistaminic and anti-serotonergic agents that will mask the degranulation effect.

III.2.2.5. Dextrans

Dextrans are glucose polymers linked by glucosidic bonds, non-toxic when used in small concentrations [299]. They are commercially available labeled either with a fluorophore (e.g., fluorescein isothiocynate, tetramethylrhodamine, Texas red) or biotin with their chain length varying from 3 to 2000 kDa. The biotin-labeled form is particularly valuable as it can be visualized under both optical and electron microscope [295].

The main advantage of using dextrans is that they can be used at different molecular sizes to assess BBB permeability [296-298]. Thus, small dextrans, such as Texas Red dextran for example (3 kDa), are often used to assess the permeability of small/medium molecules, while larger dextrans, such as fluorescein isothiocynate-dextran (FITC-dextran) for example (70 kDa) can be used to assess the permeability of large molecules.

IV. REFERENCES

1. Thakkar, J.P.; Dolecek, T.A.; Horbinski, C.; et al. Epidemiologic and molecular prognostic review of glioblastoma. *Cancer Epidemiol Biomarkers Prev* **2014**, *23*, 1985-1996, doi:10.1158/1055-9965.Epi-14-0275.
2. Cloughesy, T.F.; Cavenee, W.K.; Mischel, P.S. Glioblastoma: from molecular pathology to targeted treatment. *Annu Rev Pathol* **2014**, *9*, 1-25, doi:10.1146/annurev-pathol-011110-130324.
3. Wesseling, P.; Capper, D. WHO 2016 Classification of gliomas. *Neuropathol Appl Neurobiol* **2018**, *44*, 139-150, doi:10.1111/nan.12432.
4. Ellor, S.V.; Pagano-Young, T.A.; Avgeropoulos, N.G. Glioblastoma: background, standard treatment paradigms, and supportive care considerations. *J Law Med Ethics* **2014**, *42*, 171-182, doi:10.1111/jlme.12133.
5. Wanis, H.A.; Møller, H.; Ashkan, K.; et al. The incidence of major subtypes of primary brain tumors in adults in England 1995-2017. *Neuro Oncol* **2021**, *23*, 1371-1382, doi:10.1093/neuonc/noab076.
6. Tamimi, A.F.; Juweid, M. Epidemiology and Outcome of Glioblastoma. In *Glioblastoma*, De Vleeschouwer, S., Ed.; Codon Publications: Brisbane (AU), **2017**.
7. Chen, B.; Chen, C.; Zhang, Y.; et al. Recent incidence trend of elderly patients with glioblastoma in the United States, 2000-2017. *BMC Cancer* **2021**, *21*, 54, doi:10.1186/s12885-020-07778-1.
8. Stupp, R.; Tonn, J.C.; Brada, M.; et al. High-grade malignant glioma: ESMO Clinical Practice Guidelines for diagnosis, treatment and follow-up. *Ann Oncol* **2010**, *21 Suppl 5*, v190-193, doi:10.1093/annonc/mdq187.
9. Stupp, R.; Taillibert, S.; Kanner, A.; et al. Effect of Tumor-Treating Fields Plus Maintenance Temozolomide vs Maintenance Temozolomide Alone on Survival in Patients With Glioblastoma: A Randomized Clinical Trial. *JAMA* **2017**, *318*, 2306-2316, doi:10.1001/jama.2017.18718.
10. Gately, L.; McLachlan, S.A.; Philip, J.; et al. Long-term survivors of glioblastoma: a closer look. *J Neurooncol* **2018**, *136*, 155-162, doi:10.1007/s11060-017-2635-1.
11. Dieudonné, N.; De Micheli, R.; Hottinger, A. Palliative care for glioblastoma. *Rev Med Suisse* **2016**, *12*, 853-856.
12. Louis, D.N.; Ohgaki, H.; Wiestler, O.D.; et al. The 2007 WHO classification of tumours of the central nervous system. *Acta Neuropathol* **2007**, *114*, 97-109, doi:10.1007/s00401-007-0243-4.
13. Wesseling, P.; Kros, J.M.; Jeuken, J.W.M. The pathological diagnosis of diffuse gliomas: towards a smart synthesis of microscopic and molecular information in a multidisciplinary context. *Diagn Histopathol* **2011**, *17*, 486-494, doi:10.1016/j.mpdhp.2011.08.005.
14. Anjum, K.; Shagufta, B.I.; Abbas, S.Q.; et al. Current status and future therapeutic perspectives of glioblastoma multiforme (GBM) therapy: A review. *Biomed Pharmacother* **2017**, *92*, 681-689, doi:10.1016/j.biopha.2017.05.125.
15. Urbańska, K.; Sokołowska, J.; Szmidt, M.; et al. Glioblastoma multiforme - an overview. *Contemp Oncol (Pozn)* **2014**, *18*, 307-312, doi:10.5114/wo.2014.40559.

16. Ohgaki, H.; Kleihues, P. The definition of primary and secondary glioblastoma. *Clin Cancer Res* **2013**, *19*, 764-772, doi:10.1158/1078-0432.Ccr-12-3002.

17. Aldape, K.; Zadeh, G.; Mansouri, S.; et al. Glioblastoma: pathology, molecular mechanisms and markers. *Acta Neuropathol* **2015**, *129*, 829-848, doi:10.1007/s00401-015-1432-1.

18. Zhao, H.; Wang, S.; Song, C.; et al. The prognostic value of MGMT promoter status by pyrosequencing assay for glioblastoma patients' survival: a meta-analysis. *World J Surg Oncol* **2016**, *14*, 261, doi:10.1186/s12957-016-1012-4.

19. Hegi, M.E.; Diserens, A.C.; Gorlia, T.; et al. MGMT gene silencing and benefit from temozolomide in glioblastoma. *N Engl J Med* **2005**, *352*, 997-1003, doi:10.1056/NEJMoa043331.

20. Limam, S.; Missaoui, N.; Abdessayed, N.; et al. Prognostic significance of MGMT methylation and expression of MGMT, P53, EGFR, MDM2 and PTEN in glioblastoma multiforme. *Ann Biol Clin (Paris)* **2019**, *77*, 307-317, doi:10.1684/abc.2019.1448.

21. Pinson, H.; Hallaert, G.; Van der Meulen, J.; et al. Weak MGMT gene promoter methylation confers a clinically significant survival benefit in patients with newly diagnosed glioblastoma: a retrospective cohort study. *J Neurooncol* **2020**, *146*, 55-62, doi:10.1007/s11060-019-03334-5.

22. Rivera, A.L.; Pelloski, C.E.; Gilbert, M.R.; et al. MGMT promoter methylation is predictive of response to radiotherapy and prognostic in the absence of adjuvant alkylating chemotherapy for glioblastoma. *Neuro Oncol* **2010**, *12*, 116-121, doi:10.1093/neuonc/nop020.

23. Watts, G.S.; Pieper, R.O.; Costello, J.F.; et al. Methylation of discrete regions of the O6-methylguanine DNA methyltransferase (MGMT) CpG island is associated with heterochromatinization of the MGMT transcription start site and silencing of the gene. *Mol Cell Biol* **1997**, *17*, 5612-5619, doi:10.1128/mcb.17.9.5612.

24. Louis, D.N.; Perry, A.; Reifenberger, G.; et al. The 2016 World Health Organization Classification of Tumors of the Central Nervous System: a summary. *Acta Neuropathol* **2016**, *131*, 803-820, doi:10.1007/s00401-016-1545-1.

25. Louis, D.N.; Perry, A.; Wesseling, P.; et al. The 2021 WHO Classification of Tumors of the Central Nervous System: a summary. *Neuro Oncol* **2021**, *23*, 1231-1251, doi:10.1093/neuonc/noab106.

26. Komori, T. The 2021 WHO classification of tumors, 5th edition, central nervous system tumors: the 10 basic principles. *Brain Tumor Pathol* **2022**, *39*, 47-50, doi:10.1007/s10014-022-00428-3.

27. Smith, H.L.; Wadhwani, N.; Horbinski, C. Major Features of the 2021 WHO Classification of CNS Tumors. *Neurotherapeutics* **2022**, *19*, 1691-1704, doi:10.1007/s13311-022-01249-0.

28. Almairac, F. Plasticité des cellules tumorales de glioblastomes : inter-conversion d'un phénotype différencié et souche en fonction du microenvironnement. Université de Nice-Sophia Antipolis, 2016.

29. Info-radiologie.ch. Imagerie par résonance magnétique (IRM) [Internet]. [quoted 12 november 2023]. Available on: https://www.info-radiologie.ch/resonance_magnetique.php

30. Ku, M.-C.; Waiczies, S.; Niendorf, T.; et al. Assessment of Blood Brain Barrier Leakage with Gadolinium-Enhanced MRI. In *Preclinical MRI: Methods and Protocols*, García Martín, M.L.;López Larrubia, P., Eds.; Springer New York: New York (NY), **2018**; pp. 395-408.

31. Stuckey, S.L.; Goh, T.D.; Heffernan, T.; et al. Hyperintensity in the subarachnoid space on FLAIR MRI. *AJR Am J Roentgenol* **2007**, *189*, 913-921, doi:10.2214/ajr.07.2424.

32. Schultz, T.; Vilanova, A. Diffusion MRI visualization. *NMR Biomed* **2019**, *32*, e3902, doi:10.1002/nbm.3902.

33. Tsien, C.; Cao, Y.; Chenevert, T. Clinical applications for diffusion magnetic resonance imaging in radiotherapy. *Semin Radiat Oncol* **2014**, *24*, 218-226, doi:10.1016/j.semradonc.2014.02.004.

34. Papaevangelou, E.; Almeida, G.S.; Jamin, Y.; et al. Diffusion-weighted MRI for imaging cell death after cytotoxic or apoptosis-inducing therapy. *Br J Cancer* **2015**, *112*, 1471-1479, doi:10.1038/bjc.2015.134.

35. Schmainda, K.M. Diffusion-weighted MRI as a biomarker for treatment response in glioma. *CNS Oncol* **2012**, *1*, 169-180, doi:10.2217/cns.12.25.

36. Zhang, N.; Zhang, L.; Qiu, B.; et al. Correlation of volume transfer coefficient Ktrans with histopathologic grades of gliomas. *J Magn Reson Imaging* **2012**, *36*, 355-363, doi:10.1002/jmri.23675.

37. Santarosa, C.; Castellano, A.; Conte, G.M.; et al. Dynamic contrast-enhanced and dynamic susceptibility contrast perfusion MR imaging for glioma grading: Preliminary comparison of vessel compartment and permeability parameters using hotspot and histogram analysis. *Eur J Radiol* **2016**, *85*, 1147-1156, doi:10.1016/j.ejrad.2016.03.020.

38. Zhao, M.; Guo, L.L.; Huang, N.; et al. Quantitative analysis of permeability for glioma grading using dynamic contrast-enhanced magnetic resonance imaging. *Oncol Lett* **2017**, *14*, 5418-5426, doi:10.3892/ol.2017.6895.

39. Li, X.; Zhu, Y.; Kang, H.; et al. Glioma grading by microvascular permeability parameters derived from dynamic contrast-enhanced MRI and intratumoral susceptibility signal on susceptibility weighted imaging. *Cancer Imaging* **2015**, *15*, 4, doi:10.1186/s40644-015-0039-z.

40. Andreelli, F.; Mosbah, H. IRM fonctionnelle cérébrale : les principes. *Médecine des Maladies Métaboliques* **2014**, *8*, 13-19, doi:10.1016/S1957-2557(14)70677-7.

41. Albert, N.L.; Weller, M.; Suchorska, B.; et al. Response Assessment in Neuro-Oncology working group and European Association for Neuro-Oncology recommendations for the clinical use of PET imaging in gliomas. *Neuro Oncol* **2016**, *18*, 1199-1208, doi:10.1093/neuonc/now058.

42. Herholz, K. Brain Tumors: An Update on Clinical PET Research in Gliomas. *Semin Nucl Med* **2017**, *47*, 5-17, doi:10.1053/j.semnuclmed.2016.09.004.

43. la Fougère, C.; Suchorska, B.; Bartenstein, P.; et al. Molecular imaging of gliomas with PET: opportunities and limitations. *Neuro Oncol* **2011**, *13*, 806-819, doi:10.1093/neuonc/nor054.

44. Palanichamy, K.; Chakravarti, A. Diagnostic and Prognostic Significance of Methionine Uptake and Methionine Positron Emission Tomography Imaging in Gliomas. *Front Oncol* **2017**, *7*, 257, doi:10.3389/fonc.2017.00257.

45. Verger, A.; Arbizu, J.; Law, I. Role of amino-acid PET in high-grade gliomas: limitations and perspectives. *Q J Nucl Med Mol Imaging* **2018**, *62*, 254-266, doi:10.23736/s1824-4785.18.03092-3.

46. Birkó, Z.; Nagy, B.; Klekner, Á.; et al. Novel Molecular Markers in Glioblastoma-Benefits of Liquid Biopsy. *Int J Mol Sci* **2020**, *21*, doi:10.3390/ijms21207522.

47. Cha, G.D.; Kang, T.; Baik, S.; et al. Advances in drug delivery technology for the treatment of glioblastoma multiforme. *J Control Release* **2020**, *328*, 350-367, doi:10.1016/j.jconrel.2020.09.002

48. Young, R.M.; Jamshidi, A.; Davis, G.; et al. Current trends in the surgical management and treatment of adult glioblastoma. *Ann Transl Med* **2015**, *3*, 121-121, doi:10.3978/j.issn.2305-5839.2015.05.10.

49. Fazeny-Dörner, B.; Wenzel, C.; Veitl, M.; et al. Survival and prognostic factors of patients with unresectable glioblastoma multiforme. *Anticancer Drugs* **2003**, *14*, 305-312, doi:10.1097/00001813-200304000-00008.

50. Yabroff, K.R.; Harlan, L.; Zeruto, C.; et al. Patterns of care and survival for patients with glioblastoma multiforme diagnosed during 2006. *Neuro Oncol* **2012**, *14*, 351-359, doi:10.1093/neuonc/nor218.

51. Lesueur, P.; Lequesne, J.; Grellard, J.M.; et al. Phase I/IIa study of concomitant radiotherapy with olaparib and temozolomide in unresectable or partially resectable glioblastoma: OLA-TMZ-RTE-01 trial protocol. *BMC Cancer* **2019**, *19*, 198, doi:10.1186/s12885-019-5413-y.

52. Walker, M.D.; Alexander, E., Jr.; Hunt, W.E.; et al. Evaluation of BCNU and/or radiotherapy in the treatment of anaplastic gliomas. A cooperative clinical trial. *J Neurosurg* **1978**, *49*, 333-343, doi:10.3171/jns.1978.49.3.0333.

53. Dhermain, F. Radiotherapy of high-grade gliomas: current standards and new concepts, innovations in imaging and radiotherapy, and new therapeutic approaches. *Chin J Cancer* **2014**, *33*, 16-24, doi:10.5732/cjc.013.10217.

54. Stupp, R.; Mason, W.P.; van den Bent, M.J.; et al. Radiotherapy plus concomitant and adjuvant temozolomide for glioblastoma. *N Engl J Med* **2005**, *352*, 987-996, doi:10.1056/NEJMoa043330.

55. West, H.J.; Jin, J.O. JAMA Oncology Patient Page. Performance Status in Patients With Cancer. *JAMA Oncol* **2015**, *1*, 998, doi:10.1001/jamaoncol.2015.3113.

56. Weller, M.; van den Bent, M.; Preusser, M.; et al. EANO guidelines on the diagnosis and treatment of diffuse gliomas of adulthood. *Nat Rev Clin Oncol* **2021**, *18*, 170-186, doi:10.1038/s41571-020-00447-z.

57. Braun, K.; Ahluwalia, M.S. Treatment of Glioblastoma in Older Adults. *Current Oncology Reports* **2017**, *19*, 81, doi:10.1007/s11912-017-0644-z.

58. Arora, A.; Somasundaram, K. Glioblastoma vs temozolomide: can the red queen race be won? *Cancer Biol Ther* **2019**, *20*, 1083-1090, doi:10.1080/15384047.2019.1599662.

59. Zhang, J.; Stevens, M.F.; Bradshaw, T.D. Temozolomide: mechanisms of action, repair and resistance. *Curr Mol Pharmacol* **2012**, *5*, 102-114, doi:10.2174/1874467211205010102.

60. Davis, M.E. Glioblastoma: Overview of Disease and Treatment. *Clin J Oncol Nurs* **2016**, *20*, S2-S8, doi:10.1188/16.CJON.S1.2-8.

61. Tesileanu, C.M.S.; Sanson, M.; Wick, W.; et al. Temozolomide and Radiotherapy versus Radiotherapy Alone in Patients with Glioblastoma, IDH-wildtype: Post Hoc Analysis of the EORTC Randomized Phase III CATNON Trial. *Clin Cancer Res* **2022**, *28*, 2527-2535, doi:10.1158/1078-0432.Ccr-21-4283.

62. Birzu, C.; French, P.; Caccese, M.; et al. Recurrent Glioblastoma: From Molecular Landscape to New Treatment Perspectives. *Cancers (Basel)* **2020**, *13*, doi:10.3390/cancers13010047.

63. Cohen, M.H.; Shen, Y.L.; Keegan, P.; et al. FDA drug approval summary: bevacizumab (Avastin) as treatment of recurrent glioblastoma multiforme. *Oncologist* **2009**, *14*, 1131-1138, doi:10.1634/theoncologist.2009-0121.

64. Kreisl, T.N.; Kim, L.; Moore, K.; et al. Phase II trial of single-agent bevacizumab followed by bevacizumab plus irinotecan at tumor progression in recurrent glioblastoma. *J Clin Oncol* **2009**, *27*, 740-745, doi:10.1200/jco.2008.16.3055.

65. Friedman, H.S.; Prados, M.D.; Wen, P.Y.; et al. Bevacizumab alone and in combination with irinotecan in recurrent glioblastoma. *J Clin Oncol* **2009**, *27*, 4733-4740, doi:10.1200/jco.2008.19.8721.

66. Diaz, R.J.; Ali, S.; Qadir, M.G.; et al. The role of bevacizumab in the treatment of glioblastoma. *J Neurooncol* **2017**, *133*, 455-467, doi:10.1007/s11060-017-2477-x.

67. Chinot, O.L.; Wick, W.; Mason, W.; et al. Bevacizumab plus radiotherapy-temozolomide for newly diagnosed glioblastoma. *N Engl J Med* **2014**, *370*, 709-722, doi:10.1056/NEJMoa1308345.

68. Gilbert, M.R.; Dignam, J.J.; Armstrong, T.S.; et al. A randomized trial of bevacizumab for newly diagnosed glioblastoma. *N Engl J Med* **2014**, *370*, 699-708, doi:10.1056/NEJMoa1308573.

69. Reardon, D.A.; Brandes, A.A.; Omuro, A.; et al. Effect of Nivolumab vs Bevacizumab in Patients With Recurrent Glioblastoma: The CheckMate 143 Phase 3 Randomized Clinical Trial. *JAMA Oncol* **2020**, *6*, 1003-1010, doi:10.1001/jamaoncol.2020.1024.

70. van der Meulen, M.; Chahal, M.; Mason, W.P. The Value of Etoposide for Recurrent Glioma. *Can J Neurol Sci* **2023**, 1-4, doi:10.1017/cjn.2023.276.

71. Schmidt, T.; Agkatsev, S.; Feldheim, J.; et al. Feasibility and tolerability of trofosfamide and etoposide in progressive glioblastoma. *Neurooncol Adv* **2023**, *5*, vdad090, doi:10.1093/noajnl/vdad090.

72. Detti, B.; Scoccianti, S.; Teriaca, M.A.; et al. Bevacizumab in recurrent high-grade glioma: a single institution retrospective analysis on 92 patients. *Radiol Med* **2021**, *126*, 1249-1254, doi:10.1007/s11547-021-01381-5.

73. Dongpo, S.; Zhengyao, Z.; Xiaozhuo, L.; et al. Efficacy and Safety of Bevacizumab Combined with Other Therapeutic Regimens for Treatment of Recurrent Glioblastoma: A Network Meta-analysis. *World Neurosurg* **2022**, *160*, e61-e79, doi:10.1016/j.wneu.2021.12.091.

74. Davis, M.E.; Stoiber, A.M. Glioblastoma multiforme: enhancing survival and quality of life. *Clin J Oncol Nurs* **2011**, *15*, 291-297, doi:10.1188/11.Cjon.291-297.

75. Muir, M.; Patel, R.; Traylor, J.I.; et al. Laser interstitial thermal therapy for newly diagnosed glioblastoma. *Lasers Med Sci* **2022**, *37*, 1811-1820, doi:10.1007/s10103-021-03435-6.

76. Afshari, A.R.; Sanati, M.; Aminyavari, S.; et al. Advantages and drawbacks of dexamethasone in glioblastoma multiforme. *Crit Rev Oncol Hematol* **2022**, *172*, 103625, doi:10.1016/j.critrevonc.2022.103625.

77. Esquenazi, Y.; Lo, V.P.; Lee, K. Critical Care Management of Cerebral Edema in Brain Tumors. *J Intensive Care Med* **2017**, *32*, 15-24, doi:10.1177/0885066615619618.

78. Mistry, A.M.; Jonathan, S.V.; Monsour, M.A.; et al. Impact of postoperative dexamethasone on survival, steroid dependency, and infections in newly diagnosed glioblastoma patients. *Neurooncol Pract* **2021**, *8*, 589-600, doi:10.1093/nop/npab039.

79. Petrelli, F.; De Stefani, A.; Ghidini, A.; et al. Steroids use and survival in patients with glioblastoma multiforme: a pooled analysis. *J Neurol* **2021**, *268*, 440-447, doi:10.1007/s00415-020-09731-5.

80. Rominiyi, O.; Vanderlinden, A.; Clenton, S.J.; et al. Tumour treating fields therapy for glioblastoma: current advances and future directions. *Br J Cancer* **2021**, *124*, 697-709, doi:10.1038/s41416-020-01136-5.

81. Stupp, R.; Wong, E.T.; Kanner, A.A.; et al. NovoTTF-100A versus physician's choice chemotherapy in recurrent glioblastoma: a randomised phase III trial of a novel treatment modality. *Eur J Cancer* **2012**, *48*, 2192-2202, doi:10.1016/j.ejca.2012.04.011.

82. Lai, A.; Tran, A.; Nghiemphu, P.L.; et al. Phase II study of bevacizumab plus temozolomide during and after radiation therapy for patients with newly diagnosed glioblastoma multiforme. *J Clin Oncol* **2011**, *29*, 142-148, doi:10.1200/jco.2010.30.2729.

83. Vredenburgh, J.J.; Desjardins, A.; Herndon, J.E., 2nd; et al. Bevacizumab plus irinotecan in recurrent glioblastoma multiforme. *J Clin Oncol* **2007**, *25*, 4722-4729, doi:10.1200/jco.2007.12.2440.

84. Nabors, L.B.; Fink, K.L.; Mikkelsen, T.; et al. Two cilengitide regimens in combination with standard treatment for patients with newly diagnosed glioblastoma and unmethylated MGMT gene promoter: results of the open-label, controlled, randomized phase II CORE study. *Neuro Oncol* **2015**, *17*, 708-717, doi:10.1093/neuonc/nou356.

85. Stupp, R.; Hegi, M.E.; Gorlia, T.; et al. Cilengitide combined with standard treatment for patients with newly diagnosed glioblastoma with methylated MGMT promoter (CENTRIC EORTC 26071-22072 study): a multicentre, randomised, open-label, phase 3 trial. *Lancet Oncol* **2014**, *15*, 1100-1108, doi:10.1016/s1470-2045(14)70379-1.

86. Prados, M.D.; Chang, S.M.; Butowski, N.; et al. Phase II study of erlotinib plus temozolomide during and after radiation therapy in patients with newly diagnosed glioblastoma multiforme or gliosarcoma. *J Clin Oncol* **2009**, *27*, 579-584, doi:10.1200/jco.2008.18.9639.

87. Uhm, J.H.; Ballman, K.V.; Wu, W.; et al. Phase II evaluation of gefitinib in patients with newly diagnosed Grade 4 astrocytoma: Mayo/North Central Cancer Treatment Group Study N0074. *Int J Radiat Oncol Biol Phys* **2011**, *80*, 347-353, doi:10.1016/j.ijrobp.2010.01.070.

88. Westphal, M.; Heese, O.; Steinbach, J.P.; et al. A randomised, open label phase III trial with nimotuzumab, an anti-epidermal growth factor receptor monoclonal antibody in the treatment of newly diagnosed adult glioblastoma. *Eur J Cancer* **2015**, *51*, 522-532, doi:10.1016/j.ejca.2014.12.019.

89. Lv, S.; Teugels, E.; Sadones, J.; et al. Correlation of EGFR, IDH1 and PTEN status with the outcome of patients with recurrent glioblastoma treated in a phase II clinical trial with the EGFR-blocking monoclonal antibody cetuximab. *Int J Oncol* **2012**, *41*, 1029-1035, doi:10.3892/ijo.2012.1539.

90. Mellinghoff, I.K.; Ellingson, B.M.; Touat, M.; et al. Ivosidenib in Isocitrate Dehydrogenase 1-Mutated Advanced Glioma. *J Clin Oncol* **2020**, *38*, 3398-3406, doi:10.1200/jco.19.03327.

91. Mellinghoff, I.K.; Penas-Prado, M.; Peters, K.B.; et al. Vorasidenib, a Dual Inhibitor of Mutant IDH1/2, in Recurrent or Progressive Glioma; Results of a First-in-Human Phase I Trial. *Clin Cancer Res* **2021**, *27*, 4491-4499, doi:10.1158/1078-0432.Ccr-21-0611.

92. Bausart, M.; Préat, V.; Malfanti, A. Immunotherapy for glioblastoma: the promise of combination strategies. *J Exp Clin Cancer Res* **2022**, *41*, 35, doi:10.1186/s13046-022-02251-2.

93. ERC news. ERC granted FDA Fast Track designation sitoiganap patients recurrent glioblastoma. [Internet]. [quoted 20 march 2024]. Available on: https://www.erc-immunotherapy.com/media/news/erc-granted-fda-fast-track-designation-sitoiganap-patients-recurrent-glioblastoma

94. Schuster, J.; Lai, R.K.; Recht, L.D.; et al. A phase II, multicenter trial of rindopepimut (CDX-110) in newly diagnosed glioblastoma: the ACT III study. *Neuro Oncol* **2015**, *17*, 854-861, doi:10.1093/neuonc/nou348.

95. Ahmed, N.; Salsman, V.S.; Kew, Y.; et al. HER2-specific T cells target primary glioblastoma stem cells and induce regression of autologous experimental tumors. *Clin Cancer Res* **2010**, *16*, 474-485, doi:10.1158/1078-0432.Ccr-09-1322.

96. Johnson, L.A.; Scholler, J.; Ohkuri, T.; et al. Rational development and characterization of humanized anti-EGFR variant III chimeric antigen receptor T cells for glioblastoma. *Sci Transl Med* **2015**, *7*, 275ra222, doi:10.1126/scitranslmed.aaa4963.

97. Brahmer, J.R.; Tykodi, S.S.; Chow, L.Q.; et al. Safety and activity of anti-PD-L1 antibody in patients with advanced cancer. *N Engl J Med* **2012**, *366*, 2455-2465, doi:10.1056/NEJMoa1200694.

98. Buchbinder, E.I.; Desai, A. CTLA-4 and PD-1 Pathways: Similarities, Differences, and Implications of Their Inhibition. *Am J Clin Oncol* **2016**, *39*, 98-106, doi:10.1097/coc.0000000000000239.

99. Bastiancich, C.; Malfanti, A.; Préat, V.; et al. Rationally designed drug delivery systems for the local treatment of resected glioblastoma. *Adv Drug Deliv Rev* **2021**, *177*, 113951, doi:10.1016/j.addr.2021.113951.

100. Bock, H.C.; Puchner, M.J.; Lohmann, F.; et al. First-line treatment of malignant glioma with carmustine implants followed by concomitant radiochemotherapy: a multicenter experience. *Neurosurg Rev* **2010**, *33*, 441-449, doi:10.1007/s10143-010-0280-7.

101. Bastiancich, C.; Lemaire, L.; Bianco, J.; et al. Evaluation of lauroyl-gemcitabine-loaded hydrogel efficacy in glioblastoma rat models. *Nanomedicine (Lond)* **2018**, *13*, 1999-2013, doi:10.2217/nnm-2018-0057.

102. McCrorie, P.; Mistry, J.; Taresco, V.; et al. Etoposide and olaparib polymer-coated nanoparticles within a bioadhesive sprayable hydrogel for post-surgical localised delivery to brain tumours. *Eur J Pharm Biopharm* **2020**, *157*, 108-120, doi:10.1016/j.ejpb.2020.10.005.

103. Hicks, W.H.; Bird, C.E.; Traylor, J.I.; et al. Contemporary Mouse Models in Glioma Research. *Cells* **2021**, *10*, doi:10.3390/cells10030712.

104. Huszthy, P.C.; Daphu, I.; Niclou, S.P.; et al. In vivo models of primary brain tumors: pitfalls and perspectives. *Neuro Oncol* **2012**, *14*, 979-993, doi:10.1093/neuonc/nos135.

105. Martens, T.; Laabs, Y.; Günther, H.S.; et al. Inhibition of glioblastoma growth in a highly invasive nude mouse model can be achieved by targeting epidermal growth factor receptor but not vascular endothelial growth factor receptor-2. *Clin Cancer Res* **2008**, *14*, 5447-5458, doi:10.1158/1078-0432.Ccr-08-0147.

106. Mahesparan, R.; Read, T.A.; Lund-Johansen, M.; et al. Expression of extracellular matrix components in a highly infiltrative in vivo glioma model. *Acta Neuropathol* **2003**, *105*, 49-57, doi:10.1007/s00401-002-0610-0.

107. Kijima, N.; Hosen, N.; Kagawa, N.; et al. Wilms' tumor 1 is involved in tumorigenicity of glioblastoma by regulating cell proliferation and apoptosis. *Anticancer Res* **2014**, *34*, 61-67.

108. Akter, F.; Simon, B.; de Boer, N.L.; et al. Pre-clinical tumor models of primary brain tumors: Challenges and opportunities. *Biochim Biophys Acta Rev Cancer* **2021**, *1875*, 188458, doi:10.1016/j.bbcan.2020.188458.

109. Frese, K.K.; Tuveson, D.A. Maximizing mouse cancer models. *Nat Rev Cancer* **2007**, *7*, 654-658, doi:10.1038/nrc2192.

110. Anderson, R.C.; Elder, J.B.; Brown, M.D.; et al. Changes in the immunologic phenotype of human malignant glioma cells after passaging in vitro. *Clin Immunol* **2002**, *102*, 84-95, doi:10.1006/clim.2001.5152.

111. Ernst, A.; Hofmann, S.; Ahmadi, R.; et al. Genomic and expression profiling of glioblastoma stem cell-like spheroid cultures identifies novel tumor-relevant genes associated with survival. *Clin Cancer Res* **2009**, *15*, 6541-6550, doi:10.1158/1078-0432.Ccr-09-0695.

112. Clark, M.J.; Homer, N.; O'Connor, B.D.; et al. U87MG decoded: the genomic sequence of a cytogenetically aberrant human cancer cell line. *PLoS Genet* **2010**, *6*, e1000832, doi:10.1371/journal.pgen.1000832.

113. Ganipineni, L.P.; Ucakar, B.; Joudiou, N.; et al. Magnetic targeting of paclitaxel-loaded poly(lactic-co-glycolic acid)-based nanoparticles for the treatment of glioblastoma. *Int J Nanomedicine* **2018**, *13*, 4509-4521, doi:10.2147/ijn.S165184.

114. Jin, K.; Teng, L.; Shen, Y.; et al. Patient-derived human tumour tissue xenografts in immunodeficient mice: a systematic review. *Clin Transl Oncol* **2010**, *12*, 473-480, doi:10.1007/s12094-010-0540-6.

115. Hidalgo, M.; Amant, F.; Biankin, A.V.; et al. Patient-derived xenograft models: an emerging platform for translational cancer research. *Cancer Discov* **2014**, *4*, 998-1013, doi:10.1158/2159-8290.Cd-14-0001.

116. Irtenkauf, S.M.; Sobiechowski, S.; Hasselbach, L.A.; et al. Optimization of Glioblastoma Mouse Orthotopic Xenograft Models for Translational Research. *Comp Med* **2017**, *67*, 300-314.

117. Wang, J.; Miletic, H.; Sakariassen, P.; et al. A reproducible brain tumour model established from human glioblastoma biopsies. *BMC Cancer* **2009**, *9*, 465, doi:10.1186/1471-2407-9-465.

118. da Hora, C.C.; Schweiger, M.W.; Wurdinger, T.; et al. Patient-Derived Glioma Models: From Patients to Dish to Animals. *Cells* **2019**, *8*, doi:10.3390/cells8101177.

119. Choi, Y.; Lee, S.; Kim, K.; et al. Studying cancer immunotherapy using patient-derived xenografts (PDXs) in humanized mice. *Exp Mol Med* **2018**, *50*, 1-9, doi:10.1038/s12276-018-0115-0.

120. Oh, T.; Fakurnejad, S.; Sayegh, E.T.; et al. Immunocompetent murine models for the study of glioblastoma immunotherapy. *J Transl Med* **2014**, *12*, 107, doi:10.1186/1479-5876-12-107.

121. Chulpanova, D.S.; Kitaeva, K.V.; Rutland, C.S.; et al. Mouse Tumor Models for Advanced Cancer Immunotherapy. *Int J Mol Sci* **2020**, *21*, doi:10.3390/ijms21114118.

122. Richmond, A.; Su, Y. Mouse xenograft models vs GEM models for human cancer therapeutics. *Dis Model Mech* **2008**, *1*, 78-82, doi:10.1242/dmm.000976.

123. Obermeier, B.; Daneman, R.; Ransohoff, R.M. Development, maintenance and disruption of the blood-brain barrier. *Nat Med* **2013**, *19*, 1584-1596, doi:10.1038/nm.3407.

124. Hottinger, A.F.; Stupp, R.; Homicsko, K. Standards of care and novel approaches in the management of glioblastoma multiforme. *Chin J Cancer* **2014**, *33*, 32-39, doi:10.5732/cjc.013.10207.

125. Gao, X.; Yue, Q.; Liu, Y.; et al. Image-guided chemotherapy with specifically tuned blood brain barrier permeability in glioma margins. *Theranostics* **2018**, *8*, 3126-3137, doi:10.7150/thno.24784.

126. Oberoi, R.K.; Parrish, K.E.; Sio, T.T.; et al. Strategies to improve delivery of anticancer drugs across the blood-brain barrier to treat glioblastoma. *Neuro Oncol* **2016**, *18*, 27-36, doi:10.1093/neuonc/nov164.

127. Luo, H.; Shusta, E.V. Blood-Brain Barrier Modulation to Improve Glioma Drug Delivery. *Pharmaceutics* **2020**, *12*, doi:10.3390/pharmaceutics12111085.

128. Mainprize, T.; Lipsman, N.; Huang, Y.; et al. Blood-Brain Barrier Opening in Primary Brain Tumors with Non-invasive MR-Guided Focused Ultrasound: A Clinical Safety and Feasibility Study. *Sci Rep* **2019**, *9*, 321, doi:10.1038/s41598-018-36340-0.

129. Karmur, B.S.; Philteos, J.; Abbasian, A.; et al. Blood-Brain Barrier Disruption in Neuro-Oncology: Strategies, Failures, and Challenges to Overcome. *Front Oncol* **2020**, *10*, 563840, doi:10.3389/fonc.2020.563840.

130. Obermeier, B.; Verma, A.; Ransohoff, R.M. The blood-brain barrier. *Handb Clin Neurol* **2016**, *133*, 39-59, doi:10.1016/b978-0-444-63432-0.00003-7.

131. Pardridge, W.M. CSF, blood-brain barrier, and brain drug delivery. *Expert Opin Drug Deliv* **2016**, *13*, 963-975, doi:10.1517/17425247.2016.1171315.

132. Serlin, Y.; Shelef, I.; Knyazer, B.; et al. Anatomy and physiology of the blood-brain barrier. *Semin Cell Dev Biol* **2015**, *38*, 2-6, doi:10.1016/j.semcdb.2015.01.002.

133. Lombardo, S.M.; Schneider, M.; Türeli, A.E.; et al. Key for crossing the BBB with nanoparticles: the rational design. *Beilstein J Nanotechnol* **2020**, *11*, 866-883, doi:10.3762/bjnano.11.72.

134. Sweeney, M.D.; Sagare, A.P.; Zlokovic, B.V. Blood-brain barrier breakdown in Alzheimer disease and other neurodegenerative disorders. *Nat Rev Neurol* **2018**, *14*, 133-150, doi:10.1038/nrneurol.2017.188.

135. Tietz, S.; Engelhardt, B. Brain barriers: Crosstalk between complex tight junctions and adherens junctions. *J Cell Biol* **2015**, *209*, 493-506, doi:10.1083/jcb.201412147.

136. Armulik, A.; Genové, G.; Betsholtz, C. Pericytes: developmental, physiological, and pathological perspectives, problems, and promises. *Dev Cell* **2011**, *21*, 193-215, doi:10.1016/j.devcel.2011.07.001.

137. Hall, C.N.; Reynell, C.; Gesslein, B.; et al. Capillary pericytes regulate cerebral blood flow in health and disease. *Nature* **2014**, *508*, 55-60, doi:10.1038/nature13165.

138. Peppiatt, C.M.; Howarth, C.; Mobbs, P.; et al. Bidirectional control of CNS capillary diameter by pericytes. *Nature* **2006**, *443*, 700-704, doi:10.1038/nature05193.

139. Daneman, R.; Zhou, L.; Kebede, A.A.; et al. Pericytes are required for blood-brain barrier integrity during embryogenesis. *Nature* **2010**, *468*, 562-566, doi:10.1038/nature09513.

140. Zhao, Z.; Nelson, A.R.; Betsholtz, C.; et al. Establishment and Dysfunction of the Blood-Brain Barrier. *Cell* **2015**, *163*, 1064-1078, doi:10.1016/j.cell.2015.10.067.

141. Sagare, A.P.; Bell, R.D.; Zhao, Z.; et al. Pericyte loss influences Alzheimer-like neurodegeneration in mice. *Nat Commun* **2013**, *4*, 2932, doi:10.1038/ncomms3932.

142. Sofroniew, M.V.; Vinters, H.V. Astrocytes: biology and pathology. *Acta Neuropathol* **2010**, *119*, 7-35, doi:10.1007/s00401-009-0619-8.

143. Abbott, N.J.; Patabendige, A.A.; Dolman, D.E.; et al. Structure and function of the blood-brain barrier. *Neurobiol Dis* **2010**, *37*, 13-25, doi:10.1016/j.nbd.2009.07.030.

144. Zlokovic, B.V. The blood-brain barrier in health and chronic neurodegenerative disorders. *Neuron* **2008**, *57*, 178-201, doi:10.1016/j.neuron.2008.01.003.

145. Alvarez, J.I.; Dodelet-Devillers, A.; Kebir, H.; et al. The Hedgehog pathway promotes blood-brain barrier integrity and CNS immune quiescence. *Science* **2011**, *334*, 1727-1731, doi:10.1126/science.1206936.

146. Wosik, K.; Cayrol, R.; Dodelet-Devillers, A.; et al. Angiotensin II controls occludin function and is required for blood brain barrier maintenance: relevance to multiple sclerosis. *J Neurosci* **2007**, *27*, 9032-9042, doi:10.1523/jneurosci.2088-07.2007.

147. Bell, R.D.; Winkler, E.A.; Singh, I.; et al. Apolipoprotein E controls cerebrovascular integrity via cyclophilin A. *Nature* **2012**, *485*, 512-516, doi:10.1038/nature11087.

148. Barar, J.; Rafi, M.A.; Pourseif, M.M.; et al. Blood-brain barrier transport machineries and targeted therapy of brain diseases. *Bioimpacts* **2016**, *6*, 225-248, doi:10.15171/bi.2016.30.

149. Belykh, E.; Shaffer, K.V.; Lin, C.; et al. Blood-Brain Barrier, Blood-Brain Tumor Barrier, and Fluorescence-Guided Neurosurgical Oncology: Delivering Optical Labels to Brain Tumors. *Front Oncol* **2020**, *10*, doi:10.3389/fonc.2020.00739.

150. Gawdi, R.; Shumway, K.R.; Emmady, P.D. Physiology, Blood Brain Barrier. In *StatPearls*; StatPearls Publishing LLC: Treasure Island (FL), **2023**.

151. Sanchez-Covarrubias, L.; Slosky, L.M.; Thompson, B.J.; et al. Transporters at CNS barrier sites: obstacles or opportunities for drug delivery? *Curr Pharm Des* **2014**, *20*, 1422-1449, doi:10.2174/13816128113199990463.

152. Boado, R.J.; Li, J.Y.; Nagaya, M.; et al. Selective expression of the large neutral amino acid transporter at the blood-brain barrier. *Proc Natl Acad Sci U S A* **1999**, *96*, 12079-12084, doi:10.1073/pnas.96.21.12079.

153. Villaseñor, R.; Lampe, J.; Schwaninger, M.; et al. Intracellular transport and regulation of transcytosis across the blood-brain barrier. *Cell Mol Life Sci* **2019**, *76*, 1081-1092, doi:10.1007/s00018-018-2982-x.

154. Pulgar, V.M. Transcytosis to Cross the Blood Brain Barrier, New Advancements and Challenges. *Front Neurosci* **2018**, *12*, 1019, doi:10.3389/fnins.2018.01019.

155. Jones, A.R.; Shusta, E.V. Blood-brain barrier transport of therapeutics via receptor-mediation. *Pharm Res* **2007**, *24*, 1759-1771, doi:10.1007/s11095-007-9379-0.

156. Lajoie, J.M.; Shusta, E.V. Targeting receptor-mediated transport for delivery of biologics across the blood-brain barrier. *Annu Rev Pharmacol Toxicol* **2015**, *55*, 613-631, doi:10.1146/annurev-pharmtox-010814-124852.

157. Lu, W. Adsorptive-mediated brain delivery systems. *Curr Pharm Biotechnol* **2012**, *13*, 2340-2348, doi:10.2174/138920112803341851.

158. Löscher, W.; Potschka, H. Blood-brain barrier active efflux transporters: ATP-binding cassette gene family. *NeuroRx* **2005**, *2*, 86-98, doi:10.1602/neurorx.2.1.86.

159. Begley, D.J. ABC transporters and the blood-brain barrier. *Curr Pharm Des* **2004**, *10*, 1295-1312, doi:10.2174/1381612043384844.

160. Arvanitis, C.D.; Ferraro, G.B.; Jain, R.K. The blood-brain barrier and blood-tumour barrier in brain tumours and metastases. *Nat Rev Cancer* **2020**, *20*, 26-41, doi:10.1038/s41568-019-0205-x.

161. Mo, F.; Pellerino, A.; Soffietti, R.; et al. Blood-Brain Barrier in Brain Tumors: Biology and Clinical Relevance. *Int J Mol Sci* **2021**, *22*, doi:10.3390/ijms222312654.

162. Liebner, S.; Dijkhuizen, R.M.; Reiss, Y.; et al. Functional morphology of the blood-brain barrier in health and disease. *Acta Neuropathol* **2018**, *135*, 311-336, doi:10.1007/s00401-018-1815-1.

163. Kodack, D.P.; Askoxylakis, V.; Ferraro, G.B.; et al. The brain microenvironment mediates resistance in luminal breast cancer to PI3K inhibition through HER3 activation. *Sci Transl Med* **2017**, *9*, doi:10.1126/scitranslmed.aal4682.

164. Askoxylakis, V.; Ferraro, G.B.; Kodack, D.P.; et al. Preclinical Efficacy of Ado-trastuzumab Emtansine in the Brain Microenvironment. *J Natl Cancer Inst* **2016**, *108*, doi:10.1093/jnci/djv313.

165. Lockman, P.R.; Mittapalli, R.K.; Taskar, K.S.; et al. Heterogeneous blood-tumor barrier permeability determines drug efficacy in experimental brain metastases of breast cancer. *Clin Cancer Res* **2010**, *16*, 5664-5678, doi:10.1158/1078-0432.Ccr-10-1564.

166. Osswald, M.; Blaes, J.; Liao, Y.; et al. Impact of Blood-Brain Barrier Integrity on Tumor Growth and Therapy Response in Brain Metastases. *Clin Cancer Res* **2016**, *22*, 6078-6087, doi:10.1158/1078-0432.Ccr-16-1327.

167. van Tellingen, O.; Yetkin-Arik, B.; de Gooijer, M.C.; et al. Overcoming the blood-brain tumor barrier for effective glioblastoma treatment. *Drug Resist Updat* **2015**, *19*, 1-12, doi:10.1016/j.drup.2015.02.002.

168. Gould, A.; Zhang, D.; Arrieta, V.A.; et al. Delivering albumin-bound paclitaxel across the blood-brain barrier for gliomas. *Oncotarget* **2021**, *12*, 2474-2475, doi:10.18632/oncotarget.28018.

169. Rapoport, S.I. Effect of concentrated solutions on blood-brain barrier. *Am J Physiol* **1970**, *219*, 270-274, doi:10.1152/ajplegacy.1970.219.1.270.

170. Li, P.-J.; Lai, S.-Z.; Jin, T.; et al. Radiotherapy opens the blood–brain barrier and synergizes with anlotinib in treating glioblastoma. *Radiother Oncol* **2023**, *183*, 109633, doi:10.1016/j.radonc.2023.109633.

171. Aryal, M.; Arvanitis, C.D.; Alexander, P.M.; et al. Ultrasound-mediated blood-brain barrier disruption for targeted drug delivery in the central nervous system. *Adv Drug Deliv Rev* **2014**, *72*, 94-109, doi:10.1016/j.addr.2014.01.008.

172. Jain, R.K. Normalization of tumor vasculature: an emerging concept in antiangiogenic therapy. *Science* **2005**, *307*, 58-62, doi:10.1126/science.1104819.

173. Mehta, A.M.; Sonabend, A.M.; Bruce, J.N. Convection-Enhanced Delivery. *Neurotherapeutics* **2017**, *14*, 358-371, doi:10.1007/s13311-017-0520-4.

174. Raghavan, R.; Brady, M.L.; Rodríguez-Ponce, M.I.; et al. Convection-enhanced delivery of therapeutics for brain disease, and its optimization. *Neurosurg Focus* **2006**, *20*, E12, doi:10.3171/foc.2006.20.4.7.

175. Reardon, D.A.; Rich, J.N.; Friedman, H.S.; et al. Recent advances in the treatment of malignant astrocytoma. *J Clin Oncol* **2006**, *24*, 1253-1265, doi:10.1200/jco.2005.04.5302.

176. Lonser, R.R.; Sarntinoranont, M.; Morrison, P.F.; et al. Convection-enhanced delivery to the central nervous system. *J Neurosurg* **2015**, *122*, 697-706, doi:10.3171/2014.10.Jns14229.

177. Mehta, A.I.; Choi, B.D.; Raghavan, R.; et al. Imaging of convection enhanced delivery of toxins in humans. *Toxins (Basel)* **2011**, *3*, 201-206, doi:10.3390/toxins3030201.

178. Bruce, J.N.; Fine, R.L.; Canoll, P.; et al. Regression of recurrent malignant gliomas with convection-enhanced delivery of topotecan. *Neurosurgery* **2011**, *69*, 1272-1279; discussion 1279-1280, doi:10.1227/NEU.0b013e3182233e24.

179. White, E.; Bienemann, A.; Pugh, J.; et al. An evaluation of the safety and feasibility of convection-enhanced delivery of carboplatin into the white matter as a potential treatment for high-grade glioma. *J Neurooncol* **2012**, *108*, 77-88, doi:10.1007/s11060-012-0833-4.

180. Allhenn, D.; Shetab Boushehri, M.A.; Lamprecht, A. Drug delivery strategies for the treatment of malignant gliomas. *Int J Pharm* **2012**, *436*, 299-310, doi:10.1016/j.ijpharm.2012.06.025.

181. Perry, J.; Chambers, A.; Spithoff, K.; et al. Gliadel wafers in the treatment of malignant glioma: a systematic review. *Curr Oncol* **2007**, *14*, 189-194, doi:10.3747/co.2007.147.

182. Crowe, T.P.; Greenlee, M.H.W.; Kanthasamy, A.G.; et al. Mechanism of intranasal drug delivery directly to the brain. *Life Sci* **2018**, *195*, 44-52, doi:10.1016/j.lfs.2017.12.025.

183. Erdő, F.; Bors, L.A.; Farkas, D.; et al. Evaluation of intranasal delivery route of drug administration for brain targeting. *Brain Res Bull* **2018**, *143*, 155-170, doi:10.1016/j.brainresbull.2018.10.009.

184. Grassin-Delyle, S.; Buenestado, A.; Naline, E.; et al. Intranasal drug delivery: an efficient and non-invasive route for systemic administration: focus on opioids. *Pharmacol Ther* **2012**, *134*, 366-379, doi:10.1016/j.pharmthera.2012.03.003.

185. Pardeshi, C.V.; Belgamwar, V.S. Direct nose to brain drug delivery via integrated nerve pathways bypassing the blood-brain barrier: an excellent platform for brain targeting. *Expert Opin Drug Deliv* **2013**, *10*, 957-972, doi:10.1517/17425247.2013.790887.

186. Gabathuler, R. Approaches to transport therapeutic drugs across the blood–brain barrier to treat brain diseases. *Neurobiol Dis* **2010**, *37*, 48-57, doi:10.1016/j.nbd.2009.07.028.

187. Rapoport, S.I.; Hori, M.; Klatzo, I. Testing of a hypothesis for osmotic opening of the blood-brain barrier. *Am J Physiol* **1972**, *223*, 323-331, doi:10.1152/ajplegacy.1972.223.2.323.

188. Siegal, T.; Rubinstein, R.; Bokstein, F.; et al. In vivo assessment of the window of barrier opening after osmotic blood-brain barrier disruption in humans. *J Neurosurg* **2000**, *92*, 599-605, doi:10.3171/jns.2000.92.4.0599.

189. Rapoport, S.I. Advances in osmotic opening of the blood-brain barrier to enhance CNS chemotherapy. *Expert Opin Investig Drugs* **2001**, *10*, 1809-1818, doi:10.1517/13543784.10.10.1809.

190. van Vulpen, M.; Kal, H.B.; Taphoorn, M.J.; et al. Changes in blood-brain barrier permeability induced by radiotherapy: implications for timing of chemotherapy? (Review). *Oncol Rep* **2002**, *9*, 683-688.

191. Li, C.; Ke, S.; Wu, Q.P.; et al. Tumor irradiation enhances the tumor-specific distribution of poly(L-glutamic acid)-conjugated paclitaxel and its antitumor efficacy. *Clin Cancer Res* **2000**, *6*, 2829-2834.

192. Lammers, T.; Peschke, P.; Kühnlein, R.; et al. Effect of radiotherapy and hyperthermia on the tumor accumulation of HPMA copolymer-based drug delivery systems. *J Control Release* **2007**, *117*, 333-341, doi:10.1016/j.jconrel.2006.10.032.

193. Davies Cde, L.; Lundstrøm, L.M.; Frengen, J.; et al. Radiation improves the distribution and uptake of liposomal doxorubicin (caelyx) in human osteosarcoma xenografts. *Cancer Res* **2004**, *64*, 547-553, doi:10.1158/0008-5472.can-03-0576.

194. Hart, E.; Odé, Z.; Derieppe, M.P.P.; et al. Blood-brain barrier permeability following conventional photon radiotherapy - A systematic review and meta-analysis of clinical and preclinical studies. *Clin Transl Radiat Oncol* **2022**, *35*, 44-55, doi:10.1016/j.ctro.2022.04.013.

195. Blethen, K.E.; Sprowls, S.A.; Arsiwala, T.A.; et al. Effects of whole-brain radiation therapy on the blood–brain barrier in immunocompetent and immunocompromised mouse models. *Radiat Oncol* **2023**, *18*, 22, doi:10.1186/s13014-023-02215-6.

196. Sándor, N.; Walter, F.R.; Bocsik, A.; et al. Low dose cranial irradiation-induced cerebrovascular damage is reversible in mice. *PLoS One* **2014**, *9*, e112397, doi:10.1371/journal.pone.0112397.

197. Qin, D.; Ou, G.; Mo, H.; et al. Improved efficacy of chemotherapy for glioblastoma by radiation-induced opening of blood-brain barrier: clinical results. *Int J Radiat Oncol Biol Phys* **2001**, *51*, 959-962, doi:10.1016/s0360-3016(01)01735-7.

198. Erel-Akbaba, G.; Carvalho, L.A.; Tian, T.; et al. Radiation-Induced Targeted Nanoparticle-Based Gene Delivery for Brain Tumor Therapy. *ACS Nano* **2019**, *13*, 4028-4040, doi:10.1021/acsnano.8b08177.

199. Shen, Y.; Li, S.; Wang, X.; et al. Tumor vasculature remolding by thalidomide increases delivery and efficacy of cisplatin. *J Exp Clin Cancer Res* **2019**, *38*, 427, doi:10.1186/s13046-019-1366-x.

200. Huang, Y.; Goel, S.; Duda, D.G.; et al. Vascular normalization as an emerging strategy to enhance cancer immunotherapy. *Cancer Res* **2013**, *73*, 2943-2948, doi:10.1158/0008-5472.Can-12-4354.

201. Goel, S.; Duda, D.G.; Xu, L.; et al. Normalization of the vasculature for treatment of cancer and other diseases. *Physiol Rev* **2011**, *91*, 1071-1121, doi:10.1152/physrev.00038.2010.

202. Arjaans, M.; Schröder, C.P.; Oosting, S.F.; et al. VEGF pathway targeting agents, vessel normalization and tumor drug uptake: from bench to bedside. *Oncotarget* **2016**, *7*, 21247-21258, doi:10.18632/oncotarget.6918.

203. Ansiaux, R.; Baudelet, C.; Jordan, B.F.; et al. Thalidomide radiosensitizes tumors through early changes in the tumor microenvironment. *Clin Cancer Res* **2005**, *11*, 743-750.

204. Jain, R.K. Normalizing tumor microenvironment to treat cancer: bench to bedside to biomarkers. *J Clin Oncol* **2013**, *31*, 2205-2218, doi:10.1200/jco.2012.46.3653.

205. Carmeliet, P.; Jain, R.K. Principles and mechanisms of vessel normalization for cancer and other angiogenic diseases. *Nat Rev Drug Discov* **2011**, *10*, 417-427, doi:10.1038/nrd3455.

206. Magnussen, A.L.; Mills, I.G. Vascular normalisation as the stepping stone into tumour microenvironment transformation. *Br J Cancer* **2021**, *125*, 324-336, doi:10.1038/s41416-021-01330-z.

207. Kamoun, W.S.; Ley, C.D.; Farrar, C.T.; et al. Edema control by cediranib, a vascular endothelial growth factor receptor-targeted kinase inhibitor, prolongs survival despite persistent brain tumor growth in mice. *J Clin Oncol* **2009**, *27*, 2542-2552, doi:10.1200/jco.2008.19.9356.

208. Mattheolabakis, G.; Mikelis, C.M. Nanoparticle Delivery and Tumor Vascular Normalization: The Chicken or The Egg? *Front Oncol* **2019**, *9*, 1227, doi:10.3389/fonc.2019.01227.

209. Mpekris, F.; Voutouri, C.; Panagi, M.; et al. Normalizing tumor microenvironment with nanomedicine and metronomic therapy to improve immunotherapy. *J Control Release* **2022**, *345*, 190-199, doi:10.1016/j.jconrel.2022.03.008.

210. Chauhan, V.P.; Stylianopoulos, T.; Martin, J.D.; et al. Normalization of tumour blood vessels improves the delivery of nanomedicines in a size-dependent manner. *Nat Nanotechnol* **2012**, *7*, 383-388, doi:10.1038/nnano.2012.45.

211. Treat, L.H.; McDannold, N.; Zhang, Y.; et al. Improved anti-tumor effect of liposomal doxorubicin after targeted blood-brain barrier disruption by MRI-guided focused ultrasound in rat glioma. *Ultrasound Med Biol* **2012**, *38*, 1716-1725, doi:10.1016/j.ultrasmedbio.2012.04.015.

212. Kovacs, Z.; Werner, B.; Rassi, A.; et al. Prolonged survival upon ultrasound-enhanced doxorubicin delivery in two syngenic glioblastoma mouse models. *J Control Release* **2014**, *187*, 74-82, doi:10.1016/j.jconrel.2014.05.033.

213. Alli, S.; Figueiredo, C.A.; Golbourn, B.; et al. Brainstem blood brain barrier disruption using focused ultrasound: A demonstration of feasibility and enhanced doxorubicin delivery. *J Control Release* **2018**, *281*, 29-41, doi:10.1016/j.jconrel.2018.05.005.

214. Carpentier, A.; Canney, M.; Vignot, A.; et al. Clinical trial of blood-brain barrier disruption by pulsed ultrasound. *Sci Transl Med* **2016**, *8*, 343re342, doi:10.1126/scitranslmed.aaf6086.

215. U.S. National Library of Medicine. ClinicalTrials.gov [Internet]. [quoted 22 november 2023]. Available on: https://clinicaltrials.gov/

216. Dean, R.L.; Emerich, D.F.; Hasler, B.P.; et al. Cereport (RMP-7) increases carboplatin levels in brain tumors after pretreatment with dexamethasone. *Neuro Oncol* **1999**, *1*, 268-274, doi:10.1093/neuonc/1.4.268.

217. Borlongan, C.V.; Emerich, D.F. Facilitation of drug entry into the CNS via transient permeation of blood brain barrier: laboratory and preliminary clinical evidence from bradykinin receptor agonist, Cereport. *Brain Res Bull* **2003**, *60*, 297-306, doi:10.1016/s0361-9230(03)00043-1.

218. Inamura, T.; Black, K.L. Bradykinin selectively opens blood-tumor barrier in experimental brain tumors. *J Cereb Blood Flow Metab* **1994**, *14*, 862-870, doi:10.1038/jcbfm.1994.108.

219. Raymond, J.J.; Robertson, D.M.; Dinsdale, H.B. Pharmacological modification of bradykinin induced breakdown of the blood-brain barrier. *Can J Neurol Sci* **1986**, *13*, 214-220, doi:10.1017/s0317167100036301.

220. Emerich, D.F.; Dean, R.L.; Osborn, C.; et al. The development of the bradykinin agonist labradimil as a means to increase the permeability of the blood-brain barrier: from concept to clinical evaluation. *Clin Pharmacokinet* **2001**, *40*, 105-123, doi:10.2165/00003088-200140020-00003.

221. Xie, Z.; Shen, Q.; Xie, C.; et al. Retro-inverso bradykinin opens the door of blood-brain tumor barrier for nanocarriers in glioma treatment. *Cancer Lett* **2015**, *369*, 144-151, doi:10.1016/j.canlet.2015.08.010.

222. Su, B.; Wang, R.; Xie, Z.; et al. Effect of Retro-Inverso Isomer of Bradykinin on Size-Dependent Penetration of Blood-Brain Tumor Barrier. *Small* **2018**, *14*, doi:10.1002/smll.201702331.

223. Bartus, R.T.; Elliott, P.; Hayward, N.; et al. Permeability of the blood brain barrier by the bradykinin agonist, RMP-7: evidence for a sensitive, auto-regulated, receptor-mediated system. *Immunopharmacology* **1996**, *33*, 270-278, doi:10.1016/0162-3109(96)00070-7.

224. Uchida, M.; Chen, Z.; Liu, Y.; et al. Overexpression of bradykinin type 2 receptors on glioma cells enhances bradykinin-mediated blood-brain tumor barrier permeability increase. *Neurol Res* **2002**, *24*, 739-746, doi:10.1179/016164102101200753.

225. Liu, Y.; Hashizume, K.; Chen, Z.; et al. Correlation between bradykinin-induced blood-tumor barrier permeability and B2 receptor expression in experimental brain tumors. *Neurol Res* **2001**, *23*, 379-387, doi:10.1179/016164101101198596.

226. Zhao, Y.; Xue, Y.; Liu, Y.; et al. Study of correlation between expression of bradykinin B2 receptor and pathological grade in human gliomas. *Br J Neurosurg* **2005**, *19*, 322-326, doi:10.1080/02688690500305555.

227. Côté, J.; Savard, M.; Bovenzi, V.; et al. Selective tumor blood-brain barrier opening with the kinin B2 receptor agonist [Phe(8)psi(CH(2)NH)Arg(9)]-BK in a F98 glioma rat model: an MRI study. *Neuropeptides* **2010**, *44*, 177-185, doi:10.1016/j.npep.2009.12.009.

228. Liu, L.B.; Xue, Y.X.; Liu, Y.H.; et al. Bradykinin increases blood-tumor barrier permeability by down-regulating the expression levels of ZO-1, occludin, and claudin-5 and rearranging actin cytoskeleton. *J Neurosci Res* **2008**, *86*, 1153-1168, doi:10.1002/jnr.21558.

229. Ningaraj, N.S.; Rao, M.K.; Black, K.L. Adenosine 5'-triphosphate-sensitive potassium channel-mediated blood-brain tumor barrier permeability increase in a rat brain tumor model. *Cancer Res* **2003**, *63*, 8899-8911.

230. Gu, Y.T.; Xue, Y.X.; Zhang, H.; et al. Adenosine 5'-triphosphate-sensitive potassium channel activator induces the up-regulation of caveolin-1 expression in a rat brain tumor model. *Cell Mol Neurobiol* **2011**, *31*, 629-634, doi:10.1007/s10571-011-9658-5.

231. Gu, Y.T.; Xue, Y.X.; Wang, Y.F.; et al. Minoxidil sulfate induced the increase in blood-brain tumor barrier permeability through ROS/RhoA/PI3K/PKB signaling pathway. *Neuropharmacology* **2013**, *75*, 407-415, doi:10.1016/j.neuropharm.2013.08.004.

232. Carman, A.J.; Mills, J.H.; Krenz, A.; et al. Adenosine receptor signaling modulates permeability of the blood-brain barrier. *J Neurosci* **2011**, *31*, 13272-13280, doi:10.1523/jneurosci.3337-11.2011.

233. Kim, D.G.; Bynoe, M.S. A2A Adenosine Receptor Regulates the Human Blood-Brain Barrier Permeability. *Mol Neurobiol* **2015**, *52*, 664-678, doi:10.1007/s12035-014-8879-2.

234. Zheng, S.; Bai, Y.Y.; Liu, Y.; et al. Salvaging brain ischemia by increasing neuroprotectant uptake via nanoagonist mediated blood brain barrier permeability enhancement. *Biomaterials* **2015**, *66*, 9-20, doi:10.1016/j.biomaterials.2015.07.006.

235. Bhattacharjee, A.K.; Kondoh, T.; Nagashima, T.; et al. Quantitative analysis of papaverine-mediated blood-brain barrier disruption in rats. *Biochem Biophys Res Commun* **2001**, *289*, 548-552, doi:10.1006/bbrc.2001.6029.

236. Platz, J.; Baráth, K.; Keller, E.; et al. Disruption of the blood-brain barrier by intra-arterial administration of papaverine: a technical note. *Neuroradiology* **2008**, *50*, 1035-1039, doi:10.1007/s00234-008-0455-x.

237. Xue, H.; Wang, H.; Kong, L.; et al. Opening blood-brain-barrier by intracarotid infusion of papaverine in treatment of malignant cerebral glioma. *Chin Med J (Engl)* **1998**, *111*, 751-753.

238. Wang, Z.H.; Xue, Y.X.; Liu, Y.H. The modulation of protein kinase A and heat shock protein 70 is involved in the reversible increase of blood-brain tumor barrier permeability

induced by papaverine. *Brain Res Bull* **2010**, *83*, 367-373, doi:10.1016/j.brainresbull.2010.08.009.

239. Tofts, P.S.; Brix, G.; Buckley, D.L.; et al. Estimating kinetic parameters from dynamic contrast-enhanced T(1)-weighted MRI of a diffusable tracer: standardized quantities and symbols. *J Magn Reson Imaging* **1999**, *10*, 223-232, doi:10.1002/(sici)1522-2586(199909)10:3<223::aid-jmri2>3.0.co;2-s.

240. Tietz, S.M.; Engelhardt, B. Visualizing Impairment of the Endothelial and Glial Barriers of the Neurovascular Unit during Experimental Autoimmune Encephalomyelitis In Vivo. *J Vis Exp* **2019**, doi:10.3791/59249.

241. Wilhelm, I.; Nyúl-Tóth, Á.; Suciu, M.; et al. Heterogeneity of the blood-brain barrier. *Tissue Barriers* **2016**, *4*, e1143544, doi:10.1080/21688370.2016.1143544.

242. Oh, S.S.; Lee, E.H.; Kim, J.H.; et al. The Use of Dynamic Contrast-Enhanced Magnetic Resonance Imaging for the Evaluation of Blood-Brain Barrier Disruption in Traumatic Brain Injury: What Is the Evidence? *Brain Sci* **2021**, *11*, doi:10.3390/brainsci11060775.

243. Nwe, K.; Bernardo, M.; Regino, C.A.; et al. Comparison of MRI properties between derivatized DTPA and DOTA gadolinium-dendrimer conjugates. *Bioorg Med Chem* **2010**, *18*, 5925-5931, doi:10.1016/j.bmc.2010.06.086.

244. Essig, M.; Shiroishi, M.S.; Nguyen, T.B.; et al. Perfusion MRI: the five most frequently asked technical questions. *AJR Am J Roentgenol* **2013**, *200*, 24-34, doi:10.2214/ajr.12.9543.

245. Jahng, G.H.; Li, K.L.; Ostergaard, L.; et al. Perfusion magnetic resonance imaging: a comprehensive update on principles and techniques. *Korean J Radiol* **2014**, *15*, 554-577, doi:10.3348/kjr.2014.15.5.554.

246. Raja, R.; Rosenberg, G.A.; Caprihan, A. MRI measurements of Blood-Brain Barrier function in dementia: A review of recent studies. *Neuropharmacology* **2018**, *134*, 259-271, doi:10.1016/j.neuropharm.2017.10.034.

247. Heye, A.K.; Thrippleton, M.J.; Armitage, P.A.; et al. Tracer kinetic modelling for DCE-MRI quantification of subtle blood-brain barrier permeability. *Neuroimage* **2016**, *125*, 446-455, doi:10.1016/j.neuroimage.2015.10.018.

248. Sourbron, S.P.; Buckley, D.L. Classic models for dynamic contrast-enhanced MRI. *NMR Biomed* **2013**, *26*, 1004-1027, doi:10.1002/nbm.2940.

249. Kanda, T.; Ishii, K.; Kawaguchi, H.; et al. High signal intensity in the dentate nucleus and globus pallidus on unenhanced T1-weighted MR images: relationship with increasing cumulative dose of a gadolinium-based contrast material. *Radiology* **2014**, *270*, 834-841, doi:10.1148/radiol.13131669.

250. Gulani, V.; Calamante, F.; Shellock, F.G.; et al. Gadolinium deposition in the brain: summary of evidence and recommendations. *Lancet Neurol* **2017**, *16*, 564-570, doi:10.1016/s1474-4422(17)30158-8.

251. Rasschaert, M.; Schroeder, J.A.; Wu, T.D.; et al. Multimodal Imaging Study of Gadolinium Presence in Rat Cerebellum: Differences Between Gd Chelates, Presence in the Virchow-Robin Space, Association With Lipofuscin, and Hypotheses About Distribution Pathway. *Invest Radiol* **2018**, *53*, 518-528, doi:10.1097/rli.0000000000000490.

252. Avsenik, J.; Bisdas, S.; Popovic, K.S. Blood-brain barrier permeability imaging using perfusion computed tomography. *Radiol Oncol* **2015**, *49*, 107-114, doi:10.2478/raon-2014-0029.

253. Kellogg, G.E.; Fornabaio, M.; Chen, D.L.; et al. Tools for building a comprehensive modeling system for virtual screening under real biological conditions: The Computational Titration algorithm. *J Mol Graph Model* **2006**, *24*, 434-439, doi:10.1016/j.jmgm.2005.09.001.

254. Miles, K.A.; Griffiths, M.R. Perfusion CT: a worthwhile enhancement? *Br J Radiol* **2003**, *76*, 220-231, doi:10.1259/bjr/13564625.

255. Kuhnline Sloan, C.D.; Nandi, P.; Linz, T.H.; et al. Analytical and biological methods for probing the blood-brain barrier. *Annu Rev Anal Chem (Palo Alto Calif)* **2012**, *5*, 505-531, doi:10.1146/annurev-anchem-062011-143002.

256. Harris, W.J.; Asselin, M.C.; Hinz, R.; et al. In vivo methods for imaging blood-brain barrier function and dysfunction. *Eur J Nucl Med Mol Imaging* **2023**, *50*, 1051-1083, doi:10.1007/s00259-022-05997-1.

257. Hugon, G.; Goutal, S.; Dauba, A.; et al. [(18)F]2-Fluoro-2-deoxy-sorbitol PET Imaging for Quantitative Monitoring of Enhanced Blood-Brain Barrier Permeability Induced by Focused Ultrasound. *Pharmaceutics* **2021**, *13*, doi:10.3390/pharmaceutics13111752.

258. Bagni, B.; Feggi, L.M.; Carraro, P.L.; et al. Determination of cerebral blood flow using non-diffusible tracers. *Radiol Med* **1983**, *69*, 788-791.

259. He, Y.; Zhang, Y.; Li, W.; et al. Evaluating blood-brain barrier disruption and infarction volume concurrently in rats subjected to ischemic stroke using an optical imaging system. *J Neurosci Methods* **2022**, *378*, 109630, doi:10.1016/j.jneumeth.2022.109630.

260. Kosaka, N.; Ogawa, M.; Choyke, P.L.; et al. Clinical implications of near-infrared fluorescence imaging in cancer. *Future Oncol* **2009**, *5*, 1501-1511, doi:10.2217/fon.09.109.

261. Jun-ming, S.; Yuan-Ruei, H.; Yu-Lung, W.; et al. Fluorescent imaging evidence of blood-brain-barrier permeability changing on physical surgical stroke rat animal model. *J Nucl Med* **2011**, *52*, 1543.

262. Masedunskas, A.; Milberg, O.; Porat-Shliom, N.; et al. Intravital microscopy: a practical guide on imaging intracellular structures in live animals. *Bioarchitecture* **2012**, *2*, 143-157, doi:10.4161/bioa.21758.

263. Bell, R.D.; Winkler, E.A.; Sagare, A.P.; et al. Pericytes control key neurovascular functions and neuronal phenotype in the adult brain and during brain aging. *Neuron* **2010**, *68*, 409-427, doi:10.1016/j.neuron.2010.09.043.

264. Winkler, E.A.; Nishida, Y.; Sagare, A.P.; et al. GLUT1 reductions exacerbate Alzheimer's disease vasculo-neuronal dysfunction and degeneration. *Nat Neurosci* **2015**, *18*, 521-530, doi:10.1038/nn.3966.

265. Koletar, M.M.; Dorr, A.; Brown, M.E.; et al. Refinement of a chronic cranial window implant in the rat for longitudinal in vivo two-photon fluorescence microscopy of neurovascular function. *Sci Rep* **2019**, *9*, 5499, doi:10.1038/s41598-019-41966-9.

266. Sugii, N.; Matsuda, M.; Sekine, T.; et al. Delayed Brain Edema and Swelling following Craniectomy for Evacuation of an Epidural Abscess that Improved by Cranioplasty: Case Report. *J Neurol Surg Rep* **2017**, *78*, e109-e112, doi:10.1055/s-0037-1606315.

267. Hawkins, B.T.; Egleton, R.D. Fluorescence imaging of blood-brain barrier disruption. *J Neurosci Methods* **2006**, *151*, 262-267, doi:10.1016/j.jneumeth.2005.08.006.

268. Ghabriel, M.N.; Zhu, C.; Leigh, C. Electron microscope study of blood-brain barrier opening induced by immunological targeting of the endothelial barrier antigen. *Brain Res* **2002**, *934*, 140-151, doi:10.1016/s0006-8993(02)02416-2.

269. Di Pardo, A.; Castaldo, S.; Capocci, L.; et al. Assessment of Blood-brain Barrier Permeability by Intravenous Infusion of FITC-labeled Albumin in a Mouse Model of Neurodegenerative Disease. *J Vis Exp* **2017**, doi:10.3791/56389.

270. Franke, M.; Bieber, M.; Stoll, G.; et al. Validity and Efficacy of Methods to Define Blood Brain Barrier Integrity in Experimental Ischemic Strokes: A Comparison of Albumin Western Blot, IgG Western Blot and Albumin Immunofluorescence. *Methods Protoc* **2021**, *4*, doi:10.3390/mps4010023.

271. Alarcan, H.; Vourc'h, P.; Berton, L.; et al. Implication of Central Nervous System Barrier Impairment in Amyotrophic Lateral Sclerosis: Gender-Related Difference in Patients. *Int J Mol Sci* **2023**, *24*, doi:10.3390/ijms241311196.

272. Hillmer, L.; Erhardt, E.B.; Caprihan, A.; et al. Blood-brain barrier disruption measured by albumin index correlates with inflammatory fluid biomarkers. *J Cereb Blood Flow Metab* **2023**, *43*, 712-721, doi:10.1177/0271678x221146127.

273. You, X.; Yan, L.; Li, X.; et al. Disruption of blood-brain barrier integrity associated with brain lesions in Chinese neuromyelitis optica spectrum disorder patients. *Mult Scler Relat Disord* **2019**, *27*, 254-259, doi:10.1016/j.msard.2018.10.114.

274. Butt, O.I.; Buehler, P.W.; D'Agnillo, F. Blood-brain barrier disruption and oxidative stress in guinea pig after systemic exposure to modified cell-free hemoglobin. *Am J Pathol* **2011**, *178*, 1316-1328, doi:10.1016/j.ajpath.2010.12.006.

275. Bien-Ly, N.; Boswell, C.A.; Jeet, S.; et al. Lack of Widespread BBB Disruption in Alzheimer's Disease Models: Focus on Therapeutic Antibodies. *Neuron* **2015**, *88*, 289-297, doi:10.1016/j.neuron.2015.09.036.

276. Haley, M.J.; Lawrence, C.B. The blood-brain barrier after stroke: Structural studies and the role of transcytotic vesicles. *J Cereb Blood Flow Metab* **2017**, *37*, 456-470, doi:10.1177/0271678x16629976.

277. Beard, R.S., Jr.; Reynolds, J.J.; Bearden, S.E. Hyperhomocysteinemia increases permeability of the blood-brain barrier by NMDA receptor-dependent regulation of adherens and tight junctions. *Blood* **2011**, *118*, 2007-2014, doi:10.1182/blood-2011-02-338269.

278. Akaishi, T.; Narikawa, K.; Suzuki, Y.; et al. Importance of the quotient of albumin, quotient of immunoglobulin G and Reibergram in inflammatory neurological disorders with disease-specific patterns of blood–brain barrier permeability. *Neurology and Clinical Neuroscience* **2015**, *3*, 94-100, doi:doi.org/10.1111/ncn3.158.

279. Alarcan, H.; Al Ojaimi, Y.; Lanznaster, D.; et al. Taking Advantages of Blood-Brain or Spinal Cord Barrier Alterations or Restoring Them to Optimize Therapy in ALS? *J Pers Med* **2022**, *12*, doi:10.3390/jpm12071071.

280. Janigro, D.; Mondello, S.; Posti, J.P.; et al. GFAP and S100B: What You Always Wanted to Know and Never Dared to Ask. *Front Neurol* **2022**, *13*, 835597, doi:10.3389/fneur.2022.835597.

281. Oris, C.; Kahouadji, S.; Durif, J.; et al. S100B, Actor and Biomarker of Mild Traumatic Brain Injury. *Int J Mol Sci* **2023**, *24*, doi:10.3390/ijms24076602.

282. Kanner, A.A.; Marchi, N.; Fazio, V.; et al. Serum S100beta: a noninvasive marker of blood-brain barrier function and brain lesions. *Cancer* **2003**, *97*, 2806-2813, doi:10.1002/cncr.11409.

283. Lindblad, C.; Nelson, D.W.; Zeiler, F.A.; et al. Influence of Blood-Brain Barrier Integrity on Brain Protein Biomarker Clearance in Severe Traumatic Brain Injury: A Longitudinal Prospective Study. *J Neurotrauma* **2020**, *37*, 1381-1391, doi:10.1089/neu.2019.6741.

284. Wu, C.Y.; Fan, C.H.; Chiu, N.H.; et al. Targeted delivery of engineered auditory sensing protein for ultrasound neuromodulation in the brain. *Theranostics* **2020**, *10*, 3546-3561, doi:10.7150/thno.39786.

285. Yao, L.; Xue, X.; Yu, P.; et al. Evans Blue Dye: A Revisit of Its Applications in Biomedicine. *Contrast Media Mol Imaging* **2018**, *2018*, 7628037, doi:10.1155/2018/7628037.

286. Kaya, M.; Ahishali, B. Assessment of permeability in barrier type of endothelium in brain using tracers: Evans blue, sodium fluorescein, and horseradish peroxidase. *Methods Mol Biol* **2011**, *763*, 369-382, doi:10.1007/978-1-61779-191-8_25.

287. Goldim, M.P.S.; Della Giustina, A.; Petronilho, F. Using Evans Blue Dye to Determine Blood-Brain Barrier Integrity in Rodents. *Curr Protoc Immunol* **2019**, *126*, e83, doi:10.1002/cpim.83.

288. Helmy, M.M.; Ruusuvuori, E.; Watkins, P.V.; et al. Acid extrusion via blood-brain barrier causes brain alkalosis and seizures after neonatal asphyxia. *Brain* **2012**, *135*, 3311-3319, doi:10.1093/brain/aws257.

289. Brun, E.; Carrière, M.; Mabondzo, A. In vitro evidence of dysregulation of blood-brain barrier function after acute and repeated/long-term exposure to TiO(2) nanoparticles. *Biomaterials* **2012**, *33*, 886-896, doi:10.1016/j.biomaterials.2011.10.025.

290. Miah, M.K.; Chowdhury, E.A.; Bickel, U.; et al. Evaluation of [(14)C] and [(13)C]Sucrose as Blood-Brain Barrier Permeability Markers. *J Pharm Sci* **2017**, *106*, 1659-1669, doi:10.1016/j.xphs.2017.02.011.

291. Rosenberg, G.A.; Estrada, E.Y.; Dencoff, J.E. Matrix metalloproteinases and TIMPs are associated with blood-brain barrier opening after reperfusion in rat brain. *Stroke* **1998**, *29*, 2189-2195, doi:10.1161/01.str.29.10.2189.

292. Witt, K.A.; Mark, K.S.; Sandoval, K.E.; et al. Reoxygenation stress on blood-brain barrier paracellular permeability and edema in the rat. *Microvasc Res* **2008**, *75*, 91-96, doi:10.1016/j.mvr.2007.06.004.

293. Miah, M.K.; Bickel, U.; Mehvar, R. Development and validation of a sensitive UPLC–MS/MS method for the quantitation of [13C]sucrose in rat plasma, blood, and brain: Its application to the measurement of blood-brain barrier permeability. *J Chromatogr B Analyt Technol Biomed Life Sci* **2016**, *1015-1016*, 105-110, doi:10.1016/j.jchromb.2016.02.017.

294. Connell, J.J.; Chatain, G.; Cornelissen, B.; et al. Selective permeabilization of the blood-brain barrier at sites of metastasis. *J Natl Cancer Inst* **2013**, *105*, 1634-1643, doi:10.1093/jnci/djt276.

295. Cunningham, T.L.; Cartagena, C.M.; Lu, X.C.; et al. Correlations between blood-brain barrier disruption and neuroinflammation in an experimental model of penetrating ballistic-like brain injury. *J Neurotrauma* **2014**, *31*, 505-514, doi:10.1089/neu.2013.2965.

296. Choi, J.J.; Wang, S.; Tung, Y.S.; et al. Molecules of various pharmacologically-relevant sizes can cross the ultrasound-induced blood-brain barrier opening in vivo. *Ultrasound Med Biol* **2010**, *36*, 58-67, doi:10.1016/j.ultrasmedbio.2009.08.006.

297. Baseri, B.; Choi, J.J.; Tung, Y.S.; et al. Multi-modality safety assessment of blood-brain barrier opening using focused ultrasound and definity microbubbles: a short-term study. *Ultrasound Med Biol* **2010**, *36*, 1445-1459, doi:10.1016/j.ultrasmedbio.2010.06.005.

298. Natarajan, R.; Northrop, N.; Yamamoto, B. Fluorescein Isothiocyanate (FITC)-Dextran Extravasation as a Measure of Blood-Brain Barrier Permeability. *Curr Protoc Neurosci* **2017**, *79*, 9.58.51-59.58.15, doi:10.1002/cpns.25.

299. Hoffmann, A.; Bredno, J.; Wendland, M.; et al. High and Low Molecular Weight Fluorescein Isothiocyanate (FITC)-Dextrans to Assess Blood-Brain Barrier Disruption: Technical Considerations. *Transl Stroke Res* **2011**, *2*, 106-111, doi:10.1007/s12975-010-0049-x.

300. Banks, W.A.; Farr, S.A.; Morley, J.E. Permeability of the Blood-Brain Barrier to Albumin and Insulin in the Young and Aged SAMP8 Mouse. *The Journals of Gerontology: Series A* **2000**, *55*, B601-B606, doi:10.1093/gerona/55.12.B601.

301. Petzold, A.; Keir, G.; Lim, D.; et al. Cerebrospinal fluid (CSF) and serum S100B: release and wash-out pattern. *Brain Res Bull* **2003**, *61*, 281-285, doi:10.1016/s0361-9230(03)00091-1.

302. Zimmer, D.B.; Cornwall, E.H.; Landar, A.; et al. The S100 protein family: history, function, and expression. *Brain Res Bull* **1995**, *37*, 417-429, doi:10.1016/0361-9230(95)00040-2.

303. Haimoto, H.; Hosoda, S.; Kato, K. Differential distribution of immunoreactive S100-alpha and S100-beta proteins in normal nonnervous human tissues. *Lab Invest* **1987**, *57*, 489-498.

304. Fernández-López, D.; Faustino, J.; Daneman, R.; et al. Blood-brain barrier permeability is increased after acute adult stroke but not neonatal stroke in the rat. *J Neurosci* **2012**, *32*, 9588-9600, doi:10.1523/jneurosci.5977-11.2012.

305. Kassner, A.; Merali, Z. Assessment of Blood-Brain Barrier Disruption in Stroke. *Stroke* **2015**, *46*, 3310-3315, doi:10.1161/strokeaha.115.008861.

306. Saunders, N.R.; Dziegielewska, K.M.; Møllgård, K.; et al. Markers for blood-brain barrier integrity: how appropriate is Evans blue in the twenty-first century and what are the alternatives? *Front Neurosci* **2015**, *9*, 385, doi:10.3389/fnins.2015.00385.

307. Giger, M.; Baumgartner, H.R.; Zbinden, G. Toxicological effects of Evans blue and Congo red on blood platelets. *Agents Actions* **1974**, *4*, 173-180, doi:10.1007/bf01970259.

308. Hoffman, H.J.; Olszewski, J. Spread of sodium fluorescein in normal brain tissue. A study of the mechanism of the blood-brain barrier. *Neurology* **1961**, *11*, 1081-1085, doi:10.1212/wnl.11.12.1081.

309. Malmgren, L.T.; Olsson, Y. Differences between the peripheral and the central nervous system in permeability to sodium fluorescein. *J Comp Neurol* **1980**, *191*, 103-107, doi:10.1002/cne.901910106.

310. Salem, H.; Loux, J.J.; Smith, S.; et al. Evaluation of the toxicologic and teratogenic potentials of sodium fluorescein in the rat. *Toxicology* **1979**, *12*, 143-150, doi:10.1016/0300-483x(79)90040-4.

311. Reese, T.S.; Karnovsky, M.J. Fine structural localization of a blood-brain barrier to exogenous peroxidase. *J Cell Biol* **1967**, *34*, 207-217, doi:10.1083/jcb.34.1.207.

312. Reyners, H.; de Reyners, E.G.; Jadin, J.M.; et al. An ultrastructural quantitative method for the evaluation of the permeability to horseradish peroxidase of cerebral cortex endothelial cells of the rat. *Cell Tissue Res* **1975**, *157*, 93-99, doi:10.1007/bf00223232.

313. Broadwell, R.D.; Charlton, H.M.; Balin, B.J.; et al. Angioarchitecture of the CNS, pituitary gland, and intracerebral grafts revealed with peroxidase cytochemistry. *J Comp Neurol* **1987**, *260*, 47-62, doi:10.1002/cne.902600105.

314. Brightman, M.W.; Reese, T.S. Junctions between intimately apposed cell membranes in the vertebrate brain. *J Cell Biol* **1969**, *40*, 648-677, doi:10.1083/jcb.40.3.648.

315. Majno, G.; Palade, G.E.; Schoefl, G.I. Studies on inflammation. II. The site of action of histamine and serotonin along the vascular tree: a topographic study. *J Biophys Biochem Cytol* **1961**, *11*, 607-626, doi:10.1083/jcb.11.3.607.

CHAPTER II
AIM OF THE THESIS

Glioblastoma (GB) is currently the most common and aggressive primary tumor of the central nervous system in adults. This tumor is characterized by a high proliferation rate, intra- and inter-tumoral heterogeneity, resistance to chemotherapy and highly invasive properties with infiltrating cells that spread into adjacent brain tissue, making GB a very difficult cancer to treat [1]. Despite maximal initial resection and multimodality therapy, the prognosis remains poor with 70% of GBM patients that will experience disease progression within one year of diagnosis and less than 5% of patients surviving five years after diagnosis [2,3]. GB's intrinsic resistance to conventional treatments is exacerbated by the blood-brain barrier (BBB), which hinders effective drug delivery to the tumor. Even though it has been shown to be disrupted in GB, an intact BBB is still found peritumorally. This heterogeneous disruption leads to a poor heterogenous drug delivery to the tumor site, especially to the infiltrative tumor cells in the tumor margins, lying behind an intact BBB, which are at the origins of recurrence. There is therefore an important need in GB to enhance the BBB opening in the tumor margins in order to reach these peripheral infiltrating cells.

The aim of this Ph.D. thesis was to evaluate innovative strategies for opening the BBB in glioblastoma. The hypothesis was that opening the tumor vascular bed using a mechanical (osmotic shock), physical (radiotherapy) or pharmacological (normalization of vascularization in the early stages of anti-angiogenic treatments) approach could lead to increased drug delivery, particularly to infiltrating cells that are protected by an intact BBB.

Thus, three methods were used to open the BBB (Figure 1):

- Osmotic shock with an intra-carotid injection of a hypertonic solution of mannitol 25% (m/v) [4]

- Radiotherapy (5Gy, 10Gy and 15Gy as a single dose) using cesium-137 irradiator [5-7]

- Normalization of tumor vessels using anti-angiogenic agents (cediranib and thalidomide) [8-12]

These strategies were carried out on a glioblastoma model of NMRI-nu mice injected with human U87MG cells. Two different methods were used to assess BBB opening (Figure 1): a histological method with injection of Evans Blue [13] (a fluorescent marker of vascular permeability) and a method using dynamic contrast-enhanced MRI (DCE-MRI) [14] with injection of gadolinium-DOTA as contrast agent, allowing determination of hemodynamic parameters in the core and margins of the tumor.

For the histological studies, Evans blue, a fluorescent marker of vascular leakage, was used to assess the functionality of the blood-brain barrier [15]. This dye forms a tight bond with the plasma protein, albumin, in the bloodstream. Albumin, under normal circumstances, is too large to cross

the intact blood-brain barrier. However, in the event of disruption of the BBB, Evans Blue bound to albumin could penetrate the brain parenchyma.

Regarding DCE-MRI method, two different pharmacokinetic models were used to monitor the hemodynamic parameters of the tumor: : the extended Tofts model [16] and the Patlak model [17]. The extended Tofts model is one of the most widely used in the literature for studying tumor perfusion/permeability in glioblastoma. It's a two-compartmental model suited to describe highly perfused tissues such as those found in glioblastoma. The Patlak model is comparable to the extended Tofts model but ignores the backflux and is therefore adapted to assess changes for a low-level BBB permeability where backflux is negligible, as found especially in the margins of glioblastoma tumors.

An immunohistochemistry study labelling the endothelial cell marker CD31 was also carried out for the study of tumor vessel normalization strategy, in order to evaluate tumor angiogenesis more clearly, in particular the evolution of vascular density and vascular integrity in the tumor [18-20].

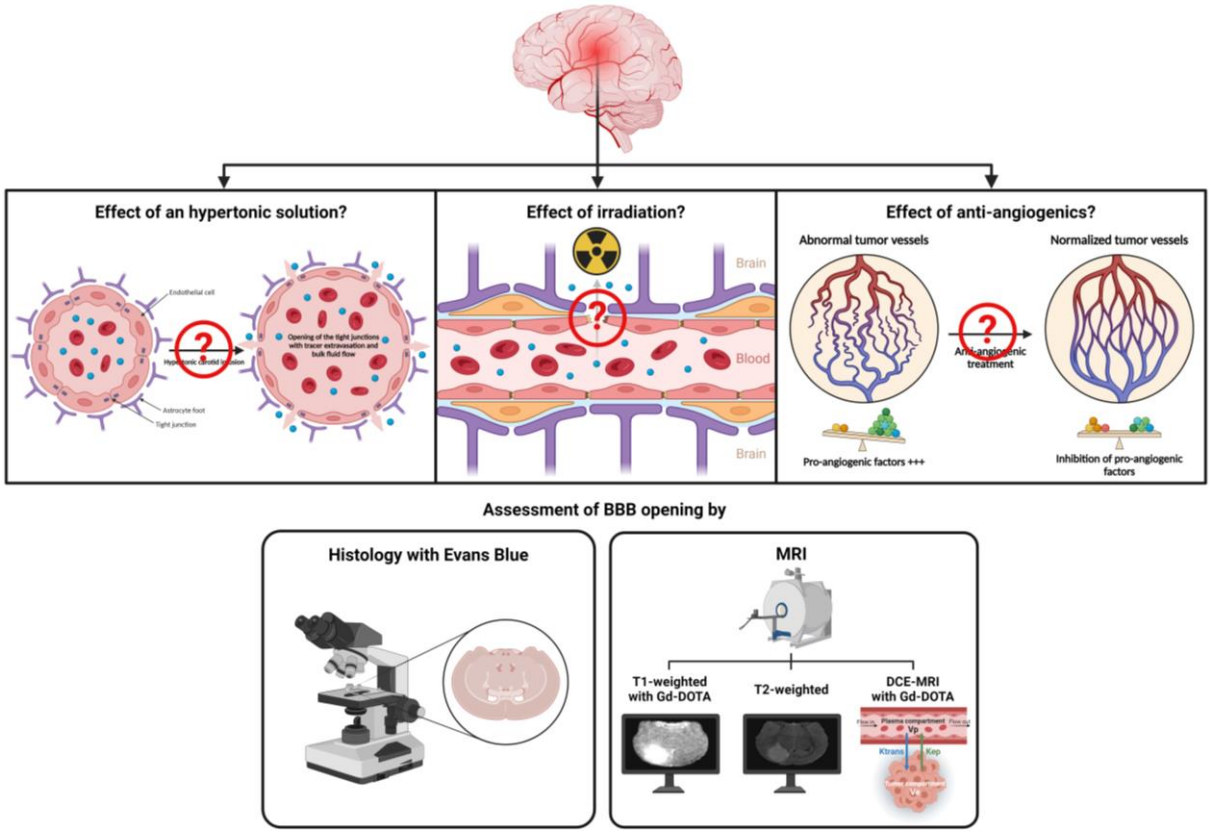

Figure 1. Schematic representation of the aim of the thesis (adapted from [4,21]).
Abbreviations: BBB = Blood-brain barrier; DCE-MRI = Dynamic contrast-enhanced magnetic resonance imaging; Gd-DOTA = Gadolinium-Gadoteric acid.

I. REFERENCES

1. Anjum, K.; Shagufta, B.I.; Abbas, S.Q.; et al. Current status and future therapeutic perspectives of glioblastoma multiforme (GBM) therapy: A review. *Biomed Pharmacother* **2017**, *92*, 681-689, doi:10.1016/j.biopha.2017.05.125.
2. Stupp, R.; Mason, W.P.; van den Bent, M.J.; et al. Radiotherapy plus concomitant and adjuvant temozolomide for glioblastoma. *N Engl J Med* **2005**, *352*, 987-996, doi:10.1056/NEJMoa043330.
3. Ostrom, Q.T.; Bauchet, L.; Davis, F.G.; et al. The epidemiology of glioma in adults: a "state of the science" review. *Neuro Oncol* **2014**, *16*, 896-913, doi:10.1093/neuonc/nou087.
4. Rapoport, S.I. Advances in osmotic opening of the blood-brain barrier to enhance CNS chemotherapy. *Expert Opin Investig Drugs* **2001**, *10*, 1809-1818, doi:10.1517/13543784.10.10.1809.
5. Erel-Akbaba, G.; Carvalho, L.A.; Tian, T.; et al. Radiation-Induced Targeted Nanoparticle-Based Gene Delivery for Brain Tumor Therapy. *ACS Nano* **2019**, *13*, 4028-4040, doi:10.1021/acsnano.8b08177.
6. Qin, D.; Ou, G.; Mo, H.; et al. Improved efficacy of chemotherapy for glioblastoma by radiation-induced opening of blood-brain barrier: clinical results. *Int J Radiat Oncol Biol Phys* **2001**, *51*, 959-962, doi:10.1016/s0360-3016(01)01735-7.
7. Sabatasso, S.; Fernandez-Palomo, C.; Hlushchuk, R.; et al. Transient and Efficient Vascular Permeability Window for Adjuvant Drug Delivery Triggered by Microbeam Radiation. *Cancers (Basel)* **2021**, *13*, doi:10.3390/cancers13092103.
8. Ansiaux, R.; Baudelet, C.; Jordan, B.F.; et al. Thalidomide radiosensitizes tumors through early changes in the tumor microenvironment. *Clin Cancer Res* **2005**, *11*, 743-750.
9. Batchelor, T.T.; Sorensen, A.G.; di Tomaso, E.; et al. AZD2171, a pan-VEGF receptor tyrosine kinase inhibitor, normalizes tumor vasculature and alleviates edema in glioblastoma patients. *Cancer Cell* **2007**, *11*, 83-95, doi:10.1016/j.ccr.2006.11.021.
10. Peterson, T.E.; Kirkpatrick, N.D.; Huang, Y.; et al. Dual inhibition of Ang-2 and VEGF receptors normalizes tumor vasculature and prolongs survival in glioblastoma by altering macrophages. *Proc Natl Acad Sci USA* **2016**, *113*, 4470-4475, doi:10.1073/pnas.1525349113.
11. Segers, J.; Di Fazio, V.; Ansiaux, R.; et al. Potentiation of cyclophosphamide chemotherapy using the anti-angiogenic drug thalidomide: importance of optimal scheduling to exploit the 'normalization' window of the tumor vasculature. *Cancer Lett* **2006**, *244*, 129-135, doi:10.1016/j.canlet.2005.12.017.
12. Sorensen, A.G.; Emblem, K.E.; Polaskova, P.; et al. Increased survival of glioblastoma patients who respond to antiangiogenic therapy with elevated blood perfusion. *Cancer Res* **2012**, *72*, 402-407, doi:10.1158/0008-5472.Can-11-2464.
13. Nicaise, C.; Mitrecic, D.; Demetter, P.; et al. Impaired blood-brain and blood-spinal cord barriers in mutant SOD1-linked ALS rat. *Brain Res* **2009**, *1301*, 152-162, doi:10.1016/j.brainres.2009.09.018.
14. Yankeelov, T.E.; Gore, J.C. Dynamic Contrast Enhanced Magnetic Resonance Imaging in Oncology: Theory, Data Acquisition, Analysis, and Examples. *Curr Med Imaging Rev* **2009**, *3*, 91-107, doi:10.2174/157340507780619179.
15. Ahishali, B.; Kaya, M. Evaluation of Blood-Brain Barrier Integrity Using Vascular Permeability Markers: Evans Blue, Sodium Fluorescein, Albumin-Alexa Fluor Conjugates,

and Horseradish Peroxidase. *Methods Mol Biol* **2021**, *2367*, 87-103, doi:10.1007/7651_2020_316.

16. Tofts, P.S.; Brix, G.; Buckley, D.L.; et al. Estimating kinetic parameters from dynamic contrast-enhanced T(1)-weighted MRI of a diffusable tracer: standardized quantities and symbols. *J Magn Reson Imaging* **1999**, *10*, 223-232, doi:10.1002/(sici)1522-2586(199909)10:3<223::aid-jmri2>3.0.co;2-s.

17. Heye, A.K.; Thrippleton, M.J.; Armitage, P.A.; et al. Tracer kinetic modelling for DCE-MRI quantification of subtle blood-brain barrier permeability. *Neuroimage* **2016**, *125*, 446-455, doi:10.1016/j.neuroimage.2015.10.018.

18. Bianconi, D.; Herac, M.; Posch, F.; et al. Microvascular density assessed by CD31 predicts clinical benefit upon bevacizumab treatment in metastatic colorectal cancer: results of the PassionATE study, a translational prospective Phase II study of capecitabine and irinotecan plus bevacizumab followed by capecitabine and oxaliplatin plus bevacizumab or the reverse sequence in patients in mCRC. *Ther Adv Med Oncol* **2020**, *12*, 1758835920928635, doi:10.1177/1758835920928635.

19. Afshar Moghaddam, N.; Mahsuni, P.; Taheri, D. Evaluation of Endoglin as an Angiogenesis Marker in Glioblastoma. *Iran J Pathol* **2015**, *10*, 89-96.

20. Majchrzak, K.; Kaspera, W.; Szymaś, J.; et al. Markers of angiogenesis (CD31, CD34, rCBV) and their prognostic value in low-grade gliomas. *Neurol Neurochir Pol* **2013**, *47*, 325-331, doi:10.5114/ninp.2013.36757.

21. Jain, R.K. Normalizing tumor microenvironment to treat cancer: bench to bedside to biomarkers. *J Clin Oncol* **2013**, *31*, 2205-2218, doi:10.1200/jco.2012.46.3653.

CHAPTER III

ASSESSMENT OF HYPEROSMOLAR BLOOD-BRAIN BARRIER OPENING IN GLIOBLASTOMA VIA HISTOLOGY WITH EVANS BLUE AND DCE-MRI

Adapted from **Conq J**, Joudiou N, Ucakar B, Vanvarenberg K, Préat V, Gallez B. Assessment of Hyperosmolar Blood-Brain Barrier Opening in Glioblastoma via Histology with Evans Blue and DCE-MRI. Biomedicines 2023;11(7):1957

Abstract:

Background: While the blood–brain barrier (BBB) is often compromised in glioblastoma (GB), the perfusion and consequent delivery of drugs are highly heterogeneous. Moreover, the accessibility of drugs is largely impaired in the margins of the tumor and for infiltrating cells at the origin of tumor recurrence. In this work, we evaluate the value of methods to assess hemodynamic changes induced by a hyperosmolar shock in the core and the margins of a tumor in a GB model.

Methods: Osmotic shock was induced with an intracarotid infusion of a hypertonic solution of mannitol in mice grafted with U87-MG cells. The distribution of fluorescent dye (Evans blue) within the brain was assessed via histology. Dynamic contrast-enhanced (DCE)-MRI with an injection of Gadolinium-DOTA as the contrast agent was also used to evaluate the effect on hemodynamic parameters and the diffusion of the contrast agent outside of the tumor area.

Results: The histological study revealed that the fluorescent dye diffused much more largely outside of the tumor area after osmotic shock than in control tumors. However, the study of tumor hemodynamic parameters via DCE-MRI did not reveal any change in the permeability of the BBB, whatever the studied MRI parameter.

Conclusions: The use of hypertonic mannitol infusion seems to be a promising method to increase the delivery of compounds in the margins of GB. Nevertheless, the DCE-MRI analysis method using gadolinium-DOTA as a contrast agent seems of limited value for determining the efficacy of opening the BBB in GB after osmotic shock.

Keywords: blood–brain barrier; glioblastoma; osmotic shock; mannitol; DCE-MRI; Evans blue

TABLE OF CONTENTS

I. INTRODUCTION

Glioblastoma (GB) is the most common and aggressive malignant tumor of the central nervous system in adults, accounting for more than 50% of gliomas. The current standard of care is to remove as much tumor tissue as possible via surgical resection, followed by adjuvant radiotherapy and chemotherapy to eradicate residual infiltrating tumor cells at the origin of recurrences [1]. Despite this aggressive treatment, the prognosis of patients suffering from GB remains poor, with a high recurrence rate, a median survival time lower than 2 years, and a 5 years survival rate lower than 5% [2,3].

This tumor shows a high proliferation rate, intratumoral and intertumoral heterogeneity, highly invasive and infiltrative cell properties in the adjacent brain parenchyma, and resistance to chemotherapy, making GB a very challenging cancer to treat. Many distinctive features of GB (genetic, cytological, or anatomical) hinder the treatment efficacy and must be overcome. One of the fundamental issues for treating GB is linked to the blood–brain barrier (BBB). This physiological barrier controls the entry of compounds into the brain and significantly inhibits the passage of drugs from the bloodstream to the brain, reducing the effectiveness of chemotherapeutic agents' systemic delivery [4]. While the BBB is often compromised in GB, the perfusion and consequent delivery of drugs are highly heterogeneous. Indeed, tumoral BBB is characterized by an aberrant distribution of pericytes, a loss of astrocytic end-feet, as well as a loss of tight junction proteins between endothelial cells. Unlike the healthy BBB, the leaky tumoral BBB allows the passage of large molecules between endothelial cells, where the paracellular pathway is damaged [5]. However, tumoral BBB permeability is highly heterogeneous and varies not only between GB but also within the same tumor, with tumor regions (mainly in the margins of the tumor) where the BBB is still intact, which limit the access of drugs to the infiltrating tumor cells at the origin of the tumor recurrence [6,7]. Therefore, the tumoral BBB remains a major hurdle to overcome.

Many efforts have been made in past decades to develop new approaches in order to overcome it and improve the delivery of drugs to the tumor, especially in its margins. One of the strategies that we will examine deeper in this article is osmotic shock. Previous works have shown that hypertonic solution infusion induces a reversible opening of a healthy BBB [8,9]. The mechanism of action of this method is explained in Figure 1.

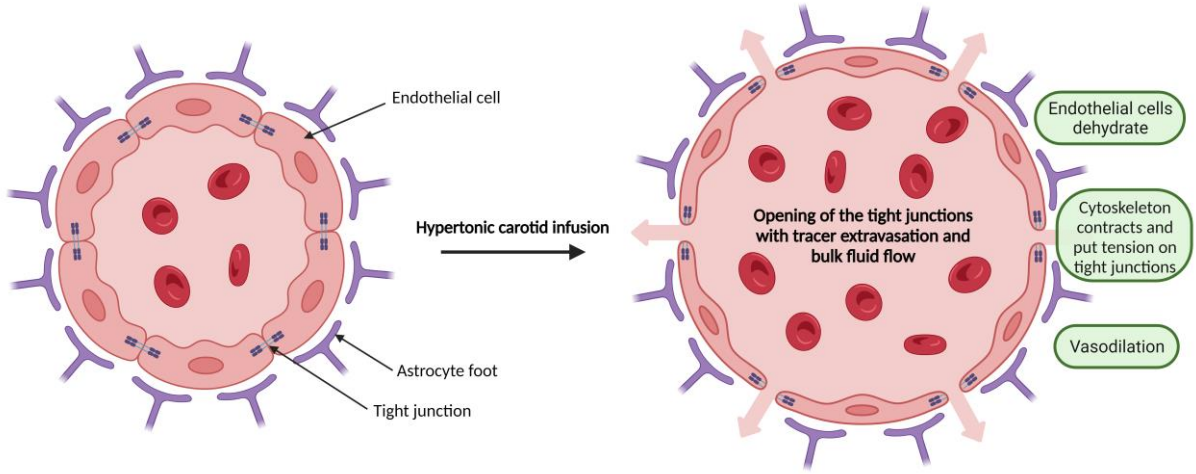

Figure 1. Model for the opening of the inter-endothelial tight junctions via carotid infusion of a hypertonic solution. During infusion, endothelial cells dehydrate, water leaves the brain, leading to vasodilation, and the endothelial cell cytoskeleton contracts. Tension is exerted at tight junctional areas due to each of these factors, leading to a reversible opening of the junctions [9].

In this work, our aim was to evaluate whether this strategy can be used for tumoral BBB opening in GB, especially for the margins of the tumor. To do so, we evaluated whether a hyperosmolar shock may change hemodynamic parameters in the core and the margins of the tumor in a GB model. Two methods have been used to evaluate the efficacy of the treatment on perfusion/permeability parameters: a non-invasive one, based on magnetic resonance imaging (MRI) analysis (T_1-weighted and T_2-weighted imaging as well as dynamic contrast-enhanced (DCE)-MRI), and an invasive one, based on histological analysis with a fluorescent vascular leakage marker (Evans blue).

For the MRI analysis, we determined the core of the tumor through the use of T_2-weighted contrast. In addition, T_1-weighted images were obtained after the administration of a contrast agent to analyze the diffusion of the contrast agent within the bulk of the tumor and in its margins. Gadolinium-DOTA was used because this hydrophilic contrast agent is unable to cross the intact BBB, offering the possibility to tackle changes in BBB permeability. We defined the tumor margins as the difference between the area of the T_1-enhancing region after the injection of the contrast agent and the area depicted by the T_2-weighted contrast delineating the core of the tumor. The hypothesis was that, if there is an increase in the permeability of the BBB, the contrast agent should pass the barrier more easily and diffuse much more largely outside of the tumor area into the brain parenchyma. As a consequence, a larger contrast uptake area should be seen in the T_1-weighted postcontrast image compared to the T_2-weighted anatomical image. In other words, an increase in T_1 in the T_2 tumor surface ratio would indicate the opening of the BBB. In addition, DCE-MRI

analysis gave access to complementary tumor hemodynamic parameters that may be biomarkers of the change in BBB permeability [10].

For the histological analysis, BBB integrity and vascular leakage were assessed by perfusing mice with Evans blue fluorescent dye which binds to plasma albumin with a very high affinity. Albumin cannot cross an intact BBB. However, when compromised, albumin-bound Evans blue can diffuse into the brain parenchyma and be visualized by fluorescence [11].

II. MATERIALS AND METHODS

II.1. ORTHOTOPIC U-87MG MOUSE MODEL

All experiments were performed in accordance with the European Directive 2010/63/EU and following the Belgian national regulation guidelines, and were approved by the ethical committee for animal care by the Faculty of Medicine of the Université Catholique de Louvain (2019/UCL/MD/004). Water and food were given ad libitum. Animal body weight was constantly monitored throughout the experiment.

Six-week-old female NMRI-nude mice (Janvier, France) were anesthetized by intraperitoneal injection of ketamine/xylazine (100 and 13 mg/kg, respectively) and fixed on a stereotaxic frame. 4 x 10^4 cells of U-87MG (ATCC) in 2 µL of native EMEM (Gibco™, ThermoFisher Scientific, Waltham, MA, USA) were injected into the right frontal lobe using an infusion syringe pump (Harvard Apparatus, Holliston, MA, USA) mounted with a Hamilton syringe (26S gauge needle). The injection coordinates were 2.1 mm lateral and 0.5 mm posterior from the bregma, and 2.6 mm deep from the outer border of the cranium [12]. The tumor size monitoring was performed via MRI (see MRI part).

II.2. MANNITOL-INDUCED HYPEROSMOTIC BBB DISRUPTION

When the tumor size reached 7 ± 1 mm^3, osmotic shock was induced with an intracarotid infusion of a hypertonic solution of mannitol 25% v/m (the control group received NaCl 0.9%). Mice were anesthetized with isoflurane mixed with air (2.5% for induction, 1.5% for maintenance). The common carotid artery (CCA) bifurcation was isolated. A polyethylene microcatheter (PE 10, inner diameter 0.28 mm and outer diameter 0.61mm, BD Intramedic™, Sparks, NV, USA) was inserted into the CCA via a small arteriotomy and moved into the internal carotid artery for an infusion of warm and filtered mannitol 25% or normal saline (200 µL/min for 1 min) [13].

II.3. MRI

MRI was performed using a 11.7 T Bruker Biospec MRI system (Bruker, Ettlingen, Germany) equipped with a ^{1}H quadrature transmit/receive birdcage coil (21 mm inner diameter, RAPID Biomedical Rimpar Germany). Mice were anesthetized with isoflurane mixed with air (2.5% for induction, 1.5% for maintenance). Animals were covered with a heating blanket and the temperature was monitored. A pressure pad was used to monitor the respiration rate.

Anatomical images were obtained using T_2-weighted rapid acquisition with refocused echoes (RARE) sequence (echo time = 30 ms; repetition time = 2500 ms; number of slices = 25; field of view = 20 mm × 20 mm; matrix size = 200 × 200; resolution = 0.1 mm x 0.1 mm; slice thickness = 0.3 mm; acquisition time = 5 min 20 s; averages = 8). Tumor volume was determined from manually drawn region of interest (ROI) using Paravision 6.0.1 software (Bruker BioSpin), on day 14 following tumor induction, and then daily until the tumor size reached 7 ± 1 mm^3.

For DCE-MRI acquisition, T_1-weighted gradient echo images were obtained with a fast low-angle shot (FLASH) sequence (echo time = 1.4 ms; repetition time = 11.719 ms; flip angle = 10.0°; field of view = 20 mm x 20 mm; matrix size = 128 × 128; resolution = 0.156 mm x 0.156 mm; slice thickness = 0.9 mm; averages = 1; total acquisition time = 22 min 40sec). A set of 450 scans with a temporal resolution of 3.02 s was acquired, with Gadolinium-DOTA (Dotarem® 0.5 mol/mL; Guerbet, Villepinte, France) administered intravenously at a dose of 0.29 mmol/kg after the 10^{th} scan over 5 s. DCE-MRI acquisition was performed 24 h before (day 0), 5 min after (day 1), and 24 h (day 2) after the injection of mannitol 25% or saline.

II.4. HISTOLOGICAL STUDY

Evans blue dye (EB: 2% in normal saline; Alfa Aesar, Haverhill, MA, USA) was intravenously injected (3 ml/kg) at day 1, 5 min after Mannitol or NaCl intra-carotid injection. Thirty min later, the mice were euthanized and intracardially perfused with paraformaldehyde (PFA) 4% to discard all the remaining dye in the blood vessels and fix the tissue. Brains were then removed, fixed overnight in PFA 4%, cryoprotected in sucrose 20%, included in optimal cutting temperature compound (OCT, Sakura Finetek, Alphen aan den Rijn, Netherland), and kept at -80°C. Cryostat 30 μm sections were counterstained with diamidino-2-phenylindole (DAPI, Thermofisher, Waltham, MA, USA) and examined under a fluorescence microscope slide scanner (Panoramic 250 Flash III, 3DHistech, Budapest, Hungary) with DAPI and Cyanine 5 (Cy5) filter [14,15].

II.5. IMAGE PROCESSING AND STATISTICAL ANALYSES

DCE-MRI data were analyzed using in-house software written in Matlab (version 9.6). Regions of interest (ROI) were manually delineated. We considered ROI T_1 as the delineation of the entire tumor area using T_1-weighted images with Gd-DOTA as the contrast agent, ROI T_2 as the delineation of the tumor bulk area using T_2-weighted anatomical images, and ROI Delta as the ROI T_1 from which we subtracted ROI T_2 in order to cover the margins of the tumor. In this way, we were able to study the hemodynamic parameters for the whole tumor region but also for the margins of the tumor.

The hemodynamics parameters were computed using a two compartmental model, the Extended Tofts Model [16]. This model takes into account the contribution of the vascular compartment, which is not negligible in tumors.

$$C_t(t) = v_p \cdot C_p(t) + K^{trans} \int_0^t C_p(\tau) e^{-k_{ep}(t-\tau)} d\tau \qquad (1)$$

where K^{trans} is the volume transfer constant between blood plasma and extravascular extracellular space (EES) [min−1], v_p is the blood plasma volume per unit volume of tissue, and k_{ep} is the flux rate constant between EES and blood plasma [min−1] [17]. V_e is the EES volume per unit volume of tissue calculated as:

$$v_e = K^{trans}/k_{ep} \qquad (2)$$

We were also interested in AUC60 and AUC90 corresponding to the area under the curve (AUC) of contrast agent concentration as a function of time from 0 to 60 or to 90 seconds.

Histological images were analyzed using Qupath (version 0.3.2) [18]. The tumor ROI and the Evans Blue diffusion ROI were manually delineated.

For statistical analyses, two-way ANOVA tests (Tukey's test) and t-tests were performed using GraphPad Prism (version 9.1.2) with p-values < 0.05 (*), $p < 0.01$ (**), $p < 0.001$ (***) and $p <$ 0.0001 (****) considered as levels of significance. The results are presented as mean ± standard deviation (SD).

III. RESULTS

III.1. HISTOLOGICAL STUDY

BBB integrity was assessed by perfusing mice with EB dye, a fluorescent vascular leakage marker. On the brain sections treated with osmotic shock, the fluorescent dye diffused more largely outside of the tumor area than on the brain sections of the untreated tumors (Figure 2). We observed that the surface stained with EB was about two times larger than the tumor surface area (1.93 ± 0.43, mean ± SD, $n = 4$) in the control mice (treated with saline). The EB stained/tumor surface ratio in the group of mice receiving osmotic shock (3.282 ± 0.74; mean ± SD, $n = 4$) was significantly higher ($p < 0.0001$) than in the control group receiving saline, a result consistent with an opening of the BBB.

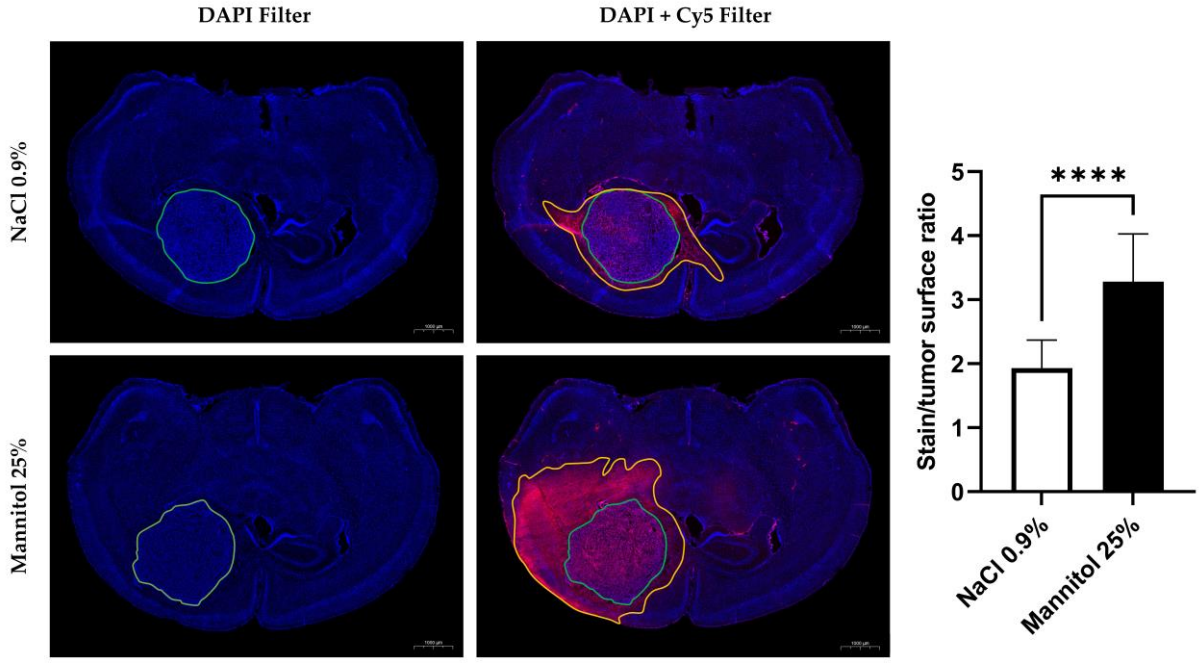

Figure 2. Assessment of diffusion of contrast agent outside the tumor area via histology with Evans Blue dye. Representative histological images of brain sections from a control mouse (treated with NaCl 0.9%, top row) and a mouse treated with osmotic shock (mannitol 25%, bottom row). The tumor area is encircled in green and the area of diffusion of EB is delineated in orange. The right panel shows the ratio of the surface stained with EB on the tumor surface for mice treated with osmotic shock ($n = 4$) and control mice ($n = 4$). The fluorescent dye diffused more largely outside the tumor area after osmotic shock than in untreated tumors. The results are expressed as means ± SD. ****$p<0.0001$.

III.2. MRI STUDIES

III.2.1. T_1/T_2 tumor surface ratio

BBB permeability was additionally evaluated using MRI. Here, we determined the anatomical tumor size using T_2-weighted contrast images and diffusion of the tracer inside and outside the tumor using T_1-weighted images after administration of Gd-DOTA used as contrast agent (Figure 3). There was no significant difference ($p > 0.05$) between the T_1/T_2 surfaces ratio of the treated (1.68 ± 0.24, mean ± SD, $n = 7$) and untreated group (1.63 ± 0.21, mean ± SD, $n = 5$). These results indicate that this MRI assessment was unable to detect any difference in the BBB permeability between these two groups.

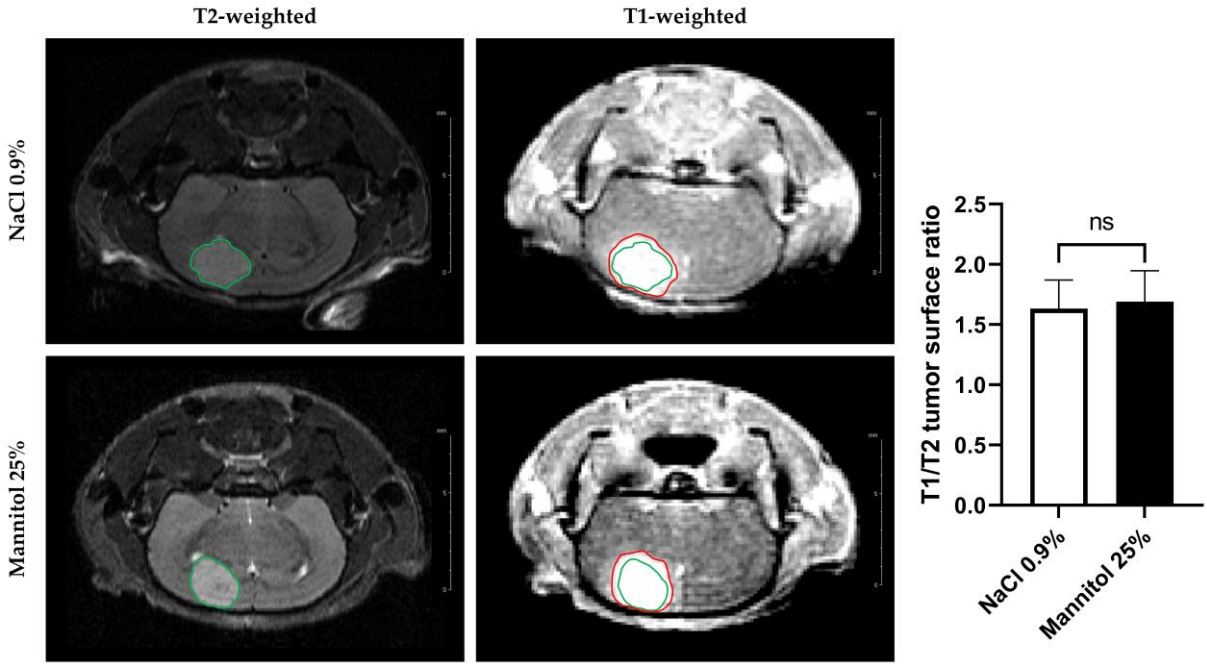

Figure 3. Assessment of diffusion of contrast agent outside the tumor area using MRI. MRI images of brains from control mice (receiving NaCl 0.9%, top row) and mice treated with osmotic shock (receiving mannitol 25%, bottom row), with T_2-weighted contrast (left) and T_1-weighted contrast after administration of Gd-DOTA (right). The T_2-weighted images allow the anatomical delineation of the tumor (encircled in green) and the post-contrast T_1-weighted images allow the assessment of vascular leakage (encircled in red). The right panel shows the ratio between T_1 and T_2 surface areas. Using this procedure, no significant difference in BBB permeability was observed between tumors receiving saline ($n = 5$) or mannitol ($n = 7$). MRI acquisitions were performed on day 1, 30 min after the injection of mannitol 25% or saline. Results are expressed as means ± SD.

III.2.2. DCE-MRI

To further investigate BBB disruption, we also performed DCE-MRI to provide hemodynamics parameters such as contrast agent efflux transfer constant (K^{trans}), contrast agent reflux transfer constant (k_{ep}), the intravascular volume fraction (v_p), the extravascular volume fraction (v_e), and the area under the curve of contrast agent concentration as a function of time from 0 to 60 or to 90 seconds (AUC60 and AUC90). Those parameters were analyzed in two different regions of the tumor: one region using ROI T_1 corresponding to the whole tumor region, and another region using ROI Delta corresponding to the margin tumor area.

We did not observe any significant difference in the tumor hemodynamic parameters between tumors in mice treated with mannitol ($n = 7$) or saline ($n = 5$), whatever the parameter studied and the ROI studied (Figure 4 and Figure 5).

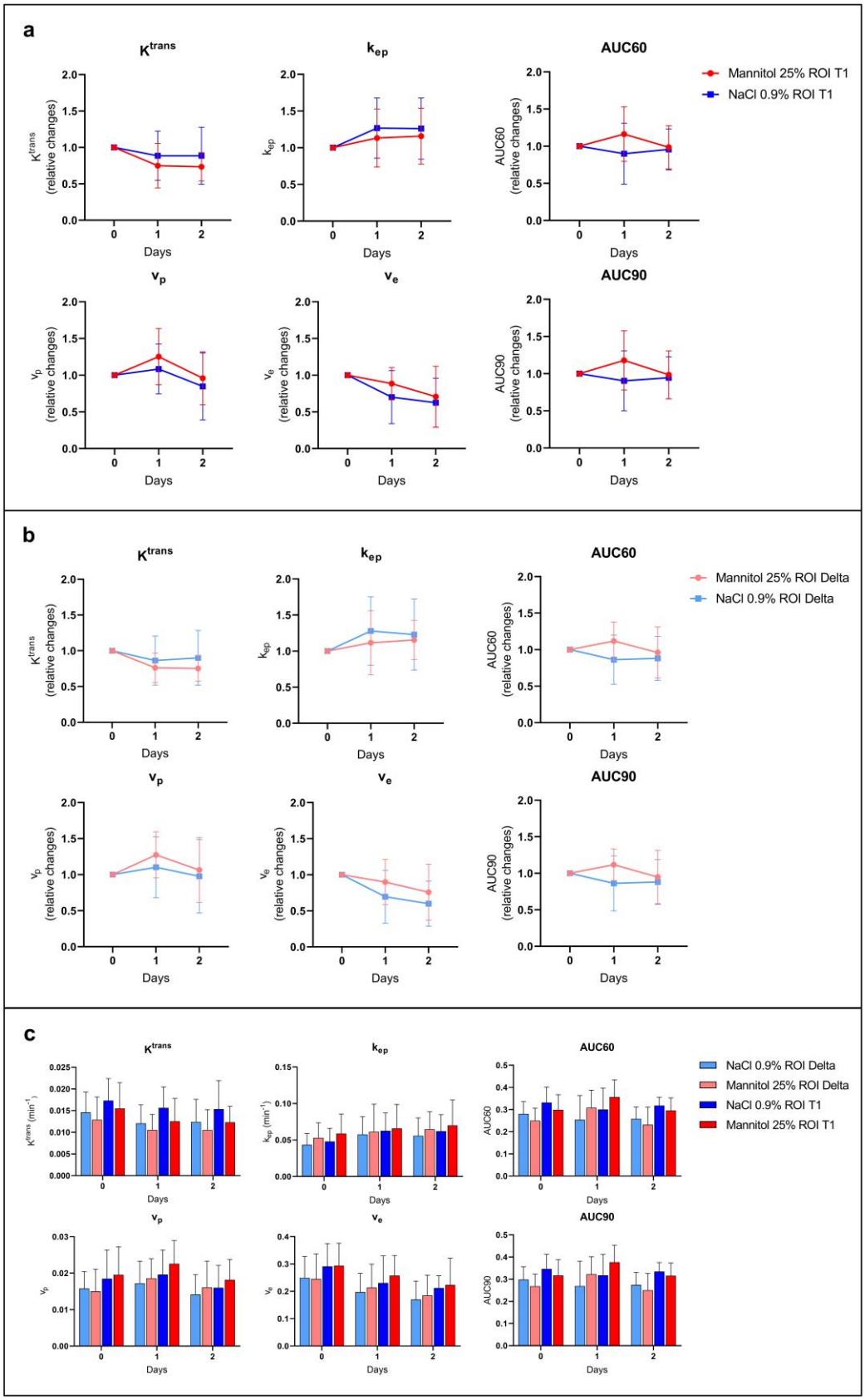

Figure 4. Hemodynamic parameters measured by DCE-MRI study. (**a**) Relative changes of tumor hemodynamic parameters (K^{trans}, k_{ep}, v_p, v_e, AUC60 and AUC90) between mice treated with osmotic shock (dark red) and control mice (dark blue) using ROI T_1; (**b**) relative changes of tumor hemodynamic parameters between mice treated with osmotic shock (light red) and control mice (light blue) using ROI Delta corresponding to the margin tumor area; note that the changes observed in the margins (**b**) are rather comparable to changes observed in the core of the tumor (**a**),

the variability being generally larger in the tumor margins; (**c**) tumor hemodynamic parameters values between mice treated with osmotic shock using ROI Delta (light red) and using ROI T_1 (dark red), and control mice using ROI Delta (light blue) and ROI T_1 (dark blue). DCE-MRI acquisition was performed 24 h before (day 0), 5 min after (day 1) and 24 h (day 2) after the injection of mannitol 25% or saline. There was no significant difference in the tumor hemodynamic parameters between tumors receiving mannitol ($n = 7$) and saline ($n = 5$), whatever the parameter and the ROI studied. Results are expressed as means ± SD.

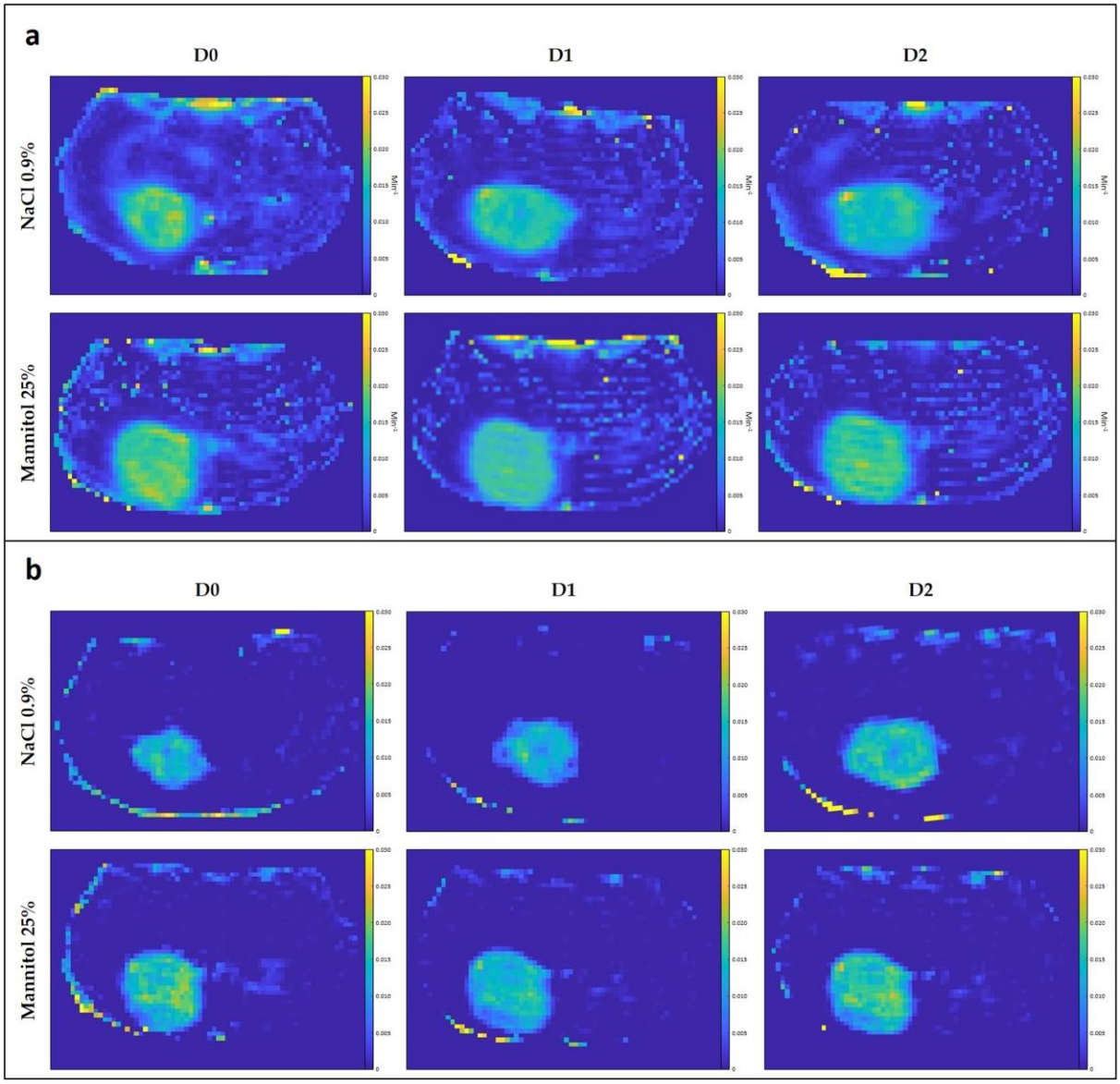

Figure 5. DCE-MRI parametric maps. Illustration of typical K^{trans} (**a**) and v_p (**b**) maps obtained from an untreated (NaCl 0.9%) and a treated mouse (mannitol 25%) with each Gd-DOTA. DCE-MRI acquisition was performed 24 h before (day 0), 5 min after (day 1) and 24 h (day 2) after the injection of mannitol 25% or saline.

IV. DISCUSSION

While the BBB is generally disrupted at the site of the tumor bulk in glioblastoma, the BBB remains intact in the infiltrating part of the tumor margins, that is, at the origin of subsequent tumor recurrence [19-22]. This feature limits the conventional systemic delivery of many chemotherapy drugs and allows residual tumor cells to escape to cytotoxic treatments [23]. Several strategies have emerged to overcome this limited accessibility of drugs to residual tumor cells by temporarily and reversibly opening the BBB. Among the strategies, our present study has been focused on the use of the intraarterial infusion of a hypertonic solution. In preclinical studies, EB staining is often used to assess BBB permeability/integrity, including in glioblastoma models [24-26]. While this histological tool is highly effective in preclinical models, it requires the sacrifice of the animal and is obviously useless for clinical applications. To monitor treatment-induced changes in BBB permeability, DCE-MRI is particularly attractive as contrast-enhanced MRI is systematically used for the characterization of brain tumors in patients. Previous studies have shown that contrast-enhanced MRI was useful in preclinical models to assess changes in BBB permeability and to evaluate the effect of strategies opening the BBB [13,27,28]. Of note, most studies focused on the BBB opening in the brain parenchyma. A few examples evaluated ultrasound-mediated BBB opening in glioblastomas [29-31], but, as far as we know, none evaluated the ability of DCE-MRI to monitor osmotic-shock-induced BBB opening in brain tumors. In our study, particular attention was paid to the ability of the treatment to enlarge the delivery of compounds into the margins of the tumor. For this purpose, we compared areas accessible to BBB-impermeable agents with the anatomical areas of the tumors, with or without osmotic treatment.

In the histological studies, we observed that the area accessible to EB was 93% larger than the anatomic area in the group of mice receiving saline (control mice) (Figure 2). This suggests that the BBB is already permeable in regions surrounding the bulk tumor in the U-87MG mouse glioblastoma model. The diffusion of EB significantly increased after the infusion of 20% mannitol solution in the carotid artery: the accessible area to the dye was 3.28 times the area covered by the bulk tumor, as defined via DAPI staining (Figure 2). This increased diffusion capability could be particularly interesting to exploit in order to increase the delivery of anticancer drugs, whatever their mode of action.

To mimic the endpoints measured via histology in the MRI study, we compared T_2-weighted images (corresponding to the anatomical image of the bulk tumor) and T_1- weighted images after Gd-DOTA administration (corresponding to areas accessible by the BBB-impermeable contrast agent). In the group of mice receiving saline (control mice), the area accessible to Gd-DOTA

visualized in the T_1-weighted images was 68% larger than the bulk area of the tumor seen in the T_2-weighted images (Figure 3). The area accessible to Gd-DOTA was not significantly altered for the group receiving the mannitol infusion (Figure 3). In contrast to the EB assay, non-invasive MRI using Gd-DOTA thus seemed unable to tackle these changes in BBB permeability in the surrounding margins of the tumor. In addition to the focus on diffusion patterns outside of the tumor bulk area, we sought to identify possible changes in intratumoral and marginal hemodynamics. For this purpose, we interrogated possible changes in K_{trans}, k_{ep}, v_e, v_p, AUC60, and AUC90 in these tumor regions. There were no significant relative changes in these parameters compared to the basal values recorded one day before the treatment (Figure 4).

The differences in the results obtained through both methods regarding the assessment of BBB opening deserve discussion. It is first important to note that the values recorded via histology or MRI cannot be superimposed. First is the invasive nature of histology in terms of repeating the measurement on the same animal: the histological images obtained in the control and treated mice came from different cohorts of animals, while the MR images were measured longitudinally on the same animals. More importantly, it is important to realize that tracers differ in their molecular and biodistribution properties. Fluorescent EB (960 Da, molecular weight) strongly binds to albumin (68 kDa), while Gd-DOTA (580 Da) is a highly hydrophilic compound that does not bind to albumin. These properties mean that they have differences in their ability to cross vessel fenestrations. Gd-DOTA can diffuse easily in the extracellular compartment of normal vessels, except for those located in the BBB due to inter-endothelial tight junctions. In contrast, due to its binding to albumin, EB remains in the vessels, is unable to cross small fenestrations in the vascular wall, and can only cross large fenestrations. As osmotic shock induces a change in tight junctions between endothelial cells, we can assume that the observed change in permeability would be more pronounced for larger molecules (complex EB-albumin) than for smaller molecules (Gd-DOTA) that were already able to cross small fenestrations of the damaged tumoral BBB. Comparative studies have indeed reported differences in glioblastoma accumulation for small Gd complexes and radiolabeled albumin measured via PET [32]. In the future, it could be interesting to test the size-dependent ability to report on BBB opening using larger molecular entities or gadolinium-based contrast agents with high affinity for albumin, such as gadobenate (Gd-BOPTA), that would better mimic the distribution behavior of EB [33]. Moreover, it is important to notice that both methods present differences in terms of sensitivity and resolution. Indeed, the optical fluorescent method has a higher sensitivity of detection of probes informing on BBB permeability and much higher spatial resolution than the MRI method.

Regarding the DCE-MRI study, it is likely that the changes in hemodynamic parameters could be too subtle to be detected through the use of the pharmacokinetic model (the extended Tofts model). This model is a two-compartmental model widely used to study hemodynamic parameters in tumors [17,34]. It takes into account the contribution of the vascular compartment which is not negligible in tumors. Several studies have used this model to describe variations in hemodynamic parameters (K_{trans}, k_{ep}, v_e, and v_p) after the disruption of the BBB [35-39].Here, however, we were unable to tackle any variation in these parameters using the extended Tofts model. Measuring subtle BBB leakage using DCE-MRI presents unique challenges. Among the kinetic models described in the literature, the Patlak model has been reported to detect subtle changes in hemodynamics associated with BBB disruption [40-42]. This model seems to be appropriate for studying low-level blood-brain barrier leakage where the back-flux from the interstitium to the capillaries is negligible [42-45]. In the tumor core of the GB, the BBB is damaged and the extended Tofts model seems to be more appropriate as the back-flux is not negligible. However, in further studies, it could be interesting to apply the Patlak model in the margins of the tumor where the BBB is less fenestrated and where the back-flux from the interstitium can be neglected. The parameters AUC60 and AUC90 that are model-independent could have potentially hinted a change in contrast agent uptake. While there was a trend for an increased AUC60 and AUC90, the changes were not significant.

It is important to highlight that the anesthetic regimen used in the present study may have played a role in our assessment of hemodynamics. We used isoflurane because previous studies have shown that this mode of anesthesia preserved the oxygenation in most tissues and peripheric tumors [46,47]. However, in the brain, several reports have suggested that isoflurane presents a vasodilatory effect that can increase baseline cerebral blood flow. This effect of isoflurane may decrease the vasodilatory reserve that can be recruited, as reported in functional MRI studies [48-51]. Therefore, isoflurane could have potentially affected our ability to see hemodynamic changes at the brain tumor level. However, we should notice that isoflurane was used for both EB and MRI assessments. As we observed, regarding the permeabilization of the BBB using EB, it is unlikely that our inability to see this phenomenon using MRI was due to the sole effect of isoflurane.

V. REFERENCES

1. Cha, G.D.; Kang, T.; Baik, S.; et al. Advances in drug delivery technology for the treatment of glioblastoma multiforme. *J Control Release* **2020**, *328*, 350-367, doi:10.1016/j.jconrel.2020.09.002
2. Lukas, R.V.; Wainwright, D.A.; Ladomersky, E.; et al. Newly Diagnosed Glioblastoma: A Review on Clinical Management. *Oncology* **2019**, *33*, 91-100.
3. Hottinger, A.F.; Stupp, R.; Homicsko, K. Standards of care and novel approaches in the management of glioblastoma multiforme. *Chin J Cancer* **2014**, *33*, 32-39, doi:10.5732/cjc.013.10207.
4. Obermeier, B.; Daneman, R.; Ransohoff, R.M. Development, maintenance and disruption of the blood-brain barrier. *Nat Med* **2013**, *19*, 1584-1596, doi:10.1038/nm.3407.
5. Arvanitis, C.D.; Ferraro, G.B.; Jain, R.K. The blood-brain barrier and blood-tumour barrier in brain tumours and metastases. *Nat Rev Cancer* **2020**, *20*, 26-41, doi:10.1038/s41568-019-0205-x.
6. Lockman, P.R.; Mittapalli, R.K.; Taskar, K.S.; et al. Heterogeneous blood-tumor barrier permeability determines drug efficacy in experimental brain metastases of breast cancer. *Clin Cancer Res* **2010**, *16*, 5664-5678, doi:10.1158/1078-0432.Ccr-10-1564.
7. Osswald, M.; Blaes, J.; Liao, Y.; et al. Impact of Blood-Brain Barrier Integrity on Tumor Growth and Therapy Response in Brain Metastases. *Clin Cancer Res* **2016**, *22*, 6078-6087, doi:10.1158/1078-0432.Ccr-16-1327.
8. Rapoport, S.I.; Hori, M.; Klatzo, I. Testing of a hypothesis for osmotic opening of the blood-brain barrier. *Am J Physiol* **1972**, *223*, 323-331, doi:10.1152/ajplegacy.1972.223.2.323.
9. Rapoport, S.I. Advances in osmotic opening of the blood-brain barrier to enhance CNS chemotherapy. *Expert Opin Investig Drugs* **2001**, *10*, 1809-1818, doi:10.1517/13543784.10.10.1809.
10. Louis, D.N.; Ohgaki, H.; Wiestler, O.D.; et al. The 2007 WHO classification of tumours of the central nervous system. *Acta Neuropathol* **2007**, *114*, 97-109, doi:10.1007/s00401-007-0243-4.
11. Ahishali, B.; Kaya, M. Evaluation of Blood-Brain Barrier Integrity Using Vascular Permeability Markers: Evans Blue, Sodium Fluorescein, Albumin-Alexa Fluor Conjugates, and Horseradish Peroxidase. *Methods Mol Biol* **2021**, *2367*, 87-103, doi:10.1007/7651_2020_316.
12. Bianco, J.; Bastiancich, C.; Joudiou, N.; et al. Novel model of orthotopic U-87 MG glioblastoma resection in athymic nude mice. *J Neurosc Methods* **2017**, *284*, 96-102, doi:10.1016/j.jneumeth.2017.04.019.
13. Chu, C.; Liu, G.; Janowski, M.; et al. Real-Time MRI Guidance for Reproducible Hyperosmolar Opening of the Blood-Brain Barrier in Mice. *Front Neurol* **2018**, *9*, 921, doi:10.3389/fneur.2018.00921.
14. Nicaise, C.; Mitrecic, D.; Demetter, P.; et al. Impaired blood-brain and blood-spinal cord barriers in mutant SOD1-linked ALS rat. *Brain Res* **2009**, *1301*, 152-162, doi:10.1016/j.brainres.2009.09.018.
15. del Valle, J.; Camins, A.; Pallàs, M.; et al. A new method for determining blood-brain barrier integrity based on intracardiac perfusion of an Evans Blue-Hoechst cocktail. *J Neurosci Methods* **2008**, *174*, 42-49, doi:10.1016/j.jneumeth.2008.06.025.

16. Sourbron, S.P.; Buckley, D.L. Classic models for dynamic contrast-enhanced MRI. *NMR Biomed* **2013**, *26*, 1004-1027, doi:10.1002/nbm.2940.

17. Tofts, P.S.; Brix, G.; Buckley, D.L.; et al. Estimating kinetic parameters from dynamic contrast-enhanced T(1)-weighted MRI of a diffusable tracer: standardized quantities and symbols. *J Magn Reson Imaging* **1999**, *10*, 223-232, doi:10.1002/(sici)1522-2586(199909)10:3<223::aid-jmri2>3.0.co;2-s.

18. Bankhead, P.; Loughrey, M.B.; Fernández, J.A.; et al. QuPath: Open source software for digital pathology image analysis. *Sci Rep* **2017**, *7*, 16878, doi:10.1038/s41598-017-17204-5.

19. van Tellingen, O.; Yetkin-Arik, B.; de Gooijer, M.C.; et al. Overcoming the blood-brain tumor barrier for effective glioblastoma treatment. *Drug Resist Updat* **2015**, *19*, 1-12, doi:10.1016/j.drup.2015.02.002.

20. Kane, J.R. The Role of Brain Vasculature in Glioblastoma. *Mol Neurobiol* **2019**, *56*, 6645-6653, doi:10.1007/s12035-019-1561-y.

21. Zhang, D.Y.; Dmello, C.; Chen, L.; et al. Ultrasound-mediated Delivery of Paclitaxel for Glioma: A Comparative Study of Distribution, Toxicity, and Efficacy of Albumin-bound Versus Cremophor Formulations. *Clin Cancer Res* **2020**, *26*, 477-486, doi:10.1158/1078-0432.Ccr-19-2182.

22. Gould, A.; Zhang, D.; Arrieta, V.A.; et al. Delivering albumin-bound paclitaxel across the blood-brain barrier for gliomas. *Oncotarget* **2021**, *12*, 2474-2475, doi:10.18632/oncotarget.28018.

23. Gebhardt, B.J.; Dobelbower, M.C.; Ennis, W.H.; et al. Patterns of failure for glioblastoma multiforme following limited-margin radiation and concurrent temozolomide. *Radiat Oncol* **2014**, *9*, 130, doi:10.1186/1748-717x-9-130.

24. Dong, Q.; He, L.; Chen, L.; et al. Opening the Blood-Brain Barrier and Improving the Efficacy of Temozolomide Treatments of Glioblastoma Using Pulsed, Focused Ultrasound with a Microbubble Contrast Agent. *Biomed Res Int* **2018**, *2018*, 6501508, doi:10.1155/2018/6501508.

25. Stegmayr, C.; Oliveira, D.; Niemietz, N.; et al. Influence of Bevacizumab on Blood-Brain Barrier Permeability and O-(2-(18)F-Fluoroethyl)-l-Tyrosine Uptake in Rat Gliomas. *J Nucl Med* **2017**, *58*, 700-705, doi:10.2967/jnumed.116.187047.

26. Leten, C.; Struys, T.; Dresselaers, T.; et al. In vivo and ex vivo assessment of the blood brain barrier integrity in different glioblastoma animal models. *J Neurooncol* **2014**, *119*, 297-306, doi:10.1007/s11060-014-1514-2.

27. Rhine, W.D.; Benaron, D.A.; Enzmann, D.R.; et al. Gd-DTPA MR detection of blood-brain barrier opening in rats after hyperosmotic shock. *J Comput Assist Tomogr* **1993**, *17*, 563-566, doi:10.1097/00004728-199307000-00008.

28. Blanchette, M.; Pellerin, M.; Tremblay, L.; et al. Real-time monitoring of gadolinium diethylenetriamine penta-acetic acid during osmotic blood-brain barrier disruption using magnetic resonance imaging in normal wistar rats. *Neurosurgery* **2009**, *65*, 344-350; discussion 350-341, doi:10.1227/01.Neu.0000349762.17256.9e.

29. Ahmed, M.H.; Hernández-Verdin, I.; Quissac, E.; et al. Low-Intensity Pulsed Ultrasound-Mediated Blood-Brain Barrier Opening Increases Anti-Programmed Death-Ligand 1 Delivery and Efficacy in Gl261 Mouse Model. *Pharmaceutics* **2023**, *15*, doi:10.3390/pharmaceutics15020455.

30. Wang, J.; Li, Z.; Pan, M.; et al. Ultrasound-mediated blood-brain barrier opening: An effective drug delivery system for theranostics of brain diseases. *Adv Drug Deliv Rev* **2022**, *190*, 114539, doi:10.1016/j.addr.2022.114539.

31. Coluccia, D.; Figueiredo, C.A.; Wu, M.Y.; et al. Enhancing glioblastoma treatment using cisplatin-gold-nanoparticle conjugates and targeted delivery with magnetic resonance-guided focused ultrasound. *Nanomedicine* **2018**, *14*, 1137-1148, doi:10.1016/j.nano.2018.01.021.

32. Brady, M.; Raghavan, R.; Sampson, J. Determinants of Intraparenchymal Infusion Distributions: Modeling and Analyses of Human Glioblastoma Trials. *Pharmaceutics* **2020**, *12*, doi:10.3390/pharmaceutics12090895.

33. Cavagna, F.M.; Maggioni, F.; Castelli, P.M.; et al. Gadolinium chelates with weak binding to serum proteins. A new class of high-efficiency, general purpose contrast agents for magnetic resonance imaging. *Invest Radiol* **1997**, *32*, 780-796, doi:10.1097/00004424-199712000-00009.

34. Sourbron, S.P.; Buckley, D.L. On the scope and interpretation of the Tofts models for DCE-MRI. *Magn Reson Med* **2011**, *66*, 735-745, doi:10.1002/mrm.22861.

35. Oghabian, M.A.; Fatemidokht, A.; Haririchian, M.H. Quantification of Blood-Brain-Barrier Permeability Dysregulation and Inflammatory Activity in MS Lesions by Dynamic-Contrast Enhanced MR Imaging. *Basic Clin Neurosci* **2022**, *13*, 117-128, doi:10.32598/bcn.2022.575.1.

36. Oh, S.S.; Lee, E.H.; Kim, J.H.; et al. The Use of Dynamic Contrast-Enhanced Magnetic Resonance Imaging for the Evaluation of Blood-Brain Barrier Disruption in Traumatic Brain Injury: What Is the Evidence? *Brain Sci* **2021**, *11*, doi:10.3390/brainsci11060775.

37. Yoen, H.; Yoo, R.E.; Choi, S.H.; et al. Blood-Brain Barrier Disruption in Mild Traumatic Brain Injury Patients with Post-Concussion Syndrome: Evaluation with Region-Based Quantification of Dynamic Contrast-Enhanced MR Imaging Parameters Using Automatic Whole-Brain Segmentation. *Korean J Radiol* **2021**, *22*, 118-130, doi:10.3348/kjr.2020.0016.

38. Inglese, M.; Ordidge, K.L.; Honeyfield, L.; et al. Reliability of dynamic contrast-enhanced magnetic resonance imaging data in primary brain tumours: a comparison of Tofts and shutter speed models. *Neuroradiology* **2019**, *61*, 1375-1386, doi:10.1007/s00234-019-02265-2.

39. Keil, V.C.; Gielen, G.H.; Pintea, B.; et al. DCE-MRI in Glioma, Infiltration Zone and Healthy Brain to Assess Angiogenesis: A Biopsy Study. *Clin Neuroradiol* **2021**, *31*, 1049-1058, doi:10.1007/s00062-021-01015-3.

40. Heye, A.K.; Thrippleton, M.J.; Armitage, P.A.; et al. Tracer kinetic modelling for DCE-MRI quantification of subtle blood-brain barrier permeability. *Neuroimage* **2016**, *125*, 446-455, doi:10.1016/j.neuroimage.2015.10.018.

41. Heye, A.K.; Culling, R.D.; Valdés Hernández Mdel, C.; et al. Assessment of blood-brain barrier disruption using dynamic contrast-enhanced MRI. A systematic review. *Neuroimage Clin* **2014**, *6*, 262-274, doi:10.1016/j.nicl.2014.09.002.

42. Manning, C.; Stringer, M.; Dickie, B.; et al. Sources of systematic error in DCE-MRI estimation of low-level blood-brain barrier leakage. *Magn Reson Med* **2021**, *86*, 1888-1903, doi:10.1002/mrm.28833.

43. Rosenberg, G.A.; Wallin, A.; Wardlaw, J.M.; et al. Consensus statement for diagnosis of subcortical small vessel disease. *J Cereb Blood Flow Metab* **2016**, *36*, 6-25, doi:10.1038/jcbfm.2015.172.

44. Thrippleton, M.J.; Backes, W.H.; Sourbron, S.; et al. Quantifying blood-brain barrier leakage in small vessel disease: Review and consensus recommendations. *Alzheimers Dement* **2019**, *15*, 840-858, doi:10.1016/j.jalz.2019.01.013.

45. Wong, S.M.; Jansen, J.F.A.; Zhang, C.E.; et al. Measuring subtle leakage of the blood-brain barrier in cerebrovascular disease with DCE-MRI: Test-retest reproducibility and its influencing factors. *J Magn Reson Imaging* **2017**, *46*, 159-166, doi:10.1002/jmri.25540.

46. Baudelet, C.; Gallez, B. Effect of anesthesia on the signal intensity in tumors using BOLD-MRI: Comparison with flow measurements by Laser Doppler flowmetry and oxygen measurements by luminescence-based probes. *Magn Reson Med* **2004**, *22*, 905-912, doi:10.1016/j.mri.2004.02.005.

47. Gallez, B. Oxygenation Status in Normal Tissues, Pathological Tissues and Malignant Tumors: A pO2 Database Based on Electron Paramagnetic Resonance (EPR) Oximetry Measurements. *Appl Magn Reson* **2021**, *52*, 1395-1450, doi:10.1007/s00723-021-01358-7.

48. Schroeter, A.; Schlegel, F.; Seuwen, A.; et al. Specificity of stimulus-evoked fMRI responses in the mouse: the influence of systemic physiological changes associated with innocuous stimulation under four different anesthetics. *Neuroimage* **2014**, *94*, 372-384, doi:10.1016/j.neuroimage.2014.01.046.

49. Grandjean, J.; Schroeter, A.; Batata, I.; et al. Optimization of anesthesia protocol for resting-state fMRI in mice based on differential effects of anesthetics on functional connectivity patterns. *Neuroimage* **2014**, *102 Pt 2*, 838-847, doi:10.1016/j.neuroimage.2014.08.043.

50. Wu, T.; Grandjean, J.; Bosshard, S.C.; et al. Altered regional connectivity reflecting effects of different anaesthesia protocols in the mouse brain. *Neuroimage* **2017**, *149*, 190-199, doi:10.1016/j.neuroimage.2017.01.074.

51. Munting, L.P.; Derieppe, M.P.P.; Suidgeest, E.; et al. Influence of different isoflurane anesthesia protocols on murine cerebral hemodynamics measured with pseudo-continuous arterial spin labeling. *NMR Biomed* **2019**, *32*, e4105, doi:10.1002/nbm.4105.

CHAPTER IV

EXPLORING THE IMPACT OF IRRADIATION ON GLIOBLASTOMA BLOOD-BRAIN BARRIER PERMEABILITY: INSIGHTS FROM DCE-MRI AND HISTOLOGICAL ANALYSIS

Adapted from **Conq J**, Joudiou N, Préat V, Gallez B. Exploring the Impact of Irradiation on Glioblastoma Blood-Brain Barrier Permeability: Insights from DCE-MRI and Histological Analysis. Submitted

Abstract:

Glioblastoma (GB) presents a formidable challenge in neuro-oncology due to its aggressive nature, limited treatment options, and poor prognosis. The blood-brain barrier (BBB) complicates treatment by hindering drug delivery to the tumor site, in particular to the infiltrative cells in the margin of the tumor, which are mainly responsible for tumor recurrence. Innovative strategies are therefore needed to enhance drug delivery in the margins of the tumor. This study explores whether irradiation can enhance BBB permeability by assessing hemodynamic changes and the distribution of contrast agents in the core and the margins of GB tumors in mice grafted with U-87MG cells that were exposed to irradiation. Distribution of contrast agents and hemodynamic parameters were evaluated using both non-invasive MRI with Gd-DOTA as a contrast agent and invasive histological analysis with the fluorescent dye Evans Blue. The histological study revealed a complex dose-dependent effect of irradiation on BBB integrity, with increased vascular leakage at 5 Gy but reduced leakage at higher doses (10 and 15 Gy). However, no significant increase in the diffusion of Gd-DOTA outside the tumor area by MRI. The increase in BBB permeability could be an interesting approach to enhance drug delivery in glioblastoma margins for low irradiation doses. In this model, DCE-MRI analysis was of limited value to assess the BBB opening in glioblastoma after irradiation.

Keywords: blood–brain barrier; glioblastoma; radiotherapy; DCE-MRI; diffusion-MRI; Evans blue

Graphical abstract

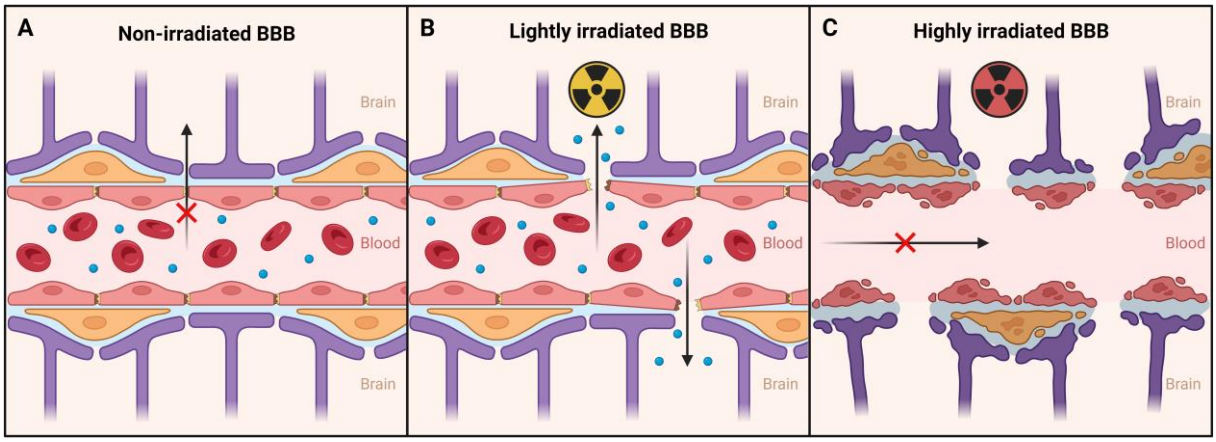

Illustration of the effect of irradiation on the BBB. (**A**) Non-fenestrated BBB (as in tumor margins) when not exposed to irradiation, the permeability remains low. (**B**) A low dose of irradiation may damage the tight junctions and endothelial cells without compromising the structural integrity of the vessel, resulting in an enhanced BBB permeability. (**C**) At a higher dose of irradiation, cytotoxicity would be so intense for the BBB cells that the vessel will be destroyed, leading to a reduction in perfusion and diffusion.

TABLE OF CONTENTS

I. INTRODUCTION

Glioblastoma (GB) is a highly aggressive and malignant brain cancer that remains a formidable challenge in the realm of neuro-oncology, with limited treatment options and a poor prognosis. The current therapeutic approach for GB involves a combination of surgical resection, radiation therapy, and chemotherapy, commonly employing temozolomide [1]. Despite these efforts, the prognosis for GB remains bleak, largely due to the tumor's infiltrative nature and high recurrence rates, with a median survival of around 15 months post-diagnosis [2,3].

This cancer is characterized by a rapid growth, a high degree of cellular and genetic heterogeneity, a resistance to chemotherapy, and highly invasive properties with infiltrative cells that spread into surrounding brain tissues making complete surgical removal challenging and contributing to high rates of recurrence [4].

The intrinsic resistance of GB to conventional treatments is exacerbated by the blood-brain barrier (BBB), hindering effective drug delivery to the tumor site. The BBB is a highly selective, semipermeable barrier that regulates the passage of substances between the bloodstream and the brain to protect the brain from potentially harmful agents, including toxins, pathogens and, of interest here, drugs while maintaining an optimal microenvironment for neural function [5]. In glioblastoma, although the tumoral BBB is leaky due to a paracellular pathway that is damaged, its permeability is highly heterogeneous and varies not only between GB but also within the same tumor leading to a perfusion and a consequent delivery of drugs highly heterogeneous [6]. Indeed, the BBB is often compromised in the tumor core allowing the passage of drugs, but in the margins of the tumor, the barrier is still intact or only slightly compromised, limiting significantly the passage of drugs, especially for reaching the infiltrating tumor cells that will be at the origins of the tumor recurrence [7-10]. Thus, there is an urgent need to develop methods for an opening of the BBB, so that drugs can be delivered evenly to the tumor site. Recognizing this challenge, emerging research explores innovative approaches, such as irradiation-induced disruption of the BBB. Indeed, previous works have shown that irradiation can induce an opening of healthy BBB or tumor vascular bed in other cancers than glioblastoma [11-15], or even increase the drug delivery in glioblastoma [16,17], reflecting an opening of the BBB.

This article explores the potential of irradiation to open the tumoral BBB in GB, especially in the margins of the tumor, providing a promising avenue for enhanced drug delivery, and therefore improved therapeutic efficacy (Figure 1). Indeed, as radiotherapy is included in the standard therapeutic protocol, this would give us a better understanding of its impact on the delivery/diffusion of the concomitant chemotherapy, and enable us to assess whether there is an

irradiation dose for which diffusion would be the most ideal, to adapt the protocol of concomitant chemotherapy in the future.

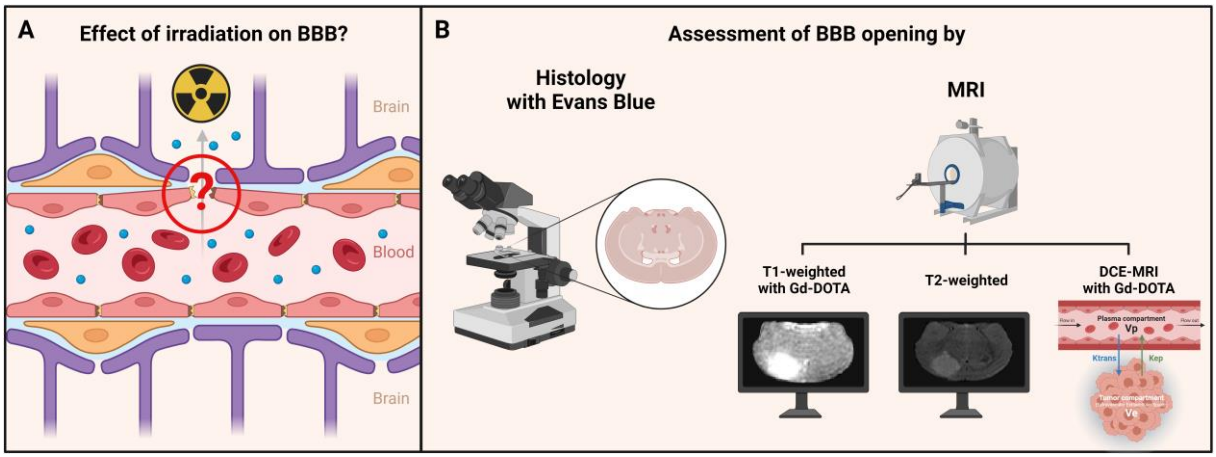

Figure 1. Assessment of the impact of irradiation on the BBB. (**A**) When not exposed to irradiation, a non-fenestrated BBB (as in tumor margins) has a very low permeability. The purpose here was to assess the effect of irradiation on the BBB. (**B**) This assessment was carried out by histological analysis with Evans Blue and MRI techniques (T_1-weighted, T_2-weighted, and dynamic contrast-enhanced MRI) with gadolinium-DOTA as contrast agent.

For this purpose, we evaluated whether a radiotherapy protocol may change hemodynamic parameters in the core and the margins of the tumor in a GB model. Two methods have been used to evaluate the efficacy of the treatment on perfusion/permeability parameters: a non-invasive one, based on magnetic resonance imaging (MRI) analysis (T_1-weighted and T_2-weighted imaging as well as dynamic contrast-enhanced (DCE)-MRI), and an invasive one, based on histological analysis with a fluorescent vascular leakage marker (Evans blue).

For the MRI analysis, the tumor core was determined using T_2-weighted contrast images. Moreover, T_1-weighted images were acquired following the administration of a contrast agent to assess the diffusion of the contrast agent within both the bulk of the tumor and its margins. Gadolinium-DOTA was selected as a contrast agent due to its inability to cross the intact blood-brain barrier (BBB), providing an avenue to investigate changes in BBB permeability. Tumor margins were defined as the difference between the T_1-enhancing area post-contrast agent injection and the area demarcated by T_2-weighted contrast outlining the tumor core [18]. The hypothesis was that an increased BBB permeability would facilitate the passage of the contrast agent, resulting in a more extensive diffusion beyond the tumor zone into the brain parenchyma. Consequently, an increase in the area of contrast uptake in the post-contrast T_1-weighted image compared to the anatomical T_2-weighted image would signify the opening of the BBB. Additionally, DCE-MRI analysis gave access to complementary tumor hemodynamic parameters that may be biomarkers of the change in BBB permeability [19]. These parameters were computed using two different models:

the extended Tofts model [20] and the Patlak model [21]. The extended Tofts model is one of the most widely used in the literature for studying tumor perfusion/permeability in glioblastoma. It's a two-compartmental model suited to describe highly perfused tissues such as those found in glioblastoma. The Patlak model is comparable to the extended Tofts model but ignores the backflux and is therefore adapted to assess changes for a low-level BBB permeability where backflux is negligible, as found especially in the margins of glioblastoma tumors. This model may allow us to better assess than the extended Tofts model whether there are subtle changes in the hemodynamic parameters in tumor margins.

A diffusion-MRI study was also carried out. Diffusion-MRI emerges as a valuable tool in assessing the cytotoxic effects of medical treatments, particularly in the oncological domain. This imaging technique enables the study of water molecule movements within biological tissues without the use of an exogenous contrast agent, providing nuanced insights into cellular microstructure. One key parameter derived from diffusion-MRI is the Apparent Diffusion Coefficient (ADC). The ADC quantifies the ease with which water molecules move through tissues, offering valuable information about cellular density. In the context of cytotoxicity induced by treatment, the ADC can be used to define the microstructural changes associated with therapeutic response. Generally, an increase in ADC can be interpreted as an increase in water mobility, resulting in a decrease in cell density and indicating a cytotoxic response to the treatment [22-24].

For the histological study, we used Evans blue, a fluorescent marker of vascular leakage, to assess the functionality of the blood-brain barrier [25]. Indeed, administered intravenously, this dye forms a tight bond with plasma protein, albumin, in the bloodstream. Albumin, under normal circumstances, is too large to cross the intact blood-brain barrier. However, in the event of disruption of the BBB, Evans Blue bound to albumin could penetrate the brain parenchyma and be detected by fluorescence. Therefore, this approach enables us to determine a possible variation in tumor perfusion/permeability by analyzing the diffusion of Evans blue in the brain parenchyma.

II. MATERIALS AND METHODS

II.1. ORTHOTOPIC U-87MG MOUSE MODEL

All experiments were performed following the European Directive 2010/63/EU and following the Belgian national regulation guidelines, and were approved by the ethical committee for animal care by the Faculty of Medicine of the Université Catholique de Louvain (2022/UCL/MD/067). Water and food were given ad libitum. Animal body weight was daily monitored throughout the experiment.

Six-week-old female NMRI nude mice (Janvier, France) were anesthetized via intraperitoneal injection of ketamine/xylazine (100 and 13 mg/kg, respectively) and fixed on a stereotaxic frame. In 2 μL of Eagle's Minimum Essential Medium (EMEM) (Gibco™, ThermoFisher Scientific, Waltham, MA, USA), 4×10^4 cells of U-87MG (ATCC) were injected into the right frontal lobe using an infusion syringe pump (Harvard Apparatus, Holliston, MA, USA) mounted with a Hamilton syringe (26S gauge needle). The injection coordinates were 2.1 mm lateral and 0.5 mm posterior from the bregma, and 2.6 mm deep from the outer border of the cranium [26]. The tumor size monitoring was performed via MRI (see Section 2.3).

II.2. IRRADIATION PROTOCOL

When the tumor size reached 7 ± 1 mm^3, mice were randomly assigned into 4 groups and irradiated once at doses of 0 ($n = 5$), 5 ($n = 4$), 10 ($n = 4$) and 15 Gy ($n = 4$) with a dose rate of 0.846 Gy/min with a Cesium-137 irradiator.

II.3. MRI

MRI was performed using an 11.7 T Bruker Biospec MRI system (Bruker, Ettlingen, Germany) equipped with a ^{1}H quadrature transmit/receive birdcage coil (21 mm inner diameter, RAPID Biomedical, Rimpar, Germany). Mice were anesthetized with isoflurane mixed with air (2.5% for induction, 1.5% for maintenance). Animals were covered with a heating blanket and their temperature was monitored. A pressure pad was used to monitor the respiration rate.

Anatomical images were obtained using T_2-weighted rapid acquisition with a refocused echo (RARE) sequence (echo time = 30 ms; repetition time = 2500 ms; number of slices = 25; field of view = 20 mm × 20 mm; matrix size = 200 × 200; resolution = 0.1 mm × 0.1 mm; slice thickness = 0.3 mm; acquisition time = 5 min 20 s; averages = 8). Tumor volume was determined from a

manually drawn region of interest (ROI) using Paravision 6.0.1 software (Bruker BioSpin) on day 14 following tumor induction, and then daily until the tumor size reached 7 ± 1 mm^3.

For diffusion MRI acquisition, a diffusion tensor imaging (DTI) was performed using an echoplanar imaging (EPI) sequence (echo time = 23.72 ms; repetition time = 4000 ms; segments = 4; field of view = 20 x 20 mm; matrix size = 128 x 128; resolution = 0.156 mm x 0.156 mm; slice thickness = 0.9 mm; acquisition time = 10 m 40 s) with diffusion sensitization in twelve directions and b values of 700, 1000 and 1500 s/mm^2. Before DTI acquisition, an automatic shim correction was performed from the B0 map using the map_shim algorithm. Apparent diffusion coefficient (ADC) maps were computed. Diffusion MRI acquisitions were performed just before irradiation, 24 h and 48 h after irradiation.

For DCE-MRI acquisition, T_1-weighted gradient echo images were obtained via a fast low-angle shot (FLASH) sequence (echo time = 1.4 ms; repetition time = 11.719 ms; flip angle = 10.0°; field of view = 20 mm × 20 mm; matrix size = 128 × 128; resolution = 0.156 mm × 0.156 mm; slice thickness = 0.9 mm; averages = 1; total acquisition time = 22 min 40 s). A set of 450 scans with a temporal resolution of 3.02 s was acquired, with Gadolinium-DOTA (Dotarem® 0.5 mol/mL; Guerbet, Villepinte, France) administered intravenously at a dose of 0.29 mmol/kg after the 10th scan over 5 s. DCE-MRI acquisitions were performed just before irradiation, 24 h and 48 h after irradiation.

II.4. HISTOLOGICAL STUDY

Evans blue dye (EB: 2% in normal saline; Alfa Aesar, Haverhill, MA, USA) was intravenously injected (3 mL/kg) 48 hours after the first irradiation. Thirty minutes later, the mice were euthanized and intracardially perfused with paraformaldehyde (PFA) 4% to discard all the remaining dye in the blood vessels and fix the tissue. Brains were then removed, fixed overnight in PFA 4%, cryoprotected in sucrose 20%, included in optimal cutting temperature compound (OCT, Sakura Finetek, Alphen aan den Rijn, The Netherlands), and kept at −80 °C. Cryostat 30 µm sections were counterstained with diamidino-2-phenylindole (DAPI, Thermofisher, Waltham, MA, USA) and examined under a fluorescence microscope slide scanner (Panoramic 250 Flash III, 3DHistech, Budapest, Hungary) with DAPI and Cyanine 5 (Cy5) filter [25,27,28].

II.5. IMAGE PROCESSING

Diffusion MRI data were analyzed using DSI studio (version 2017/01/27). The ADC parameter was measured in the tumor area. The tumor ROI was manually delineated on the T_2-weighted anatomical images and was matched and positioned on the ADC maps.

DCE-MRI data were analyzed using in-house software written in Matlab (version 9.6). Regions of interest (ROIs) were manually delineated. We considered ROI T_1 as the delineation of the entire tumor area using T_1-weighted images with Gd-DOTA as the contrast agent, ROI T_2 as the delineation of the tumor bulk area using T_2-weighted anatomical images, and ROI Delta as the ROI T_1 from which we subtracted ROI T_2 in order to cover the margins of the tumor. In this way, we were able to study the hemodynamic parameters for the whole tumor region but also for the margins of the tumor.

The hemodynamic parameters were computed using two different pharmacokinetics models. The first one is the extended Tofts model [20] which is a two-compartmental model that describes a highly perfused tissue, as found in glioblastoma tumors, considering bidirectional transport between the blood plasma and the extracellular extravascular space (EES). The equation of this model is given by:

$$C_t(t) = v_p \cdot C_p(t) + K^{trans} \int_0^t C_p(\tau) e^{-k_{ep}(t-\tau)} d\tau \qquad (1)$$

where K^{trans} is the volume transfer constant between blood plasma and EES [min^{-1}], v_p is the blood plasma volume per unit volume of tissue, and K_{ep} is the flux rate constant between EES and blood plasma [min^{-1}] [29]. V_e is the EES volume per unit volume of tissue, calculated as follows:

$$v_e = K^{trans}/k_{ep} \qquad (2)$$

The second pharmacokinetic model used is the Patlak model [21]. This model is comparable to the extended Tofts model but it ignores the backflux from the EES into the blood plasma compartment. Consequently, it only allows for the estimation of the two parameters K^{trans} and v_p. The equation of this model is given by:

$$C_t(t) = v_p \cdot C_p(t) + K^{trans} \int_0^t C_p(\tau) d\tau \qquad (3)$$

We were also interested in AUC60 and AUC90 corresponding to the area under the curve (AUC) of contrast agent concentration as a function of time from 0 to 60 or to 90 seconds.

Histological images were analyzed using Qupath (version 0.3.2) [30]. The tumor ROI and the Evans blue diffusion ROI were manually delineated.

II.6. STATISTICAL ANALYSES

All data are expressed as means ± standard deviation (SD). All experiments were performed in triplicate or more. Two-way ANOVA tests (Tukey's test) and t-tests were performed using GraphPad Prism (version 9.1.2), with p-values < 0.05 (*), $p < 0.01$ (**), $p < 0.001$ (***), and $p < 0.0001$ (****) considered as the levels of significance.

III. RESULTS

III.1. HISTOLOGICAL STUDY

BBB integrity was assessed by perfusing mice with EB dye, a fluorescent vascular leakage marker. Compared to the control group, the fluorescent dye diffused more widely outside the tumor area for an irradiation dose of 5 Gy, but diffused less widely for an irradiation dose of 10 Gy and even less widely for an irradiation dose of 15 Gy (Figure 1). Indeed, there was a significant increase ($p < 0.05$) in the diffusion of the fluorescent marker outside the tumor (EB stained/tumor surface ratio) for mice that received an irradiation dose of 5 Gy (2.79 ± 0.30, mean ± SD, $n = 4$) compared to the control group (2.26 ± 0.21, mean ± SD, $n = 5$). For a higher irradiation dose of 10 Gy, the EB stained/tumor surface ratio (1.81 ± 0.24, mean ± SD, $n = 4$) was significantly lower ($p < 0.05$) compared to the control group, and for an even higher irradiation dose of 15 Gy, the EB stained/tumor surface ratio (1.49 ± 0.14, mean ± SD, $n = 4$) was even more significantly lower ($p < 0.01$) than in the control group.

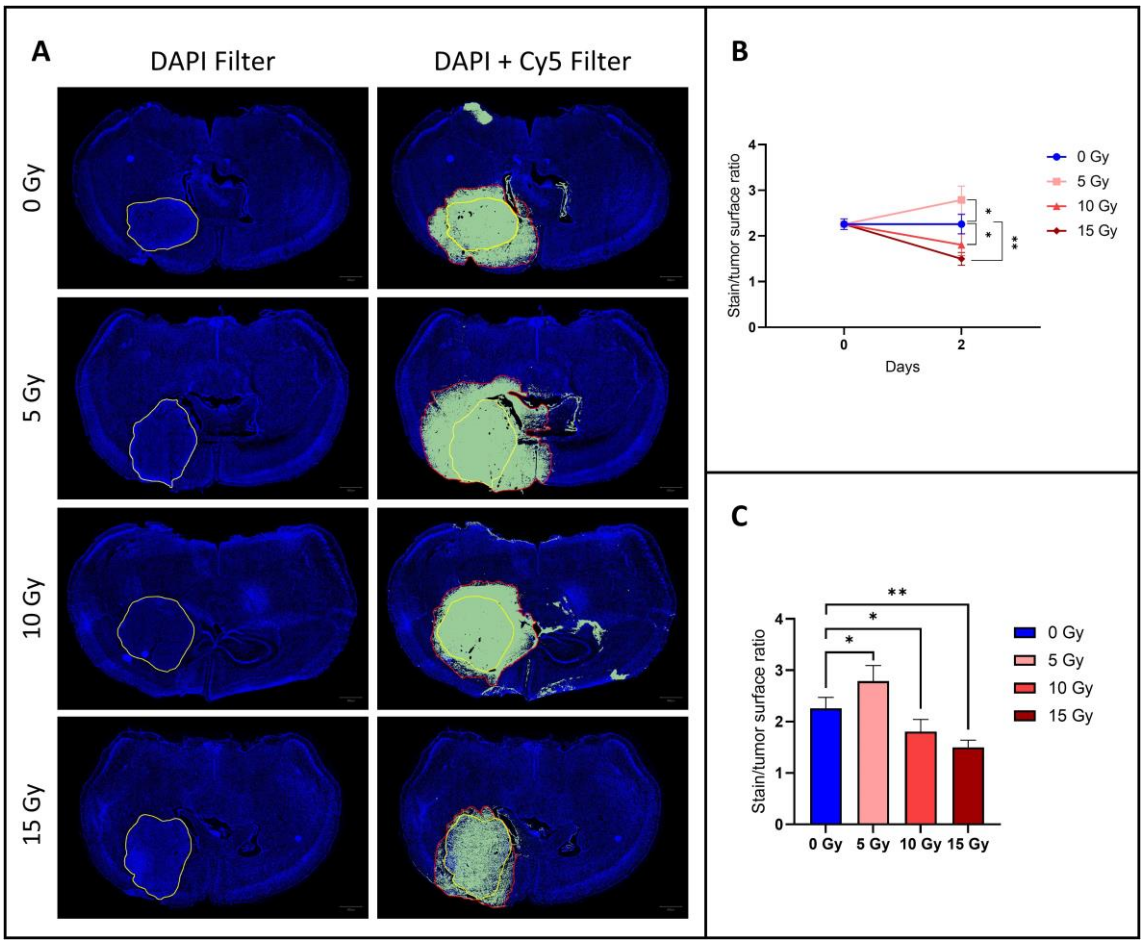

Figure 2. Evaluation of diffusion of contrast agent outside of the tumor area using histology with Evans blue dye. (**A**) Representative histological images of brain sections from a control mouse ($n = 5$) and irradiated mice with a dosage of 5 Gy ($n = 4$), 10 Gy ($n = 4$) and 15 Gy ($n = 4$). The tumor area is encircled in yellow and the area of diffusion of EB is delineated in red. (**B**) Graph showing the ratio of the surface stained with EB on the tumor surface just before irradiation (day 0), 24h (day 1) and 48h (day 2) after irradiation for the control group (blue) and group irradiated with 5 Gy (light red), 10 Gy (middle red) and 15 Gy (dark red). (**C**) Graph showing the same ratio as the top one for the same groups but focusing on day 2 after irradiation. Compared to the control group, the fluorescent dye diffused more widely outside the tumor area for an irradiation dose of 5 Gy but diffused less widely for an irradiation dose of 10 Gy and even less widely for an irradiation dose of 15 Gy. The results are expressed as means ± SD. * p-values < 0.05, ** $p < 0.01$.

III.2. MRI Studies

III.2.1. Diffusion-MRI study

The effect of irradiation on cell density, reflecting the cytotoxicity of the treatment, was assessed by monitoring ADC obtained by diffusion-MRI. We observe an increase in ADC for irradiated mice and no change in ADC for control mice. The higher the dose of irradiation used and later after irradiation, the greater the ADC increase compared to the control group (Figure 2). Indeed, there was a significant increase of the ADC at day 1 for mice irradiated at 10 Gy (0.80 ± 0.03, mean ± SD, $n = 4$, $p < 0.01$) and for mice irradiated at 15 Gy (0.87 ± 0.05, mean ± SD, $n = 4$, $p < 0$.

0001) compared to the control group (0.66 ± 0.03, mean ± SD, $n = 5$), but there was no significant difference between mice irradiated at 5 Gy (0.74 ± 0.04, mean ± SD, $n = 4$) and the control group. At day 2, there was a significant increase for the group irradiated at 5 Gy (0.78 ± 0.05, mean ± SD, $p < 0.05$) compared to the control group (0.67 ± 0.04, mean ± SD) and an even more significant increase than at day 1 for the groups irradiated at 10 Gy ((0.83 ± 0.03, mean ± SD, $p < 0.001$) and 15 Gy (0.91 ± 0.05, mean ± SD, $p < 0.0001$) compared to the control group. These results suggest that there was a cytotoxic effect of irradiation on tumor tissue, with a decrease in cell density proportional to the increase in irradiation dose received.

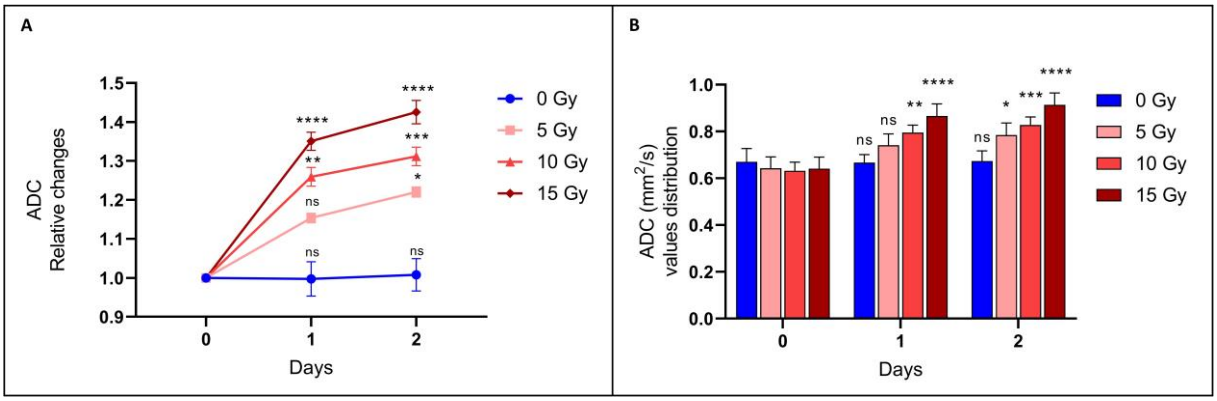

Figure 3. ADC measured by diffusion-MRI. Relative changes of ADC (**A**) and ADC values (**B**) between the control group (blue) and groups irradiated with 5 Gy (light red), 10 Gy (middle red) and 15 Gy (dark red). Diffusion-MRI acquisition was performed just before irradiation (day 0), 24h (day 1) and 48h (day 2) after irradiation. At day 1, there was a significant increase in groups irradiated with 10 Gy ($n = 4$) and 15 Gy ($n = 4$) compared to the control group ($n = 5$). At day 2, there was a significant increase in group irradiated with 5 Gy ($n = 4$) and an even more significant increase than at day 1 for groups irradiated with 10 Gy and 15 Gy. The higher the dose of irradiation used and the further in time after irradiation, the greater the ADC significantly increased compared to the control group. The results are expressed as means ± SD. * p-values < 0.05, ** $p < 0.01$, *** $p < 0.001$, **** $p < 0.0001$.

III.2.2. T_1/T_2 Tumor Surface Ratio

BBB permeability was additionally evaluated using MRI. Here, we determined the anatomical tumor size using T_2-weighted contrast images and diffusion of the tracer inside and outside of the tumor using T_1-weighted images after the administration of Gd-DOTA used as a contrast agent (Figure 3) [18]. There was no significant difference ($p > 0.05$) between the T_1/T_2 surfaces ratio of the irradiated groups with 5 Gy (1.49 ± 0.24, mean ± SD, $n = 4$), 10 Gy (1.53 ± 0.10, mean ± SD, $n = 4$) or 15 Gy (1.49 ± 0.21, mean ± SD, $n = 4$) and the control group (1.57 ± 0.27, mean ± SD, $n = 5$). These results indicate that this MRI assessment was unable to detect any difference in the BBB permeability between those groups.

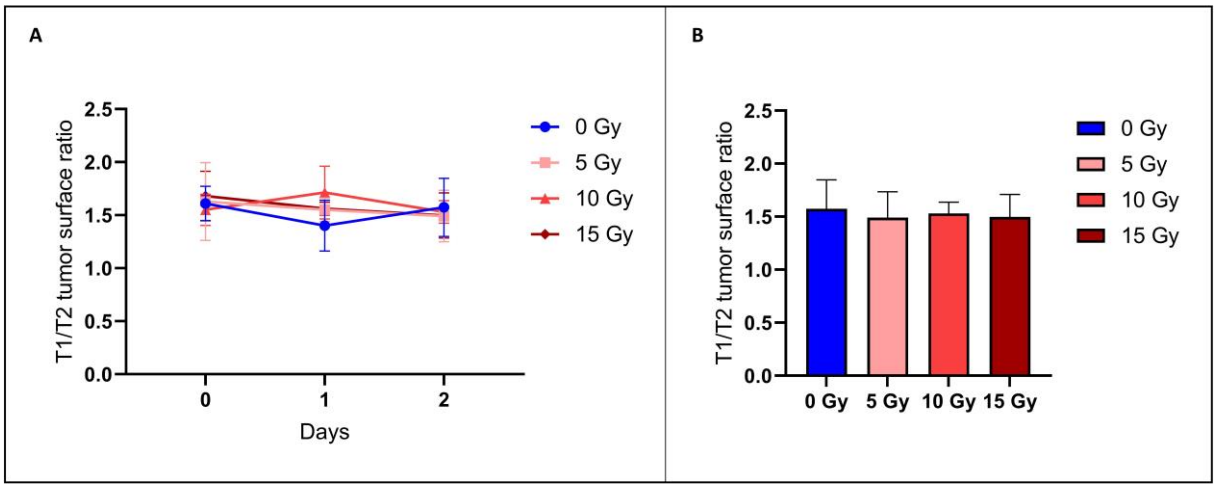

Figure 4. Assessment of diffusion of contrast agent outside of the tumor area using MRI. The left panel (**A**) shows the ratio between the T_1 and T_2 surface areas just before irradiation (day 0), 24h (day 1) and 48h (day 2) after irradiation for control group (blue) and group irradiated with 5 Gy (light red), 10 Gy (middle red) and 15 Gy (dark red). The right panel (**B**) shows the same ratio for the same groups but focusing on day 2 after irradiation. Using this procedure, no significant difference in BBB permeability was observed between control group ($n = 5$) and groups receiving 5 Gy ($n = 4$), 10 Gy ($n = 4$) or 15 Gy ($n = 4$). The results are expressed as means ± SD.

III.2.3. DCE-MRI

To further investigate BBB disruption, we also performed DCE-MRI to provide hemodynamic parameters such as contrast agent efflux transfer constant (K^{trans}), contrast agent reflux transfer constant (K_{ep}), the intravascular volume fraction (v_p), the extravascular volume fraction (v_e), and the area under the curve of contrast agent concentration as a function of time from 0 to 60 or to 90 s (AUC60 and AUC90). These parameters were computed using two different models: the extended Tofts model and the Patlak model. These parameters were also analyzed in two different regions of interest (ROIs) of the tumor: the ROI T_1 corresponding to the whole tumor region, and the ROI Delta corresponding to the margin tumor area. We did not observe any significant difference in the tumor hemodynamic parameters between the control group ($n = 5$) and groups receiving 5 Gy ($n = 4$), 10 Gy ($n = 4$) or 15 Gy ($n = 4$), whatever the studied parameter, model and ROI used.

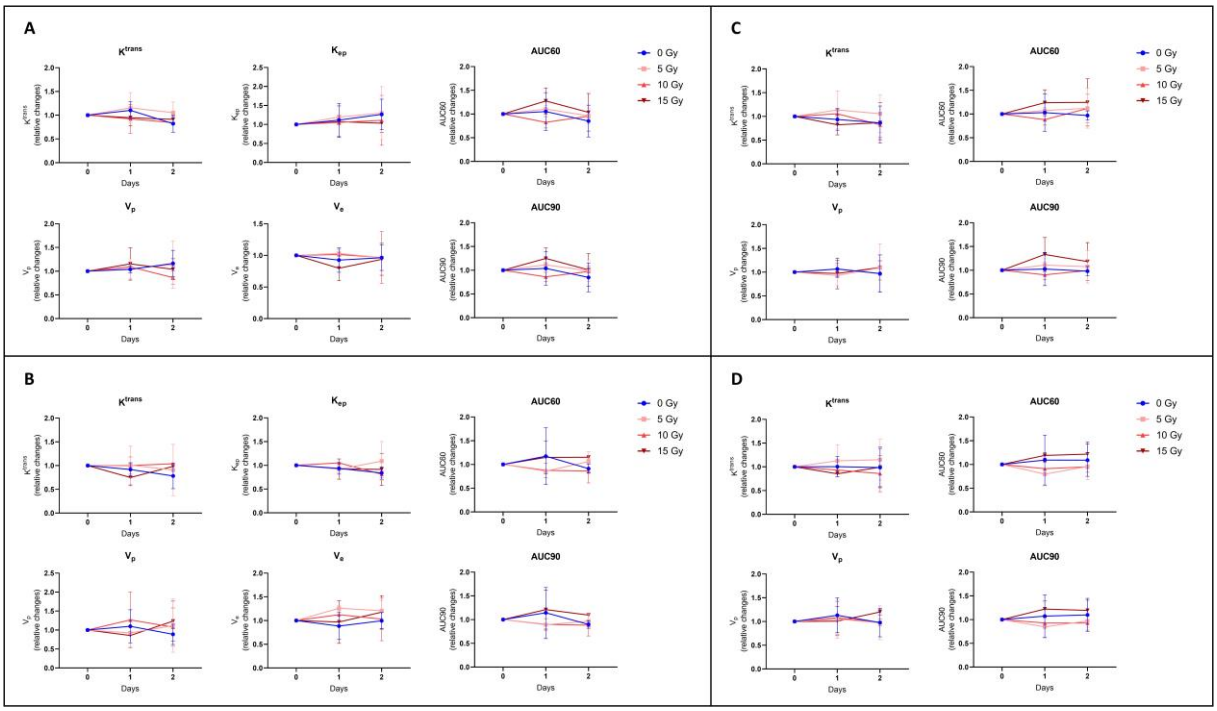

Figure 5. Hemodynamic parameters measured by DCE-MRI. Relative changes in tumor hemodynamic parameters between control group (blue), 5 Gy treated group (light red), 10 Gy treated group (middle red) and 15 Gy treated group (dark red) computed with Extended Tofts model using ROI T_1 (**A**) corresponding to the whole tumor area and using ROI Delta (**B**) corresponding to the margin tumor area or computed with Patlak model using ROI T_1 (**C**) and using ROI Delta (**D**). DCE-MRI acquisition was performed just before irradiation (day 0), 24h (day 1) and 48h (day 2) after irradiation. There was no significant difference in the tumor hemodynamic parameters between the control group ($n = 5$) and groups receiving 5 Gy ($n = 4$), 10 Gy ($n = 4$) or 15 Gy ($n = 4$), whatever the studied parameter, ROI and model used. The results are expressed as means ± SD.

We also compared the K^{trans} parametric maps between those computed using the extended Tofts model and those computed using the Patlak model (Figure 5). We calculated the ratio between the tumor surface measured on the K^{trans} map from the extended Tofts model and the tumor surface measured on the K^{trans} map from the Patlak model. We observed that this ratio was very close to 1, whatever the irradiation dose used or the day after irradiation. There was therefore no significant difference between tumor surface areas measured on K^{trans} maps obtained with the extended Tofts model and those obtained with the Patlak model.

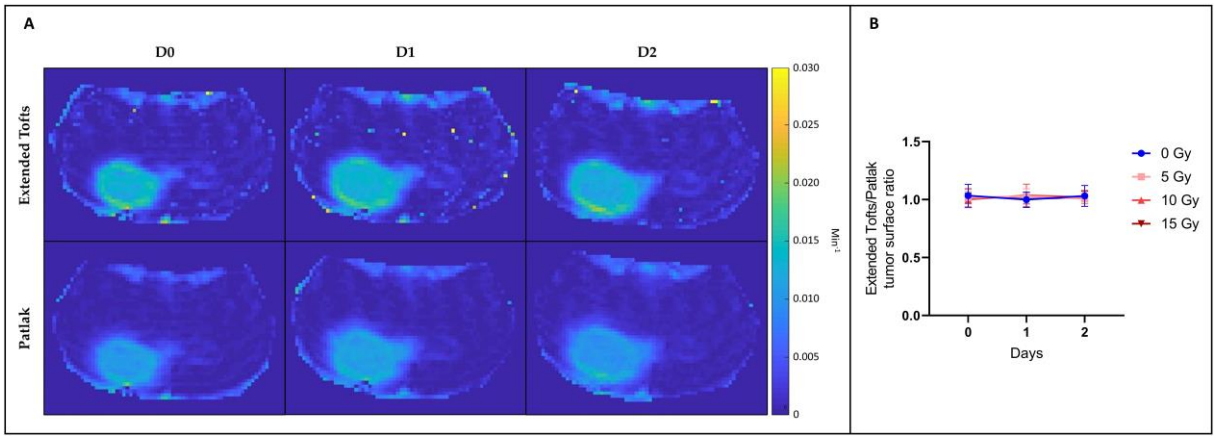

Figure 6. DCE-MRI parametric maps. (**A**) Illustration of typical K^{trans} maps obtained from 15 Gy irradiated mouse computed using extended Tofts model (top row) or Patlak model (bottom row). (**B**) The right panel shows the ratio between the tumor surface measured on the K^{trans} map from the extended Tofts model and the tumor surface measured on the K^{trans} map from the Patlak model. There is no significant difference between those tumor surface areas, whatever the irradiation dose used or the day after irradiation taken. The results are expressed as means ± SD.

IV. DISCUSSION

The heterogeneity of the BBB permeability in glioblastoma, with a BBB remaining intact in the infiltrative part of the tumor margins, limits the conventional systemic delivery of many chemotherapy drugs and allows residual tumor cells to escape cytotoxic treatments, leading to tumor recurrence [9,10,31,32]. These features underscore the need for innovative approaches to overcome this limited accessibility of drugs by achieving a homogeneous opening of the BBB [33]. In this article, we have examined the potential of irradiation to increase the permeability of the BBB in glioblastoma, particularly in the margins of the tumor. To evaluate the impact of irradiation on the tumoral BBB, a multimodal approach involving MRI and histological analysis was employed. Evans Blue is commonly used in preclinical studies as an indicator of vascular permeability, in particular, to determine BBB disruption [34-36]. However, this histological method is highly invasive, requiring the sacrifice of the animal, and is therefore not suitable for clinical use. At first sight, the imaging assessment method seems more attractive due to its non-invasive aspect and the fact that contrast-enhanced MRI is systematically used for the characterization of brain tumors in patients. Previous research has demonstrated the utility of contrast-enhanced MRI in preclinical models to examine changes in BBB permeability and assess the impact of strategies to open the BBB [37-41]. It should be pointed out that the majority of these studies have focused on the BBB opening in the brain parenchyma. While a series of studies have explored ultrasound-induced BBB opening in glioblastoma [42-44], none of them have, to our knowledge, examined the potential of DCE-MRI to monitor irradiation-induced BBB opening in glioblastoma. In this study, we focused on assessing the ability of irradiation to improve the delivery of compounds into the tumor margins.

To achieve this objective, we compared the diffusion of BBB-impermeable agents into the brain parenchyma, for different irradiation doses.

The diffusion-MRI study allows us to assess the cytotoxic effects of irradiation by monitoring the Apparent Diffusion Coefficient (ADC). The results demonstrate a dose-dependent increase of the ADC, reflecting a decrease in cell density and indicating a cytotoxic response, especially at higher irradiation doses. This aligns with the expected response to irradiation [23].

Histological evaluation using Evans blue dye indicates a dose-dependent effect of irradiation on BBB integrity. Indeed, a significant increase in vascular leakage was observed for an irradiation dose of 5 Gy, followed by a significant reduction in leakage at higher irradiation doses (10 Gy and 15 Gy) (Figure 1). This suggests a complex relationship between irradiation dose and BBB disruption. We hypothesize that a low dose of irradiation will damage the tight junctions and endothelial cells without compromising the structural integrity of the vessel, resulting in an enhanced BBB permeability. However, with a higher dose of irradiation, cytotoxicity will be so intense for the endothelial cells that the vessel will be destroyed, leading to a reduction in perfusion and diffusion. The decrease in the diffusion of the contrast product in the brain parenchyma at high irradiation doses would therefore not be due to the BBB closing up but rather to the destruction of the vessel. We can also add to this study that the area accessible to EB was 2.26 times larger than the anatomic area in the control group (Figure 1). This suggests that the BBB is already permeable in regions surrounding the bulk tumor in the U-87MG mouse glioblastoma model.

In the MRI study, to determine the BBB permeability, we assessed the diffusion of a contrast agent outside the tumor area, as for the histological study, but here with gadolinium DOTA. To do so, we compared T_2-weighted images (corresponding to the anatomical image of the bulk tumor) and T_1-weighted images after Gd-DOTA administration (corresponding to areas accessible by the BBB-impermeable contrast agent). In the control group, the area accessible to Gd-DOTA visualized in the T_1-weighted images was 57% larger than the bulk area of the tumor seen in the T_2-weighted images (Figure 3). The area accessible to Gd-DOTA was not significantly altered for the irradiated mice whatever the dose of irradiation (Figure 3). Unlike the histological method, non-invasive MRI with Gd-DOTA appears unable to identify alterations in BBB permeability in adjacent tumor margins.

Regarding the DCE-MRI study, various models have been used to identify possible changes in hemodynamic parameters such as K^{trans}, K_{ep}, v_e, v_p, AUC60 and AU90 in the core and margins of the tumor. There were no significant changes in these parameters between control and irradiated

groups whatever the parameter studied, the model used or the area analyzed (Figure 4). Furthermore, we could have thought that with the Patlak model, which allows us to better assess a subtle change in BBB leakage of the poorly permeable tumor margin than with the extended Tofts model, we might have a slight different between tumor surface measured on the Patlak K^{trans} map and tumor surface measured on the extended Tofts model K^{trans} map. However, as shown in Figure 5, there is no significant difference between those tumor surface.

The disparate results observed between MRI and Evans Blue staining to assess the opening of the tumoral BBB could be attributed to fundamental differences in the molecular and distribution properties of the contrast agents used for each technique. Indeed, Evans blue (960 Da, molecular weight) is a fluorescent dye that binds to albumin, a plasma protein with a high molecular weight (68 kDa), whereas Gd-DOTA is a small hydrophilic complex (MW=580 Da). Thus, Evans blue bound to albumin can only cross the BBB when it is sufficiently compromised, whereas Gd-DOTA, because of its small size, can diffuse more easily into the brain parenchyma even through a weakly compromised BBB. As radiotherapy may damage the tight junctions between endothelial cells, we can assume that the observed change in permeability would be more pronounced for larger molecules (complex EB-albumin) than for smaller molecules (Gd-DOTA) that were already able to cross small fenestrations of the damaged tumoral BBB. Comparative studies have indeed reported differences in glioblastoma accumulation for small gadolinium complexes and radiolabeled albumin measured via PET [45]. These variations in results highlight the importance of selecting the right contrast agent depending on the specific objective of the BBB study. In future studies, it would be interesting to use Gd-based contrast agents with high affinity for albumin for the MRI method, such as gadobenate (Gd-BOPTA), which would better mimic the distribution behavior of Evans Blue.

In addition, it is important to note that the values recorded via histology or MRI cannot be superimposed. Indeed, the invasive nature of the histological method requires the sacrifice of animals and therefore the images obtained in control and treated groups came from different cohorts of animals, whereas the non-invasive MRI method enabled images measured longitudinally on the same animals to be obtained.

It is also essential to point out in this study that there are differences in sensitivity and resolution between the two approaches. Indeed, the optical fluorescence method demonstrates superior sensitivity in the detection of probes providing information on BBB permeability and offering significantly higher spatial resolution than the MRI technique.

V. REFERENCES

1. Stupp, R.; Mason, W.P.; van den Bent, M.J.; et al. Radiotherapy plus concomitant and adjuvant temozolomide for glioblastoma. *The New England Journal of Medicine* **2005**, *352*, 987-996, doi:10.1056/NEJMoa043330.
2. Omuro, A.; DeAngelis, L.M. Glioblastoma and other malignant gliomas: a clinical review. *JAMA* **2013**, *310*, 1842-1850, doi:10.1001/jama.2013.280319.
3. Cha, G.D.; Kang, T.; Baik, S.; et al. Advances in drug delivery technology for the treatment of glioblastoma multiforme. *J Control Release* **2020**, *328*, 350-367, doi:10.1016/j.jconrel.2020.09.002
4. Anjum, K.; Shagufta, B.I.; Abbas, S.Q.; et al. Current status and future therapeutic perspectives of glioblastoma multiforme (GBM) therapy: A review. *Biomed Pharmacother* **2017**, *92*, 681-689, doi:10.1016/j.biopha.2017.05.125.
5. Obermeier, B.; Daneman, R.; Ransohoff, R.M. Development, maintenance and disruption of the blood-brain barrier. *Nat Med* **2013**, *19*, 1584-1596, doi:10.1038/nm.3407.
6. Arvanitis, C.D.; Ferraro, G.B.; Jain, R.K. The blood-brain barrier and blood-tumour barrier in brain tumours and metastases. *Nat Rev Cancer* **2020**, *20*, 26-41, doi:10.1038/s41568-019-0205-x.
7. Lockman, P.R.; Mittapalli, R.K.; Taskar, K.S.; et al. Heterogeneous blood-tumor barrier permeability determines drug efficacy in experimental brain metastases of breast cancer. *Clin Cancer Res* **2010**, *16*, 5664-5678, doi:10.1158/1078-0432.Ccr-10-1564.
8. Osswald, M.; Blaes, J.; Liao, Y.; et al. Impact of Blood-Brain Barrier Integrity on Tumor Growth and Therapy Response in Brain Metastases. *Clin Cancer Res* **2016**, *22*, 6078-6087, doi:10.1158/1078-0432.Ccr-16-1327.
9. van Tellingen, O.; Yetkin-Arik, B.; de Gooijer, M.C.; et al. Overcoming the blood-brain tumor barrier for effective glioblastoma treatment. *Drug Resist Updat* **2015**, *19*, 1-12, doi:10.1016/j.drup.2015.02.002.
10. Gould, A.; Zhang, D.; Arrieta, V.A.; et al. Delivering albumin-bound paclitaxel across the blood-brain barrier for gliomas. *Oncotarget* **2021**, *12*, 2474-2475, doi:10.18632/oncotarget.28018.
11. van Vulpen, M.; Kal, H.B.; Taphoorn, M.J.; et al. Changes in blood-brain barrier permeability induced by radiotherapy: implications for timing of chemotherapy? (Review). *Oncol Rep* **2002**, *9*, 683-688.
12. Li, C.; Ke, S.; Wu, Q.P.; et al. Tumor irradiation enhances the tumor-specific distribution of poly(L-glutamic acid)-conjugated paclitaxel and its antitumor efficacy. *Clin Cancer Res* **2000**, *6*, 2829-2834.
13. Lammers, T.; Peschke, P.; Kühnlein, R.; et al. Effect of radiotherapy and hyperthermia on the tumor accumulation of HPMA copolymer-based drug delivery systems. *J Control Release* **2007**, *117*, 333-341, doi:10.1016/j.jconrel.2006.10.032.
14. Davies Cde, L.; Lundstrøm, L.M.; Frengen, J.; et al. Radiation improves the distribution and uptake of liposomal doxorubicin (caelyx) in human osteosarcoma xenografts. *Cancer Res* **2004**, *64*, 547-553, doi:10.1158/0008-5472.can-03-0576.
15. Hart, E.; Odé, Z.; Derieppe, M.P.P.; et al. Blood-brain barrier permeability following conventional photon radiotherapy - A systematic review and meta-analysis of clinical and preclinical studies. *Clin Transl Radiat Oncol* **2022**, *35*, 44-55, doi:10.1016/j.ctro.2022.04.013.

16. Erel-Akbaba, G.; Carvalho, L.A.; Tian, T.; et al. Radiation-Induced Targeted Nanoparticle-Based Gene Delivery for Brain Tumor Therapy. *ACS Nano* **2019**, *13*, 4028-4040, doi:10.1021/acsnano.8b08177.

17. Qin, D.; Ou, G.; Mo, H.; et al. Improved efficacy of chemotherapy for glioblastoma by radiation-induced opening of blood-brain barrier: clinical results. *Int J Radiat Oncol Biol Phys* **2001**, *51*, 959-962, doi:10.1016/s0360-3016(01)01735-7.

18. Conq, J.; Joudiou, N.; Ucakar, B.; et al. Assessment of Hyperosmolar Blood-Brain Barrier Opening in Glioblastoma via Histology with Evans Blue and DCE-MRI. *Biomedicines* **2023**, *11*, doi:10.3390/biomedicines11071957.

19. Shukla, G.; Alexander, G.S.; Bakas, S.; et al. Advanced magnetic resonance imaging in glioblastoma: a review. *Chin Clin Oncol* **2017**, *6*, 40, doi:10.21037/cco.2017.06.28.

20. Tofts, P.S.; Brix, G.; Buckley, D.L.; et al. Estimating kinetic parameters from dynamic contrast-enhanced T(1)-weighted MRI of a diffusable tracer: standardized quantities and symbols. *J Magn Reson Imaging* **1999**, *10*, 223-232, doi:10.1002/(sici)1522-2586(199909)10:3<223::aid-jmri2>3.0.co;2-s.

21. Heye, A.K.; Thrippleton, M.J.; Armitage, P.A.; et al. Tracer kinetic modelling for DCE-MRI quantification of subtle blood-brain barrier permeability. *Neuroimage* **2016**, *125*, 446-455, doi:10.1016/j.neuroimage.2015.10.018.

22. Tsien, C.; Cao, Y.; Chenevert, T. Clinical applications for diffusion magnetic resonance imaging in radiotherapy. *Semin Radiat Oncol* **2014**, *24*, 218-226, doi:10.1016/j.semradonc.2014.02.004.

23. Papaevangelou, E.; Almeida, G.S.; Jamin, Y.; et al. Diffusion-weighted MRI for imaging cell death after cytotoxic or apoptosis-inducing therapy. *Br J Cancer* **2015**, *112*, 1471-1479, doi:10.1038/bjc.2015.134.

24. Schmainda, K.M. Diffusion-weighted MRI as a biomarker for treatment response in glioma. *CNS Oncol* **2012**, *1*, 169-180, doi:10.2217/cns.12.25.

25. Ahishali, B.; Kaya, M. Evaluation of Blood-Brain Barrier Integrity Using Vascular Permeability Markers: Evans Blue, Sodium Fluorescein, Albumin-Alexa Fluor Conjugates, and Horseradish Peroxidase. *Methods Mol Biol* **2021**, *2367*, 87-103, doi:10.1007/7651_2020_316.

26. Bianco, J.; Bastiancich, C.; Joudiou, N.; et al. Novel model of orthotopic U-87 MG glioblastoma resection in athymic nude mice. *J Neurosc Methods* **2017**, *284*, 96-102, doi:10.1016/j.jneumeth.2017.04.019.

27. del Valle, J.; Camins, A.; Pallàs, M.; et al. A new method for determining blood-brain barrier integrity based on intracardiac perfusion of an Evans Blue-Hoechst cocktail. *J Neurosci Methods* **2008**, *174*, 42-49, doi:10.1016/j.jneumeth.2008.06.025.

28. Nicaise, C.; Mitrecic, D.; Demetter, P.; et al. Impaired blood-brain and blood-spinal cord barriers in mutant SOD1-linked ALS rat. *Brain Res* **2009**, *1301*, 152-162, doi:10.1016/j.brainres.2009.09.018.

29. Sourbron, S.P.; Buckley, D.L. Classic models for dynamic contrast-enhanced MRI. *NMR Biomed* **2013**, *26*, 1004-1027, doi:10.1002/nbm.2940.

30. Bankhead, P.; Loughrey, M.B.; Fernández, J.A.; et al. QuPath: Open source software for digital pathology image analysis. *Sci Rep* **2017**, *7*, 16878, doi:10.1038/s41598-017-17204-5.

31. Kane, J.R. The Role of Brain Vasculature in Glioblastoma. *Mol Neurobiol* **2019**, *56*, 6645-6653, doi:10.1007/s12035-019-1561-y.

32. Zhang, D.Y.; Dmello, C.; Chen, L.; et al. Ultrasound-mediated Delivery of Paclitaxel for Glioma: A Comparative Study of Distribution, Toxicity, and Efficacy of Albumin-bound Versus Cremophor Formulations. *Clin Cancer Res* **2020**, *26*, 477-486, doi:10.1158/1078-0432.Ccr-19-2182.

33. Gebhardt, B.J.; Dobelbower, M.C.; Ennis, W.H.; et al. Patterns of failure for glioblastoma multiforme following limited-margin radiation and concurrent temozolomide. *Radiat Oncol* **2014**, *9*, 130, doi:10.1186/1748-717x-9-130.

34. Dong, Q.; He, L.; Chen, L.; et al. Opening the Blood-Brain Barrier and Improving the Efficacy of Temozolomide Treatments of Glioblastoma Using Pulsed, Focused Ultrasound with a Microbubble Contrast Agent. *Biomed Res Int* **2018**, *2018*, 6501508, doi:10.1155/2018/6501508.

35. Stegmayr, C.; Oliveira, D.; Niemietz, N.; et al. Influence of Bevacizumab on Blood-Brain Barrier Permeability and O-(2-(18)F-Fluoroethyl)-l-Tyrosine Uptake in Rat Gliomas. *J Nucl Med* **2017**, *58*, 700-705, doi:10.2967/jnumed.116.187047.

36. Leten, C.; Struys, T.; Dresselaers, T.; et al. In vivo and ex vivo assessment of the blood brain barrier integrity in different glioblastoma animal models. *J Neurooncol* **2014**, *119*, 297-306, doi:10.1007/s11060-014-1514-2.

37. Chu, C.; Liu, G.; Janowski, M.; et al. Real-Time MRI Guidance for Reproducible Hyperosmolar Opening of the Blood-Brain Barrier in Mice. *Front Neurol* **2018**, *9*, 921, doi:10.3389/fneur.2018.00921.

38. Rhine, W.D.; Benaron, D.A.; Enzmann, D.R.; et al. Gd-DTPA MR detection of blood-brain barrier opening in rats after hyperosmotic shock. *J Comput Assist Tomogr* **1993**, *17*, 563-566, doi:10.1097/00004728-199307000-00008.

39. Blanchette, M.; Pellerin, M.; Tremblay, L.; et al. Real-time monitoring of gadolinium diethylenetriamine penta-acetic acid during osmotic blood-brain barrier disruption using magnetic resonance imaging in normal wistar rats. *Neurosurgery* **2009**, *65*, 344-350; discussion 350-341, doi:10.1227/01.Neu.0000349762.17256.9e.

40. Chang, K.W.; Hong, S.W.; Chang, W.S.; et al. Characteristics of Focused Ultrasound Mediated Blood-Brain Barrier Opening in Magnetic Resonance Images. *J Korean Neurosurg Soc* **2023**, *66*, 172-182, doi:10.3340/jkns.2022.0236.

41. Hersh, A.M.; Bhimreddy, M.; Weber-Levine, C.; et al. Applications of Focused Ultrasound for the Treatment of Glioblastoma: A New Frontier. *Cancers (Basel)* **2022**, *14*, doi:10.3390/cancers14194920.

42. Ahmed, M.H.; Hernández-Verdin, I.; Quissac, E.; et al. Low-Intensity Pulsed Ultrasound-Mediated Blood-Brain Barrier Opening Increases Anti-Programmed Death-Ligand 1 Delivery and Efficacy in Gl261 Mouse Model. *Pharmaceutics* **2023**, *15*, doi:10.3390/pharmaceutics15020455.

43. Wang, J.; Li, Z.; Pan, M.; et al. Ultrasound-mediated blood-brain barrier opening: An effective drug delivery system for theranostics of brain diseases. *Adv Drug Deliv Rev* **2022**, *190*, 114539, doi:10.1016/j.addr.2022.114539.

44. Coluccia, D.; Figueiredo, C.A.; Wu, M.Y.; et al. Enhancing glioblastoma treatment using cisplatin-gold-nanoparticle conjugates and targeted delivery with magnetic resonance-guided focused ultrasound. *Nanomedicine* **2018**, *14*, 1137-1148, doi:10.1016/j.nano.2018.01.021.

45. Brady, M.; Raghavan, R.; Sampson, J. Determinants of Intraparenchymal Infusion Distributions: Modeling and Analyses of Human Glioblastoma Trials. *Pharmaceutics* **2020**, *12*, doi:10.3390/pharmaceutics12090895.

CHAPTER V

CHANGES IN BBB PERMEABILITY IN GLIOBLASTOMA MODEL INDUCED BY THE ANTI-ANGIOGENIC AGENTS CEDIRANIB AND THALIDOMIDE

Adapted from **Conq J**, Joudiou N, Préat V, Gallez B. Changes in perfusion and permeability in glioblastoma model induced by the anti-angiogenic agents cediranib and thalidomide. Submitted

Abstract:

Glioblastoma is the most aggressive malignant brain tumor with a poor prognosis. The poor delivery of drugs to infiltrating tumor cells contributes to therapeutic failure. It has been suggested that, during the early phase of an anti-angiogenic treatment, a remodelling of the tumor vasculature could occur, leading to a more structured and functional vessel network that could enhance drug delivery. However, the restructuration of blood vessels could in turn increase the proportion of normal endothelial cells that could be a barrier for the free diffusion of drugs. The net balance, in favor or not, of a better delivery of compounds during the course of an antiangiogenic treatment remains to be established in glioblastoma. In the present study, we explored whether the anti-angiogenic agents cediranib and thalidomide could modulate perfusion and vessel permeability in the U87 tumor model implanted in the brain of mice. Cediranib and thalidomide effectively reduced tumor size over time. We focused on the dynamic evolution of the diffusion of agents outside the tumor core using the fluorescent dye Evans Blue in histology and Gd-DOTA using dynamic contrast-enhanced (DCE)-MRI. The accessibility of Evans Blue outside the tumor core continuously decreased over time. CD31 labelling of endothelial cells revealed that the vascular density was significantly decreased after treatment while the proportion of normal vessels remained unchanged over time. In contrast to histological studies, DCE-MRI did not tackle any significant change in hemodynamic parameters, in the core or margins of the tumor, whatever the parameter used (K^{trans}, k_{ep}, v_p, v_e, AUC60, AUC90) or the pharmacokinetic model used (Tofts or Patlak). In conclusion, in the U87 model, cediranib and thalidomide were effective in decreasing the tumor size, but ineffective in transiently increasing the delivery of agents in the core and the margins of the tumor.

Keywords: blood–brain barrier; perfusion; permeability; glioblastoma; anti-angiogenic treatment; DCE-MRI; Evans blue

TABLE OF CONTENTS

I. INTRODUCTION

Glioblastoma (GB) is the most aggressive and common malignant primary brain tumor in adults, accounting for more than 50% of all gliomas. Despite an aggressive treatment involving surgical resection (when possible) followed by concurrent radiotherapy/chemotherapy, prognosis for patients with GB remains poor, with a relapse almost inevitable and a median overall survival of around 10 to 16 months post-diagnosis [1-4]. GB is characterized by a rapid growth, a high degree of cellular and genetic heterogeneity, high infiltrative properties and high angiogenic activity due to excessive levels of pro-angiogenic factors such as members of the vascular endothelial growth factor (VEGF) family [5,6]. Tumor angiogenesis leads to abnormal tumor vessels that present a tortuous and disorganized structure preventing a proper delivery of the anti-cancer drugs to the tumor site [7,8]. Another factor that may impair the delivery of chemotherapeutic agents is the blood-brain barrier (BBB). In physiological conditions, the brain vasculature is a highly specialized interface involving three main cell types: endothelial cells, astrocytes, and pericytes. Together, they form and regulate the BBB, which selectively permits the exchange of molecules between the intra-cerebral system and the rest of the body [9]. In GB, even though the BBB is often compromised in the tumor core, the highly permeable leaky vessels contribute to a high interstitial fluid pressure and an impaired delivery of drugs [10-14]. Of note, the BBB generally remains intact or is only slightly compromised in the tumor margins, significantly limiting the passage of drugs to reach the infiltrating tumor cells that will be at the origin of the tumor recurrence [10,13-15].

Innovative strategies are emerging to face the problem of impaired drug delivery, including appropriate use of anti-angiogenic treatments that were originally developed to starve tumors. It has been suggested that, during the early phase of an anti-angiogenic treatment, a transient effect of tumor vessels normalization could occur with an improvement in the delivery of anticancer drugs administered during this normalization window [16-20]. The pruning of immature vessels could lead to a remodelling of the tumor vasculature, making it more structured and functional, leading to an improvement in blood perfusion as well as a decrease in tumor hypoxia and intra-tumoral pressure [21-24]. The increase in blood perfusion would increase the supply of anti-cancer drugs at the blood-tumor interface and the decrease in intra-tumoral pressure would facilitate their penetration into the tumor. However, the restructuration of blood vessels could result in an increase in the proportion of normal endothelial cells that could in turn be a barrier for the free diffusion of drugs. The net balance, in favour or not, of a better delivery of compounds in the core and the margins of the tumors, during the course of an antiangiogenic treatment, remains to be established.

In this work, we evaluated whether an anti-angiogenic treatment could alter hemodynamic parameters and the distribution of compounds in the core and the margins of the GB tumor model U87. This model was selected because it presents a well-delineated bulky tumor core, facilitating the analysis of perfusion/permeability in the core and in the margins of the tumor (where infiltrative cells may be present). For this purpose, we used two different antiangiogenic agents, cediranib and thalidomide, that were previously investigated for a potential normalization effect at an early stage of treatment [21,25-28]. Our analysis included a time-dependent evolution of hemodynamics as the normalization time window could be transient after the initiation of the treatment. We performed a histological analysis with a focus on the capability of the Evans Blue dye to diffuse outside the tumor core and to reach the margins of the tumors. Evans blue, a fluorescent marker of vascular leakage, was used to assess the functionality of the blood-brain barrier [29]. This dye forms a tight bond with the plasma protein, albumin, in the bloodstream. Albumin, under normal circumstances, is too large to cross the intact blood-brain barrier. However, in the event of disruption of the BBB, Evans Blue bound to albumin could penetrate the brain parenchyma. The studies were completed by non-invasive DCE-MRI studies to investigate the possibility of this technology to tackle subtle changes in tumor hemodynamics that could be induced by antiangiogenic agents. Studies were completed by immunohistochemistry with the endothelial cell marker CD31 (also known as PECAM-1 or Platelet Endothelial Cell Adhesion Molecule-1), a transmembrane glycoprotein expressed by endothelial cells to assess the evolution of vascular density and vascular integrity in the tumor [30-32].

II. MATERIALS AND METHODS

II.1. ORTHOTOPIC U-87MG MOUSE MODEL

All experiments were performed in accordance with the European Directive 2010/63/EU and following the Belgian national regulation guidelines, and were approved by the ethical committee for animal care by the Faculty of Medicine of the UCLouvain (2019/UCL/MD/004). Water and food were given ad libitum. Animal body weight was constantly monitored throughout the experiment.

Six-week-old female NMRI nude mice (Janvier, France) were anesthetized via intraperitoneal injection of ketamine/xylazine (100 and 13 mg/kg, respectively) and fixed on a stereotaxic frame. In 2 μL of Eagle's Minimum Essential Medium (EMEM) (Gibco™, ThermoFisher Scientific, Waltham, MA, USA), 4×10^4 cells of U-87MG (ATCC) were injected into the right frontal lobe using an infusion syringe pump (Harvard Apparatus, Holliston, MA, USA) mounted with a

Hamilton syringe (26S gauge needle). The injection coordinates were 2.1 mm lateral and 0.5 mm posterior from the bregma, and 2.6 mm deep from the outer border of the cranium [33,34]. The tumor size monitoring was performed via MRI (see Section 2.3).

II.2. ANTI-ANGIOGENIC TREATMENT PROTOCOL

When the tumor size reached 7 ± 1 mm^3, treatment was started with either cediranib (Hölzel Biotech, Köln, Germany), racemic thalidomide (Sigma-Aldrich, Saint Louis, MO, USA) or saline (control). Cediranib was administered via oral gavage at the dose of 6 mg/kg each day [35]. Thalidomide was administered intraperitoneally at a dose of 200 mg/kg each day [16,21].

II.3. MRI

MRI was performed using an 11.7 T Bruker Biospec MRI system (Bruker, Ettlingen, Germany) equipped with a ^1H quadrature transmit/receive birdcage coil (21 mm inner diameter, RAPID Biomedical, Rimpar, Germany). Mice were anesthetized with isoflurane mixed with air (2.5% for induction, 1.5% for maintenance). Animals were covered with a heating blanket and their temperature was monitored. A pressure pad was used to monitor the respiration rate.

Anatomical images were obtained using T_2-weighted rapid acquisition with a refocused echo (RARE) sequence (echo time = 30 ms; repetition time = 2500 ms; number of slices = 25; field of view = 20 mm × 20 mm; matrix size = 200 × 200; resolution = 0.1 mm × 0.1 mm; slice thickness = 0.3 mm; acquisition time = 5 min 20 s; averages = 8). Tumor volume was determined from a manually drawn region of interest (ROI) using Paravision 6.0.1 software (Bruker BioSpin) on day 14 following tumor induction, and then daily until the tumor size reached 7 ± 1 mm^3. After that, anatomical image acquisitions were performed on day 0, day 2, day 4 and day 6 after the beginning of the treatment.

For DCE-MRI acquisition, T_1-weighted gradient echo images were obtained via a fast low-angle shot (FLASH) sequence (echo time = 1.4 ms; repetition time = 11.719 ms; flip angle = 10.0°; field of view = 20 mm × 20 mm; matrix size = 128 × 128; resolution = 0.156 mm × 0.156 mm; slice thickness = 0.9 mm; averages = 1; total acquisition time = 22 min 40 s). A set of 450 scans with a temporal resolution of 3.02 s was acquired, with Gd-DOTA (Dotarem® 0.5 mol/mL; Guerbet, Villepinte, France) administered intravenously at a dose of 0.29 mmol/kg after the 10th scan over 5 s. DCE-MRI acquisitions were performed on day 0, day 2, day 4 and day 6 after the beginning of the treatment.

II.4. HISTOLOGY AND IMMUNOHISTOCHEMISTRY

Evans blue dye (EB: 2% in normal saline; Alfa Aesar, Haverhill, MA, USA) was intravenously injected (3 mL/kg) on day 0, day 2, day 4 or day 6 after the beginning of the treatment. Thirty minutes later, the mice were euthanized and intracardially perfused with paraformaldehyde (PFA) 4% to discard all the remaining dye in the blood vessels and fix the tissue. Brains were then removed, fixed overnight in PFA 4%, cryoprotected in sucrose 20%, included in optimal cutting temperature compound (OCT, Sakura Finetek, Alphen aan den Rijn, The Netherlands), and kept at −80 °C. Cryostat 30 μm sections were counterstained with diamidino-2-phenylindole (DAPI, Thermofisher, Waltham, MA, USA) and immunohistologically stained with an antibody against CD31.

For the immunostaining, slides were subjected to antigen retrieval by heating at 98 °C for 30 min in 10 mM citrate buffer (pH 5.7). Endogenous peroxidases were inhibited using 1% H_2O_2 and non-specific antigenic sites were neutralized with 5%BSA/TBS/Tween solution. Between all the consecutive steps of the staining procedure, sections were rinsed three times for 3 min in TBS/Tween solution. Primary rabbit anti-mouse CD31 antibody (Cell Signaling Technology, Danvers, MA, USA) diluted 1/150 in 1%BSA/TBS/Tween solution was applied to sections overnight at 4°C. Next, the sections were incubated at room temperature for 40 min with a secondary anti-rabbit antibody (Agilent, Belgium). The slides were then incubated for tyramide signal amplification with Alexa Fluor 488-tyramide reagent (Invitrogen™, ThermoFisher Scientific, UK) diluted 1/200 in 0.1M borate buffer (pH 7.8) supplemented with 0.003% H_2O_2, for 10 min at room temperature. Finally, coverslips were mounted with a DAKO fluorescence mounting medium (Agilent, Belgium).

The brain sections were then scanned under a fluorescence microscope slide scanner (Panoramic 250 Flash III, 3DHistech, Budapest, Hungary) with DAPI, Fluorescein Isothiocyanate (FITC) and Cyanine 5 (Cy5) filters [36,37].

II.5. IMAGE PROCESSING

DCE-MRI data were analysed using in-house software written in Matlab (version 9.6). Regions of interest (ROIs) were manually delineated. We considered ROI T_1 as the delineation of the entire tumor area using T_1-weighted images with Gd-DOTA as the contrast agent, ROI T_2 as the delineation of the tumor bulk area using T_2-weighted anatomical images, and ROI Delta as the ROI T_1 from which we subtracted ROI T_2 in order to cover the margins of the tumor. In this way, we

were able to study the hemodynamic parameters for the whole tumor region but also for the margins of the tumor as previously described [34].

The hemodynamic parameters were computed using two different pharmacokinetics models. The first one is the extended Tofts model [38] which is a two-compartmental model that describes a highly perfused tissue, as found in glioblastoma tumors, considering bidirectional transport between the blood plasma and the extracellular extravascular space (EES). The equation of this model is given by:

$$C_t(t) = v_p \cdot C_p(t) + K^{trans} \int_0^t C_p(\tau) e^{-k_{ep}(t-\tau)} d\tau \quad (1)$$

where K^{trans} is the volume transfer constant between blood plasma and EES [min^{-1}], v_p is the blood plasma volume per unit volume of tissue, and k_{ep} is the flux rate constant between EES and blood plasma [min^{-1}] [39]. V_e is the EES volume per unit volume of tissue, calculated as follows:

$$v_e = K^{trans}/k_{ep} \quad (2)$$

The second pharmacokinetic model used is the Patlak model [40]. This model is comparable to the extended Tofts model but it ignores the backflux from the EES into the blood plasma compartment. Consequently, it only allows for the estimation of the two parameters K^{trans} and v_p. The equation of this model is given by:

$$C_t(t) = v_p \cdot C_p(t) + K^{trans} \int_0^t C_p(\tau) d\tau \quad (3)$$

We were also interested in AUC60 and AUC90 corresponding to the area under the curve (AUC) of contrast agent concentration as a function of time from 0 to 60 or to 90 s.

Histological images were analysed using Qupath (version 0.3.2) [41]. The tumor ROI and the Evans blue diffusion ROI were manually delineated. Tumor vessel density quantification and the percentage of vessels with intact endothelial linings were counted manually.

II.6. STATISTICAL ANALYSES

Data are represented as means ± standard deviation (SD). All experiments were performed in triplicate or more. Two-way ANOVA tests (Tukey's test) and t-tests were performed using

GraphPad Prism (version 9.1.2), with p-values < 0.05 (*), $p < 0.01$ (**), $p < 0.001$ (***), and $p < 0.0001$ (****) considered as the levels of significance.

III. RESULTS

III.1. HISTOLOGICAL STUDIES

Perfusion and permeability were assessed by perfusing mice with EB dye, a fluorescent vascular leakage marker. The area accessible to the EB dye is larger than the tumor bulk area as measured using DAPI (Figure 1A). On the brain sections of mice treated with anti-angiogenic agents, the fluorescent dye diffused less largely outside of the tumor area in mice treated with antiangiogenic agents compared to the untreated mice (Figure 1A and 1B). On day 6 after the start of the treatment, there was a significant decrease in the EB stained/tumor surface ratio for mice treated with cediranib (1.59 ± 0.11, mean ± SD, $n = 4$, $p < 0.01$) and thalidomide (1.74 ± 0.11, mean ± SD, $n = 4$, $p < 0.05$), compared to the control group (2.16 ± 0.15, mean ± SD, $n = 4$). This result suggests either a decrease in vessel permeability, or a destruction of tumor vessels and a consequent decrease in tumor perfusion.

The evolution of tumor size between treated and untreated mice was also studied on brain sections. The tumor size was significantly decreased after 6 days of treatment in mice treated with cediranib (8.51 ± 2.19 mm^2, mean ± SD, $n = 4$, $p < 0.001$) and thalidomide (9.71 ± 1.29 mm^2, mean ± SD, $n = 4$, $p < 0.01$) compared to untreated mice (15.48 ± 3.55 mm^2, mean ± SD, $n = 4$) (Figure 1C).

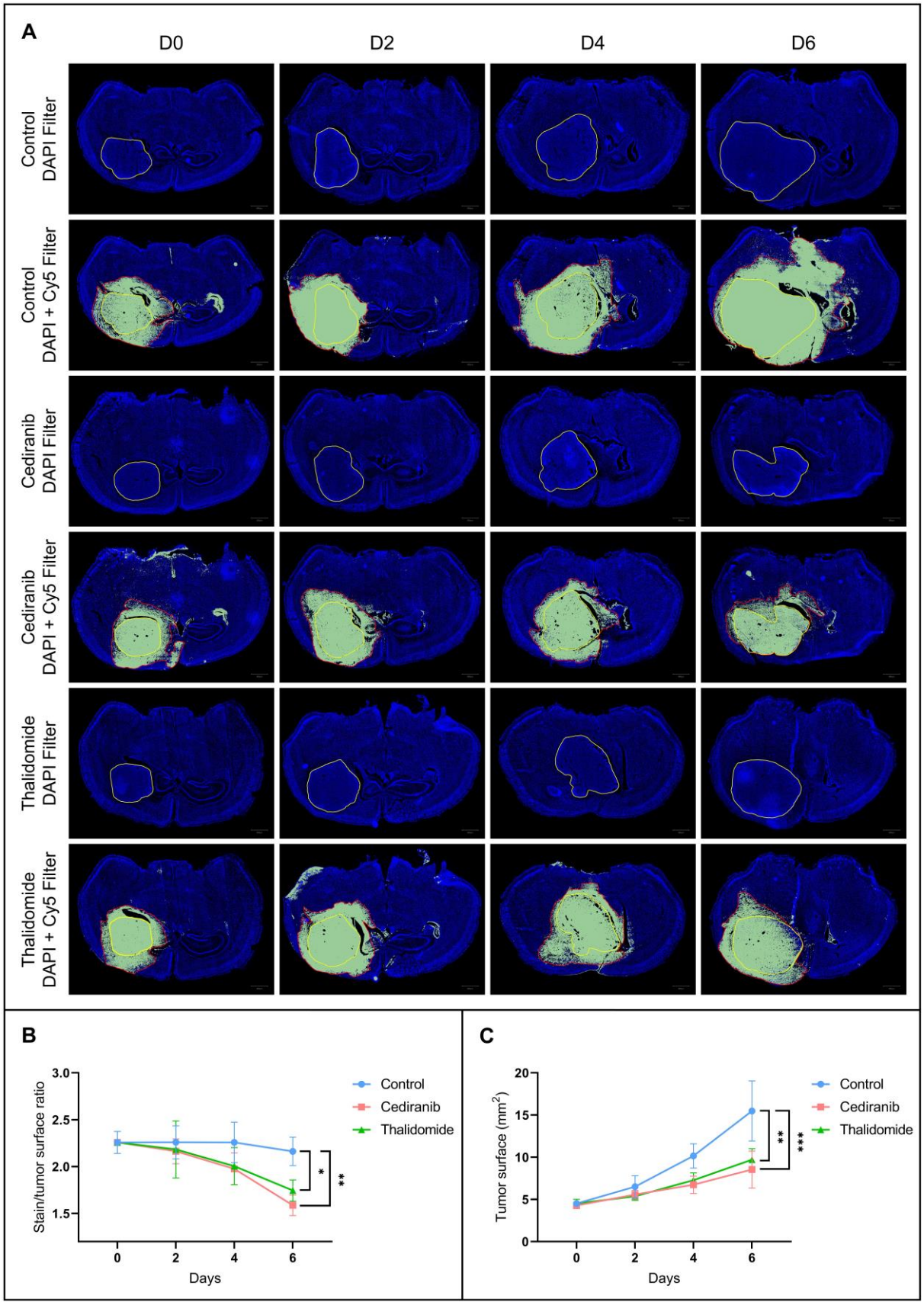

Figure 1. Histological analyses. (**A**) Representative histological images of brain sections from control mice (*n = 4*) and mice treated with cediranib (6 mg/kg/day, p.o., *n = 4)* and thalidomide (200 mg/kg/day i.p., *n = 4)* on day 0, 2, 4 and 6 after the beginning of the treatment. The use of DAPI filter allows the delineation of tumor area (yellow delineation).

The use of Cy5 filter allows the delineation of areas accessible to the Evans Blue dye (delineation in red). (**B**) Evolution over time of the diffusion of the Evans Blue outside the tumor core. Compared to the untreated group, the fluorescent dye diffused less widely outside the tumor area in mice treated with cediranib and thalidomide. (**C**) Evolution over time of the tumor size. The tumor size was significantly decreased in both groups treated with anti-angiogenic agents compared to the untreated group. The results are expressed as means ± SD. * *p*-values < 0.05, ** $p < 0.01$, *** $p < 0.001$, two-way ANOVA tests (Tukey's test).

In addition, tumor angiogenesis was assessed by immunochemistry with CD31 labelling, providing parameters for vascular density and vascular integrity (Figure 2A-D). The vascular density significantly decreased on day 6 for mice treated with cediranib (266 ± 53 vessels/mm^2, mean ± SD, $n = 4$, $p < 0.001$) and thalidomide (296 ± 33 vessels/mm^2, mean ± SD, $n = 4$, $p < 0.01$) compared to untreated mice (408 ± 39 vessels/mm^2, mean ± SD, $n = 4$) (Figure 2B). We studied the percentage of vessels with continuous endothelial linings, as marker of vascular integrity (Figure 2C). We did not observe any significant difference ($p > 0.05$) in the proportion of vessels presenting vascular integrity between the control group ($n = 4$) and groups receiving cediranib ($n = 4$) or thalidomide ($n = 4$), whatever the day studied (Figure 2D).

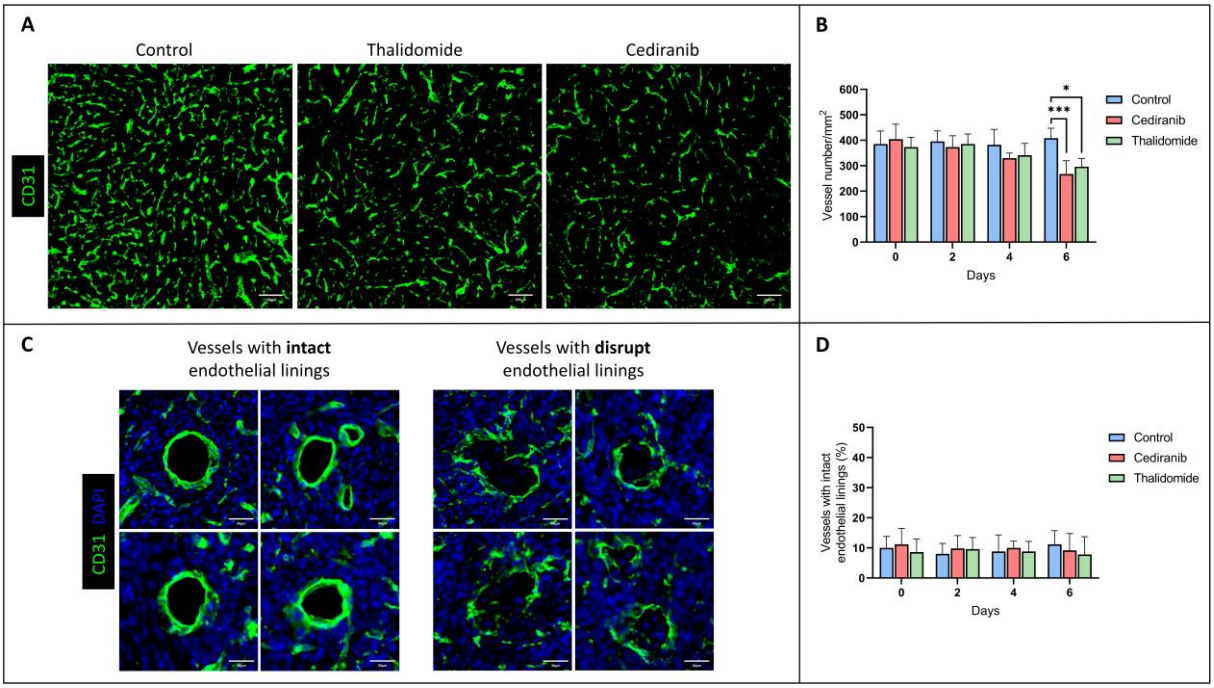

Figure 2. Assessment of tumor vascularity using immune-histological staining for the endothelial cell marker CD31. (**A**) Representative histological images of brain sections with CD31 labelling from control mice ($n = 4$) and mice treated with cediranib ($n = 4$) and thalidomide ($n = 4$) on day 6 after starting the treatment. (**B**) Evolution of vascular density over time in control, cediranib and thalidomide treated mice. The vascular density significantly decreased on day 6 for mice treated with anti-angiogenic agents compared to the control group. (**C**) Illustration of vessels with intact and disrupted endothelial linings in brain sections with CD31 labelling. (**D**) Percentage of tumor vessels with intact endothelial linings over time for the control group and groups treated with cediranib and thalidomide. There was no significant difference in the vascular integrity between treated and untreated groups, whatever the day studied. The results are expressed as means ± SD. * *p*-values < 0.05, *** $p < 0.001$, two-way ANOVA tests (Tukey's test).

III.2. MRI STUDIES

III.2.1. Diffusion of Gd-DOTA outside the tumor core

The diffusion of the contrast agent Gd-DOTA outside of the tumor was evaluated by comparing the T_2-weighted images, corresponding to the anatomical delineation of the tumor core, and T_1-weighted images corresponding to the area in which the contrast agent was able to diffuse (Figure 3A) [34]. For all tumors, we observed leakage of the contrast agent outside the tumor core, indicating a high permeability of the vessels and/or a non-integrity of the BBB. There was no significant difference ($p > 0.05$) between the T_1/T_2 surface ratio of mice treated with cediranib or with thalidomide compared to the untreated group, whatever the day studied. The analysis of T_2-weighted images also revealed that the tumor volume evolved differently in the different groups, with a significantly smaller tumor volume from day 4 for mice treated with cediranib (15.81 ± 5.51 mm^3, mean ± SD, $n = 7$, $p < 0.001$) compared to control mice (29.01 ± 8.29 mm^3, mean ± SD, $n = 8$) and from day 6 for mice treated with thalidomide (30.88 ± 10.08 mm^3, mean ± SD, $n = 7$, $p < 0.0001$) compared to control mice (57.09 ± 14.32 mm^3, mean ± SD) with an even more significant difference on day 6 for mice treated with cediranib (24.94 ± 13.78 mm^3, mean ± SD, $p < 0.0001$). The decrease in tumor size observed by MRI was consistent with the changes observed by histology.

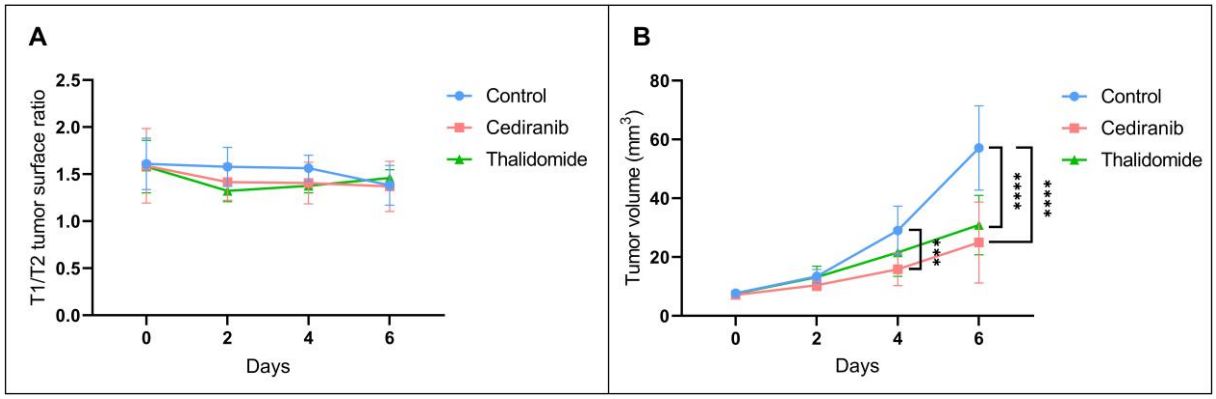

Figure 3. Evolution over time of the diffusion of the contrast agent Gd-DOTA outside the tumor core and of the tumor volume evolution using MRI. (**A**) Ratio between the T_1 and T_2 surface areas reflecting the diffusion of the contrast agent outside the tumor core over time. Measurements were performed on day 0, 2, 4 and 6 after the beginning of the treatment for control mice (blue, $n = 8$) and mice treated with cediranib (red, $n = 7$) and thalidomide (green, $n = 7$). No significant difference was observed between the different groups. (**B**) Evolution of tumor size over time. Compared to the control group, the tumor size was significantly lower from day 4 for mice treated with cediranib and from day 6 for mice treated with thalidomide compared to the untreated mice. The results are expressed as means ± SD. *** p-values < 0.001, **** $p < 0.0001$, two-way ANOVA tests (Tukey's test).

III.2.2. Hemodynamic parameters assessed by DCE-MRI

To further investigate perfusion/permeability, we performed DCE-MRI to provide hemodynamic parameters including the contrast agent efflux transfer constant (K^{trans}), the contrast agent reflux transfer constant (K_{ep}), the intravascular volume fraction (v_p), the extravascular volume fraction (v_e), and the area under the curve of contrast agent concentration as a function of time from 0 to 60 or 90 s (AUC60 and AUC90, respectively) (Figure 4). These parameters were computed using two different pharmacokinetic models: the extended Tofts model [38] and the Patlak model [40]. The extended Tofts model is a two-compartmental model widely used in the literature for studying tumor perfusion/permeability in glioblastoma. The Patlak model is comparable to the extended Tofts model but ignores the backflux and is therefore adapted to assess changes for a low-level BBB permeability where backflux is negligible, as found especially in the margins of glioblastoma tumors. The hemodynamic parameters were analysed in two different regions of interest (ROIs) of the tumor: the ROI T_1 corresponding to the whole tumor region, and the ROI Delta corresponding to the margin tumor area. We did not observe any significant difference in the tumor hemodynamic parameters between the control group (*n = 8*) and groups receiving cediranib (*n = 7*) or thalidomide (*n = 7*), whatever the studied parameter (K^{trans}, k_{ep}, v_p, v_e), pharmacokinetic model and ROI (whole tumor or margins) used (Figure 4).

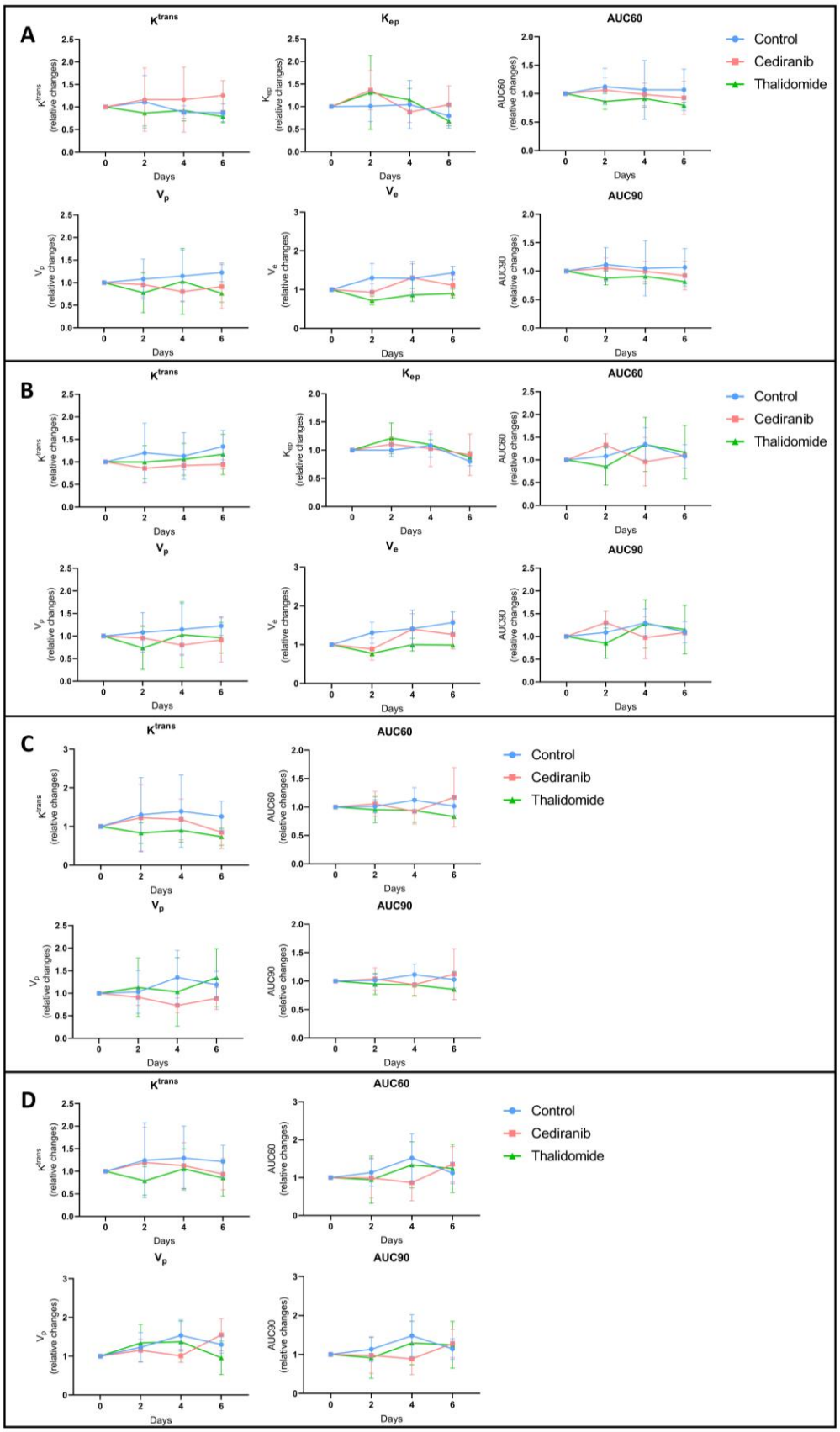

Figure 4. Hemodynamic parameters measured by DCE-MRI. Relative changes in tumor hemodynamic parameters between control group (blue), mice treated with cediranib (red), and mice treated with thalidomide (green). (**A**) Parameters computed with Extended Tofts model using ROI T_1, corresponding to the whole tumor area. (**B**)

Parameters computed with Extended Tofts model using ROI Delta corresponding to the margin tumor area. (**C**) Parameters computed with Patlak model using ROI T_1, corresponding to the whole tumor area. (**D**) Parameters computed with Patlak model using ROI Delta. DCE-MRI acquisitions were performed just before the beginning of the treatment (day 0), and on day 2, 4 and 6 after starting the treatment. There was no significant difference in the tumor hemodynamic parameters between control group ($n = 8$) and groups receiving cediranib ($n = 7$) or thalidomide ($n = 7$), whatever the studied parameter, ROI and model used. The results are expressed as means ± SD.

We also compared the K^{trans} parametric maps generated by the extended Tofts model and the Patlak model (Figure 5). We calculated the ratio between the area accessible to the contrast agent using the K^{trans} map from the extended Tofts model and the one measured using the Patlak model. We observed that this ratio was very close to 1, whatever the treatment taken the day after the beginning of the treatment. There was, therefore, no significant difference between tumor surface areas measured on K^{trans} maps obtained with the extended Tofts model and those obtained with the Patlak model (Figure 5).

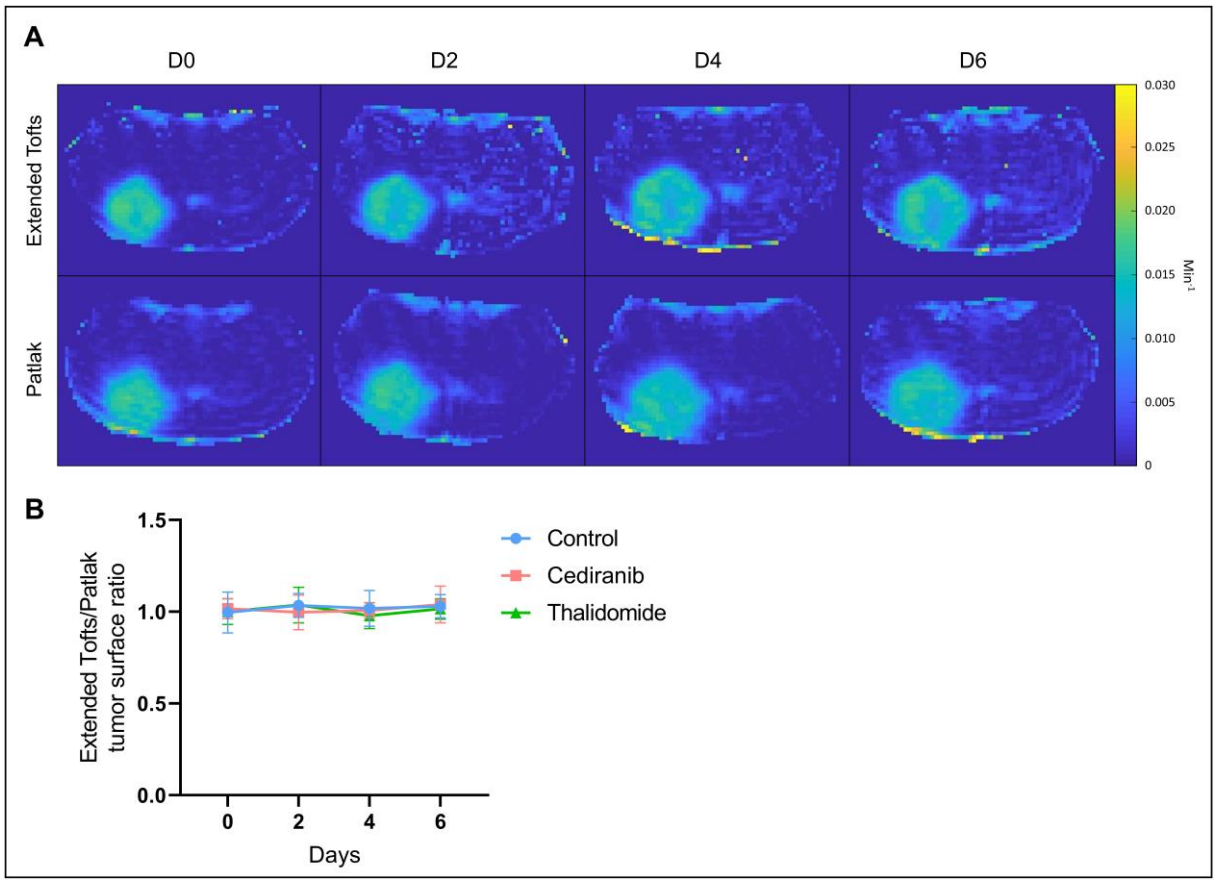

Figure 5. Comparison between K^{trans} parametric maps generated by the extended Tofts model and the Patlak model. (**A**) Illustrative K^{trans} maps obtained from cediranib treated mouse computed using extended Tofts model (top row) or Patlak model (bottom row). (**B**) Ratio between the area accessible to the contrast agent using the K^{trans} map from the extended Tofts model and the one measured using the Patlak model. No significant difference was observed over time between these areas. The results are expressed as means ± SD.

IV. DISCUSSION

Treating glioblastoma presents a unique challenge in oncology. In addition to many other factors, the poor delivery of drugs to infiltrating tumor cells contributes to therapeutic failure [13,14,42]. In this context, strategies to open the BBB and/or increase the drug diffusion inside and outside the tumor core are actively investigated. The use of anti-angiogenic agents to normalize tumor vessels has been suggested as an innovative strategy to improve the delivery of anti-cancer agents in GB [16-20]. Theoretically, pruning the most immature vessels should result in a more efficient perfusion. In turn, as the immature vessels coming from angiogenesis are known to offer large fenestrations, their elimination could decrease the permeability and hamper the diffusion of compounds. To establish the resulting balance, we evaluated the distribution of Evans Blue, a marker that integrates both perfusion and permeability. As Evans Blue avidly binds to albumin, it may diffuse in a tissue only if this tissue is perfused and if the vessels are sufficiently permeable, either because the BBB is compromised or because present in regions rich in immature vessels. Even though both treatments (cediranib and thalidomide) were efficient in decreasing the tumor size, contrary to our expectation, we did not observe any increase, even transient, in the diffusion of this marker outside the tumor core during treatment. On the contrary, the stained surface by this marker continuously and significantly decreased over time for treated animals compared to untreated animals (Figure 2). This decrease in Evans Blue extravasation could be due to either a refenestration of the BBB during normalization (with a reduction in the size of the pores between the endothelial cells during vascular restructuring), or a decrease in vessel density due to the antiangiogenic effect, decreasing the amount of Evans Blue able to diffuse into the brain parenchyma. The discrimination between both aspects was clarified by the results obtained using immunochemistry with CD31. We observed a significant decrease in the number of vessels for mice that were treated with anti-angiogenic agents (Figure 2). On day 6, we measured a significantly lower number of vessels in histological sections coming from treated mice compared to untreated mice (Figure 2B). Importantly, we did not observe a significant change over time in the proportion of vessels displaying vascular integrity whatever the anti-angiogenic agent used or the day studied, with the percentage of vessels with intact endothelial linings remaining around 10% (Figure 2D). Together, the decrease in diffusion of the dye outside the tumor core and the decrease in tumor vascular density with unchanged vascular integrity, pleads for a pruning of vasculature without any obvious normalising effect. We may wonder why we did not observe any normalization window in the early phase of the treatment. Thalidomide and cediranib were previously suggested to offer a normalization window [21,25-28]. Because the normalization has been reported to be dose- and time-dependent, we used the same dose and scheme of treatment than in other studies [16,21,35]. Even though we performed

histological and MRI analyses every two days, we were unable to demonstrate any transient increase in contrast agent (Evans Blue or Gd-DOTA) uptake inside and outside the tumor core. This normalization effect could likely depend on the tumor model used. We initially thought the U87 GB model was appropriate because we previously used this model to monitor changes in permeability induced by osmotic shock [34]. In the future, it could be interesting to analyse these effects in other glioblastoma models. It could be also interesting to analyse hemodynamics changes every day instead of every other day so as not to miss a possible increase in the delivery of agents.

Lessons from the MRI study also deserve commentary. Contrary to histological studies, MRI is fully non-invasive and could potentially be used as a marker of early changes in hemodynamic parameters that could be translated in patients for guiding treatment. A significant decrease in tumor size over time was observed for mice treated with cediranib and thalidomide, indicating the efficacy of those treatments. The MRI results are fully consistent with those obtained by histology. However, none of the parameters tested, K^{trans}, k_{ep}, v_e, v_p, AUC60 and AUC90, in the core and margins of the tumor, were significantly modified during the course of treatments using cediranib or thalidomide compared to untreated mice (Figures 4-5). By analysing many different parameters, we hypothesized that DCE-MRI could provide more information about subtle changes linked to perfusion and permeability. As none of the parameters changed, we cannot conclude about real hemodynamic changes induced by the treatments on the sole basis of MRI. We may wonder why DCE-MRI (with Gd-DOTA) did not provide the same results as histology (with Evans Blue) regarding the ability of the marker to diffuse outside the tumor core. Indeed, histology suggested a decreased ability to diffuse outside the tumor core while no change in diffusion outside the tumor core was found in MRI. The disparate results observed between MRI and Evans Blue staining to assess vessel permeability could likely be attributed to fundamental differences in the molecular and distribution properties of the contrast agents used for each technique. Indeed, Evans blue (960 Da, molecular weight) is a fluorescent dye that binds to albumin, a plasma protein with a high molecular weight (68 kDa), whereas Gd-DOTA is a small hydrophilic complex (MW=580 Da). As Evans blue is bound to albumin, it can only cross highly permeable vessels (i.e. in areas with compromised BBB or area rich in immature vessels coming from angiogenesis. In turn, Gd-DOTA, because of its small size, can diffuse more easily into the brain parenchyma even through a weakly compromised BBB. Focusing on the tight junctions between endothelial cells, we can assume that the observed change in permeability would be more pronounced for larger molecules (complex Evans Blue - albumin) than for smaller molecules (Gd-DOTA) that were already able to cross small fenestrations of the damaged tumoral BBB. In future studies, it would be interesting to

use Gd-based contrast agents with high affinity for albumin for the MRI method, such as gadobenate (Gd-BOPTA), which would better mimic the distribution behavior of Evans Blue.

V. REFERENCES

1. Stupp, R.; Mason, W.P.; van den Bent, M.J.; et al. Radiotherapy plus concomitant and adjuvant temozolomide for glioblastoma. *The New England Journal of Medicine* **2005**, *352*, 987-996, doi:10.1056/NEJMoa043330.
2. Omuro, A.; DeAngelis, L.M. Glioblastoma and other malignant gliomas: a clinical review. *JAMA* **2013**, *310*, 1842-1850, doi:10.1001/jama.2013.280319.
3. Cha, G.D.; Kang, T.; Baik, S.; et al. Advances in drug delivery technology for the treatment of glioblastoma multiforme. *J Control Release* **2020**, *328*, 350-367, doi:10.1016/j.jconrel.2020.09.002
4. Gately, L.; McLachlan, S.A.; Philip, J.; et al. Long-term survivors of glioblastoma: a closer look. *J Neurooncol* **2018**, *136*, 155-162, doi:10.1007/s11060-017-2635-1.
5. Anjum, K.; Shagufta, B.I.; Abbas, S.Q.; et al. Current status and future therapeutic perspectives of glioblastoma multiforme (GBM) therapy: A review. *Biomed Pharmacother* **2017**, *92*, 681-689, doi:10.1016/j.biopha.2017.05.125.
6. Urbańska, K.; Sokołowska, J.; Szmidt, M.; et al. Glioblastoma multiforme - an overview. *Contemp Oncol (Pozn)* **2014**, *18*, 307-312, doi:10.5114/wo.2014.40559.
7. Brighi, C.; Puttick, S.; Rose, S.; et al. The potential for remodelling the tumour vasculature in glioblastoma. *Adv Drug Deliv Rev* **2018**, *136-137*, 49-61, doi:10.1016/j.addr.2018.10.001.
8. Stylianopoulos, T.; Munn, L.L.; Jain, R.K. Reengineering the Tumor Vasculature: Improving Drug Delivery and Efficacy. *Trends Cancer* **2018**, *4*, 258-259, doi:10.1016/j.trecan.2018.02.010.
9. Obermeier, B.; Daneman, R.; Ransohoff, R.M. Development, maintenance and disruption of the blood-brain barrier. *Nat Med* **2013**, *19*, 1584-1596, doi:10.1038/nm.3407.
10. Arvanitis, C.D.; Ferraro, G.B.; Jain, R.K. The blood-brain barrier and blood-tumour barrier in brain tumours and metastases. *Nat Rev Cancer* **2020**, *20*, 26-41, doi:10.1038/s41568-019-0205-x.
11. Lockman, P.R.; Mittapalli, R.K.; Taskar, K.S.; et al. Heterogeneous blood-tumor barrier permeability determines drug efficacy in experimental brain metastases of breast cancer. *Clin Cancer Res* **2010**, *16*, 5664-5678, doi:10.1158/1078-0432.Ccr-10-1564.
12. Osswald, M.; Blaes, J.; Liao, Y.; et al. Impact of Blood-Brain Barrier Integrity on Tumor Growth and Therapy Response in Brain Metastases. *Clin Cancer Res* **2016**, *22*, 6078-6087, doi:10.1158/1078-0432.Ccr-16-1327.
13. van Tellingen, O.; Yetkin-Arik, B.; de Gooijer, M.C.; et al. Overcoming the blood-brain tumor barrier for effective glioblastoma treatment. *Drug Resist Updat* **2015**, *19*, 1-12, doi:10.1016/j.drup.2015.02.002.
14. Gould, A.; Zhang, D.; Arrieta, V.A.; et al. Delivering albumin-bound paclitaxel across the blood-brain barrier for gliomas. *Oncotarget* **2021**, *12*, 2474-2475, doi:10.18632/oncotarget.28018.
15. Belykh, E.; Shaffer, K.V.; Lin, C.; et al. Blood-Brain Barrier, Blood-Brain Tumor Barrier, and Fluorescence-Guided Neurosurgical Oncology: Delivering Optical Labels to Brain Tumors. *Front Oncol* **2020**, *10*, doi:10.3389/fonc.2020.00739.

16. Shen, Y.; Li, S.; Wang, X.; et al. Tumor vasculature remolding by thalidomide increases delivery and efficacy of cisplatin. *J Exp Clin Cancer Res* **2019**, *38*, 427, doi:10.1186/s13046-019-1366-x.

17. Huang, Y.; Goel, S.; Duda, D.G.; et al. Vascular normalization as an emerging strategy to enhance cancer immunotherapy. *Cancer Res* **2013**, *73*, 2943-2948, doi:10.1158/0008-5472.Can-12-4354.

18. Goel, S.; Duda, D.G.; Xu, L.; et al. Normalization of the vasculature for treatment of cancer and other diseases. *Physiol Rev* **2011**, *91*, 1071-1121, doi:10.1152/physrev.00038.2010.

19. Arjaans, M.; Schröder, C.P.; Oosting, S.F.; et al. VEGF pathway targeting agents, vessel normalization and tumor drug uptake: from bench to bedside. *Oncotarget* **2016**, *7*, 21247-21258, doi:10.18632/oncotarget.6918.

20. Jain, R.K. Normalization of tumor vasculature: an emerging concept in antiangiogenic therapy. *Science* **2005**, *307*, 58-62, doi:10.1126/science.1104819.

21. Ansiaux, R.; Baudelet, C.; Jordan, B.F.; et al. Thalidomide radiosensitizes tumors through early changes in the tumor microenvironment. *Clin Cancer Res* **2005**, *11*, 743-750.

22. Jain, R.K. Normalizing tumor microenvironment to treat cancer: bench to bedside to biomarkers. *J Clin Oncol* **2013**, *31*, 2205-2218, doi:10.1200/jco.2012.46.3653.

23. Carmeliet, P.; Jain, R.K. Principles and mechanisms of vessel normalization for cancer and other angiogenic diseases. *Nat Rev Drug Discov* **2011**, *10*, 417-427, doi:10.1038/nrd3455.

24. Magnussen, A.L.; Mills, I.G. Vascular normalisation as the stepping stone into tumour microenvironment transformation. *Br J Cancer* **2021**, *125*, 324-336, doi:10.1038/s41416-021-01330-z.

25. Segers, J.; Di Fazio, V.; Ansiaux, R.; et al. Potentiation of cyclophosphamide chemotherapy using the anti-angiogenic drug thalidomide: importance of optimal scheduling to exploit the 'normalization' window of the tumor vasculature. *Cancer Lett* **2006**, *244*, 129-135, doi:10.1016/j.canlet.2005.12.017.

26. Batchelor, T.T.; Sorensen, A.G.; di Tomaso, E.; et al. AZD2171, a pan-VEGF receptor tyrosine kinase inhibitor, normalizes tumor vasculature and alleviates edema in glioblastoma patients. *Cancer Cell* **2007**, *11*, 83-95, doi:10.1016/j.ccr.2006.11.021.

27. Sorensen, A.G.; Emblem, K.E.; Polaskova, P.; et al. Increased survival of glioblastoma patients who respond to antiangiogenic therapy with elevated blood perfusion. *Cancer Res* **2012**, *72*, 402-407, doi:10.1158/0008-5472.Can-11-2464.

28. Peterson, T.E.; Kirkpatrick, N.D.; Huang, Y.; et al. Dual inhibition of Ang-2 and VEGF receptors normalizes tumor vasculature and prolongs survival in glioblastoma by altering macrophages. *Proc Natl Acad Sci USA* **2016**, *113*, 4470-4475, doi:10.1073/pnas.1525349113.

29. Ahishali, B.; Kaya, M. Evaluation of Blood-Brain Barrier Integrity Using Vascular Permeability Markers: Evans Blue, Sodium Fluorescein, Albumin-Alexa Fluor Conjugates, and Horseradish Peroxidase. *Methods Mol Biol* **2021**, *2367*, 87-103, doi:10.1007/7651_2020_316.

30. Bianconi, D.; Herac, M.; Posch, F.; et al. Microvascular density assessed by CD31 predicts clinical benefit upon bevacizumab treatment in metastatic colorectal cancer: results of the PassionATE study, a translational prospective Phase II study of capecitabine and irinotecan plus bevacizumab followed by capecitabine and oxaliplatin plus bevacizumab or the reverse sequence in patients in mCRC. *Ther Adv Med Oncol* **2020**, *12*, 1758835920928635, doi:10.1177/1758835920928635.

31. Afshar Moghaddam, N.; Mahsuni, P.; Taheri, D. Evaluation of Endoglin as an Angiogenesis Marker in Glioblastoma. *Iran J Pathol* **2015**, *10*, 89-96.

32. Majchrzak, K.; Kaspera, W.; Szymaś, J.; et al. Markers of angiogenesis (CD31, CD34, rCBV) and their prognostic value in low-grade gliomas. *Neurol Neurochir Pol* **2013**, *47*, 325-331, doi:10.5114/ninp.2013.36757.

33. Bianco, J.; Bastiancich, C.; Joudiou, N.; et al. Novel model of orthotopic U-87 MG glioblastoma resection in athymic nude mice. *J Neurosc Methods* **2017**, *284*, 96-102, doi:10.1016/j.jneumeth.2017.04.019.

34. Conq, J.; Joudiou, N.; Ucakar, B.; et al. Assessment of Hyperosmolar Blood-Brain Barrier Opening in Glioblastoma via Histology with Evans Blue and DCE-MRI. *Biomedicines* **2023**, *11*, doi:10.3390/biomedicines11071957.

35. Kamoun, W.S.; Ley, C.D.; Farrar, C.T.; et al. Edema control by cediranib, a vascular endothelial growth factor receptor-targeted kinase inhibitor, prolongs survival despite persistent brain tumor growth in mice. *J Clin Oncol* **2009**, *27*, 2542-2552, doi:10.1200/jco.2008.19.9356.

36. Nicaise, C.; Mitrecic, D.; Demetter, P.; et al. Impaired blood-brain and blood-spinal cord barriers in mutant SOD1-linked ALS rat. *Brain Res* **2009**, *1301*, 152-162, doi:10.1016/j.brainres.2009.09.018.

37. del Valle, J.; Camins, A.; Pallàs, M.; et al. A new method for determining blood-brain barrier integrity based on intracardiac perfusion of an Evans Blue-Hoechst cocktail. *J Neurosci Methods* **2008**, *174*, 42-49, doi:10.1016/j.jneumeth.2008.06.025.

38. Tofts, P.S.; Brix, G.; Buckley, D.L.; et al. Estimating kinetic parameters from dynamic contrast-enhanced T(1)-weighted MRI of a diffusable tracer: standardized quantities and symbols. *J Magn Reson Imaging* **1999**, *10*, 223-232, doi:10.1002/(sici)1522-2586(199909)10:3<223::aid-jmri2>3.0.co;2-s.

39. Sourbron, S.P.; Buckley, D.L. Classic models for dynamic contrast-enhanced MRI. *NMR Biomed* **2013**, *26*, 1004-1027, doi:10.1002/nbm.2940.

40. Heye, A.K.; Thrippleton, M.J.; Armitage, P.A.; et al. Tracer kinetic modelling for DCE-MRI quantification of subtle blood-brain barrier permeability. *Neuroimage* **2016**, *125*, 446-455, doi:10.1016/j.neuroimage.2015.10.018.

41. Bankhead, P.; Loughrey, M.B.; Fernández, J.A.; et al. QuPath: Open source software for digital pathology image analysis. *Sci Rep* **2017**, *7*, 16878, doi:10.1038/s41598-017-17204-5.

42. Kane, J.R. The Role of Brain Vasculature in Glioblastoma. *Mol Neurobiol* **2019**, *56*, 6645-6653, doi:10.1007/s12035-019-1561-y.

CHAPTER VI
DISCUSSION AND PERSPECTIVES

TABLE OF CONTENTS

I. MAJOR FINDINGS

GB is currently the most common and aggressive primary malignant tumor of the central nervous system in adults. Despite an aggressive treatment involving surgical resection followed by concurrent radiotherapy/chemotherapy, the prognosis for patients with GB remains poor with a high recurrence rate. The intrinsic resistance of GB to conventional therapies is accentuated by the BBB, which prevents effective drug delivery to the tumor site. Indeed, although the BBB is often compromised in GB, it is not homogeneously: the permeability is important in the tumor core, but very low in the periphery due to an almost non-existent fenestration. Drug delivery is therefore highly heterogeneous, with a severely compromised access to tumor margins, where the infiltrating cells responsible for recurrence are located [1]. Thus, there is an urgent need to develop methods for an opening of the BBB, so that drugs can be delivered evenly to the tumor site (Chapter I).

In this thesis, we aimed to assess different innovative strategies for opening the BBB in glioblastoma. The hypothesis was that an opening of the tumor vascular bed by a mechanical (osmotic shock), physical (radiotherapy), or pharmacological (tumor vessel normalization at the early stage of anti-angiogenic treatments) approach could lead to an increase in drug delivery in glioblastoma, especially to infiltrating cells that are protected by an intact BBB (Chapter II).

Regarding the opening of the BBB by osmotic shock via infusion of a 25% (m/v) mannitol solution, a histological study using a high-molecular-weight permeability marker (EB) showed an opening of the BBB: the fluorescent dye diffused much more widely outside the tumor area after osmotic shock than in untreated tumors. However, the study of tumor hemodynamic parameters by DCE-MRI using gadolinium-DOTA as a contrast agent did not reveal any change in the BBB, whatever the parameter studied (Chapter III).

For the irradiation study, the histological study with EB revealed a complex dose-dependent effect of irradiation on BBB integrity, with increased vascular leakage at low doses (5Gy) but reduced leakage at higher doses (10Gy and 15Gy). The study of tumor hemodynamic parameters by DCE-MRI again revealed no change in BBB permeability, whatever the hemodynamic parameter studied, the pharmacokinetic model applied or the irradiation dose used (Chapter IV).

Finally, with regard to the experience of tumor vessel normalization through the use of anti-angiogenic agents (cediranib and thalidomide), the DCE-MRI and histological results did not show an exploitable time window of normalization in the U87MG GB model used. Nevertheless, the histological study, the immunohistochemical study of tumor angiogenesis and the monitoring of

tumor size did reveal a "classic" anti-angiogenic effect, indicating the efficacy of those treatments (Chapter V).

Thus, we have demonstrated that the use of a hypertonic mannitol solution to induce osmotic shock and low-dose irradiation appear to be promising methods to enhance the delivery of compounds to tumor margins in glioblastoma, while the normalization effect using an anti-angiogenic agent is still to be further investigated to be able to state a potential efficacy of its use in the treatment of glioblastoma. Furthermore, the DCE-MRI analysis method using gadolinium-DOTA as a contrast agent seems of limited value for determining the efficacy of BBB opening in this model of glioblastoma for these strategies.

The main results obtained during this Ph.D. thesis (Chapter III, IV and V) are gathered in Figure 1.

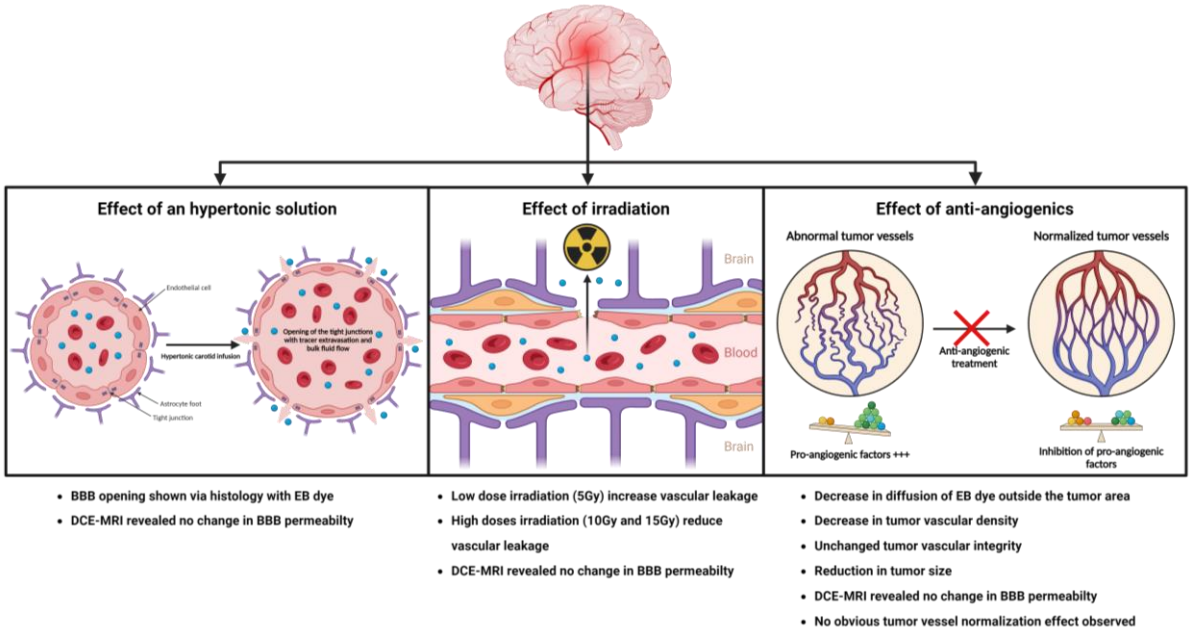

Figure 1. Major findings of the Ph.D. thesis. For the strategy assessing the effect of an hypertonic solution, the histological study with Evans blue revealed an opening of the BBB. Regarding the strategy evaluating the effect of irradiation, we observed an increase in vascular leakage for a low irradiation dose (5Gy) and a decrease in vascular leakage for higher irradiation doses (10Gy and 15Gy). For the strategy assessing the effect of anti-angiogenic agents, we did not observe any obvious tumor vessel normalization effect. Finally, for the 3 different strategies evaluated, the DCE-MRI study with Gd-DOTA as a contrast agent revealed no change in BBB permeability.
Abbreviations: BBB = Blood-brain barrier; DCE-MRI = Dynamic contrast-enhance magnetic resonance imaging.

II. DISCUSSION

II.1. SELECTION OF MARKERS TO ASSESS BBB DISRUPTION

In the three studies carried out during this thesis, we observed that DCE-MRI was of limited value to assess subtle changes in hemodynamics that likely occur after treatment, as observed by Evans Blue staining. This was true whatever the pharmacokinetic model that we used (extended Tofts or Patlak) and whatever the region under interest (tumor core or margins).

One possible reason for this problem may lie in the contrast agent used. Indeed, gadolinium-DOTA is a small molecular-sized contrast agent (580 Da) and its small size would not allow assessment of permeability modulation in an already highly fenestrated BBB.

Other gadolinium-based contrast agents (GBCAs) with a larger molecular size, such as Gadobenate dimeglumine (1058 Da) [2], could thus have been used. An additional advantage of using Gadobenate, although clinically indicated for liver imaging, is that it has a high affinity for albumin which would mimic the distribution behavior of EB, allowing better comparison with histological study [3].

However, the choice of Gd-DOTA as a contrast agent was justified for several reasons. Firstly, because this contrast agent has a clinical indication for the characterization of brain tumors in patients. Secondly, previous studies have shown that MRI with this contrast agent or GBCAs with a similar molecular weight (Gadoteridol = 558 Da, Gd-DTPA = 547 Da, or Gadobutrol = 604 Da) was useful in preclinical models to assess changes in BBB permeability and to evaluate the effect of strategies opening the BBB [4-9]. Thirdly, as the BBB is poorly or not fenestrated at tumor margins, the use of this small-sized contrast agent was suitable to assess the opening modulation of this poorly permeabilized BBB.

An LC/MS measurement of gadolinium-DOTA on brain sections could also have been carried out to provide a more accurate quantification of Gd-DOTA diffusion in the brain parenchyma.

Regarding the marker used in the histological studies, EB was a good vascular leakage marker to use. Indeed, in addition to being a fluorescent agent allowing its diffusion in the brain parenchyma to be correctly visualized by fluorescent microscopy, it binds to plasmatic albumin making it a large marker of vascular leakage, enabling the opening modulation of the highly permeabilized BBB in GB to be seen. It is probably thanks to this size characteristic that we were able to see significant differences in its diffusion in the brain parenchyma after the opening of the tumoral BBB.

However, its major disadvantage is that it cannot be translated into clinical applications, given the invasive aspect of its use. Moreover, even for pre-clinical studies, it is not the easiest to set up, and in terms of animal ethics, it does not participate in the 3R principle (replacement, reduction, refinement) [10], since it requires the sacrifice of many animals if we want to assess marker diffusion in the brain parenchyma at several time points.

II.2. RELEVANCE OF THE GLIOBLASTOMA MODEL USED

An important limitation is that the studies were carried out on a single model of glioblastoma, the orthotopic U87MG model grafted onto nude mice.

The main advantage of this model is that it has a well delimited volume in the brain, enabling the tumor core to be clearly defined, facilitating the analysis by MRI. It also has high engraftment rates and good reproducibility [11]. However, its main advantage is also its main drawback, as its well delimited volume is due to a lack of typical infiltrative and proliferative pattern that is observed in human glioblastoma, and therefore do not truly reflect the biological nature of glioblastoma [12-14]. Its phenotypic and genomic characteristics also do not faithfully reflect the patient's original tumors [15-18]. Furthermore, as U87MG cells are human glioblastoma cells, it can only be transplanted into immunodeficient mice, and the tumor immune environment in this model differs innately from that found in humans [19].

Thus, it would have been interesting to use other animal models for the evaluation of BBB opening, a model that better reflects the features of glioblastoma, such as the GL261 model for example. Indeed, although this is a syngeneic model with murine tumor cells grafted, it better recapitulates the histological and biological characteristics of glioblastoma [20]. Moreover, the greatest advantage of syngeneic model is that it uses immunocompetent mice and is therefore more representative of the tumor immune environment [21]. However, as the model is largely diffusing in the brain parenchyma, the tumor volume is much less well defined, and MRI analysis would have been more complex to do.

Furthermore, it is important to emphasize the limitation of using an animal model to translate scientific findings into practical clinical applications, particularly in the cancer field [22]. Indeed, the perfect model imitating exactly all characteristics of human GB (e.g., intratumoral heterogeneity, invasive properties, resistance to radio- and chemotherapy) doesn't exist – so far [23]. One feature that differs significantly between human glioblastoma and glioblastoma animal models that is important to consider in our studies as it may impact tumor perfusion and BBB permeability, is tumor angiogenesis. Indeed, GB animal models have a rapid tumor growth compared to human

glioblastoma, leading to a much more pronounced angiogenic activity and thus a different vascularization pattern.

II.3. LIMITATIONS OF THE BBB OPENING STRATEGIES USED

Regarding osmotic shock, one of the main limitations of this technique is that, although it is transient, it does not target tumor tissue. Indeed, it spreads throughout the brain, which can be highly toxic for brain parenchyma tissue that is still healthy and would be problematic from a clinical point of view [24,25]. However, based on the histological study, we observe a BBB opening only in the periphery of the tumor and not throughout the brain, even if we increase the intensity of the Cy5 filter (Figure 1A). This could possibly be explained by the fact that the opening is dependent of the hypertonic solution perfusion in the blood vessels. Yet the tumor area is much more perfused than the healthy area of the brain, resulting in a better opening around the tumor area than in the healthy area. Further studies would be necessary to confirm or refute this tumor-focused effect of BBB opening by osmotic shock in glioblastoma. In addition, the technique is invasive, requiring an intra-carotid injection, which is another drawback to its clinical application [26].

To implement this strategy, we opted for a hypertonic mannitol solution. Indeed, this solution is the most widely described and used in the literature for BBB opening by osmotic shock. However, other hypertonic solutions have been described in the literature to open the BBB by osmotic shock. A hypertonic arabinose solution, for example, with the advantage of being less viscous than a mannitol solution [25,27].

Concerning irradiation, although three different incremental doses were administered to assess BBB permeability as a function of the increasing dose given, this administration was done in single-dose. However, this is not representative of the fractionated or hypofractionated regimen that can be found clinically for the treatment of newly diagnosed or recurrent glioblastoma [28,29]. The use of a regimen with increasing doses but fractionated administration would better mimic the clinical situation.

In addition, it's important to highlight that irradiation was carried out on the whole brain, thus irradiating healthy brain tissue. Indeed, the cesium-137 irradiator used for the study was not suitable for targeted radiotherapy, and we did not have any targeted irradiation equipment at our disposal.

However, as with osmotic shock BBB opening, based on the histological study, we observe a BBB opening only in the periphery of the tumor and not throughout the brain, even if we increase the

intensity of the Cy5 filter (Figure 1B). To date, we have no definitive explanation for this. One tentative of explanation could be that the vessels in the periphery of the tumor would already be slightly fenestrated but would not be fenestrated enough to allow the passage of the Evans blue-albumin complex (high molecular weight, 69 kDa) when there is no irradiation and would open sufficiently to allow the passage of the Evans blue-albumin complex when irradiation is applied, whereas healthy vessels are not fenestrated at baseline and would never be sufficiently fenestrated with low doses of irradiation to allow the passage of Evans blue-albumin complex, and increasing the irradiation dose would directly destroy the vessels without seeing a fenestration step. Further studies would be necessary to assess the BBB opening modulation by irradiation in the healthy brain parenchyma in glioblastoma.

Moreover, studying the effect of targeted radiotherapy on the opening of the BBB tumor would be of interest and would have the advantage of being transposable to the clinic.

Highly targeted irradiation use would also have the advantage of being able to considerably increase the irradiation dose used, since only the tumor region would be targeted and healthy regions would less be affected by the irradiation, as described by Sabatasso et al. [30] where they showed a transient increase in vessel permeability in a time-dependent manner with a maximum between 45 min and 2 h after irradiation, using microbeam irradiation with irradiation doses of up to 150Gy in one shot. However, to achieve these irradiation doses and precision, they had to use a synchrotron, which is a difficult-to-access machine.

For the tumor vessel normalization strategy, because the normalization effect has been reported to be dose- and time-dependent [31-33], we used the same dose and scheme of treatment than in other studies [34-36]. The timing of acquisition or the dose used may not have been the most suitable for the glioblastoma model we used. Therefore, it could be interesting to analyze hemodynamics changes every day instead of every other day or use anti-angiogenic agents at different dosages so as not to miss a possible normalization windows effect. It might also be interesting to analyze these effects in other glioblastoma models.

A final BBB opening strategy that could have been evaluated during this thesis in collaboration with a Paris university is the use of FUS with microbubbles [37]. Unfortunately, due to the covid-19 pandemic, this collaboration was not possible. It would have been very interesting to be able to evaluate this strategy in glioblastoma, as it is currently the most successful and promising strategy to open the BBB, with also the most clinical studies ongoing [38-40].

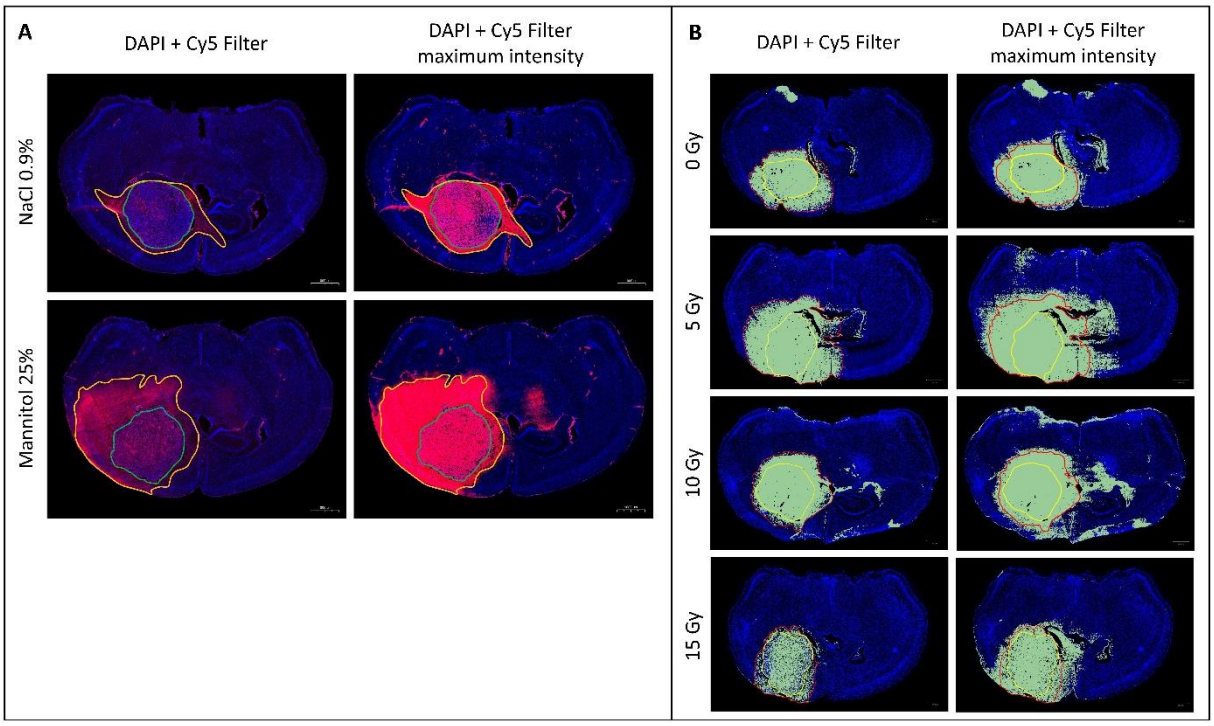

Figure 2. Illustration of the histological studies for the strategies of BBB opening by osmotic shock and irradiation with increased Cy5 filter intensity. We can see here that even with the Cy5 filter intensity increased to the maximum for the histological studies of the strategies for BBB opening by osmotic shock (**A**) and by irradiation (**B**), we still do not see any diffusion of the Evans Blue vascular leakage marker in the healthy brain parenchyma.

III. PERSPECTIVES

III.1. OPTIMIZATION OF BBB OPENING PROTOCOLS

As mentioned in the II.3. Limitations section, evaluation of BBB opening with a fractionated irradiation protocol closer to the clinical situation should be performed. The experimental scheme for fractionated irradiation with increasing doses could be as follows: 5 groups of mice each receiving 3x0Gy (control), 3x2Gy (6Gy), 3x3Gy (9Gy), 3x4Gy (12Gy) and 3x5Gy (15Gy), with administration of the irradiation doses at 1-day intervals, ideally using an irradiator allowing radiotherapy to be focused on the tumor tissue. Getting closer to the clinical protocol would enable us to see on the one hand whether there is indeed a modulation of BBB opening with fractionated or hypofractionated administration, and on the other hand, if there is BBB opening, at what time this opening occurs in order to potentially adapt the clinical protocol of concomitant chemotherapy administration to administer them at the time of greatest BBB fenestration by irradiation. This would maximize the synergistic effect between radiotherapy and chemotherapy.

Another important point would be to extend the strategy of BBB opening by irradiation to brachytherapy. Indeed, although the use of brachytherapy iodine-125 has not shown a significant

survival advantage for newly diagnosed patients [41], it remains an option used in the treatment of recurrent GB [42]. Furthermore, previous work has shown that low dose rate (LDR) brachytherapy (1.5 Gy per day), using 0.5 mCi iodine-125 seeds, increased pO_2 and blood perfusion in a liver tumor respectively 24h and 72h after seeds implantation [43]. Thus, it would be relevant to investigate the effect of brachytherapy on BBB opening.

In the same field, it would also be interesting to extend the strategy of opening the BBB by irradiation to tumor-targeted radiolabeled compounds (radioisotopes coupled to antibodies, peptides or nanomedicines). Indeed, previous works have shown an interest in using these radiotoxic compounds in the treatment of glioblastoma [44,45]. Thus, it would be of interest to evaluate the potential effect of these irradiating compounds on the modulation of BBB opening.

For the osmotic shock study, as described in II.3 Limitations section, it would be interesting to complete the study using an arabinose-based hypertonic solution in order to compare the effect of different hypertonic solutions on this BBB opening strategy.

With regard to normalization, in addition to modifying the timing of data acquisition or adjusting the dosage of anti-angiogenic agents to ensure that the normalization window is not missed, the use of other anti-angiogenic agents should be used. Bevacizumab, for example, is an ideal candidate as it already has FDA approval for clinical use in recurrent GB. It would also be interesting to combine different anti-angiogenic agents to study the synergistic effect they might have on tumor perfusion and permeability.

Finally, it would be relevant to evaluate the association of different BBB opening strategies, such as the opening of irradiation with the normalization of tumor vessels for example, to allow synergy between improved tumor perfusion from normalization and improved BBB permeability from irradiation. Or combine one of the BBB opening strategies with other BBB crossing strategies such as active targeting of the BBB transcellular transport mechanisms to improve transcellular passage by grafting the drug with transferin (targeting the transferin receptor) [46] or angiopep-2 (targeting the low-density lipoprotein receptor linked to protein 1) [47] for example, thus enabling synergy between facilitated paracellular and transcellular passage to improve drug delivery.

III.2. IMPROVING BBB OPENING ASSESSMENT TECHNIQUES

To complement the histological studies, dextran would be highly relevant here as a marker of vascular leakage, given that it can come in a variety of sizes. This would allow us to define the modulation of BBB opening much more precisely, and thus give a range of molecular sizes that may or may not pass the BBB before and after opening.

With regard to the use of MRI as an imaging system to assess BBB opening, a DCE-MRI study should be repeated using another more suitable contrast agent, such as gadobenate, as described previously. Moreover, studies should be complemented with other MRI techniques such as DSC-MRI to provide an overview of tumor perfusion, which would be a definite benefit, especially for the study of normalization. Here, DCE-MRI provides an overview of BBB permeability, but only an indirect idea of tumor perfusion. DSC-MRI has already been described in I.3.2 Medical imaging section of the introduction. Briefly, based on the first pass of a GBCA, this MRI technique can be used to determine perfusion parameters such as blood volume, blood flow and mean transit time.

The use of radiolabeled albumin measured via PET to assess BBB opening could also be of interest [48]. Indeed, like MRI with gadobenate, it would mimic the distribution behavior of EB, thus allowing a comparison with the histological study.

III.3. EFFECTIVENESS OF ANTI-CANCER DRUGS ASSOCIATED WITH BBB OPENING STRATEGIES

Apart from better drug delivery to tumor cells, the real endpoint of these studies is to improve the efficacy of drugs on GB.

Thus, in addition to the study of BBB-opening strategies' impact on the biodistribution of an anti-cancer drug, which would already be a worthwhile first step, an evaluation of the anti-cancer drug's efficacy (overall survival study or tumor size monitoring) in association with a BBB-opening technique would be important to carry out.

In terms of anti-cancer drugs that can be used, we could consider chemotherapies such as doxorubicin, paclitaxel or albumin-paclitaxel (abraxane), which have shown interesting preclinical effects on glioblastoma [49-53], or targeted therapies such as erlotinib [54], cilengitib [55,56], gefitinib [57], nimotuzumab [58] or cetuximab [59,60], which have demonstrated sufficient efficacy in preclinical studies to reach clinical trials, but have failed to reveal a real clinical benefit (on progression-free survival and overall survival), perhaps due to a lack of BBB passage impeding a sufficient therapeutic concentration at the tumor site. Therefore, completing these studies in

association with a BBB-opening strategy may provide better results (mainly for large molecules such as antibodies). Bevacizumab could also be used here, this time as a therapeutic agent and not to normalize tumor vessels, given that it has not shown any clinical benefit in newly diagnosed glioblastoma either.

As part of the biodistribution study, labelling with a PET radioactive probe would be the most suitable, enabling the delivery of the drug to be seen directly and very accurately. The use of nanomedicines would also have a definite advantage. Indeed, besides all the advantages that the nanoparticulate delivery system can already bring to the active pharmaceutical ingredient (increasing its stability and solubility, enabling targeted delivery, etc.), the size of the nanomedicines could be varied to assess more precisely the modulation of the BBB opening and the size of nanomedicine that could enter. Furthermore, it would be possible to load the nanomedicines with USPIOs (ultrasmall superparamagnetic iron oxid) nanoparticles for instance or to radiolabel them to monitor their distribution in the brain parenchyma using MRI or PET imaging [61,62].

III.4. PERSONAL OPINION ON PRIORITIES AND MI-TERMS PROJECTS

Glioblastoma is a cancer presenting a very poor prognosis and with, to date, a very ineffective therapeutic protocol. There is therefore an urgent need to develop new strategies for its treatment. However, the intrinsic characteristics of this cancer constitute numerous obstacles to the development of these new therapeutic strategies.

In this thesis, we considered different strategies focused on the tumoral BBB opening, in particular at the tumor margins, since the BBB is a major obstacle to the success of the treatment by severely limiting the delivery of the drug to the tumor site.

Among the 3 strategies evaluated during this thesis, the most promising for me would be the BBB opening by irradiation. In fact, it offers several advantages: firstly, we were able to observe an opening of the BBB for low doses of irradiation, thus limiting radiotoxicity for healthy tissues. Secondly, although not observed in our studies, this strategy is described as transient, thus limiting the neurotoxicity associated with a permanently open BBB. Finally, the greatest strength of this strategy is that radiotherapy is already included in the SOC protocol for glioblastoma. Furthermore, the field of radiotherapy is vast and we could, as mentioned earlier, apply this strategy to different methods of irradiation: brachytherapy, radioimmunotherapy or targeted radiotherapy, for example.

Regarding the BBB opening by osmotic shock, it has shown interesting results, however it requires an injection of at least one minute into the carotid artery each time we want a BBB opening. Thus, this strategy seems to me to be difficult to transpose into clinics, given its invasive nature, the complexity of implementing it in a clinical protocol and, above all, the fact that it is too exhausting and constraining for the patient, who is already undergoing heavy treatment.

As for improving drug delivery by normalizing tumor vessels, we have not observed any such effect with the anti-angiogenic agents cediranib and thalidomide. Although the normalization effect has been shown in the literature for other cancers, I do not think it is the most promising therapeutic strategy, at least applied to glioblastoma, and if I had to continue research in this field, I would not continue with this strategy.

Finally, a technique to open the BBB which I believe to be the most promising nowadays, and which unfortunately I was not able to try out during this thesis, is the FUS with microbubbles. Indeed, this method has several advantages: it is non-invasive (or at least very few invasive if we include the IV injection of the microbubbles), it is reversible and, above all, it is targeted, with very few side-effects for the patient to date. In addition, numerous clinical trials are currently undergoing for the treatment of newly diagnosed glioblastoma or recurrent glioblastoma, and are already showing promising results.

Concerning the methods used to assess the BBB opening, we have seen that the use of gd-DOTA for MRI was not conclusive. I believe that the use of gadobenate would be more appropriate for future MRI studies. The use of Evans blue as a marker of vascular leakage was conclusive and would therefore be a marker to keep for future studies. Other methods to complete the assessment of BBB opening would also be interesting to consider for future experiments, such as the assessment of tight junction protein expression or the measurement of gadolinium by LC/MS in brain tissue.

Thus, if I were to continue my work on this project, I would focus on the strategies of BBB opening by hypofractionated irradiation and focused ultrasound with microbubble injection, as well as combining these two strategies to see if there is a synergistic effect, using MRI as a method to assess BBB opening but this time with gadobenate as a contrast agent. In addition, to complement this MRI assessment, I would again use Evans blue as a marker of vascular leakage, measure gadolinium in brain tissue more sensitively by LC/MS, assess tight junction protein expression and evaluate angiogenesis by CD31.

IV. REFERENCES

1. Zhou, Y.; Peng, Z.; Seven, E.S.; et al. Crossing the blood-brain barrier with nanoparticles. *J Control Release* **2018**, *270*, 290-303, doi:10.1016/j.jconrel.2017.12.015.
2. Spampinato, M.V.; Nguyen, S.A.; Rumboldt, Z. Comparison of gadobenate dimeglumine and gadodiamide in the evaluation of spinal vascular anatomy with MR angiography. *AJNR Am J Neuroradiol* **2010**, *31*, 1151-1156, doi:10.3174/ajnr.A1974.
3. Cavagna, F.M.; Maggioni, F.; Castelli, P.M.; et al. Gadolinium chelates with weak binding to serum proteins. A new class of high-efficiency, general purpose contrast agents for magnetic resonance imaging. *Invest Radiol* **1997**, *32*, 780-796, doi:10.1097/00004424-199712000-00009.
4. Chu, C.; Liu, G.; Janowski, M.; et al. Real-Time MRI Guidance for Reproducible Hyperosmolar Opening of the Blood-Brain Barrier in Mice. *Front Neurol* **2018**, *9*, 921, doi:10.3389/fneur.2018.00921.
5. Rhine, W.D.; Benaron, D.A.; Enzmann, D.R.; et al. Gd-DTPA MR detection of blood-brain barrier opening in rats after hyperosmotic shock. *J Comput Assist Tomogr* **1993**, *17*, 563-566, doi:10.1097/00004728-199307000-00008.
6. Blanchette, M.; Pellerin, M.; Tremblay, L.; et al. Real-time monitoring of gadolinium diethylenetriamine penta-acetic acid during osmotic blood-brain barrier disruption using magnetic resonance imaging in normal wistar rats. *Neurosurgery* **2009**, *65*, 344-350; discussion 350-341, doi:10.1227/01.Neu.0000349762.17256.9e.
7. Ahmed, M.H.; Hernández-Verdin, I.; Quissac, E.; et al. Low-Intensity Pulsed Ultrasound-Mediated Blood-Brain Barrier Opening Increases Anti-Programmed Death-Ligand 1 Delivery and Efficacy in Gl261 Mouse Model. *Pharmaceutics* **2023**, *15*, doi:10.3390/pharmaceutics15020455.
8. Wang, J.; Li, Z.; Pan, M.; et al. Ultrasound-mediated blood–brain barrier opening: An effective drug delivery system for theranostics of brain diseases. *Advanced Drug Delivery Reviews* **2022**, *190*, 114539, doi:10.1016/j.addr.2022.114539.
9. Coluccia, D.; Figueiredo, C.A.; Wu, M.Y.; et al. Enhancing glioblastoma treatment using cisplatin-gold-nanoparticle conjugates and targeted delivery with magnetic resonance-guided focused ultrasound. *Nanomedicine: Nanotechnology, Biology and Medicine* **2018**, *14*, 1137-1148, doi:10.1016/j.nano.2018.01.021.
10. Hubrecht, R.C.; Carter, E. The 3Rs and Humane Experimental Technique: Implementing Change. *Animals (Basel)* **2019**, *9*, doi:10.3390/ani9100754.
11. Huszthy, P.C.; Daphu, I.; Niclou, S.P.; et al. In vivo models of primary brain tumors: pitfalls and perspectives. *Neuro Oncol* **2012**, *14*, 979-993, doi:10.1093/neuonc/nos135.
12. Mahesparan, R.; Read, T.A.; Lund-Johansen, M.; et al. Expression of extracellular matrix components in a highly infiltrative in vivo glioma model. *Acta Neuropathol* **2003**, *105*, 49-57, doi:10.1007/s00401-002-0610-0.
13. Kijima, N.; Hosen, N.; Kagawa, N.; et al. Wilms' tumor 1 is involved in tumorigenicity of glioblastoma by regulating cell proliferation and apoptosis. *Anticancer Res* **2014**, *34*, 61-67.
14. Akter, F.; Simon, B.; de Boer, N.L.; et al. Pre-clinical tumor models of primary brain tumors: Challenges and opportunities. *Biochim Biophys Acta Rev Cancer* **2021**, *1875*, 188458, doi:10.1016/j.bbcan.2020.188458.

15. Frese, K.K.; Tuveson, D.A. Maximizing mouse cancer models. *Nat Rev Cancer* **2007**, *7*, 654-658, doi:10.1038/nrc2192.

16. Anderson, R.C.; Elder, J.B.; Brown, M.D.; et al. Changes in the immunologic phenotype of human malignant glioma cells after passaging in vitro. *Clin Immunol* **2002**, *102*, 84-95, doi:10.1006/clim.2001.5152.

17. Ernst, A.; Hofmann, S.; Ahmadi, R.; et al. Genomic and expression profiling of glioblastoma stem cell-like spheroid cultures identifies novel tumor-relevant genes associated with survival. *Clin Cancer Res* **2009**, *15*, 6541-6550, doi:10.1158/1078-0432.Ccr-09-0695.

18. Clark, M.J.; Homer, N.; O'Connor, B.D.; et al. U87MG decoded: the genomic sequence of a cytogenetically aberrant human cancer cell line. *PLoS Genet* **2010**, *6*, e1000832, doi:10.1371/journal.pgen.1000832.

19. Hicks, W.H.; Bird, C.E.; Traylor, J.I.; et al. Contemporary Mouse Models in Glioma Research. *Cells* **2021**, *10*, doi:10.3390/cells10030712.

20. Oh, T.; Fakurnejad, S.; Sayegh, E.T.; et al. Immunocompetent murine models for the study of glioblastoma immunotherapy. *J Transl Med* **2014**, *12*, 107, doi:10.1186/1479-5876-12-107.

21. Chulpanova, D.S.; Kitaeva, K.V.; Rutland, C.S.; et al. Mouse Tumor Models for Advanced Cancer Immunotherapy. *Int J Mol Sci* **2020**, *21*, doi:10.3390/ijms21114118.

22. Mak, I.W.; Evaniew, N.; Ghert, M. Lost in translation: animal models and clinical trials in cancer treatment. *Am J Transl Res* **2014**, *6*, 114-118.

23. Haddad, A.F.; Young, J.S.; Amara, D.; et al. Mouse models of glioblastoma for the evaluation of novel therapeutic strategies. *Neurooncol Adv* **2021**, *3*, vdab100, doi:10.1093/noajnl/vdab100.

24. Rapoport, S.I. Effect of concentrated solutions on blood-brain barrier. *Am J Physiol* **1970**, *219*, 270-274, doi:10.1152/ajplegacy.1970.219.1.270.

25. Rapoport, S.I.; Hori, M.; Klatzo, I. Testing of a hypothesis for osmotic opening of the blood-brain barrier. *Am J Physiol* **1972**, *223*, 323-331, doi:10.1152/ajplegacy.1972.223.2.323.

26. Siegal, T.; Rubinstein, R.; Bokstein, F.; et al. In vivo assessment of the window of barrier opening after osmotic blood-brain barrier disruption in humans. *J Neurosurg* **2000**, *92*, 599-605, doi:10.3171/jns.2000.92.4.0599.

27. Rapoport, S.I. Advances in osmotic opening of the blood-brain barrier to enhance CNS chemotherapy. *Expert Opin Investig Drugs* **2001**, *10*, 1809-1818, doi:10.1517/13543784.10.10.1809.

28. Dhermain, F. Radiotherapy of high-grade gliomas: current standards and new concepts, innovations in imaging and radiotherapy, and new therapeutic approaches. *Chin J Cancer* **2014**, *33*, 16-24, doi:10.5732/cjc.013.10217.

29. Stupp, R.; Mason, W.P.; van den Bent, M.J.; et al. Radiotherapy plus concomitant and adjuvant temozolomide for glioblastoma. *N Engl J Med* **2005**, *352*, 987-996, doi:10.1056/NEJMoa043330.

30. Sabatasso, S.; Fernandez-Palomo, C.; Hlushchuk, R.; et al. Transient and Efficient Vascular Permeability Window for Adjuvant Drug Delivery Triggered by Microbeam Radiation. *Cancers (Basel)* **2021**, *13*, doi:10.3390/cancers13092103.

31. Jain, R.K. Normalization of tumor vasculature: an emerging concept in antiangiogenic therapy. *Science* **2005**, *307*, 58-62, doi:10.1126/science.1104819.

32. Jain, R.K. Normalizing tumor microenvironment to treat cancer: bench to bedside to biomarkers. *J Clin Oncol* **2013**, *31*, 2205-2218, doi:10.1200/jco.2012.46.3653.

33. Jain, R.K. Antiangiogenesis strategies revisited: from starving tumors to alleviating hypoxia. *Cancer Cell* **2014**, *26*, 605-622, doi:10.1016/j.ccell.2014.10.006.

34. Ansiaux, R.; Baudelet, C.; Jordan, B.F.; et al. Thalidomide radiosensitizes tumors through early changes in the tumor microenvironment. *Clin Cancer Res* **2005**, *11*, 743-750.

35. Kamoun, W.S.; Ley, C.D.; Farrar, C.T.; et al. Edema control by cediranib, a vascular endothelial growth factor receptor-targeted kinase inhibitor, prolongs survival despite persistent brain tumor growth in mice. *J Clin Oncol* **2009**, *27*, 2542-2552, doi:10.1200/jco.2008.19.9356.

36. Shen, Y.; Li, S.; Wang, X.; et al. Tumor vasculature remolding by thalidomide increases delivery and efficacy of cisplatin. *J Exp Clin Cancer Res* **2019**, *38*, 427, doi:10.1186/s13046-019-1366-x.

37. Aryal, M.; Arvanitis, C.D.; Alexander, P.M.; et al. Ultrasound-mediated blood-brain barrier disruption for targeted drug delivery in the central nervous system. *Adv Drug Deliv Rev* **2014**, *72*, 94-109, doi:10.1016/j.addr.2014.01.008.

38. Treat, L.H.; McDannold, N.; Zhang, Y.; et al. Improved anti-tumor effect of liposomal doxorubicin after targeted blood-brain barrier disruption by MRI-guided focused ultrasound in rat glioma. *Ultrasound Med Biol* **2012**, *38*, 1716-1725, doi:10.1016/j.ultrasmedbio.2012.04.015.

39. Kovacs, Z.; Werner, B.; Rassi, A.; et al. Prolonged survival upon ultrasound-enhanced doxorubicin delivery in two syngenic glioblastoma mouse models. *J Control Release* **2014**, *187*, 74-82, doi:10.1016/j.jconrel.2014.05.033.

40. Alli, S.; Figueiredo, C.A.; Golbourn, B.; et al. Brainstem blood brain barrier disruption using focused ultrasound: A demonstration of feasibility and enhanced doxorubicin delivery. *J Control Release* **2018**, *281*, 29-41, doi:10.1016/j.jconrel.2018.05.005.

41. Barani, I.J.; Larson, D.A. Radiation therapy of glioblastoma. *Cancer Treat Res* **2015**, *163*, 49-73, doi:10.1007/978-3-319-12048-5_4.

42. Davis, M.E. Glioblastoma: Overview of Disease and Treatment. *Clin J Oncol Nurs* **2016**, *20*, S2-8, doi:10.1188/16.Cjon.S1.2-8.

43. Cron, G.O.; Beghein, N.; Crokart, N.; et al. Changes in the tumor microenvironment during low-dose-rate permanent seed implantation iodine-125 brachytherapy. *Int J Radiat Oncol Biol Phys* **2005**, *63*, 1245-1251, doi:10.1016/j.ijrobp.2005.07.971.

44. Bailly, C.; Vidal, A.; Bonnemaire, C.; et al. Potential for Nuclear Medicine Therapy for Glioblastoma Treatment. *Front Pharmacol* **2019**, *10*, 772, doi:10.3389/fphar.2019.00772.

45. Cordier, D.; Krolicki, L.; Morgenstern, A.; et al. Targeted Radiolabeled Compounds in Glioma Therapy. *Semin Nucl Med* **2016**, *46*, 243-249, doi:10.1053/j.semnuclmed.2016.01.009.

46. Cui, Y.; Xu, Q.; Chow, P.K.; et al. Transferrin-conjugated magnetic silica PLGA nanoparticles loaded with doxorubicin and paclitaxel for brain glioma treatment. *Biomaterials* **2013**, *34*, 8511-8520, doi:10.1016/j.biomaterials.2013.07.075.

47. Xin, H.; Jiang, X.; Gu, J.; et al. Angiopep-conjugated poly(ethylene glycol)-co-poly(ε-caprolactone) nanoparticles as dual-targeting drug delivery system for brain glioma. *Biomaterials* **2011**, *32*, 4293-4305, doi:10.1016/j.biomaterials.2011.02.044.

48. Brady, M.; Raghavan, R.; Sampson, J. Determinants of Intraparenchymal Infusion Distributions: Modeling and Analyses of Human Glioblastoma Trials. *Pharmaceutics* **2020**, *12*, doi:10.3390/pharmaceutics12090895.

49. Lu, J.; Xu, F.; Rao, C.; et al. Mechanism of action of paclitaxel for treating glioblastoma based on single-cell RNA sequencing data and network pharmacology. *Front Pharmacol* **2022**, *13*, 1076958, doi:10.3389/fphar.2022.1076958.

50. Lesniak, M.S.; Upadhyay, U.; Goodwin, R.; et al. Local delivery of doxorubicin for the treatment of malignant brain tumors in rats. *Anticancer Res* **2005**, *25*, 3825-3831.

51. Norouzi, M.; Yathindranath, V.; Thliveris, J.A.; et al. Doxorubicin-loaded iron oxide nanoparticles for glioblastoma therapy: a combinational approach for enhanced delivery of nanoparticles. *Scientific Reports* **2020**, *10*, 11292, doi:10.1038/s41598-020-68017-y.

52. Zhang, D.Y.; Dmello, C.; Chen, L.; et al. Ultrasound-mediated Delivery of Paclitaxel for Glioma: A Comparative Study of Distribution, Toxicity, and Efficacy of Albumin-bound Versus Cremophor Formulations. *Clin Cancer Res* **2020**, *26*, 477-486, doi:10.1158/1078-0432.Ccr-19-2182.

53. Gould, A.; Zhang, D.; Arrieta, V.A.; et al. Delivering albumin-bound paclitaxel across the blood-brain barrier for gliomas. *Oncotarget* **2021**, *12*, 2474-2475, doi:10.18632/oncotarget.28018.

54. Prados, M.D.; Chang, S.M.; Butowski, N.; et al. Phase II study of erlotinib plus temozolomide during and after radiation therapy in patients with newly diagnosed glioblastoma multiforme or gliosarcoma. *J Clin Oncol* **2009**, *27*, 579-584, doi:10.1200/jco.2008.18.9639.

55. Nabors, L.B.; Fink, K.L.; Mikkelsen, T.; et al. Two cilengitide regimens in combination with standard treatment for patients with newly diagnosed glioblastoma and unmethylated MGMT gene promoter: results of the open-label, controlled, randomized phase II CORE study. *Neuro Oncol* **2015**, *17*, 708-717, doi:10.1093/neuonc/nou356.

56. Stupp, R.; Hegi, M.E.; Gorlia, T.; et al. Cilengitide combined with standard treatment for patients with newly diagnosed glioblastoma with methylated MGMT promoter (CENTRIC EORTC 26071-22072 study): a multicentre, randomised, open-label, phase 3 trial. *Lancet Oncol* **2014**, *15*, 1100-1108, doi:10.1016/s1470-2045(14)70379-1.

57. Uhm, J.H.; Ballman, K.V.; Wu, W.; et al. Phase II evaluation of gefitinib in patients with newly diagnosed Grade 4 astrocytoma: Mayo/North Central Cancer Treatment Group Study N0074. *Int J Radiat Oncol Biol Phys* **2011**, *80*, 347-353, doi:10.1016/j.ijrobp.2010.01.070.

58. Westphal, M.; Heese, O.; Steinbach, J.P.; et al. A randomised, open label phase III trial with nimotuzumab, an anti-epidermal growth factor receptor monoclonal antibody in the treatment of newly diagnosed adult glioblastoma. *Eur J Cancer* **2015**, *51*, 522-532, doi:10.1016/j.ejca.2014.12.019.

59. Lv, S.; Teugels, E.; Sadones, J.; et al. Correlation of EGFR, IDH1 and PTEN status with the outcome of patients with recurrent glioblastoma treated in a phase II clinical trial with the EGFR-blocking monoclonal antibody cetuximab. *Int J Oncol* **2012**, *41*, 1029-1035, doi:10.3892/ijo.2012.1539.

60. Combs, S.E.; Heeger, S.; Haselmann, R.; et al. Treatment of primary glioblastoma multiforme with cetuximab, radiotherapy and temozolomide (GERT)--phase I/II trial: study protocol. *BMC Cancer* **2006**, *6*, 133, doi:10.1186/1471-2407-6-133.

61. Houston, Z.H.; Bunt, J.; Chen, K.S.; et al. Understanding the Uptake of Nanomedicines at Different Stages of Brain Cancer Using a Modular Nanocarrier Platform and Precision Bispecific Antibodies. *ACS Cent Sci* **2020**, *6*, 727-738, doi:10.1021/acscentsci.9b01299.

62. Lammers, T.; Koczera, P.; Fokong, S.; et al. Theranostic USPIO-Loaded Microbubbles for Mediating and Monitoring Blood-Brain Barrier Permeation. *Adv Funct Mater* **2015**, *25*, 36-43, doi:10.1002/adfm.201401199.